Mathematical modeling and evolutionary processes

Martín Andrade Restrepo

▶ **To cite this version:**

Martín Andrade Restrepo. Mathematical modeling and evolutionary processes. Molecular biology. Université Sorbonne Paris Cité, 2019. English. NNT : 2019USPCC021 . tel-02535689v2

HAL Id: tel-02535689

https://theses.hal.science/tel-02535689v2

Submitted on 5 Oct 2020

HAL is a multi-disciplinary open access archive for the deposit and dissemination of scientific research documents, whether they are published or not. The documents may come from teaching and research institutions in France or abroad, or from public or private research centers.

L'archive ouverte pluridisciplinaire **HAL**, est destinée au dépôt et à la diffusion de documents scientifiques de niveau recherche, publiés ou non, émanant des établissements d'enseignement et de recherche français ou étrangers, des laboratoires publics ou privés.

Université Sorbonne Paris Cité

université PARIS DIDEROT PARIS 7

Thèse de Doctorat

de l'Université Sorbonne Paris Cité

Préparée à l'Université Paris Diderot

École Doctorale 393: Pierre Louis de Santé Publique à Paris
Epidémiologie et Sciences de l'Information Biomédicale

Equipe de Biologie Computationnelle et Biomathématiques à l'Institut Jacques Monod

Mathematical Modeling and Evolutionary Processes

Martín Andrade Restrepo

Thèse de Doctorat de Biomathématique

Dirigée par Khashayar PAKDAMAN

Présentée et soutenue publiquement à Paris le 26 Juin 2019

Président du jury:	M.	Benoit Perthame	Sorbonne Université
Rapporteure:	Mme.	Annick Lesne	Sorbonne Université
Rapporteur:	M.	Nicolas Meunier	Université d'Évry Val d'Essonne
Examinateur:	M.	Regis Ferrière	ENS & University of Arizona
Examinateur:	M.	Nicolas Champagnat	Université de Lorraine
Examinateur:	M.	Jens Starke	University of Rostock
Examinatrice:	Mme.	Silvia De Monte	ENS
Directeur de thèse:	M.	Khashayar Pakdaman	Université Paris Diderot

Mathematical Modeling and Evolutionary Processes

Abstract: The research presented in this thesis concerns different topics in the field of Biomathematics. I address diverse questions arising in biology (and related to complex systems) with mathematical and numerical methods. These questions are: (i) Are passive-processes enough to justify the asymmetric distribution of damaged proteins during and after yeast cytokinesis? (ii) What processes are behind the complex patterns of expansion of Amyloid beta in the brains of patients with Alzheimer's disease? (iii) What is behind the clustering and cline-like dichotomy in models of evolution along environmental gradients? (iv) How does this dichotomy affect the spatial dynamics of invasions and range expansions? (v) How does multi-stability manifest in these models? These questions are approached (at different scales, some fully and some partially) with different theoretical methods. Results are expected to shed light on the biological processes analyzed and to motivate further experimental and empirical work which can help solve lingering uncertainties.

Keywords : Mathematical modeling, Asymmetric cell division, Aggregate-dependent aging in yeast, Adaptive evolution, Adaptive diversification, Spatial invasions, Equation-free analysis

Modélisation Mathématique et Processus Évolutifs

Résumé: La recherche présentée dans cette thèse concerne différents sujets dans le domaine de la biomathématique. J'aborde diverses questions en biologie (et liées aux systèmes complexes) avec des méthodes mathématiques et numériques. Ces questions sont les suivantes: (i) Les processus passifs sont-ils suffisants pour justifier la distribution asymétrique des protéines endommagées pendant et après la cytokinèse de la levure? (ii) Quels processus sont à l'origine des schémas complexes d'expansion de l'amyloïde bêta dans le cerveau des patients atteints de la maladie d'Alzheimer? (iii) Qu'y a-t-il derrière la dichotomie de 'clusters' vs. 'cline-like' dans les modèles d'évolution le long de gradients environnementaux? (iv) Comment cette dichotomie affecte-t-elle la dynamique spatiale des invasions? (v) Comment la multi-stabilité se manifeste-t-elle dans ces modèles? Ces questions sont abordées (à différentes échelles, certaines totalement et certaines partiellement) avec différentes méthodes théoriques. Les résultats devraient permettre de mieux comprendre les processus biologiques analysés et de motiver la poursuite des travaux expérimentaux et empiriques susceptibles de contribuer à résoudre les incertitudes persistantes.

Mots clés : Modélisation mathématique, Division cellulaire asymétrique, Vieillissement chez la levure, Évolution adaptative, Diversification adaptative, Invasions spatiales, Analyse sans équations

Acknowledgements

Gracias a la familia, a los amigos y todos los que hicieron parte de este proceso en mayor o menor medida. A los que están y a los que ya no. En especial a mis padres, mi hermano, mi abuela, Aure y mis amigos más cercanos (acá y allá). También a June, Antares, Loki, Alaska, Mono y Pitu. Y gracias también a los otros, cuyo nombre merecería estar acá y sin los cuales todo habría sido distinto.
I would like to thank Khashayar for his invaluable contributions to this achievement, in all its forms. I would also like to thank Régis, Nicolas and Jens for their guidance, their time and their dedication to our projects. Same goes to Paul, Léon, Laurent and Sorin. Special thanks to Maria for all her help and her company throughout this period. I would also like to thank Colciencias and the people behind the Cemracs for providing me with the means to train myself as a (hopefully) better scientist.

Résumé

Cette thèse est divisée en deux sections principales. La première consiste en une recherche utilisant des modèles empiriques pour traiter différentes questions relatives à l'agrégation des protéines, à la protéostase et à la protéotoxicité. La deuxième partie est axée sur la théorie (même si elle est biologiquement motivée) et concerne la recherche basée sur un modèle mécaniste d'évolution spatialement explicite et ses prédictions concernant l'évolution de la diversité et la dynamique spatiale de l'invasion de populations colonisatrices.

La première partie de la thèse (Chapitres II et III) présente deux projets de recherche: un finalisée et publiée et un en cours (avec les résultats présentés sous la forme d'une 'proceeding' attendue a évoluer dans une autre publication). La recherche dans cette partie était motivé expérimentalement. Des questions ouvertes en biologie cellulaire et médicale découlant d'observations expérimentales et empiriques devaient être traitées (du moins en partie) par des analyses mathématiques et numériques. Le premier est: les mécanismes passifs sont-ils suffisants pour expliquer la ségrégation asymétrique des protéines endommagées entre les cellules mères et filles pendant et après la division des cellules de levure? Et le second: Comment les processus moléculaires et mésoscopiques dictent-ils (modèlent-ils) la dynamique de propagation et de prolifération des oligomères dans le cerveau des patients atteints de la maladie d'Alzheimer? Quel est le lien entre les signes et symptômes macroscopiques et ces interactions à une échelle inférieure?

L'origine des deux questions peut être attribuée à des articles expérimentaux fondamentaux publiés au cours des deux dernières décennies [1–6]. Dans les deux cas, les croyances traditionnelles concernant les processus biologiques complexes ont été remises en cause par de nouvelles preuves expérimentales, ouvrant ainsi une fenêtre sur laquelle une analyse mathématique et numérique pourrait aider à résoudre les enquêtes en cours ou récemment développées.

La deuxième partie de la thèse - et de ce manuscrit - (Chapitres IV et V) est centrée sur un sujet de recherche majeur dans le domaine des mathématiques éco-évolutives. Il s'agit d'analyser, à l'aide de méthodes mathématiques et numériques, la dynamique d'un modèle (et de certaines de ses extensions) introduite pour la première fois dans [7]. Cette recherche a évolué en deux articles —un non publié (disponible sur HAL [8] et *figshare*), qui a par la suite été inclus dans le 'Supporting Information' du second [9]– et un 'working paper' avec des résultats qui sont présentés ici. Le modèle original basé sur les individus stochastiques - sur lequel cette recherche est motivée - [7] decrit la dynamique évolutive et spatiale (et leur interaction) d'une population le long d'un gradient environnemental et soumise aux interactions

écologiques. Le modèle met en évidence une dynamique complexe du comportement collectif ayant de fortes implications sur l'émergence de la diversification (et de la spéciation lorsque la reproduction est sexuée) et sur la dynamique des invasions spatiales. Ce fragment de la thèse étudie le comportement de ce modèle en utilisant différentes approches numériques et mathématiques. En outre, il étudie également ses extensions et sa signification biologique, en particulier en ce qui concerne l'émergence et l'établissement de la diversité et le comportement des modèles d'invasion lorsque l'évolution interagit à travers une adaptation locale avec une dispersion.

Première partie

S. cerevisiae vieillissement

Objectifs de recherche

Dans cette partie de la thèse, le but est d'évaluer les processus intracellulaires potentiels responsables de l'hérédité asymétrique des agrégats de protéines endommagés après la cytokinèse, et donc du vieillissement, chez la levure, bien que l'on espère que les résultats seront étendus à d'autres organismes plus complexes. Un travail mathématique et numérique est nécessaire compte tenu du fait que la recherche expérimentale est restée jusqu'à présent peu concluante. Des expériences parfois similaires ont montré des résultats fondamentalement différents [1, 2, 10]. Cela suggère que l'organisme et les processus impliqués pourraient être complexes et très sensibles à l'environnement expérimental.

Le premier objectif est de construire un modèle complet incluant tous les mécanismes (possibles) essentiels pouvant potentiellement affecter la dynamique des agrégats ainsi que les processus passifs évalués. Deux grands organites pouvant fortement interférer avec la diffusion des agrégats sont également inclus. La fusion et la croissance d'agrégats sont aussi incorporés, ainsi qu'une jeune cellule en croissance avec une dilution spécifique. De plus, le mouvement des agrégats entre les deux cellules est également incorporé.

Toutes les valeurs des paramètres sont basées sur les données expérimentales existantes tout en vérifiant soigneusement les conditions expérimentales dans lesquelles elles ont été acquises afin d'éviter toute interprétation erronée des résultats.

Une comparaison approfondie entre les résultats fournis par le modèle et les données expérimentales disponibles à court et à long terme est effectuée pour évaluer la robustesse de la suffisance des mécanismes passifs. Naturellement, le modèle devrait reproduire les observations utilisées pour plaider en sa faveur, mais il semble essentiel d'évaluer ses performances en ce qui concerne la comparaison avec d'autres données 'externes' de diverses publications. Plus précisément, celle acquise dans différentes conditions expérimentales et sur différentes échelles de temps (le cycle de vie complet).

Finalement, on vérifie si les prédictions du modèle s'améliorent ou empirent lorsque des mécanismes actifs sont incorporés.

Méthodologie

Le modèle à trois dimensions est construit dans le but de tester la suffisance des mécanismes passifs. Les processus incorporés sont illustrés dans la Figure II.1 du Chapitre II. Un grand nombre de simulations numériques de ce modèle pour des échelles de temps courtes (sur un cycle de division) et longues (sur tout le cycle cellulaire) sont effectuées afin de calculer des statistiques sur des quantités pour lesquelles une mesure expérimentale est disponible. Ces statistiques sont: les volumes globaux totaux des agrégats (et les concentrations relatives dans chaque cellule) et leurs nombres, la probabilité d'héritage par la fille d'au moins un agrégat (le cas échéant) et du plus grand agrégat, le nombre de croisements entre compartiments dans chaque direction et le déplacement quadratique moyen.

Les résultats numériques sont validés avec un modèle mathématique original constitué d'un système d'équations différentielles ordinaires couplées. Le modèle calcule le comportement temporel du nombre moyen d'agrégats et de volumes d'agrégats dans chaque cellule et s'inspire du travail de [11–13]. L'accord entre les modèles mathématiques et informatiques est très précis à court et à moyen terme (jusqu'à une ou plusieurs divisions). À plus long terme, le modèle mathématique sert de limite supérieure aux concentrations globales chez la mère car il traite tous les agrégats de la même manière, minimisant ainsi la fusion dépendante de la taille et les taux d'échappement.

Un modèle comportant différentes formes de contrôle de qualité actif peu fréquent (et difficile à détecter expérimentalement) est également introduit. Le principe de base est que la plupart des agrégats sont à tout moment soumis uniquement à des forces passives. Parfois, cependant, le mouvement des agrégats peut être perturbé (individuellement) par dérive vers le pôle de la cellule mère, confinement aux surfaces organellaires ou fixation sur la membrane. Ces variantes permettent de vérifier si le contrôle de qualité actif peu fréquent peut potentiellement réconcilier le travail et les conclusions d'études expérimentales divergentes.

Résultats obtenus

À des échelles de temps courtes et moyennes (au plus un cycle de division cellulaire) et, comme prévu, le modèle de type passif ('passive-only-model' POM) réussit bien à reproduire les mesures empiriques utilisées pour justifier la suffisance de mécanismes passifs [1, 14]. En particulier, le déplacement quadratique moyen des agrégats est en accord avec la prédiction (à mi-temps) de [1]. Il reproduit également les résultats de [1, 14, 15] en ce qui concerne la concentration relative de protéines mal repliées dans les deux compartiments. De plus, le modèle reproduit également les résultats numériques et expérimentaux de [14] concernant les nombres agrégés et les événements de fusion.

Un avertissement est émis lors de la comparaison du nombre d'événements de croisement (dans les deux sens) calculés à l'aide du POM et des observations expérimentales de [1, 14]. Contrairement aux prévisions des événements de croisement du cou entre les deux compartiments de [14], elles sont très fréquentes et presque vingt fois plus importantes que celles mesurées dans leurs expériences. Ce résultat a été validé avec les prédictions mathématiques dérivées concernant les temps de sortie moyens des particules diffusantes dans des domaines

confinés. De plus, il a été testé à partir de différentes valeurs de paramètres qui correspondraient à différentes configurations expérimentales. Il est rappelé que l'hypothèse d'un mouvement peu fréquent entre les compartiments était la prémisse qui consistait à écarter le transport entre les compartiments dans le modèle de calcul de [14].

Aux longues échelles de temps (sur tout le cycle cellulaire de la levure), la divergence entre les prévisions du modèle et leurs mesures expérimentales respectives augmente. Bien que le nombre d'agrégats - sous les valeurs de paramètres correspondant aux taux d'agrégation dans les cellules dans la nature - concorde avec les résultats de [16], presque toutes les prévisions sont en désaccord avec les données expérimentales disponibles concernant l'accumulation de protéines endommagées. Spécifiquement, les volumes d'agrégats se stabilisent après quelques générations, ce qui contredit l'hypothèse selon laquelle les protéines endommagées s'accumulent avec l'âge réplicatif et entraînent les cellules de levure vers un vieillissement dépendant de l'agrégat. Les probabilités d'héritage d'au moins un agrégat et du plus grand agrégat par la fille ne concordent pas non plus avec les mesures empiriques de [17]; ils sont respectivement environ trois fois et dix fois plus élevés.

Le nombre de croisements entre compartiments reste supérieur de son équivalent expérimental à long terme. Bien que le nombre diminue après quelques générations (ou augmente à des taux d'agrégation faibles), à mesure que la taille des agrégats augmente, il se stabilise généralement à une valeur supérieure d'environ un ordre de grandeur.

Lors de l'ajout du contrôle de qualité actif au POM, le désaccord avec les données expérimentales est considérablement réduit. Le nombre de passages à niveau est fortement réduit (pour tous les taux d'agrégation) à des échelles de temps courtes et longues et l'accumulation de dommages se produit à des taux similaires aux mesures empiriques, de même que les probabilités d'heritage de au moins un agrégat et du plus grand. De plus, en raison de sa faible fréquence, le contrôle de qualité actif est également compatible avec le déplacement quadratique moyen mesuré expérimentalement. Il est à noter que les résultats de ce modèle reposent sur des paramètres pour lesquels aucune validation expérimentale n'a été effectuée.

Discussion

À des échelles de temps courtes, correspondant à un cycle de division, le modèle (passif uniquement) est capable de reproduire les résultats expérimentaux utilisés en faveur de l'absence du contrôle de qualité actif. Cependant, le transport entre compartiments est significativement plus fréquent que celui observé dans les expériences [1, 14]. À longue échéance, l'accumulation de dommages graduels dans les cellules plus anciennes ne se produit que dans des taux d'agrégation élevés, semblables à ceux observés dans les cellules induites par le stress. Ceci contraste les observations de [18]. Lors de l'introduction du contrôle de qualité actif, les différences avec les données expérimentales sont substantiellement améliorées, suggérant sa présence dans des cellules de levure réelles.

La recherche détaillée et complète sur le sujet est présentée au chapitre II sous la forme de la version acceptée de l'article, qui a par la suite été publiée dans *Biophysical Journal* [19].

Propagation spatiale amyloïde-bêta (Aβ) dans la maladie d'Alzheimer

Objectifs de recherche

La recherche sur la dynamique spatiale de la propagation et de la prolifération de Aβ a pour objectif général de construire (ou de contribuer à la formation de) un modèle mathématique et numerique à plusieurs échelles; des processus biomoléculaires microscopiques à la dynamique macroscopique de grands Aβ dépôts (plaques et fibrilles) en s'appuyant fortement sur les mécanismes biologiques intervenant à chaque échelle. En partant de la dynamique moléculaire élémentaire des peptides Aβ et de leur interaction avec un ou plusieurs neurones, la complexité augmente à différentes échelles en incorporant les différents processus biologiques connus pour avoir un effet sur la propagation de l'amyloïde.

Dans le travail présenté dans le cadre de cette thèse, l'objectif est d'introduire ce modèle mathématique fondamental, potentiellement valable aux échelles microscopique et mésoscopique. En outre, décrire les processus qu'il incorpore, ses motivations biomoléculaires, sa forme sans dimension, ainsi que les résultats obtenus concernant les solutions d'équilibre avant la nucléation primaire et sa formulation variationnelle. Le modèle de calcul utilisé pour les simulations est basé sur la méthode des éléments finis.

Méthodologie

Le modèle mathématique, présenté au chapitre III, analyse la dynamique moléculaire des espèces monomères, proto-oligomères (solubles) et oligomères (insolubles et stables) Aβ dans un domaine spatial à deux dimensions représentant la région autour d'un ou de quelques neurones. Il suppose un contexte *in vivo* dans lequel la nucléation primaire a déjà eu lieu (puisqu'il s'agit d'un événement rare) et se concentre sur la dynamique de concentration ultérieure, supposée déterministe. Le modèle est basé sur des observations empiriques concernant le comportement de la polymérisation (agrégation) et de la dépolymérisation des peptides Aβ jusqu'à ce qu'une taille d'oligomère insoluble de type micelle stable soit atteinte au moment où protéotoxicité est maximale. La taille des oligomères est supposée être discrète (en termes de monomères) en conséquence des échelles spatiales microscopiques considérées. Les nouveaux monomères sont produits à partir d'une source homogène située à la membrane des neurones. Cette production est progressivement modifiée à mesure que la concentration en oligomères augmente au voisinage des cellules. La manière exacte dont les effets protéotoxiques des oligomères Aβ affectent la production future dépend linéairement de l'historique de la concentration. Pour des raisons de simplicité, le modèle ne considère pas les prions directement. Les proto-oligomères sont formés par polymérisation de monomères et peuvent se fragmenter en proto-oligomères de taille inférieure à moins d'atteindre la taille critique à laquelle ils deviennent stables. La diffusion est supposée être le principal moteur déterminant la répartition spatiale des concentrations; il dépend de la taille et suit la relation de Stokes-Einstein.

Mathématiquement, le modèle consiste en un système de i_0 équations aux dérivées partielles couplées (EDP de réaction-diffusion); i_0 étant la taille des oligomères pour lesquels les conformations deviennent stables et insolubles. Le terme de réaction correspond aux vitesses de polymérisation, de dépolymérisation et de fragmentation et le terme de diffusion

à la diffusion dépendant de la taille.

Le modèle computationnel est dérivé de la forme variationnelle du système d'équations différentielles. Pour les simulations, une méthode d'éléments finis est utilisée.

Résultats obtenus

Les résultats incluent la formulation et l'introduction des modèles mathématique (y compris sa forme sans dimension) et numérique. Aussi, des résultats mathématiques du système sont obtenus. Cela concerne la dynamique de masse (et la liaison) et la solution d'équilibre pour la concentration de monomères autour d'un seul neurone de l'état de santé du système avant la nucléation primaire.

Avec le modèle numérique, des résultats des simulations ont été obtenus qui montrent déjà une relation complexe entre la propagation spatiale et les paramètres du modèle. En particulier, une relation non linéaire entre la propagation rapide des oligomères (provoquant la mort neuronale) et les taux de fragmentation. Lorsque les taux de fragmentation sont élevés, la diffusion rapide de petits oligomères et de monomères entraîne la propagation de Aβ mal repliée, mais seule une faible concentration d'oligomères prétéotoxiques autour des cellules se produit. En revanche, une très faible fragmentation donne une concentration élevée en oligomères mais qui se propagent lentement dans tout le domaine.

Deuxième partie

Diversification adaptative dans les gradients environnementaux

Contexte scientifique

Le contexte spatial des branchements évolutifs concerne les conditions et les mécanismes sous-jacents à l'apparition et au maintien de la diversité phénotypique et de la spéciation au sein de populations explicitement spatiales [20–22]. C'est une extension naturelle des modèles unidimensionnels puisque les formes de spéciation et de diversification sont définies en fonction de leur contexte spatial. L'émergence de diversité ou de nouvelles espèces (en cours de reproduction sexuée) est associée à l'apparition d'une multimodalité dans l'espace phénotypique, qui s'accompagne généralement d'un regroupement le long des dimensions spatiales apparaissant comme conséquence de l'interaction entre processus évolutifs et écologiques.

Il existe un fort consensus sur le fait que la diversification (spéciation) [23–26] se produit fréquemment dans l'allopatrie en raison de l'obstruction au mouvement et/ou du flux de gènes par des barrières géologiques ou géographiques. Cependant, en l'absence d'obstacles géographiques, les conditions précises qui favorisent ou entravent l'émergence de la diversité restent floues malgré un intérêt croissant, car les preuves expérimentales et empiriques se sont accumulées au cours des dernières années pour les organismes sexuées [27–35] et asexuées [33, 36–40].

.

Objectifs de recherche

Des questions fondamentales concernant la formation et la dynamique des groupes spatiales et phénotypiques en réponse à l'adaptation et à la dispersion locales restent sans réponse. Premièrement, notre compréhension des conditions requises pour la formation et la persistance de ces groupes est encore incomplète. En particulier, comment la mobilité individuelle affecte-t-elle leur formation et comment l'effet de la mobilité individuelle interagit-il avec l'échelle à laquelle les individus se disputent les ressources? Quel est le comportement des dynamiques transitoires et leur relation avec leurs limites asymptotiques? Comment la nature délimitée de l'espace géographique et phénotypique influence-t-elle la dynamique du regroupement spatial et phénotypique? Pouvons-nous prédire les caractéristiques clés de la structure émergente de la population, telles que la distance inter-groupale et le nombre de groupes, à partir de paramètres individuels?

Dans la recherche présentée dans le "Supporting Information" du Chapitre IV, ces questions sont traitées selon différentes méthodes mathématiques et numériques afin de fournir un cadre théorique plus solide pour l'étude de la diversification le long de gradients environnementaux.

Méthodologie

La recherche repose sur un modèle stochastique et son approximation d'EDP [7]. La dynamique du système, à la fois asymptotique et transitoire, est étudiée par analyse numérique et mathématique. En particulier, leur lien avec les paramètres individuels, les conditions initiales et les conditions limites. Cela se fait par des simulations numériques (utilisant une méthode explicite d'Euler) et par une analyse de stabilité de Turing (à la fois analytique et numérique). En outre, une approche Hamilton-Jacobi basée sur la concentration [41–45] est utilisée pour prédire les caractéristiques de modèles périodiques asymptotiques. Cette approche est complétée par un modèle numérique qui utilise des méthodes raffinées.

Résultats et discussion

Les résultats montrent des gammes plus larges de paramètres sur lesquels se produisent des goupes spatiales et phénotypiques; différents régimes transitoires de la dynamique des phénotypes et la relation avec des multiples attracteurs; et sur des aperçus quantitatifs du comportement asymptotique. Ces dernières sont basées sur l'analyse de stabilité et sur l'approximation Hamilton-Jacobi, où les distances entre les groupes ainsi que leur direction d'apparition sont calculées. De plus, nous présentons des simulations de la dynamique spatiale sous aucune évolution, ce qui corrobore l'idée que le regroupement est renforcé par la rétroaction entre les processus écologiques et évolutifs.

De plus, les résultats conduisent à deux résultats remarquables sur la dynamique des clusters. Premièrement, le système présente multi-stabilité. Par conséquent, de petites variations dans les conditions initiales peuvent conduire à différents attracteurs. De plus, les perturbations peuvent amener la population à basculer rapidement entre différents états stables de distribution spatiale et de composition phénotypique. Ceci est exploré plus en détail dans le travail effectué dans le chapitre V. Deuxièmement, les taux de formation de

groupes ne sont pas constants. Lorsque la population se propage, le temps de formation des groupes périphériques varie, ce qui entraîne une invasion fluctuante dans laquelle la dynamique transitoire de l'adaptation locale dans les groupes établies est essentielle pour prédire la dynamique à long terme de l'invasion.

La recherche détaillée et complète sur ce sujet est disponible sur HAL [8]. Ici, une version modifiée est présentée dans le "Supporting Information" de l'article accepté par *Ecology Letters*.

La dynamique spatiale des invasions

Contexte scientifique

Comprendre la dynamique d'invasion des populations biologiques colonisant de nouveaux environnements a acquis une importance sans précédent et substantielle au cours des dernières années en raison des taux alarmants de destructions d'habitat dues aux expansions agricole et urbaine, au changement climatique impulsé par l'homme et à l'exploitation minière, entre autres causes diverses. Dans ce contexte, des modèles mécanistes sont nécessaires pour traiter des problèmes liés a la prévision et le contrôle des invasions biologiques et la gestion des translocations, et les introductions et réintroductions d'espèces.

Les modèles théoriques classiques des expansions spatiales, fondés sur les principes de la dynamique des populations et de la génétique quantitative, ont prédit l'expansion à une vitesse constante [46–48]. Des observations récentes montrant des invasions non constantes ont été attribuées à des facteurs environnementaux ou stochastiques extrinsèques. Cependant, il a été suggéré ces dernières années que les facteurs écologiques pourraient également influer sur la dynamique de l'invasion [49, 50].

Objectifs de recherche

Dans le chapitre IV, la recherche traite de la manière dont les effets combinés de l'adaptation locale et de l'évolution de la dispersion affectent la dynamique éco-évolutive des invasions spatiales. Cette recherche s'appuie sur les résultats résumés dans la section précédente. Plus particulièrement, sur la manière dont la dichotomie de groupements *vs* expansion continue influence les taux et les structures de répartition spatiale de la population. Il est présenté comme la version acceptée de l'article, publiée ultérieurement dans *Ecology Letters* [9].

Méthodologie

La recherche repose sur deux modèles. Le premier étant le modèle introduit dans [7]. Le second est construit comme une extension avec une dispersion qui évolue. Dans ce dernier cas, la dispersion a un coût énergétique qui augmente les taux de mortalité naturelle à un degré dépendant d'un nouveau paramètre θ.

Les modèles sont analysés avec des simulations du modèle stochastique et du limite d'EDP. Les simulations permettent de mesurer les vitesses d'invasion spatiale. L'analyse de la stabilité de Turing est étendue à la dispersion évolutive et l'approche de Hamilton Jacobi

[41] est orientée vers l'analyse des invasions spatiales.

Enfin, différentes extensions du modèle sont explorées (avec 'Allee Effects', deux dimensions spatiales et une pente de gradient arbitraire) pour montrer que les résultats qualitatifs sont conservés dans des scénarios plus réalistes.

Résultats obtenus

Les premiers résultats obtenus à partir de notre analyse sont basés sur le modèle original. Les simulations montrent que les expansions spatiales ne se produisent pas nécessairement comme des ondes progressives en expansion. Au lieu de cela, et en fonction des paramètres, les expansions peuvent être 'tirées' par la formation de groupes ou 'poussées' par l'expansion frontale d'une onde progressive. De plus, les distributions transitoires peuvent ne pas refléter les schémas asymptotiques de la population..

La vitesse d'invasion peut varier qualitativement et quantitativement en fonction des différents régimes d'expansion. Les fronts d'invasion 'tirés' ont des vitesses d'invasion oscillantes (qui peuvent chuter à zéro) en conséquence des phases d'invasion et d'adaptation. En revanche, les invasions 'poussées' montrent des vitesses d'invasion constantes plus conformes aux prédictions traditionnelles. Pour les valeurs du paramètre situées entre les deux cas, l'invasion peut se dérouler à des vitesses légèrement variables.

L'approche Hamilton-Jacobi révèle que les groupes spatiales et phénotypiques s'influencent mutuellement, ce qui explique également pourquoi les vitesses d'invasion varient.

Lorsque la dispersion et les traits de niche évoluent simultanément, la dispersion moyenne a tendance à diminuer en raison de l'augmentation des coûts de mortalité. Toutefois, cela n'est pas homogène, car les individus très dispersés peuvent être sélectionnés positivement sur les fronts de la population et dans les régions situées entre les groupes. De plus, trois régimes d'invasion alternatifs peuvent être observés. Pour une très faible dispersion, l'invasion procède par la formation de groupes qui 'tirent' l'expansion. Pour une dispersion très élevée, l'invasion est 'poussée' par l'expansion d'une onde continue. En ce qui concerne la dispersion intermédiaire, les deux régimes peuvent coïncider, en conséquence de l'interaction des rétroactions éco-évolutives. Ces différents schémas d'expansion entraînent différents régimes temporels de vitesse d'invasion.

Discussion

Les résultats de cette recherche sont pertinents car ils suggèrent de nouvelles explications alternatives pour les vitesses non constantes dans les extensions de la plage de population. En particulier, il est suggéré que l'interaction entre l'adaptation locale et l'évolution de la dispersion, puisse conjointement justifier les fluctuations de la vitesse d'invasion.

Analyse sans-équation de la diversification adaptative

Contexte scientifique

L'Analyse sans-équation, [51–53], a été développée au cours des dernières décennies comme méthode pour étudier des systèmes complexes où les descriptions se situent à l'échelle microscopique et l'intérêt réside dans le comportement macroscopique. Dans ces systèmes, les 'règles' régissant les actions d'un grand nombre d'individus (ou de parties) sont claires. En revanche, les équations décrivant le comportement macroscopique (en termes de faible nombre de quantités macroscopiques) sont considérablement difficiles à analyser ou, dans la plupart des cas, indisponibles.

La méthode repose sur de courtes simulations des configurations microscopiques initialisées de manière appropriée ('expériences numériques') qui permettent d'estimer des quantités qu'il faudrait inférer autrement par l'analyse mathématique de formules ou d'équations explicites décrivant le comportement macroscopique. D'où le terme 'sans équation', puisque ces équations n'ont pas besoin d'être explicitement écrites.

Objectifs de recherche

L'objectif de la recherche dans le Chapitre V est d'utiliser des méthodes sans équation pour analyser les équilibres macroscopiques et la multi-stabilité dans le système stochastique introduit dans [7]. Multi-stabilité des distributions asymptotiques qui se fragmentent en un nombre différent de groupes isolés, fortement dépendants des conditions initiales et de la frontière du domaine.

Méthodologie

Les simulations du modèle microscopique (le pas de temps microscopique) sont effectuées selon la méthodologie décrite dans IV. La première analyse est limitée à la dépendance macroscopique du paramètre δ (la force de la concurrence) et elle étudie chaque transition d'équilibres asymptotiques séparément. Dans chaque cas, les macro-variables naturelles sont les coefficients de Fourier de la densité des projections sur la ligne diagonale (c'est-à-dire où la population se concentre normalement).

Résultats obtenus

L'implémentation de la méthode 'semi-implicite' peut servir de cadre général à utiliser lorsque les systèmes microscopiques sont fortement stochastiques et que les temps de simulation sont longs.

Les résultats des simulations ont montré une relation concernant N (la taille de la population) et δ. En ce qui concerne les équilibres macroscopiques et la multi-stabilité, une très forte hystérésis a été détectée. De plus, il a été observé que près des valeurs critiques, où la stabilité des distributions microscopiques est perdue, le système peut être fortement désordonné, de manière similaire aux particules proches des transitions de phase.

La recherche devrait évoluer vers le calcul d'un diagramme de bifurcation en fonction du paramètre δ. Les résultats suggèrent une progression de 'saddle nodes'. Si elles sont confirmées, les prévisions permettraient de mieux comprendre la dépendance quantitative de la multi-stabilité.

Contents

I – Thesis Overview

This thesis is divided into two major sections. The first is data-driven and consists on research which uses empirical models to address different questions related to protein aggregation, proteostasis and proteotoxicity. The second part is theory-driven (albeit biologically motivated) and concerns research based on a mechanistic model of spatially-explicit evolution and its predictions concerning the evolution of diversity and the spatial dynamics of invasion of colonizing populations.

Research in the first part is based on a thorough analysis of empirical observations and data from biological systems. Mathematical and computational models were made to answer questions that remained elusive despite experimental and/or empirical work. In contrast, research in the second part built upon an existing mechanistic mathematical model and aimed to analyze its dynamics –and of its extensions– and their biological significance.

The first part of the thesis (Chapters II and III) presents two research projects: one concluded and published and one in progress (with results submitted in the form of a proceeding which are expected to evolve shortly into another publication). Research in this part was experimentally and data-driven. Specific interrogatives and open questions in Cell and in Medical Biology arising from experimental and empirical observations were aimed to be answered (at least partially) through mathematical and numerical analysis. The first one being: are passive mechanisms enough to account for the asymmetric segregation of damaged proteins between mother and daughter cells throughout and after yeast cell division? And the second one: How do molecular and mesoscopic processes dictate (shape) the dynamics of propagation and proliferation of oligomers in the brains of patients with Alzheimer's Disease? How do the macroscopic signs and symptoms relate to these lower-scale interactions?

The origin of both questions can be traced to seminal experimental articles published in the last two decades [1–6]. In both cases, traditional beliefs concerning complex biological processes were challenged through new experimental evidence, hence opening a window where mathematical and computational analysis could help solve the lingering or recently developed inquiries.

The second part of the thesis –and of this manuscript– (Chapters IV and V) is centered around one major research topic in the field of Eco-Evolutionary Mathematics. It aims to analyze, with both mathematical and numerical methods, the dynamics of a model (and some of its extensions) first introduced in [7]. This research evolved into two articles – one unpublished (available on HAL [8] and *figshare*) which was later included as part of the

Supporting Information of the second one [9]– and one working paper with results which are presented here and which have opened the door to further perspective explorations. The original stochastic individual-based model –on which this research is motivated– [7] aims to describe the evolutionary and spatial dynamics (and their interplay) of a population along an environmental gradient when subject to ecological interactions. The model shows complex dynamics of collective behavior with strong implications concerning the emergence of diversification (and speciation when reproduction is sexual) and the dynamics of spatial invasions. This fragment of the thesis investigates the behavior of this model using different computational and mathematical approaches. In addition, it also studies its extensions and biological significance, particularly concerning the emergence and establishment of diversity and the behavior of patterns of invasion when evolution interacts through local adaptation with dispersal.

I.1 Part I

Aging is a evolutionarily conserved process which manifests and affects living cells ranging from unicellular microorganisms to complex mammalian cells [54–57]. In general, aging occurs through a gradual decay in cellular and organelle functions which affect the most basic cellular processes and molecular pathways, and reduce reproduction and survival rates [56, 58]. In mammals, this deterioration increases risk of disease in general and, to a larger extent, the risk of age-related diseases which normally involve disease-associated proteins with complex pathways [59–61].

Throughout their lives, cells can accumulate detrimental material which accelerates aging [55, 62]. Aggregate-dependent aging refers to the a accumulation of damage in the form of protein aggregates [63] and its rate depends on several aspects both internal (*e.g* genetic [64]) and external (*e.g* environmental factors [65]). The accumulation of aggregated damaged, oxidized or misfolded proteins (or peptides) in intracellular and extracellular compounds compromises cell function and cell reproduction and can ultimately cause cell death [66–68]. In humans, the accumulation of oxidized and misfolded proteins is the cause of age-related diseases referred to as Amyloidosis and also have been found to play an essential role in the development of Alzheimer's and Parkinson's Disease [61, 69, 70]. Although the exact molecular mechanisms may vary, these detrimental (toxic) proteins (or peptides) normally alter molecular pathways and metabolic functions and harmfully interact with organelles and cell membranes, compromising their functions and their permeability [66, 71–74]. This is referred to as proteotoxicity. It is accentuated in non-dividing cells (*e.g* neurons) where damage accumulates faster thus accelerating aging (no damage is released and no cell substitution occurs). Naturally, cells have mechanisms of repair and protein refolding [74–76], referred to as quality-control (QC) mechanisms. However, these processes can be energy costly and eventually can not compensate for the damage caused.

One essential organelle which is most affected by aggregate accumulation is the mitochondria [77, 78], which eventually loses function as a consequence of diverse harmful effects of cell aging [56, 67]. Mitochondria dysfunction in humans has been linked to Parkinson's, Alzheimer's and heart disease as well as cancer and diabetes [78–80]. The exact mechanisms in which aggregate accumulation is linked to loss of function in this organelle are believed to be various and diverse [56], with one being through the deterioration of the Lysosome (Vacuole in yeast) [81]. The Lysosome is one of the organelles that has been found to have functions related to QC [82]. Likewise, one other form of QC is asymmetric cell division, which prevents damage inheritance by newly born cells and resets cell's life-span by fully regenerating their offspring [58, 83].

Different factors related to aggregate-dependent aging are difficult to analyze in human cells. Besides the technical and ethical constraints, aging processes in humans occur over time-scales (in years) which hinder experimental and theoretical developments. Moreover, complex molecular pathways and genetic factors in human cells can add further complications. For this reason, model organisms as budding yeast (*Saccharomyces cerevisiae*) –where many age-related aspects are preserved– are frequently used to gain insight into basic aging related cellular processes and mechanisms. For instance, aging-related genes are frequently

identified in simpler model organisms before being searched for in humans. Moreover, extensive research aims to study aging processes and why aging increases risk of diseases through experiments with yeast [84–87]. Yeast cell aging (replicative aging) is easier to detect with the use of fluorescent methods which use stains to detect the number of scars (divisions).

Research in Part I aims to study aggregate dependent aging (or aggregate-dependent age-related diseases) with two different approaches. In the first paper, microscopic intracellular processes related to asymmetric damage distribution in the model organism *Saccharomyces cerevisiae* are analyzed with mathematical and computational methods. In the second, focus is set on the extracellular (spatial, non-local) propagation and proliferation of harmful misfolded peptides (small proteins) in Alzheimer's disease, rather than on the intracellular molecular mechanisms of pathways which induce or hinder cell damage.

In both cases, the ultimate goal is to provide research which can help shed light on age-related processes as well as have a potential impact in prognosis and diagnostics of age-related diseases and on human health in general.

I.1.1 Aggregate-dependent *S. cerevisiae* aging

Scientific context

Biological cells assemble proteins that are fundamental for cell function and life in general through synthesis inside the ribosome. Proteins are formed from chains of amino acids (a protein's primary structure) that fold according to the hydrophobic effect (the most thermodynamically favorable configuration) in which hydrophobic regions (repelled by water) are surrounded by hydrophilic regions (attracted to water) of the protein [74, 88]. This structure minimizes contact between water molecules and hydrophobic regions and is preserved by non-covalent bonds. Protein misfolding (and unfolding) can occur naturally or from mutations in the DNA sequence, as well as problems in the transcription and translation phases and from environmental stresses [74]. Moreover, aging in cells (which itself can be an outcome of protein-aggregate accumulation) contributes to the increased formation of misfolded proteins.

Environmental causes, particularly heat (by disrupting bonds), freezing, mechanical agitation, pH (alkalinization) or oxidative stress –where an increase in ROS (reactive-oxygen-species) is not compensated by the production of antioxidants– modify the folding structure of proteins causing exposure of hydrophobic regions [89]. In the case of the latter, oxygen is not reduced to water (or water molecules are disrupted). This generates molecules with free electrons (ROS) that interact with side-chains of proteins and cell membranes through a process commonly known as oxidation. Misfolded proteins are prone to (susceptible to) binding through their exposed hydrophobic regions, thus forming aggregates or 'clumps' of damaged structures [74, 89]. Depending on the aggregation process, aggregation rates and the nature of aggregates differ [90, 91]. In particular, aggregates can be covalent or non-covalent (*e.g* binded by Van der Waals forces, hydrophobic or electrostatic interactions). Aggregation may be reversible or irreversible; to counter the toxicity of aggregates, cells produce protein chaperons (HSP or heat-shock-proteins) that through their interaction with aggregates assist in un-folding/re-folding (disaggregation) of protein aggregates [91, 92]. Nevertheless, some aggregates can not be repaired and in some cases the chaperones themselves can contribute to

further misfolding [93, 94]. This occurs, for instance with HSP104 proteins in *Saccharomyces cerevisiae*. HSP104 refers to the heat-shock-protein-104 of which its production is regulated by the HSP104 gene; the number being its size in kilodaltons. Exposed hydrophobic structures trigger continuous growth of existing aggregates through binding upon collision. These aggregates then can interact with the phospholipid bilayer of membranes (in which one layer is hydrophobic and the other hydrophilic) and cause damage which propagates along membranes hence compromising their permeability [95].

In [96] protein aggregation, detection and quantification are explained in detail in the context pharmaceutical procedures.

The relation between cell aging and damaged (misfolded) protein aggregate accumulation is strongly influenced by asymmetric cell division. In early cellular organisms, reproduction was symmetrical. Hence, (statistically speaking) all lineages would be equally susceptible to deterioration from accumulated damage and eventually would disappear completely unless cells developed QC mechanisms which would keep damage to a constant level over generations [97]. Thus, aging in cells would not occur since all cells (all lineage) would be (statistically) equivalent (without taking into account environmental factors). In contrast, if organisms age, cell reproduction, when present, must be asymmetrical [58, 98, 99].

Asymmetrical cell division rejuvenates lineages by resetting cell's life-span through the formation of young progeny while simultaneously leaving behind older cells. Although initially believed to have evolve in the first Eukaryotes, it was recently found to be present in some Procaryotic organisms [58, 100]. In [58] observation of rejuvenating asymmetric reproduction (hence aging) was found in the species *Caulobacter crescentus* (procaryote) resulting in a stalked old cell with reduced reproduction rates and swarmer young one. Also, in [100] *E. coli* cells inheriting old poles showed diminished growth and reproduction rates and life expectancy. The process underlaying this asymmetry was uncovered in [101], where misfolded protein aggregates were found to co-localize with old poles during cell division and to correlate with aging.

Similarly as with *E. coli*, in budding yeast *S. cerevisiae*, aging is strongly associated with asymmetric cellular division and with the asymmetrical distribution of damaged and misfolded proteins [18]. Oxidized proteins aggregates, such as Hsp-104-associated aggregates affect mortality of yeast cells by deteriorating their fitness and maintenance at late stages of the life cycle [64] and ultimately cause cell death. These protein aggregates distribute asymmetrically during and after cell division (budding) between daughter and mother cells. An asymmetry which decreases with replicative age [18]. The cellular mechanisms (or processes) causing this asymmetry remain unclear. In particular, whether or not an active-quality-control (AQC) mechanism is necessary remains elusive.

The modest inheritance of Hsp-104-associated aggregates by rejuvenated progeny and their distribution during cytokinesis has motivated substantial and diverse work ([1, 10, 14, 64] to name a few) but its cause has not been entirely clarified. Moreover, experimental observations have been occasionally conflictive under the same (or similar) reported conditions (*e.g* [1, 2, 10]). In [2, 10, 18, 64, 102, 103] a dependence on the formation of the

Actin-Cytoskeleton was proposed. When suppressing the expression of the *SIR2* gene (a gene also present in humans) –linked to formation of the actin-cytoskeleton [104]– aggregate concentrations (and numbers) balanced during and after division. Altered cells did not show any significant difference with respect to wild-type (WT) cells in terms of the diameter length of the neck connecting both compartments (the two cells). The same results were also reported in [64] when injecting WT cells with Latrunculin-A (Lat-A) – which inhibits actin polymerization. Hence, these works suggest that aggregates interact with actin cables and are transported via cable flow away from the daughter cell and towards the mother.

In [105, 106] aggregates were tracked and analyzed after stress (which induces protein aggregation). Small aggregates of misfolded protein were observed to accumulate in inclusions (intracellular deposits) which locate at peri-nuclear, peri-vacuolar and peri-mithochondrial sites (the IPOD, the JUNQ and the MAGIC). Moreover, in [16, 17] protein precursors in WT cells were found to adhere to the endoplasmic reticulum (ER) through their interaction with farnesylated YDj1. Once there, they were observed to accumulate to form a single deposit. In [107] aggregates formed on the (ER) were observed to tether to mithocondrial surfaces, which links observations in [16, 17] and [106]. Once in either of these deposits, aggregates are either retained inside the mother cell (which hinders their crossing to daughter cells) or disaggregated by proteases (enzymes). Aged mother cells were found to lose this ability, hence explaining the more symmetrical distribution of aggregates in the latter stages of the life cycle. Some genetic pathways, participating in this process have been found recently as well [108]. Moreover, the trafficking routes favoring aggregation into peri-organellar deposits have been also studied, with a possible participation of the actin cytoskeleton in this process [108].

Overall, the potential mechanisms described to this point, claim on the existence of a complex energy-requiring mechanism which protects progeny from proteotoxicity through clearance (transport), restriction, or dissaggregation. This is referred to as the active quality control (AQC) machinery of *S. cerevisiae*.

In contrast with the AQC hypothesis, it has also been suggested that passive mechanisms (which do not require an energetic machinery running on ATP) are sufficient to justify asymmetric segregation and inheritance of misfolded proteins. In [1], heat-induced and naturally formed aggregates were tracked and their motion was analyzed with no apparent directional bias detected. Experimental results concerning aggregate movement and concentrations were accompanied with numerical simulations of non-dimensional, non-interacting particles diffusing inside a domain composed by two spheres connected by a neck. Their numerical results were after validated with a mathematical model in [15].

In the same line, and based on the fact that formation of aggregates is concentration-dependent (if there is a high concentration of proteins, crowding and fusion increase) [14] builds on the results from [109] in Fission Yeast *S. pombe* to propose that aggregate fusion, combined with bud-specific aggregate dilution are enough to justify for low aggregate numbers in daughters. Furthermore, they support their claims with a mathematical (and computational) model which replicates their experimental observations based on the assumption of no compartmental exchange of aggregates.

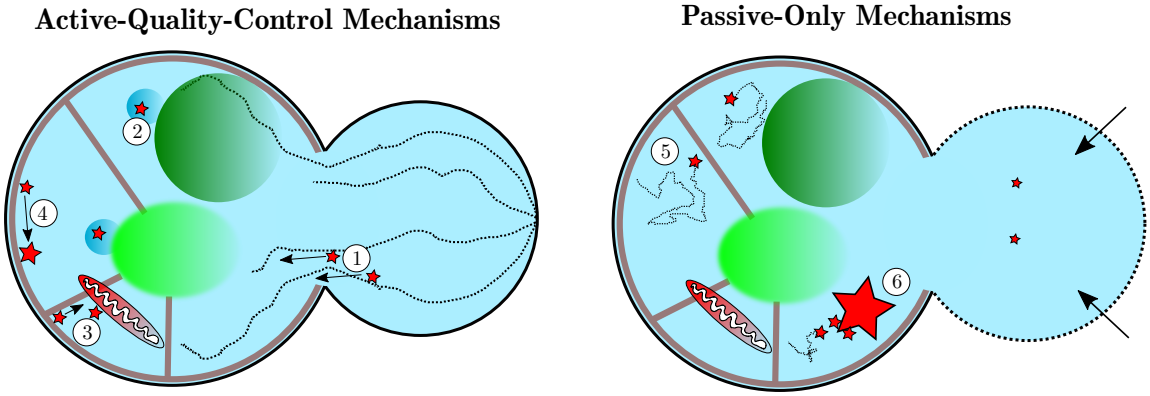

Figure I.1: Active-quality-control (AQC) mechanisms vs Passive-only mechanisms (PO). 1. Actin-cable driven transport [2, 10, 18, 64, 102, 103]. 2. Confinement to peri-organellar deposits [105, 106]. 3. ER-mediated tethering to mitochondria [107] 4. Confinement and aggregation in ER [16]. 5. Confined diffusion of aggregates [1]. 6. Aggregate fusion and bud-specific dilution [14].

All the mechanisms that have been suggested to be the main drivers of the asymmetric distribution of aggregated proteins during yeast cytokinesis are summarized in Fig. I.1 together with their references.

Research Objectives

In recent years there has been significant work dedicated to analyze the molecular mechanisms in which aggregates of misfolded proteins cause mitochondrial or organelle dysfunction (see [110]). Most, with the aim of providing biochemical developments with therapeutic applications. Throughout this part of the thesis, instead, the focus is set on evaluating the potential intracellular processes that cause aggregate accumulation and hence aging in budding yeast –although results are hoped to be extended to other more complex organisms. Other mathematical and computational research (*e.g.* [111]) has also targeted aggregate-dependent aging in budding yeast but at different temporal and spatial scales, looking at how relation between asymmetric reproduction, aggregate repair and aggregate retention relate to replicative life-spans in terms of a finite energy constraint. However, theoretical work targeting the necessity or redundancy of AQC has been uncommon and mostly complementary. It has usually aimed to confirm experimentally-based hypotheses while taking into account only the passive processes at test. Further mathematical and computational work is required considering how experimental research has until now remained inconclusive. Furthermore, occasionally analogous and similar experiments have shown fundamentally different results [1, 2, 10]. This suggests that the organism and the processes involved could be complex and very sensitive to the experimental environment.

When available, mathematical or numerical models used in the subject have potentially excluded essential processes which could affect their analysis. The first theoretical work addressing the sufficiency of passive mechanisms was presented in [1]. The two-dimensional aggregate mean-square-displacement (MSD) was found to be consistent with the equation

$r^2(t) = 4Dt^\alpha$ –with D being the diffusion coefficient and $\alpha \simeq 0.75 < 1$ the degree of sub-diffusion– after comparing observations with numerical simulations of diffusing particles inside two spheres joined by a neck. Numerical simulations matching experimental data were tested for concentration distributions after a time equivalent to the duration of cytokinesis and with all particles initially located in the larger compartment (the mother cell). Results were consistent with experimental measurements on compartmental concentrations and were validated by a mathematical model in [15]. Both models (computational and mathematical) excluded aggregate formation, fusion and growth and potentially oversimplified the crowded intracellular environment.

In [14] aggregation rates where measured in each of the two cells during budding as was the probability of fusion in the event of aggregate collisions. This served as a basis to construct a mathematical and computational model (based on the work from [109]) which was able to reproduce experimental measurements as the mean number of aggregates and their concentration in each compartment. The models however did not considered any cross-compartment movement based on the observation of its scarcity nor (specifically) any large organelles affecting aggregate motion.

In every case, the models where validated with limited self-produced experimental data acquired mostly under specific experimental conditions in which aggregation was induced. Moreover, data for comparison and validation was short-termed, hence potentially misleading as no long-term effects of the mechanisms at test were analyzed.

In this research, the first purpose is to construct a comprehensive model including all (possible) essential mechanisms which could potentially affect aggregate kinetics as well as the passive processes being evaluated. Like [1, 14] some of the intracellular crowdedness is captured through the diffusion coefficient. However, (two) large organelles that can strongly interfere with aggregate diffusion are also included. Moreover, unlike [1] aggregate fusion, appearance and growth is incorporated as well as a growing bud with bud-specific dilution. Additionally, and different from [14] movement between both cells through the neck is also allowed.

All the parameter values are based on existing experimental data while carefully verifying the experimental conditions under which they were acquired to avoid any possible mis-interpretations of the results.

A thorough comparison between the results provided by the model and available short term and long term experimental data is done to evaluate the robustness of the sufficiency of passive mechanisms. Naturally, the model is expected to replicate observations which are used to argue in favor, but it is believed that most essential is to evaluate its performance concerning the comparison with other "external" data from diverse publications. Specifically, that acquired under different experimental conditions and over different time-scales (*e.g.* the complete life-cycle).

Last, it is tested on whether the model's predictions ameliorate or worsen when potential active mechanisms are incorporated in some form, either by confinement to organellar sur-

faces [105–107], attachment to the cell membrane [16] or occasional transport towards the mother cell pole [2, 18].

Methodology

The three-dimensional "Passive-Only Model" (POM) is constructed with the aim of testing the sufficiency of passive mechanisms. The processes incorporated are shown in Fig. II.1 of Chapter II. A large number of numerical simulations of this model for both short (over one division cycle) and long time-scales (over the entire cell cycle) are done in order to calculate statistics over quantities for which an experimental measurement is available. These statistics are: the total aggregate volumes (and relative concentrations in each cell) and numbers, the probability of inheritance by the daughter of at least one aggregate (when it exists) and of the largest aggregate, the number of cross-compartment crossings in each direction and the MSD.

The numerical and computational results are validated with an original mathematical model consisting of a system of coupled ordinary differential equations. The model calculates the time behavior of the average number of aggregates and of aggregate volumes in each cell and is inspired on the work from [11–13]. The agreement between the mathematical and the computational models is very accurate at short and medium time-scales (up to one or a few divisions). At longer times, the mathematical model serves as an upper bound of aggregate concentrations in the mother since it treats all aggregates equally, hence minimizing the size-dependent fusion (by collision) and the escape rates.

A model where different forms of infrequent (and difficult to detect experimentally) AQC is also introduced. The basic principle is that most aggregates are at all times subject to only passive forces. Occasionally however, aggregate motion can be (individually) disrupted either by drift towards the mother cell pole, confinement to organellar surfaces or attachment to the membrane. These variants ware used to test on whether infrequent AQC can potentially reconcile the work and the conclusions from divergent experimental studies.

Results obtained

At short and mid time scales (at most one cell division cycle), and as expected, the POM performs well in replicating empirical measurements used to argue in favor of the sufficiency of passive mechanisms [1, 14]. In particular, the MSD of aggregates agrees with the (mid time-scale) prediction from [1] of $\alpha \simeq 0.75$. However, one must note that this equation is no longer valid considering the changes in the diffusion coefficient as a consequence of aggregate growth and fusion. It also replicates results from [1, 14, 15] concerning the relative concentration of misfolded proteins in both compartments. Moreover, the model also reproduces the numerical and experimental results from [14] concerning aggregate numbers and fusion events.

A red flag is raised when comparing the number of crossing events (in both directions) calculated using the POM and from the experimental observations in [1, 14]. Unlike the predictions from [14] neck-crossing events between both compartments are very frequent and almost two orders of magnitude more numerous than measured in their experiments.

For safety, this result was validated with the mathematical predictions derived from [11–13] concerning mean exit times for diffusing particles in confined domains. Moreover, it was tested from different parameter values which would correspond to different experimental set ups. It is recalled that the assumption of infrequent cross-compartment movement was the premise to discard cross compartment transport in the computational model from [14].

At long time-scales (over the entire yeast cell cycle) divergence between the model's predictions and their respective experimental measurements increases. Although the number of aggregates –under parameter values corresponding to aggregation rates in WT cells– agrees with the results from [16], almost every other prediction disagrees with available experimental data concerning the accumulation of damaged proteins. Specifically, aggregate volumes stabilize after a few generations contradicting the premise that damaged proteins accumulate with replicative age and drive yeast cells to aggregate-dependent aging. Probabilities of inheritance of at least one aggregate and of the largest aggregate by the daughter also fail to agree with the empirical measurements in [17]; they are approximately a three-fold and a ten-fold higher respectively.

The number of cross-compartment crossings remains orders of magnitude above its experimental equivalent at long time scales. Although the number decreases after a few generations (or increases at low aggregation rates), as aggregates grow in size, it generally stabilizes at a value approximately one order of magnitude above.

When adding AQC to the POM, the disagreement with experimental data is substantially reduced even at low probability values of motion interference. The number of crossings is strongly reduced (for all aggregation rates) at short and long time-scales and damage accumulation occurs at rates similar to empirical measurements, as are the probabilities of inheritance of at least one aggregate and of the largest. Moreover, due to its infrequency, AQC is also consistent with the experimentally measured MSD. It is noted that results from this model rely on parameters that have no current experimental validation.

Discussion and perspectives

The mechanisms behind the asymmetrical distribution of damaged proteins during and after yeast cytokinesis are still unclear. Accumulation of damaged or misfolded proteins is related to proteoxicity and aggregate-dependent aging in budding yeast [18]. In particular, the debate on whether AQC is necessary remains [1, 2, 14]. To address this issue, a computational and mathematical model is introduced. At short time-scales, corresponding to one division cycle, the (passive-only) model is able to replicate experimental results which were used in favor of the absence of AQC. More specifically, those concerning the establishment of asymmetrical concentrations in both cells as a consequence of aggregate constrained diffusion, fusion and growth together with bud-specific dilution. However, cross-compartment transport is significantly more frequent than observed in experiments [1, 14]. At long time-scales, gradual damage accumulation in older cells only occurs under high aggregation rates similar to those observed in stress induced cells. Aggregation rates in WT cells do not lead to the accumulation of damage but rather a constant damage release from cell division. This contrasts the observations from [18]. When introducing AQC, differences with experimental

data are substantially improved, suggesting its presence in real life yeast cells.

The detailed and complete research on the subject is presented in Chapter II in the form of the accepted version of the article which was later published in *Biophysical Journal* [19].

After the publication of the article, evidence of a dependence on ACQ mechanism has grown and the sufficiency of passive mechanisms has lost strength even among the authors who initially advocated for it [1, 106]. In particular, research has identified new genetic mechanisms which play a role in the clearance, accumulation and retention of misfolded proteins in mother cells [108]. Moreover, other periorganellar protein deposits (the MAGIC) have been identified a well as the mechanisms which favor their formation [106].

Although no specific extensions of this research have been discussed thoroughly, there is a potential to work on applying similar models to analyze the intracellular mechanisms which favor proteotoxic aggregation of phosphorylated Alpha-synuclein (aSyn). This protein has been found to play a role in the development of synucleinophathies and Parkinson's disease [112]. Additionally, there has been discussion on the option of applying equation-free methods (see below) to analyze bifurcations occurring on the asymmetric distribution of damage when gradually varying the degree of AQC yeast cells are subject to.

I.1.2 Amyloid beta (Aβ) spatial propagation in Alzheimer's Disease

Scientific context

Aggregation of misfolded proteins is not unique to microscopic organisms. Therefore, in vitro experiments often use yeast as a model organism to study human diseases. This pathophysiology has been related to a group of diseases referred to as amyloidosis, as well as with Parkinson's and Alzheimer's disease (AD).

AD consists on a gradual neuron loss not consistent with habitual aging. It is strongly associated with the Amyloid beta (Aβ) peptide (short chain of 39 to 43 amino acids) [113]. Most prominent are the Aβ40 and Aβ42 peptides. These peptides appear from the proteolysis (rupture) of the Amyloid Precursor Protein (APP) which is produced by healthy neurons and which attaches to the membrane of neuron cells with an endogenous purpose that remains unclear although believed to be related to synapse formation, neural plasticity and iron export [114]. Misfolded Aβ peptides are highly contagious (they misfold other Aβ peptides) and aggregate to form insoluble oligomers which, together with the Tau proteins (τ) are early biological markers of the disease [115, 116]. Moreover, both are believed to play a fundamental role in its development and its progression. Brains of patients with advanced AD, display amyloid plaques which form from aggregated fibrils which themselves are composed mainly from aggregated Aβ oligomers.

The relation between the disease and the Aβ peptide is multi-scaled, although some recent findings suggest that microscopic forms (small oligomers of more than 3 or 4 monomers) are the most proteotoxic to neurons [4, 117, 118] due to their fast propagation and potential neuronal damage. It has been suggested that these proteins interact and misfold glycoproteins (PrP^C) to form oligomeric prions (PrP^{Ol}): exponentially-multiplying infectious

misfolded proteins with multiple toxic interactions with biological cells [119]. In AD, prions affect membrane receptors ultimately causing abnormal and unregulated neuron death. Prion formation is also related to numerous other diseases and neurological disorders [120]. Neuron cells are also affected at other spatial scales by amyloid deposits (see Fig. 3 in [66]) *e.g.* by depletion of normal proteins or brain inflammation. The pathway in which the Aβ pathology propagates throughout the diseased brain follows what is referred to as the *cascade hypothesis* [113]. It initiates through primary nucleation (misfolding) into Aβ monomers referred to as "seeds". This is understood as a rare event and is followed by fast contagion (misfolding of healthy proteins) and oligomerization (aggregation). Recent discoveries show the existence of a positive feedback where infected cells increase production of Aβ proteins leading to a further acceleration of the pathology [121]. As the pathology progresses, fibrillar structures and plaques begin to form. These structures remain fixed or travel slowly. However, breakage of fibrils produces new "seeds" which propagate fast and drive the spatial progression and the development of AD [5]. It is only at advanced stages of the disease and at longer-time-scales that the early symptoms of dementia begin to manifest [122].

The spatial and temporal progression of biomarkers and the appearance of symptoms in AD is highly complex and heterogeneous [122–125]. They do not occur at constant velocities or constant rates. Instead, patients can have stable diagnostics and spatially steady (configurations, invasions, contaminations) before undergoing rapid decays in health due to fast spatial and cognitive-impairing bursts [122, 124, 125]. Despite its importance, the microscopic dynamics of propagation and proliferation of (small) misfolded Aβ deposits have been seldom studied both experimentally and theoretically. In the case of the former (as well as of the latter, indirectly), limitations are mainly due to technical and technological difficulties concerning the small size of this peptides (the monomers) (around 1 nm [117]). Only recently, the spatial propagation and the evolution of the concentration of Aβ oligomers has been visualized in experiments. One of which described in [126], where the progression of seeded Aβ proteins in brains of *Drosophila* flies were imaged through western blot analysis. Imaging results have been captivating and promising and have called for further state-of-the-art theoretical and empirical work which can help understand the processes behind the behaviors observed.

The dynamics of misfolded proteins and their role in neurodegenerative disorders have attracted considerable mathematical and computational work [127] with a strong increase during the last 30 years. Most seminal works have used one-dimensional systems of ODEs to model and replicate the dynamics of aggregation and proliferation of prion proteins [128–131] and have found that prion accumulation generally occurs under special conditions concerning misfolding and refolding rates and protein concentrations. Although most of these works rely on an infinite number of differential equations, each corresponding to an aggregate size, [130] reduced the number to three. Different spatial extensions to these models have been proposed under the assumption of isotropic diffusion [132], diffusion combined with a network topology [133] or lattice-like domains based on cell connectivity networks [134].

Concerning AD, modeling has focused mainly on analyzing microscopic processes related to prion replication or joint prion-Aβ dynamics [135–137]. Fewer work has aimed to under-

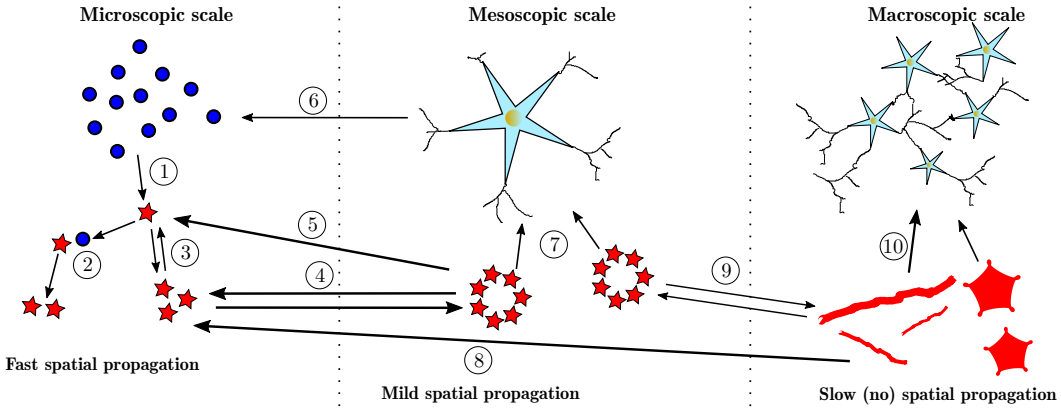

Figure I.2: Multi-scale schematic representation of Aβ propagation-associated processes. 1. Primary nucleation (protein misfolding). 2. Recruitment of healthy proteins. 3. Aggregation of misfolded proteins. 4. Fragmentation and fusion of proto-oligomers. 5. Polymerization and de-polymerization of misfolded monomers. 6. Production of amyloid precursor protein (APP). 7. Neuronal apoptosis. 8. Fibril de-polymerization. 9. Fibril cleavage and fibril formation. 10. Neuronal loss due to amyloid plaques and fibrils.

stand Aβ replication and/or spatial propagation. Although similar, some molecular processes behind Aβ and prion aggregation and proliferation are different [138]. For instance, with respect to size-dependent conditions related to the solubility of oligomers [139]. Early work [140] found critical concentrations of Aβ necessary for their aggregation and nucleation with a model composed by an infinite system of ODEs. The results showed closed agreement with experimental data. More recently, a number of multi-scale, non-spatial models have aimed to understand the evolution of monomer, oligomer, filament, fibril, and even plaque concentrations (see for instance [135–137]), some using continuous and some using discrete oligomer sizes. The two approaches are similar at larger spatial scales but can have discrepancies at microscopic levels [141–143]. In the case of discrete sizes, models generally use Becker-Döring Equations to describe the concentrations of the different species. Spatial extensions of these models have been rare with the possible exception of [144, 145] where interesting results where achieved but where potentially essential biological factors were omitted when extrapolating microscopic processes to larger-spatial scales. Integration of microscopic, mesoscopic and macroscopic scales is difficult as there different time and spatial processes intervening at each level (e.g spreading through exosomes or axons, cerebrospinal fluid). In general, few models have successfully integrated molecular and large scales with the majority of the theoretical work done separately, as explained in detail in [127].

Research Objectives

The ongoing research on the spatial dynamics of Aβ propagation and proliferation has as a general aim to construct (or contribute to the formation of) a multi-scale mathematical and computational model that builds from microscopic biomolecular processes to macroscopic dynamics of large Aβ deposits (plaques and fibrils) while strongly relying on the biological mechanisms intervening at each scale (see Fig. I.2). Starting from the elementary molecular dynamics of Aβ peptides and their interaction with a single or a handful of neurons, grad-

ually add complexity at different scales by incorporating the different biological processes which are known to have an effect on amyloid propagation. The purpose is to provide a theoretical framework which can have therapeutic applications in terms of diagnostics, prognostic predictions, and the design of control and mitigating strategies. These models exist today and are used in the treatment of other diseases (*e.g.* tumor growth in cancer [146]).

The first step towards this ambitious goal is to build a mathematical and computational model which is able to accurately represent and reproduce the microscopic and mesoscopic (up to a few neurons) spatial dynamics of Aβ concentrations. For this, recent results in experimental papers as in [126] can be used for comparison. This already imposes several challenges arising, for instance, from the uncertainty concerning how proteotoxic species affect further production of APP proteins which themselves contribute to the formation of new Aβ monomers and of larger Aβ aggregates. Recent research has suggested a positive dependence between neuronal damage and APP production which is followed by a strong collapse at the time of necrosis [121]. In addition, other challenges arise from the difficulties in measuring some of the model parameters. However, explorative simulations comparing computational results with experimental observations can serve as a first framework for their initial calibration. These simulations can as well be used to observe the parameter dependence of the propagation and spread of amyloid concentrations and the conditions under which it is favored or hindered. After this initial stage, the purpose is to progressively move forward according to a feedback between the outputs of the model and the production of experimental and empirical data which allows for further developments. For this reason the work will progress closely with Human Rezaei and the team *Macro-Assemblages Protéiques et Maladies à Prion* (INRA Jouy-en-Josas).

Mathematically, the construction of this first model poses other challenges as are demonstrating the existence and uniqueness of solutions (well-posedness), their regularity and their boundness in finite-time.

In the work presented as part of this thesis, the aim is to introduce this fundamental mathematical model, potentially valid at microscopic and mesoscopic scales. In addition, to describe the processes it incorporates, their biomolecular motivations, its dimensionless form as well as to provide results concerning the equilibrium solutions prior to primary nucleation and its variational formulation. Based on the latter, the computational model used for simulations is presented, which is based on the finite element method (FEM).

Methodology

The mathematical model, introduced in Chapter III, analyzes the molecular dynamics of monomer, proto-oligomer (soluble) and (insoluble and stable) oligomer Aβ species in a two-dimensional spatial domain representing the region around one or a few neurons. It assumes an *in vivo* context where primary nucleation has already occurred (since it is rare event) and focuses on subsequent concentration dynamics, which are assumed to be deterministic. The model is based on empirical observations concerning the polymerization (aggregation) and depolymerization behavior of the Aβ peptides until a stable insoluble, micelle-like oligomer size is reached [147, 148] where proteotoxicity is maximal. Oligomer size is assumed to be

discrete (in terms of monomers) as a consequence of the microscopic spatial scales considered. Spatial scales in Becker-Döring and Lifshitz–Slyozov equations are analyzed in [142, 143]. New monomers are produced from a homogeneous source located at the membrane of neurons. This production is gradually altered as the oligomer concentration increases in the surroundings of the cells. The exact way in which proteotoxic effects from the Aβ oligomers affect further production depends linearly on the concentration history, albeit it can be changed following recent discoveries (*e.g.* [121]). For simplicity, the model does not consider prions directly but instead through proteotoxicity inflicted on neurons. The prion-like contagious behavior of misfolded Aβ is considered through the rate of polymerization, hence avoiding the necessity of considering two families of Aβ monomers. Proto-oligomers are formed through monomer polymerization and can fragment into proto-oligomers of shorter size unless they reach the critical size at which they become stable. Diffusion is assumed to be the main driving force dictating the spatial spread of concentrations; it is size dependent and follows the Stokes-Einstein relation. These processes are schematically represented in Figs. I.2 and III.2 of Chapter III.

Mathematically, the model consists on a system of i_0 coupled partial differential equations (reaction-diffusion PDEs); i_0 being the size of the oligomers for which the conformations become stable and insoluble. The reaction term corresponds to the polymerization, depolymerization and fragmentation rates and the diffusion term to the size-dependent diffusion. The model was originally thought to be an extension of the (spatially) one dimensional models in [135, 137], but the molecular processes were modified, and the context changed from *in vitro* to *in vivo*.

The computational model is derived from the variational form of the system of differential equations. For the simulations a finite elements method is used.

The parameter values are set to experimentally to existing data from available empirical bibliography or from personal communications with Human Rezaei.

Results obtained

Other than the formulation and introduction of the mathematical (including its dimensionless form) and computational models, other mathematical results of the system are obtained. This concern the mass dynamics (and boundness) and the equilibrium solution for the concentration of monomers around a single neuron of the system's healthy state prior to primary nucleation. Proofs of existence and uniqueness have also been provided by Ionel Ciuperca, Léon Matar Tine and Paul Lemarre.

With the computational model, simulation results have been obtained which already show a complex relation between spatial propagation and the model's parameters. Particularly a non-linear relation between fast oligomer propagation (causing neuronal death) and fragmentation rates. When fragmentation rates are high, fast diffusion of small oligomers and monomers drives the propagation of misfolded Aβ but only a small concentration of preteotoxic oligomers around cells occurs. In contrast, very low fragmentation yields a high concentration of oligomers but which propagate slowly throughout the domain.

Discussion and perspectives

The work on the spatial propagation of Aβ aggregates is presented as a preprint submitted to *ESAIM: Proceedings and Surveys*. Simulation results have attracted attention from empiricists concerning possible strategies of delaying the expansion of the disease, with future conversations pending concerning further directions to explore.

Short term perspectives include a robust exploration of the parameter dependence on oligomer accumulation in the surroundings of the cells and in the speed of neuronal apoptosis. Also, to explore other (nonlinear) functional relations between monomer production and oligomer concentrations which are more faithful to the latest empirical reports.

Mid-term perspectives include the extension of the model to other spatial scales of a few tenths or hundreds of neurons and to incorporate other possible means of propagation as are exosomes [149, 150] which have a qualitative effect on the spatial topology. Moreover, the dimensionality of the model and the assumption of isotropic diffusion have to be analyzed. The latter due to the environment is also being highly heterogeneous. At this scale the first fibrillar complexes are included.

Long-term perspectives include the formulation of extensions to larger spatial scales where processes as the formation of plaques and the recycling of cerebrospinal fluid could be incorporated. At all times a thorough examination and validation through comparisons with experimental data is expected.

Concerning the mathematics of the model, proofs of existence, uniqueness and positivity of solutions of the model have been contributed by Ionel Ciuperca, Léon Matar Tine and Paul Lemarre (Institut Camille Jordan). An article introducing the mathematical and computational models together with more robust simulation explorations and the latest mathematical advances is currently in preparation.

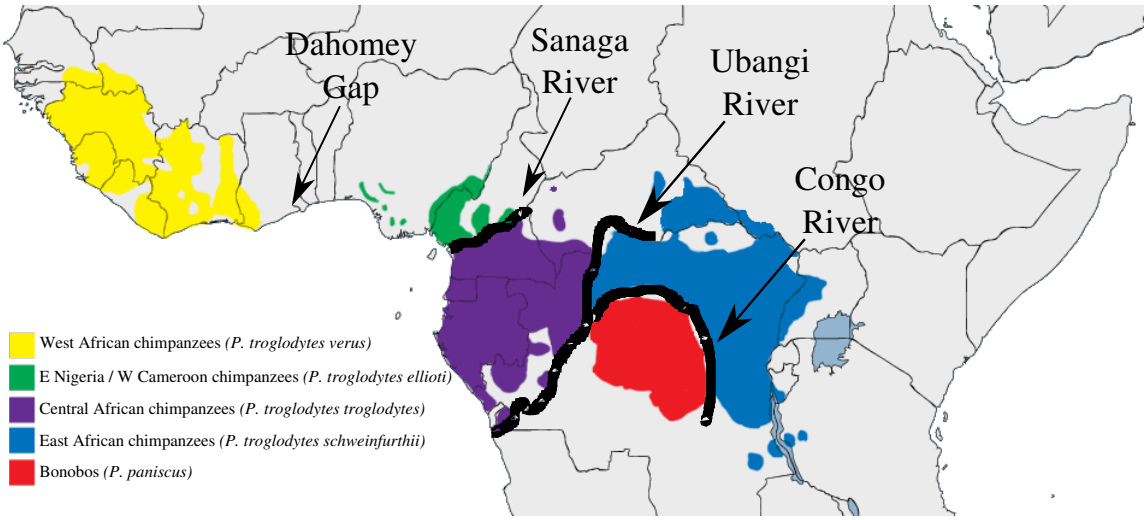

Figure I.3: Geographical distribution of chimpanzee species and subspecies. Fig. inspired from original in Hey, 2009 [151].

I.2 Part II

The evolution of diversity and the emergence and maintenance of new species are two of the most relevant research topics in Evolutionary Biology. Albeit diversification was traditionally believed to happen only as a consequence of local adaptation to different isolated environments (diversification occurring in Allopatry [23, 151–153], as the example in Fig. I.3, inspired on [151]), empirical and theoretical evidence from the last half-century, mostly attributed to advances in molecular phylogenetics, suggests that diversification is possible as well in the absence of geographical barriers. This is paradoxical with the 'optimization' view towards evolutionary processes since under its principles, deterministic convergence towards a unique optimum predicts uniformity (up to stochastic variations) due to the prevalence and superiority of the optimal phenotype. Moreover, it also confronts some principles of population genetics where, in sexual populations, mating and recombination homogenize populations and hamper linkage disequilibrium between reproductive and non-reproductive alleles hence preventing the emergence of new species [26]. According to E.Mayr [23], similar species coexisting in the same environment were believed to be an outcome of secondary contact between previously isolated populations which evolved and speciated separately in what is known as allopatric (or sometimes ecological) speciation (see for instance [154]).

The theory of evolution [155] has possibly been the most significant scientific advance of the modern era. Although initially advocated by Darwin, early research in the field generally excluded the feedback between ecological and evolutionary processes due to the difference in the time-scales over which they both occur. Recently however, gathering evidence has supported that not only can ecology affect evolution (through natural selection) but that rapid evolutionary change can also have an impact on ecological communities [156]. In principle, as a population evolves, it produces changes in the environment through ecological interactions. Environment which itself exerts selection pressures on the individuals's phenotypes and indirectly on the individuals genetic material. This results in an eco-evolutionary feedback

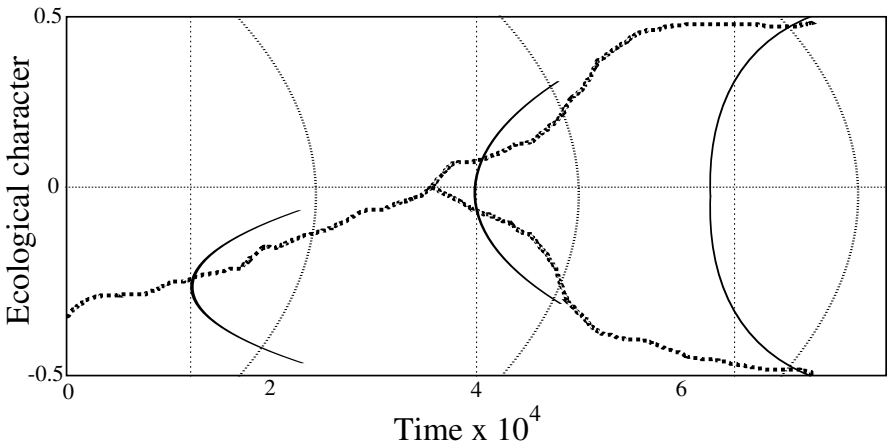

Figure I.4: Evolutionary branching from disruptive selection. Fig. inspired from original in Dieckmann *et al.*, 1999 [164]. Evolution of quantitative trait. Dashed curve shows resource distribution and continuous (inset) curve denotes fitness function. See article for complete figure description.

[157–162] which qualitatively affects evolutionary trajectories and attractors. Furthermore, it can lead to complex evolutionary dynamics which can even be potentially chaotic [163].

An remarkable outcome of eco-evolutionary feedbacks is diversification through disruptive selection (see for instance [164, 165] or [37] for theoretical and experimental reports respectively), where selection favors individuals of a population with extreme phenotypes rather than population's average [166–168]. It can produce a stable polymorphism and possibly lead to reproductive isolation and sympatric speciation –speciation over the same geographical range [164, 165, 169] (see Fig. I.4, inspired on the results from [164]). Disruptive selection is closely associated with frequency-dependent and density-dependent selection. In both, the population is part of the environment which through selective pressures determines the population's evolutionary path; the fitness landscape feedbacks on phenotype frequencies, densities and distributions. A common example of can be found disease resistance [170, 171].

Empirical and experimental evidence of diversification and speciation occurring due to eco-evolutionary feedbacks rather than geographic isolation has increased substantially in the last quarter-century in both asexual [36–40, 172] and sexual organisms whether occurring in sympatry (same geographic range) [27–34, 169, 173–175] or in parapatry (adjacent ranges) [176–178]. These studies have focused on geographic regions where environmental changes are constant or gradual and where there is no prevention to gene flow (see tables I.1-I.6).

Before this, theoretical work on the subject had already predicted this phenomenon. Foundational studies of the mathematical conditions under which disruptive selection can maintain polymorphism were presented in the seminal work of Maynard Smith [165, 167]. The disadvantage of hetero-zygotes is analyzed in models consisting on individuals with two possible alleles A and a in a heterogeneous habitat where each homo-zygote is fitter in one

of the two environments. Disruptive selection can maintain a polymorphism when selective advantages are large with respect to the relative capacities of each niche. In addition, habitat selection favors a stable polymorphism.

The work from Maynard Smith and others opened the door to the theoretical study of adaptive diversification and adaptive speciation (evolutionary branching). More recently, the development of mathematical and computational tools has stimulated the blossoming of theoretical biology. In particular it has propelled the development of studies concerning the evolution of diversity.

Evolutionary branching and the evolution of phenotypic clustering is another important prediction from eco-evolutionary models. It can occur as a consequence of negative frequency-dependent disruptive selection arising from resource competition [164]. For instance, once a population has evolved to consume the most abundant resource, it can experience decreased competition and can favor from consuming other available supplies. This can lead to an evolutionary branching point where can similar phenotypes can stably coexist.

In general, the study of evolutionary branching can reveal conditions and mechanisms involved in the evolution and adaptive persistence of phenotypic diversity [179, 180]; in sexually reproducing organisms, evolutionary branching and the evolution of reproductive isolation can reinforce one another and promote speciation (Dieckmann and Doebeli 1999 [164]) due to genetic or even plastic effects.

A growing number of models have shown that evolutionary branching and diversification in absence of geographical barriers can be a frequent and robust outcome of evolutionary processes as a consequence of various and diverse ecological interactions. Some examples include resource-competition, predator prey interactions, pathogens, parasites [181] (see also Table I.8).

Evolutionary branching is well understood, both heuristically (Metz et al. 1996 [182], Geritz et al. 1998 [183, 184]), and from a mathematical point of view (Champagnat and Méléard [185]). It occurs because of, and feedbacks on, ecological interactions. The mathematical framework under which evolutionary branching is normally studied is commonly known as Adaptive Dynamics. It studies evolution of quantitative traits which evolve according to rare mutation events. Ecological and evolutionary time-scales are separated so that one can assume that resident populations reach demographic stability before nearby mutants can or can not invade. Evolutionary dynamics then correspond to successive invasions of rare individuals with positive growth rate (invasion fitness). This fitness can normally be expressed in terms of frequency and/or density-dependent functions which correspond to particular ecological interactions. Mathematically, the evolutionary trajectory can be analyzed with the Canonical Equation of Adaptive Dynamics (CEAD): [186]

$$\frac{du}{dt} = m(u)D(u)$$

where u is the resident trait, $D(u) = \frac{\partial f(u,w)}{\partial w}|_{w=u}$ and $f(u,w)$ the invasion fitness of a trait w on a environment with a resident trait u. Evolutionary branching occurs when $D(u^*) = 0$,

$\frac{dD}{du}|_{u=u^*} < 0$ (evolutionary attractor) and $\frac{\partial^2 f(u,w)}{\partial w^2}|_{w=u=u^*} > 0$ (the point is invadable).

Evolutionary Branching in multi-dimensional trait spaces with co-evolving interacting traits and in the context of spatially explicit populations is less clear. In the case of the former, results have been conflicting [187–192]. In the case of the latter, the conditions favoring the emergence and stability of polymorphisms remain elusive. Because ecological interactions tend to take place locally in space among neighbor organisms, it is of special importance to understand evolutionary branching in the context of spatially explicit population models. This is especially true if the aim is to advance our understanding of speciation, given the potential significance of geographic factors in the origin of new species [22].

The research done for this thesis analyzing the emergence of diversity in spatially explicit populations has its foundations in an individual-based stochastic model introduced in [7] and its associated PDE. The model studies the eco-evolutionary dynamics of a population along a one-dimensional environmental gradient. In this context, adaptive diversification (speciation) concerns the formation of multimodal patterns in phenotype space which generally occur through the emergence of isolated clusters along the space-trait gradient.

The first article addressing this subject was not published but later included (in an adapted form) as the Supporting Information of the second, where most results are shown but the narrative is changed in order to address the effect of eco-evolutionary feedbacks in the context of spatial invasions and evolving dispersal. The article (available in HAL [8]) deepens on the conditions required for cluster formation and for their maintenance. Moreover, it analyzes thoroughly the parameter dependence of the observed patterns (mobility and competition and mutation ranges), the boundary effects, the transient dynamics of the system, and the characteristics of asymptotic patterns. The article also reports on cluster-formation rates and on the existence of multi-stability. The latter is later analyzed in a working paper (Chapter V).

The second article, published in *Ecology Letters*, studies how eco-evolutionary feedbacks shape the spatial dynamics of invading populations. In particular, how continuous and clustering regimes, appearing from eco-evolutionary feedbacks, influence patterns of invasion and invasion speeds.

This research, done in collaboration with Nicolas Champagnat and Regis Ferrière, aims not to focus on the mathematical properties of the dynamical systems arising from these models, but rather on the the biological relevance of the models' predictions. The work is presented in the form of the accepted version of the article in *Ecology Letters* [9] and its Supporting Information.

Multi-stability and the complex dependence of the system's dynamics on the model's parameters and the boundary conditions are the focus of ongoing work. The first part of this work is done in collaboration with Jens Starke (University of Rostock). It is based on the 'Equation-free approach' and is presented here in the form of a working paper expected to to be submitted soon. The second part, in a work in progress with Khashayar Pakdaman, multi-stability and the mathematical properties of the system are analyzed by tracing back

to elementary mathematical models which already show this behavior. This work is not presented as part of this thesis.

Before describing the research done, a short overview of the ground-breaking empirical and theoretical results on adaptive diversification and speciation is presented in the next sections.

Review of (a few) seminal empirical and experimental studies on diversification and speciation

In tables I.1-I.6, some seminal experimental or empirical studies documenting possible diversification or speciation in absence of geographical isolation are shown, together with a short description of the methodology and the species and location targeted.

Demonstrating sympatric or parapatric speciation in empirical work in substantially difficult since multiple approaches are usually required to discard possible secondary contacts. However, in controlled experimental environments, where the evolutionary dynamics of microscopic organisms (or of insect populations) can be tracked at reasonable time-scales, conditions under which phenotypic or genetic diversity can emerge and is maintained have been reported. Moreover, some of these studies have proved that these processes are robust, frequent and replicable. A few of these analyses are shown in table I.1. In tables I.2 and I.3 empirical reports of possible sympatric speciation in more complex organisms are shown. Some of these works have been controversial for their possible limitations to convincingly to disprove secondary contact. However, most of them have used multiple-based approaches to address potential issues. Moreover, they generally have focused on recently formed, or isolated environments where secondary contact is unlikely. In tables I.4-I.6 other cases of speciation (or diversification) –in experimental designs or in empirical analyses– in spatially-structured or in ecologically-diverse environments are shown. These works report on overlapping spatial ranges of the species involved, although also on the necessity of space or different ecologies for the appearance and maintenance of diversity. These works relate directly to the research done in this thesis.

Review of (a few) seminal theoretical studies on adaptive dynamics, diversification and speciation

In tables I.7 and I.8 a few of the major theoretical developments or contributions in the study of eco-evolutionary dynamics and/or the emergence of biological diversity are presented. Some of these advances, as the early theoretical developments, the field of Adaptive Dynamics or the CEAD, have been introduced in previous sections. Here, other major groundbreaking advances are also included and described. For instance, the introduction of the Hamilton-Jacobi approach, which naturally constructs continuous trait dynamics –in the limit of small mutations–from evolutionary processes of discrete mutational jumps, and which is specially useful in studying asymptotic behavior. Also, the development of the stochastic framework which analyzes evolutionary dynamics in finite probabilistic systems (more similar to real environments) and how they relate to deterministic models. Specially important for this thesis are the last two, as well as the study of diversification in spatially-explicit environments

Sympatric speciation (diversification)		
Experimental studies		
Species	Comment	Reference
Escherichia coli	Stable polymorphism in experimental environment. Differences in metabolism and growth rates.	[39]
	Stable polymorphism in experimental environment. Differences in metabolism and growth rates. Frequency-dependent fitness detected.	[40]
	Restriction Fragment Length Polymorphism (RFLP) analysis to reconstruct phylogeny from polymorphism in [40].	[193]
	Stable polymorphism in 5 of 12 experimental lines. Differences in diauxie patterns (growth phases). Frequency dependence detected.	[36]
	Stable polymorphism in experimental environment. Differences in diauxie patterns, metabolism and growth rates. Frequency dependence detected.	[194]
	Whole-genome sequencing to detect adaptive diversification. Detection of different ecotypes emerging from eco-evolutionary feedback. Similarity with mathematical models.	[37]
	Stable polymorphism in experimental environment. Sequencing reveals 3 mutations in regulatory genes which allow frequency-dependence necessary for diversification.	[195]
Anopheles gambiae and Anopheles coluzzii mosquitoes	Introgression and Sequencing to identify relation between speciation and assortative mating genes in sympatric sister species.	[196]

Table I.1: A few seminal experimental studies on sympatric speciation.

Sympatric speciation (diversification)		
Empirical studies I		
Species	Comment	Reference
Amphilophus zaliosus and Amphilophus citrinellus Midas cichlids	Convincing case of sympatric speciation inside the recently formed Lake Apoyo (Nicaragua) based on multi-method approach. The two species are reproductively isolated.	[27]
9 and 11 tilapiine or tilapia-like cichlids	Sequencing of endemic species of lakes Barombi Mbo and Bermin (Cameroon) suggests monophyly, hence one colonization by ancestors (per lake) followed by successive cases of sympatric speciations.	[30]
Tilapia deckerti cichlids	Undergoing case of sympatric speciation detected (my multi-method approach) in Lake Ejagham (Cameroon) among two morphs of the same species. Apparent reproductive isolation.	[31]
Amphilophus sp. Midas cichlids	Genome-wide analysis suggesting cases of adaptive radiation and simpatric speciation inside Lakes Apoyo and Xilo\'a (Nicaragua) by reconstruction of evolutionary history.	[197]
Amphilophus tolteca Midas cichlids	Potential case of undergoing sympatric speciation detected incrater lake Asososca Managua (Nicaragua) by morphological and isotope analysis of benthic and limnetic populations.	[198]
Sarotherodon sp. cichlids	Phylogenetic analysis of endemic species to lake Barombi Mbo reveals probable speciation in sympatry together with secondaryhybridization.	[199]
Salvelinus alpinus Fjellfrøsvatn arctic char	Morphological and behavioural analysis of two sympatric morphs (littoral and profundal) in recently the formed postglacial Lake Fjellfrosvatn (Norway) shows evidence of potential genetic differences (speciation).	[200]
Salvelinus alpinus Arctic char	Convincing cases of sympatric speciation by morphological and genetic analysis of populations in five Icelandic postglacial lakes. Complete reproductive isolation in one of them.	[28]

Table I.2: A few seminal empirical studies on sympatric speciation

Sympatric speciation (diversification) or speciation in Sympatry		
Empirical studies II		
Species	Comment	Reference
Arecaceae Howea Palm trees	Apparent sympatric speciation of two endemic sister species of Lord Howe Island determined by sequencing and significant difference of flowering times.	[29]
18 endemic and one non-endemic species of Palm trees	Evidence for sympatric speciation in populations from Lord Howe Island from genetic and ecological analysis that determine presence of ecological or geographical isolation.	[201]
Littorina saxatilis snails	Partial reproductive isolation and assortative mating detected by morphological and behavioral analysis in two morphs from Galicia (Spain). Possible case of undergoing sympatric or parapatric speciation (or along an environmental gradient).	[32]
Littorina saxatilis snails	Genetic analysis of diversification along gradient in Yorkshire (England). Evidence of disruptive selection by higher diversity than expected from cline.	[202]
Acomys cahirinus spiny mice	Evolution Canyon, Israel & Morphological and genetic analysis on a individuals from the Evolution Canyon (Israel) to determine potential incipient speciation between 'south-facing' and 'north-facing' slope populations.	[203]
Spalax galili blind mole rat	Genome-wide analysis on chalk and basalt soil populations in Israel identifies more than 300 diverging genes associated to different ecologies in possible case of sympatric speciation.	[204]
Heliconius melpomene, Heliconius cydno and Heliconius heurippa butterflies	Case of speciation (in sympatry) occurring in Panama, Colombia and Venezuela where reproductive isolation occurs due to hybrid speciation. Behavioral and morphological analysis from laboratory crosses.	[174]
Nesospiza buntings (island finches)	Morphological and phylogeographical study of populations in the Tristan da Cunha archipelago shows parallel cases of adaptive radiation occurring in sympatry. Speciation mainly ecological (selection for different environments).	[205]

Table I.3: A few seminal empirical studies on sympatric speciation. In green are two studies where speciation occurs in sympatry but as a consequence of other processes.

Speciation (diversification) in parapatry or in spatially-structured populations		
Parapatric speciation		
Species	Comment	Reference
Pollimyrus castelnaui Mormyrid fish	Morphological data and mitochondrial sequencing to identify parapatric speciation in Okavango-Upper Zambezi river systems.	[177]
Plethodon cinereus Salamander	Genetic, climate, ecological and morphological study in Long Island, NY. Pure-redback populations (west) and pure-leadback populations (east) Different ecological preferences. Spatial segregation of sympatric ecotypes for parapatric speciation.	[176]
Senecio lautus australian groundsel	Morphological and ecological data to analyze for reproductive isolation of adjacent populations in the Australian coast.	[178]
Diversification in spatially-structured populations		
Pseudomonas fluorescens	Stable polymorphism in experimental environment. Adaptive radiation (rapid diversification due to heterogeneous environment) along a spatially-structured environment.	[206] (Review [207])
	Sequencing of one the morphs in [206] to identify genetic and phenotypic characteristics.	[208]
Ring species		
Ensatina eschscholtzii salamander	High genetic distance between populations determined by analysis of protein variation of adjacent populations in California.	[209]
	Reports on reproductive isolation due to genetic rather than ecological divergence.	[210]
Phylloscopus trochiloides greenish warbler	Genetic differences and reproductive isolation found by sequencing and song playback experiments on extreme populations connected by a chain of interbreeding ones around the Tibetan Plateau.	[211]

Table I.4: A few seminal studies on speciation (diversification) occurring in absence of geographic isolation; in parapatry or in spatially-structured environments with possible gene-flow.

Other cases of adaptive radiation (rapid diversification)		
Species	Comment	Reference
Pseudomonas fluorescens bacterium	Negative impacts of environmental gradients on diversification processes found due to niche specialization (diminished resource competition).	[212]
	Analysis of impact of position and width of niche of ancestor on diversification.	[213]
Anolis lizards	Morphometric analyses in Cuba, Jamaica, Puerto Rico and Hispaniola to asses for parallel adaptive radiation in four different environments.	[214]
Placental mammals	Sequencing and phylogenetic analysis to detect parallel evolution and for the classification of placental mammal into 4 clades.	[215]
Tetragnatha spiders	Analysis of species assemblies in Hawaiian islands to analyze patterns of adaptive radiation. Detects occurrence of similar sets of ecomorphs due to dispersal and evolution. Maximum number of species in communities of intermediate age.	[216]
Cichlinae Neotropical cichlid fishes	Density-dependent burst of adaptive radiation detected by analyzing cichlid fossils from Central and South America.	[217]

Table I.5: A few seminal studies on rapid speciation (or diversification) occurring in absence of geographic isolation or under possible gene-flow.

Speciation (diversification) along environmental gradients		
Species	Comment	Reference
Coregonus fontanae and Coregonus albula Coregonid fishes	Analysis of metabolic rates (physiologogical adapations) to study speciation along a temperature-depth gradient in the post-glacial lake Stechlin in Germany.	[218]
Sebastes mentella Pelagic beaked redfish	Genetic analysis of speciation along a depth gradient to identify signs of adaptation to different depths.	[219]
Sebastes marine rockfish (66 species)	Speciation (in parapatry) along a depth gradient (depth-related morphological differences) found with phylogenetic analysis.	[220]

Table I.6: A few seminal studies on speciation (or diversification) occurring in absence of geographic isolation along environmental gradients.

or along environmental gradients.

I.2.1 Adaptive diversification and cluster formation along environmental gradients

Scientific context

The spatial context of evolutionary branching relates to the conditions and the mechanisms behind the appearance and maintenance of phenotypic diversity and speciation in spatially-explicit populations [20–22]. It is a natural extension of one-dimensional trait models since forms of speciation and diversification are defined according to their spatial context. The emergence of diversity or of new species (under sexual reproduction) associates with the appearance of multi-modality in phenotype space, which is usually accompanied by clustering along the spatial dimensions appearing as a consequence of the feedback between evolutionary processes and local ecological interactions. Here, clustering corresponds to the collective behavior, emerging from local interactions, in which individuals gather in isolated patches to form high-density groups interspersed with low density areas [237–241]. Clusters stand in contrast to continuous distributions along the space-phenotype domains [21, 242–244].

There is a strong consensus that diversification (speciation) [23–26] frequently occurs in allopatry through the obstruction of motion and/or gene-flow by geological or geographical barriers. However, in absence of geographic obstructions, the precise conditions favoring or hampering the emergence of diversity remain unclear despite growing interest, as experimental and empirical evidence have accumulated in recent years for both sexual organisms (sympatric speciation in [27–35], parapatric speciation in [176–178], adaptive radiation in [175]) and asexual organisms [33, 36–40].

To address this question, mathematical and computational models typically consider an

Adaptive Dynamics (AD) and adaptive diversification		
A few ground-breaking theoretical developments		
Topic	Comment	References (a few)
Early theoretical developments	Maynard Smith's work on the conditions for the emergence and maintenance of diversity (polymorphism) in sympatry.	[167] [221] [165]
Invasion dynamics	Mathematical framework to describe dynamics of growth and of rare invaders in resident populations when taking into account ecological interactions between the populations.	[158] [222]
AD Framework	Mathematical framework for the study of evolutionary dynamics in terms of quantitative traits. Particularly for the study of speciation and diversification. by taking into account ecological interactions.	[182] [158] [183] [184]
CEAD	Ordinary differential equation describing the evolution of a quantitative trait derived from successive mutant invasions. I assumes that separation of time-scales of ecological and evolutionary processes.	[186]
Stochastic framework	Development of stochastic framework for AD. Derivation of mathematical results from stochastic systems of evolving traits. Unification stochastic and deterministic models.	[223] [185] [7]
The Hamilton-Jacobi approach	Derivation of HJ evolution equations describing the dynamics of quantitative traits in the limit of small mutations (long evolutionary time-scales). Allows for asymptotic analysis.	[224] [225] [226] [45]
AD along environmental gradients	Derivation of models of AD in spatial contexts. Conditions for diversification in spatially-explicit models.	[22] [227] [228]

Table I.7: (Some) Important theoretical developments in adaptive dynamics and/or in the study of diversification in eco-evolutionary models.

Adaptive Dynamics (AD) and adaptive diversification		
A few ground-breaking theoretical developments		
Topic	Comment	References (a few)
Theoretical models of sympatric speciation (sexual reproduction)	Theoretical models proving the plausibility of sympatric speciation under sexual reproduction.	[165] [164] [180] [227] [22]
Multidimensional adaptive diversification	Multidimensional trait extensions of AD models and of adaptive diversification.	[187] [188] [191] [192]
Evolutionary suicide	Theoretical demonstration of how natural selection and evolutionary processes can lead to low population densities or extinction.	[229] [230]
Other extensions applications of AD framework	Seminal theoretical extensions or applications of the mathematical framework to evolving dispersal, host-parasite systems, predator-prey models and data-based studies.	[231] [232] [233] [234]
Other review papers and books		[235] [236]

Table I.8: (Some) Important theoretical developments in adaptive dynamics and/or in the study of diversification in eco-evolutionary models.

ecological scenario where environmental conditions change gradually in space. This gradual change can refer to variations in altitude, temperature, humidity or ocean depth among other abiotic characteristics. Such models predict the formation of patterns of abundance which correspond to the formation of phenotypically different sub-populations. This phenomenon is reported in [245] where different species of fish (with common ancestors) occur in parapatry with respect to oceanic depth.

Taking the spatial context of evolutionary branching raises issues. In particular, one issue of controversy has to do with boundary conditions. [227] argues that boundary conditions are likely to cause artefactual phenotypic clustering (versus a cline-like phenotypic distribution [246–249]) in a spatially extended population with local interactions. This contrasts the results in [22], where phenotype and spatial heterogeneity are attributed to local disruptive selection as in the classic case of non-spatial evolutionary branching [182]. Later, Leimar et al. (2008) [228] takes a stability analysis approach to counter [227] by showing that the evolution of phenotypic clustering is robust to boundary conditions.

Research Objectives

As the theory of spatial eco-evolutionary dynamics develops further, basic questions regarding cluster formation and dynamics in response to local adaptation and dispersal remain unanswered. First, our understanding of the conditions required for cluster formation and persistence is still incomplete. In particular, how does individual mobility affect cluster formation, and how does the effect of individual mobility interact with the scale over which individuals compete for resources? What is the behavior of the transient dynamics and their relation with their asymptotic limits? How does the bounded nature of both geographic and phenotypic space influence the dynamics of clustering? Can we predict key characteristics of the emerging population structure, such as inter-cluster distance and numbers of clusters, from individual-level parameters?

In the research done throughout this thesis, these questions are addressed with different mathematical and computational methods in light of providing a stronger theoretical background for the study of diversification along environmental gradients.

Methodology

The research has its foundations in a stochastic individual-based model and its PDE approximation [7]. Some limitations of previous approaches are removed (*e.g.* [228]). Instead of classical Gaussian competition kernels [250–253], constant competition within a spatial range and uniform competition with respect to phenotypes is incorporated. This removes spurious effects of Gaussian competition kernels on population dynamics and allows for an unambiguous measurement of the competition range. Moreover, fitness frequency-dependence is excluded from the assumptions opening the door to different adaptation and competition traits. This reflects better the observations in [245] where adaptation relates to oceanic depth and competition to food consumption, and those in [254], where competition occurs due to mate choice and adaptation occurs to other abiotic characteristics [254]. Other differences between the model and [228] can be noted: in [228], spatial dispersion occurs at births whether here individuals move according to a diffusion during their life. Intuitively, this favors mixing and sets more restrictive conditions for cluster formation. Mutations are assumed to occur by jumps at individual births. Moreover, both cases of unbounded and bounded domains are considered through periodic or mixed boundary conditions. Last, the model does not include Allee effects, that would otherwise extinguish local populations of extremely low density. The general links between this class of models and PDEs were studied by Fournier and Méléard [255], Champagnat et al. [185] and Champagnat and Méléard [7].

The dynamics of the system, both asymptotic and transient, are studied through numerical and mathematical analysis. In particular, how they relate to the individual-level parameters, initial conditions and boundary conditions. This is done through numerical simulations (using an explicit Euler's method) and through a Turing's stability analysis (both analytical and computational). In addition, a Hamilton–Jacobi approach based on [41–45] is used to predict characteristics of asymptotic periodic patterns. This approach is complemented with a computational model which uses refined methods.

Results and discussion

The research reports on broader ranges of parameters over which phenotypic clustering occurs; different transient regimes of the space-trait dynamics in relation with multiple attractors, where clustering is or is not artifactual with respect to the boundary conditions; and on quantitative insights into the long-term cluster and cline-like (continuous) patterns. The latter are based on the stability analysis and on the Hamilton–Jacobi approximation, where the distances between clusters as well as their direction of appearance are computed. In addition, we present simulations of the spatial dynamics under no evolution, which corroborate to show that clustering is reinforced by the feedback between both ecological and evolutionary processes.

Moreover, the results lead to two noticeable findings about cluster dynamics. First, the system exhibits multi-stability. Hence, small variations in initial conditions can lead to different attractors, manifesting as different cluster patterns (where the number of clusters changes). Also, disturbances may cause the population to switch rapidly between alternate stable states of spatial distribution and phenotypic composition. This is explored in more detail in the work done in Chapter V. Second, the rates of cluster formation are not constant. This is analyzed in detail in the subsequent work on the eco-evolutionary dynamics of invasion. As the population spreads from a focal location, the formation time of peripheral clusters varies, which results in a fluctuating invasion where the transient dynamics of local adaptation in established clusters is critical to predict the long-term dynamics of invasion.

The detailed and complete research on this subject is available on HAL [8]. Here, a modified version is presented as part of the main text and the Supporting Information of the article accepted by *Ecology Letters*.

Perspectives

Two extensions of the work done on the subject of diversification have been discussed and are planned for the near future. The first one concerns the eco-evolutionary dynamics of populations under a gradual variation in the environment. More specifically, the conditions concerning individual mobility, adaptation and resource competition which can or can not lead to population extinction and which uncover new evolutionary processes occurring through the interaction of dynamic environmental conditions with eco-evolutionary feedbacks. This work is relevant in consideration of present extinction rates [256, 257] and population migrations due to human-mediated climate change. Nonetheless, limited studies have incorporated eco-evolutionary processes to range dynamics [258–260].

The second extension of this work concerns the emergence of spatial and phenotypic clustering along environmental gradients under sexual reproduction. To address the topic of speciation rather than diversification, sexual reproduction needs to be taken into consideration. The work aims on studying favorable conditions (if any) under which clustering and phenotypic heterogeneity can occur when assortative mating is exclusively spatial. The novelty of this work relies on this assumption in contrast to most existing work on the subject [22, 165, 261].

I.2.2 The spatial eco-evolutionary dynamics of invasion

Scientific context

Understanding the invasion dynamics of biological populations colonizing new environments has acquired an unprecedented and substantial importance in recent years as a consequence of the alarming rates of habitat destruction due to agricultural and urban expansions, human-driven climate change and mining, among other various causes [262–267]. In this context, mechanistic models are required to address problems such as predicting and controlling biological invasions and managing translocations, introductions, and reintroductions of species [268].

Traditional theoretical models of range expansions, based on the principles of population dynamics and quantitative genetics, have predicted wave expansions with constant speed and hence have introduced the concept of invasion speed [46–48]. Recent observations showing non-constant invasions have been attributed to extrinsic environmental or stochastic factors (*e.g.* [269, 270]). However, and motivated on the discovery that population patterns of abundance depend on local ecological states, it has been suggested in recent years that ecological factors as predator-prey interactions of density dependence (in population growth and movement) could as well influence invasion dynamics [49, 50].

Research Objectives

The question on how evolutionary processes affect population range expansions generally has considered separately the influences of local adaptation [271] and of evolving dispersal [272]. In Chapter IV, the research addresses how the combined effects of local adaptation and of dispersal evolution affect the eco-evolutionary dynamics of spatial invasions. This research builds on the results summarized in the previous section. More particularly, on how the continuous *vs.* clustering dichotomy ([8, 228]) shapes the rates and the structures of spatial population spread. It is presented as the accepted version of the article, later published in *Ecology Letters* [9].

Methodology

The research is based on two models. The first being the model introduced in [7] and which is described in the previous section. The second, is constructed as an extension which incorporates evolving dispersal. In the latter, dispersal has an energetic cost which increases natural death rates in a degree which depends on a new parameter θ.

The models are analyzed through simulations of the stochastic individual-based dynamics and of their PDE limit. The PDE simulations are used to measure spatial invasion speeds and the degree of maladaptation at the population fronts in the context of a population which expands from a focal introduction site along a one dimensional environmental gradient.

Moreover, the Turing's stability analysis is extended to include evolving dispersal and the Hamilton Jacobi approach [41] is oriented towards the analysis of spatial invasions and

range expansions.

Last, different extensions of the model are explored (with Allee Effects, two spatial dimensions, and arbitrary gradient steepness) to show that qualitative results are maintained in more realistic scenarios.

Results obtained

The first results that are derived from our analysis are based on the original model which does not incorporate evolving dispersal. Simulations show that spatial expansions do not necessarily occur as expanding traveling waves. Instead, and depending on the diffusion coefficient and the competition range, expansions can be 'pulled' by continuous cluster formation, or 'pushed' by front expansion of a traveling wave. Moreover, transient distributions may not reflect asymptotic population patterns since unstable continuous expansions which break into clustering patterns can occur. Additionally, continuous expansions under can have peaks of abundance which do not necessarily occur at the population's front.

Invasion speed can vary qualitatively and quantitatively depending on the different expansion regimes. 'Pulled' invasion fronts have oscillating invasion speeds (which can drop to zero) as a consequence of invasion and adaptation phases. In contrast, 'pushed' invasions show constant invasion speeds more consistent with traditional predictions [46–48]. For parameter values in between both cases, invasion can proceed at modestly fluctuating rates.

The Hamilton-Jacobi approach applies only to clustering expansions as it is based on the assumption of slow motion. It shows that clusters influence one another, which in turn affects the rates of appearance of succeeding clusters further contributing to varying invasion speeds.

When dispersal and niche traits simultaneously evolve, mean dispersal tends to decrease due to increased mortality costs. However, this is not homogeneous since highly dispersal individuals can be positively selected at the fronts of the population and in the regions in between clusters (when present). Moreover, three alternate invasion regimes can be observed. As before, for very low dispersal, invasion proceeds through the formation of clusters which 'pull' the expansion. Similarly, for very high dispersal, invasion is 'pushed' by the expansion of a continuous wave. Notably, for intermediate dispersal, both regimes can co-occur with continuous waves breaking into a clustering expansions as a consequence of the interplay of eco-evolutionary feedbacks with selection of lower dispersal. The value of the dispersal-associated trait at which the transition occurs is approximated with a stability analysis. These different expansion patterns result in diverse temporal regimes of invasion speeds which can vary from relatively constant to strongly fluctuating. Finally, it is shown that all of these results are maintained under the incorporation of Allee effects.

Discussion and perspectives

The results from this research are relevant since they suggest new alternate explanations for non-constant velocities in population range expansions. This phenomenon has been detected in empirical studies [273] and contradicts traditional theoretical predictions [48, 274, 275].

Specifically, it is suggested that the interplay between local adaptation and dispersal evolution, together with local competition, can jointly vindicate for the fluctuations in invasion speed.

Moreover, the research sheds light on novel forms on which selection may act on dispersal which result in diverse spatially-dependent distributions of dispersal traits. Spatial sorting is generally observed (fast dispersers with high densities at the front) but dispersal is generally selected against, resulting in no selection for increased dispersal, in contrast with the observations in [276]. The dependence of invasion speeds on local adaptation rather than on increased dispersal at fronts is consistent with [277].

Discussions on continuations of the research are still pending but a few extensions have been already considered. In particular corresponding gradually changing environments and non-Brownian dispersal.

I.2.3 Equation-Free analysis of adaptive diversification along environmental gradients

Scientific context

The Equation-free framework, referred to as well as the Equation-free approach or as Equation-free or coarse analysis [51–53], has been developed over the last decades as a method to study complex multiscale systems where descriptions come at microscopic scales and the interest lies on macroscopic behavior. In these systems, there is clarity concerning the 'rules' governing the actions of the large number of individuals (or parts). In contrast, at a coarse-scale, equations describing macroscopic behavior (in terms of a low number of macroscopic quantities) are substantially difficult to analyze or, in most cases, unavailable. Some examples of these systems are pedestrian flows [278–280] and traffic models [278, 281] where microscopic descriptions can be 'naturally' derived from the forces driving the individual actions of the individuals.

The method relies on short simulations of appropriately initialized microscopic descriptions (computational 'experiments') which allow to estimate quantities that are would otherwise need to be inferred through mathematical analysis of explicit formulas or equations describing macroscopic behavior. Hence the term 'Equation-free', since these equations need not be explicitly written down [52].

Why and when to use Equation-free analysis

Simple systems are generally identified as those where the behavior of the system as a whole can be inferred directly from that of the parts. The simplest being those where the macroscopic outputs can be calculated from the addition of the outputs of each individual (*i.e.* models of exponential growth). Complex systems, on the contrary, show complex collective behavior as a consequence of individual interactions. This emergent behavior is not directly inferred from that at microscopic levels, but instead arises due to non-trivial effects as are, for instance, feedback loops or nonlinear dependencies. Some examples of complex systems with emergent collective behavior are cell systems with tumor growth, embryogenesis

or morphogenesis [282–286], ecological or economic systems wityh critical transitions [287], eco-evolutionary systems with evolutionary suicides [229, 288] or social systems with social dynamic trends [289, 290]. Complex systems can occasionally be analyzed through evolution equations, which are generally derived through averaging, infinite limit-sizes and/or scalings (*e.g.* [185]). However, in many cases, analysis from macroscopic evolution equations is inviable, either from difficulties arising from the derivation of such equations or from difficulties arising when analyzing emergent behavior through the mathematical analysis of them. Moreover, the derivation of information from complex systems concerning some of their macroscopic properties through numerical simulations can be substantially costly and impractical. Specifically, the identification of parameter dependencies, bifurcation diagrams, phase-transitions and the computation of equilibria (stable and unstable) can be computationally prohibitive through direct simulations of the system's dynamics. Moreover, since simulations build from microscopic descriptions and macroscopic and microscopic equilibria need not be simultaneous, as at macroscopic scales the system might be at rest while its parts are changing (*e.g.* molecules in a gas).

Equation-free methods [291] are used for the analysis complex systems at their macroscopic scales based on the observation that their behavior can be reduced to lower dimensions. More specifically, they build upon the computation of a few macroscopic quantities which are able to capture emergent collective behavior and observable properties. This dimensionality reduction of many to a few degrees of freedom is formalized in Fenichel's theory [292]. The low-dimensional object where the dynamics can be analyzed is referred to as the slow manifold which is where the long term dynamics of the system occur (See Fig. I.5A) given that the spatio-temporal macroscopic and microscopic are well separated. The macroscopic variables can be, for instance, the moments of the distribution, its Fourier components or the average velocities and/or momentums of the individuals (as in [279]).

Equation-free methodology

The methodology relies on continuous shifts between microscopic and macroscopic scales via the use of appropriately constructed operators, combined with (hopefully) short simulations of the microscopic system. This is used for the identification of the macroscopic dynamics which in turn allow for bifurcation analysis and numerical continuation in relation with the system's emergent behavior of interest.

The transition from microscopic to macroscopic scales is done via what is known as the Restriction Operator $\mathcal{R}$. It maps the microscopic system u from an N-dimensional space (N being the number of particles of the system) to an m-dimensional macroscopic variable X with $m \ll N$. In general, the restriction operator is build such that its output is (or are) the macroscopic variables which are found to capture the long-term dynamical behavior of the system.

In contrast, the shift from macroscopic to microscopic scales is done with the Lifting Operator $\mathcal{L}$. This operator is non-trivial and non-unique and must be appropriately chosen so that qualitative differences in microscopic configurations are captured by a continuous change in the macroscopic variable.

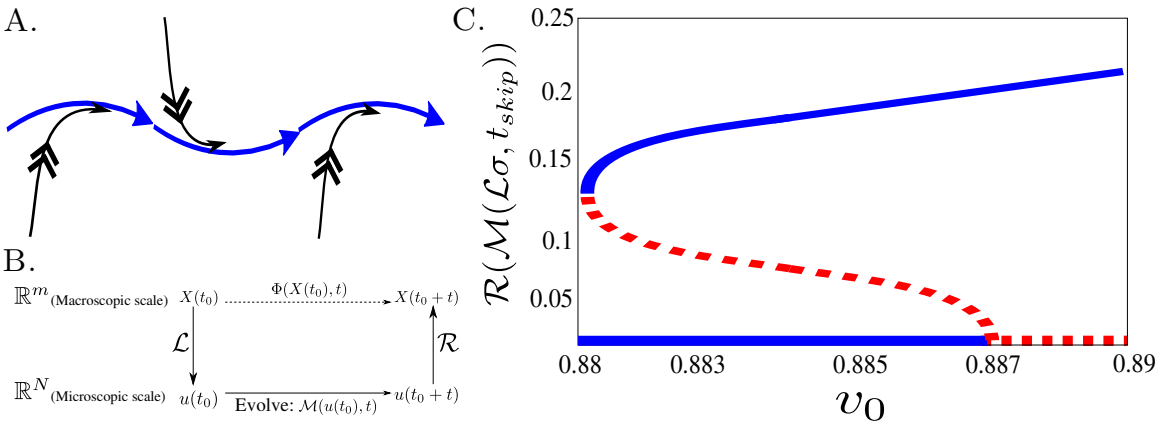

Figure I.5: Equation-free methodology and example. Figs. inspired from originals in Marschler *et al.*, 2014 [293] (panel A) and Marschler *et al.*, 2015 [278] (panels B,C). A. Schematic drawing of convergence to slow manifold. B. Equation-free methodology. Schematic drawing of the construction of the macroscopic time-stepper. C. Diagram of the equation-free bifurcation analysis in [278] of a traffic model when varying the optimal velocity parameter v_0. Blue marks stable states, while red marks unstable states. Upper branch corresponds to a traffic jam and lower branch to stable flow. Ordinate axis corresponds to a macroscopic measure describing traffic flow. For full details and descriptions see [293].

The microscopic time-stepper $\mathcal{M}$ corresponds to the time evolution of the microscopic system according to the fine-scale description of the dynamics. Equation-free analysis aims to construct a macroscopic time-stepper Φ. This is done through the *lift-evolve-restrict* scheme where the state of the macroscopic variable after a time t with initial condition $X(t_0)$ is constructed as: $\Phi(X(t_0),t) = \mathcal{R}\mathcal{M}(\mathcal{L}(X(t_0)),t)$ (see Fig. I.5B). The coarse (macroscopic) time-stepper can be combined with an interpolation method to compute the missing values of $X(t)$ (emphi.e. coarse projective integration [53, 291]). Using short simulation times δt, the *lift-evolve-restrict* scheme can also be used to calculate the derivatives $\dot{X}$, which can then be used to approximate subsequent values of $X(t_0+t)$ ($\delta t < t$) by extrapolating with the use of a first order numerical integration method (patch dynamics [53, 291]). Then, the missing gaps can be filled by interpolating, as illustrated in [53, 291, 294]. The computation of the derivatives $\dot{X}$ allows as well for the identification of macroscopic equilibria ($\dot{X} = 0$) and hence of macroscopic bifurcation analysis and numerical continuation. Macroscopic equilibria can be found using, for instance a Newton's method, on $F(X) = \dot{X}$.

It is possible that the Lifting Operator maps to microscopic states away from the slow manifold. For this reason, the construction of the macroscopic time-stepper by the *lift-evolve-restrict* scheme can be altered so that once the microscopic state is generated, the microscopic dynamics are ran for a small time t_{heal} before the analysis. Then the time image of an initial condition $X(t_0)$ is found implicitly as the solution of the equation:

$$\mathcal{R}\mathcal{M}(\mathcal{L}(y),t_{heal}) = \mathcal{R}\mathcal{M}(\mathcal{L}(X(t_0)),t+t_{heal})$$

Applications

Equation-free analysis has been used in recent years in different and diverse contexts involving complex systems and in control theory where identification of the basins of attraction of equilibria is essential. Some examples include micelle formation [295, 295], cell biology [296] and lattice gas models [297]. Fig. I.5C is inspired on the bifurcation diagram from a traffic system computed with coarse analysis and presented in [293]. The regions of stability of traffic jams *v.s* free flows (or of bistability) were identified as well as the bifurcations occuring in each of the branches. Similarly, in [279] a Hopf bifurcation was identified with respect to the size of the door separating two crowds of pedestrians walking in opposite directions. Equation-free analysis has even been considered in the context of experiments (which replace numerical simulations) for mechanical oscillators [298] and in pedestrian systems (current work from Starke and Panagiotopoulos at the University of Rostock).

Scientific context of multi-stability in eco-evolutionary models

Multi-stability has been reported in models exhibiting Turing instability where interpretations are relevant to evolutionary biology. Specifically, one-dimensional [45] (or two-dimensional [8]) models of adaptive evolution exhibiting pattern formation related with speciation and diversification. Among these models, potentially the simplest one exhibiting this phenomenon are the non-local Fisher equations, also referred to as competitive Lotka-Volterra models.

The classical Fisher equation [299] models the spatial dynamics of genes in a population. It is the outcome of combining the Logistic equation with a local diffusion term;

$$\frac{\partial\ n(x,t)}{\partial\ t} = k\ n(x,t)(1-n(x,t)) + D\frac{\partial^2\ n(x,t)}{\partial\ x^2}$$

where $k,\ D > 0$. This equation is well known to have traveling wave solutions which converge to homogeneous distributions [300, 301]. An extension of this equation, referred to as the non-local Fisher equation is studied in [45, 302]. It has the form:

$$\frac{\partial\ n(x,t)}{\partial\ t} = n(x,t)(1-\Phi * n(x,t)) + D\frac{\partial^2\ n(x,t)}{\partial\ x^2}$$

after proper re-scalings. The competition kernel Φ is positive and $\int \Phi = 1$. When the kernel is 'box-shaped enough' so that its Fourier transform is negative, the model exhibits Turing instability ([302, 303]), a behavior which is maintained in extensions as the ones considered in [228, 304, 305]. Moreover, as shown with simulations (of a concentrated variant) in [45], the system can also exhibit multi-stability of non-homogeneous patterns (at least transiently). Fig. I.6 shows long-term solutions of the non-local Fisher equation, computed with numerical simulations, which are potentially simultaneously stable.

Research objectives

The objective of the research in Chapter V is to use equation-free methods to analyze macroscopic equilibria and multi-stability in the stochastic IBM introduced in [7].

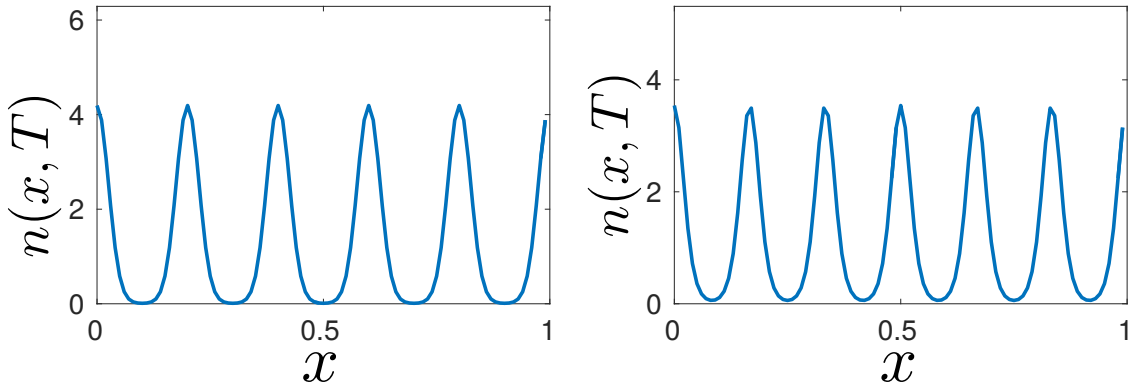

Figure I.6: Multistability in non-local Fisher equation. Simulations inspired from Perthame *et al.*, 2007 [45]. Two non-homegeneous stable solutions, after a time $T = 600$ computed numerically for the same parameter values but different initial conditions (5 and 6 peaks). Diffusion coefficient: $D = 5\times10^{-5}$, and support-width of a box-shaped kernel: $l = 2\times b = 0.3$. For full details see [45].

As previously noted, simulations of the stochastic IBM and its deterministic limit –in absence of evolving dispersal– showed a strong presence of multi-stability. Specifically, concerning macroscopic distributions which fragment into a different number of isolated clusters with a strong dependence on the initial conditions and the boundary of the domain. Multi-stability in simpler models, as are, competitive Lotka-Volterra models also referred to as nonlocal Fisher Equations has been previously reported (in a variant in [45]) but has rarely been studied. In contrast, focus has been set on the Turing instability of homogeneous distributions considering its importance in the context of diversification and speciation [8, 302–304, 306, 307]. Moreover, global stability of a non-trivial equilibrium was found in similar ecological models in [308–311], giving rise to the questions: Why does multi-stability occur in competitive Lotka-Volterra models (and in the first model of Chapter IV) and does not occur in others? How does multi-stability behave in terms of the most relevant parameters? Namely the competition range and the diffusion coefficient? The first question is the issue of an ongoing research not included in this manuscript. The second is addressed in the research in Chapter V, which is presented in the form of a working paper in collaboration with Jens Starke (University of Rostock).

To understand better the presence of multi-stability and the range of parameters under which it occurs in the model introduced in [7] and described in detail in [8, 9], equation-free analysis can be appropriate for the following reasons. First, a mathematical analysis of multi-stability in the models, both stochastic and deterministic, has proven to be substantially puzzling. Moreover, analytical methods used in previous works have had limitations and have relied on diverse assumptions (mathematical and biological). Limitations, given that focus has been set on the instability of homogeneous solutions rather than on the stability of non-homogeneous ones and how these relate to each other. And assumptions which concern, for instance, boundary conditions ([8, 45, 307]) or convergence to Dirac masses in the limit of slow motion and small mutations (as done in the Supporting Information of

Chapter IV). Moreover, large population sizes –used to derive the PDE– may not always apply (under some parameter ranges) even under a proper scaling of resources. Hence, population sizes may be sometimes large but not large enough to analyze with the continuous limit.

Direct simulations, either of the deterministic or the stochastic model are also alternatives for analyzing multi-stability. However, coarse analysis can potentially be more robust (less vulnerable to misinterpret transient regimes) and can detect the presence of equilibria regardless of their nature.

In addition, coarse analysis is versatile; it can easily be extended to different boundary conditions (most analytical work has assumed either periodic boundaries or open boundaries) and to other extensions or generalizations as the ones described in Chapter IV. In particular, deriving Hamilton-Jacobi equations based on the Hamilton-Jacobi approach [224] has proven to be substantially difficult in some of these cases (*e.g.* see extension for Allee Effects in the Supporting Information of Chapter IV).

Last, it is noted that the analysis is done on the stochastic rather than on the deterministic model. First, to consider potential finite-size effects. These can refer to, for instance, a presence of clustering which is lost in PDE models due to averaging over cluster locations, or to a possible presence of unstable macroscopic equilibria which are asymmetric with respect to the mid-point of the domain. Second, due to computational limitations. In particular, those concerning the dependence of macroscopic equilibria on the parameter δ (the competition range). This parameter (or similar measures of spread of competitive interactions) is biologically relevant and has attracted strong interest [164]. A robust stability analysis of equilibria in terms of this parameter requires a spatial discretization which makes simulations of the PDE model inviable.

Methodology

Simulations of the microscopic model (the microscopic time-stepper) are done following the methodology described in IV, which was later extended to incorporate evolving dispersal. To facilitate the initial analysis, periodic boundary conditions are considered. This hinders accumulation of individuals next to the extremes of the domain which complicates the distinction among the different asymptotic distributions. However, once this first approach is successful, the work is expected to be extended to other more realistic boundary conditions. Under periodic boundary conditions, in both dimensions, the origin of the domain is then set as the point with highest abundance (after a discretization of the domain). In addition, the first equation-free analysis is restricted to the macroscopic dependence on the parameter δ (competition range).

The initial equation-free analysis that was done presented many difficulties which required numerous refinements to the 'standard' methodology, and in the end had to be discarded due to unsolvable issues. This process is described briefly before discussing the current analysis, which is expected to solve previous problems.

After considering many candidates (see Chapter V) –most of which depended on itera-

tive algorithms– it was observed that apparently there was a one-dimensional quantity able to distinguish the abrupt transitions between all the asymptotic patterns (in terms of the number of clusters). The measure was the fourth moment of the distribution projected along the geographic dimension and restricted to a small window symmetric to the mid-point of the domain. The choice was motivated on the moment-generating function and the projection was due to the observation that separation into clusters is normally strongest along the spatial dimension. The phenomenon is generally emulated along the phenotypic dimension but to a lesser degree.

The construction of the Lifting Operator and the macroscopic time-stepper required many refinements which made the numerical analysis inconvenient. Moreover, the healing time and the time-step length were required to be substantially long, hence complicating even further the simulations. In the end it was observed that macroscopic trajectories crossed existing equilibria which unveiled problems with the dimensionality-reduction that had been done.

The analysis was modified then to study each transition –from "cline-like" equilibria to clustering patterns or between the later– separately. In each case, the natural macro-variables are the n-th Fourier coefficients of the density of projections onto the diagonal line (which is were the population normally concentrates). To avoid problems arising from the boundary conditions, the edge cluster is not considered when calculating this density.

The Lifting Operator follows the following scheme: an initial number of individuals (determined based on the parameter delta) have positions and phenotypes which are sampled from a unimodal or multimodal distribution where the width of each cluster varies gradually with the macroscopic variable. After this construction, multiple runs have to be averaged to ensure that no outliers or strong noise interfere with the correct estimation of the macroscopic time derivatives. For the equation-free analysis a 'semi-implicit' scheme is employed. A healing time is incorporated (based on observations and on the number of repetitions) and the Lifting is refined according to the rule:

$$X = \langle \mathcal{RM}(\mathcal{L}(X), t_{heal}) \rangle$$

for some equally spaced grid-points in the range of the macro-variable considered. This avoids the need of an iterative algorithm which would extend simulation times even further. The detailed methodology is described in Chapter V.

The choice of the healing time and the time-step length for the calculation of the derivatives are easier than before. This is, since the macroscopic time-behavior is more stable and seemingly always monotonic after convergence to the slow manifold.

Macroscopic equilibria and bifurcations are then expected to be computed using Newton's method on the estimated time-derivatives and by implementing a pseudo-arc-length condition, similarly as in [293].

Results obtained

It is noted first that the refinements done to the equation-free methodology have already been relevant contributions of the research. The implementation of the so-called "semi-implicit"

scheme together with the different averaging methods can serve as a general computational framework to be used when the microscopic systems at hand are strongly stochastic and simulation times extensive.

Simulations results have shown a power law with respect to N (the population size) and δ (the spatial competition range). Concerning macroscopic equilibria and multi-stability, very strong hysteresis has been detected and simultaneous co-existence (for the same parameter values) of equilibrium distributions differing by one or two clusters has been detected. Moreover, it has been observed that close to the critical values, where stability of microscopic distributions is lost, the system can be strongly disordered, in a fashion similar to particles near phase transitions. Strong oscillations in skewness and transient but recurring appearance of bimodal clusters has been observed.

The research is expected to evolve into the computation of a bifurcation diagram in terms of the parameter δ, with the possibility of extending the work to other ecologically relevant parameters. Obtained results hint towards a progressive cascade of coupled saddle nodes (folds). If confirmed, the predictions will shed light not only on the confirmation of the presence of multi-stability but also its nature and the characteristics of equilibria. In particular, the research provides quantitative estimations on how competition shapes phenotypic and spatial dynamics and distributions of populations subject to eco-evolutionary feedbacks.

Perspectives

Short term objectives include: (i) The computation of the bifurcation diagrams occurring in macroscopic space in terms of the parameters δ and D_m (the individual diffusion coefficient). Multi-stability can then be analyzed by looking at the overlapping ranges of macroscopic stable branches from each separate diagram. (ii) An analysis of equilibria and their bifurcations under different boundary conditions and in model extensions as the one introduced in Chapter IV where dispersal evolves or where Allee effects are taken into account.

Moreover, the coarse-analysis on the eco-evolutionary dynamics of a population along a space-trait gradient has opened numerous and relevant research directions. Specifically, performing a two-dimensional bifurcation analysis based on a generalized methodology where the macro-variables can be based on the two-principal component of the distributions.

A long-term methodological objective which has been discussed addresses the question of how to automatically recognize in phase space the regions where the analysis can or can not be restricted to one-dimension. No known work has been done on this subject. Another methodological question which has been posed concerns how to chose automatically the healing time based on the variance of macroscopic variable.

Perspectives on the analysis of multi-stability in nonlocal Fisher equations

To begin to answer the question on why multi-stability occurs in simpler models (as in [45]), and to serve as a validation and a platform to improve the current state of the equation-free

analysis, ongoing research looks at the most elementary traceable system where this phenomenon is present. The aim being to locate the sources of multi-stability and to understand what is essential for this phenomenon to occur.

To this end, mathematical analysis based on Fourier analysis, bifurcation and symmetry theory [312–314] are being used together with numerical simulations using Euler's Method on the PDE studied in [302].

II – Is Aggregate-Dependent Yeast Aging Fortuitous? A Model of Damage Segregation and Aggregate Dynamics

Martín Andrade-Restrepo[1]

[1] Institut Jacques Monod, CNRS UMR 7592,
Université Paris Diderot, Paris Cité Sorbonne, F-750205, Paris, France

Abstract

During cytokinesis in *Saccharomyces cerevisiae*, damaged proteins are distributed unequally between the daughter and mother cells. The retention of these proteins is correlated with yeast aging. Even though evidence suggests that aggregates are retained due to an underlying molecular mechanism, the debate on whether an active mechanism is necessary for this asymmetry remains unsolved. In particular, passive diffusion and a bud-specific dilution remain as possible explanations. Here, we provide a computational and mathematical model to test on whether passive mechanisms alone are sufficient to account for the aggregate distribution patterns and the aggregate kinetics observed in living cells. To our knowledge this is the most comprehensive model available in this subject and the only one combining key potentially essential passive-only mechanisms proposed in existing bibliography. Namely, the geometrical effect of the dividing yeast cell on the diffusion of protein aggregates and the possibility of aggregate binding and aggregate formation at different rates. Our results suggest that although passive processes alone can reproduce certain averaged observables from experimental bibliography, they are insufficient to vindicate aggregate activity observed in living budding yeast cells. We complement these results by showing that under basic forms of active-quality-control, discrepancies between the outputs of the model and experimental bibliography are reduced.

Keywords: Asymmetric cell division, Confined diffusion, Aggregate-dependent aging in yeast, Damage segregation.

II.1 Introduction

Aging in unicellular organisms is strongly associated with asymmetric cellular division [58], asymmetrical distribution of damage [101, 109], or both [18]. In asymmetrically dividing organisms as budding yeast *S. cerevisiae*, this process gives rise to an "aging" and an "immortal" lineage. The "aging" lineage consists of an old mother cell with a decreased survival rate, while the "immortal" one of a new, healthy daughter cell with a longer life span and a full replicative potential [17, 315, 316] of 25-30 generations. Studies [10, 18, 64] have observed that the difference in the average life span between the two outcomes of yeast cell division is highly connected to the asymmetrical distribution of Hsp-104-associated protein aggregates between them. Indeed, oxidized proteins, such as Hsp-104-associated aggregates affect mortality of yeast cells by deteriorating their fitness and maintenance at late stages of the life cycle [17, 317, 318].

Despite being of vital importance in the understanding of aging, the mechanisms causing the asymmetry in the inheritance of Hsp-104-associated aggregates in budding yeast remain unclear. In particular, whether or not an active-quality-control (AQC) mechanism is necessary remains indecisive. This debate has transcended to symmetrically dividing organisms that divide damage asymmetrically, where recently it was suggested that neither fission yeast *S. pombe* [109] nor *E. coli* [319] require active spatial-quality-control (SQC) machinery. Indeed, in *E. coli*, although damage usually concentrates at the old pole cell [100], aggregates seemingly follow Stokes-Einstein diffusion and segregate asymmetrically as a consequence of crowding in nucleoids. Likewise, in *S. pombe*, where aggregates also undergo diffusion, asymmetric distribution of damage is facilitated by aggregate fusion.

Returning to *S. cerevisiae*, arguing in favor of the presence of an active quality-control machinery acting throughout budding yeast's cytokinesis are the experimental studies [2, 10, 18, 102] which suggest a dependence on concentrations of compounds in the cytoplasm and on the actin-cytoskeleton. Mutated yeast cells without *SIR2*, a gene related to actin nucleation, show a more balanced distribution of damaged proteins among the two compartments after cell division [10, 102] while not showing any differences in the neck's diameter. Additionally, when the formation of the actin-cytoskeleton is suppressed with Latrunculin-A (Lat-A), which binds to the actin molecules hindering their bonding, the segregation of Hsp104-associated proteins is hampered. Thus, experiments indicate that chemical reactions between the actin and the Hsp-104-associated protein molecules facilitate transport of aggregates away from the progeny. In addition to these studies, [105] suggests that the underlying mechanism causing asymmetric segregation is instead (active) confinement of the Hsp104-associated aggregates to the organellar surfaces (of the nucleus and the vacuole) inside yeast cells. This confinement isolates damaged proteins in inclusions, namely the IPOD and the JUNQ which are themselves attached to the surfaces of these organelles, thus avoiding their crossing of the neck. Furthermore, attachment to mitochondria has also been claimed to contribute to the asymmetric inheritance of aggregates [107]. More recently, [16, 17] discovered the existence of a protein deposit which accumulates misfolded proteins, thus favoring their aggregation. In [16], it was proposed that retention of the deposit inside the mother cell occurs as its precursors bind to the endoplasmic reticulum (ER) with the mediation of farnesylated Ydj1, predominantly to the structures close to the nuclear envelope (NE).

The arguments against the necessity of an active quality-control machinery to justify asymmetric segregation of damaged proteins were first present in [1, 320]. In [1] aggregate motion was tracked and concluded to be consistent with anomalous diffusion (sub-diffusion due to confinement), with no directional bias. According to their observations, the 2D mean-square-displacement of aggregates behaves according to:

$$\left\langle r^2(t) \right\rangle = 4Dt^{\alpha}, \quad \alpha < 1$$

where t denotes time and D is the (constant) diffusion coefficient. They use this as an argument against active transport which, they argue, would be consistent with super-diffusion ($\alpha > 1$) instead. Furthermore, it is suggested that the low concentration of aggregates in the bud is a consequence of the low probability of the aggregates' trajectory to cross the neck and reach the bud. Hence, aging in yeast cells could be completely stochastic. This result was later complemented by a mathematical model presented in [15] in which aggregate concentration in both compartments (the mother and the bud) was approximated throughout cell division. They assumed a fixed number of aggregates with a fixed size and a fixed diffusion coefficient which was later observed to be potentially inaccurate. Indeed, more recently, [14] used both experiments and a mathematical model based on the work in [109] studying damage distribution in symmetrically dividing fission yeast, to suggest that –although passive as well– the main force behind the asymmetrical distribution of damage was aggregate fusion combined with the bud-specific dilution rate associated with polarized growth during division. Nevertheless, their mathematical model did not consider cross-compartment crossings –based on the experimental evidence from [1, 14]– and focused only on the establishment of asymmetrical distributions as a consequence of volume-based dilution rates affecting aggregate formation. Thus, it either assumed a mechanism of aggregate retention by the mother (and the daughter) or assumed geometry was enough to account for the low number of crossings.

In this paper we present a computational and mathematical model aiming to study the sufficiency of passive-only mechanisms. We believe that our model can contribute substantially to the debate, as it relies on simpler experimental measurements than those required when testing in favor of active transport or aggregate retention in perinuclear or perivacuolar deposits.
To our knowledge, it is the first to include key passive mechanisms and the most comprehensive one available. Furthermore, it relates single-division with life cycle processes to study the impact of the asymmetrical distribution of damage on aggregate-dependent aging in budding yeast.

In the short-term component of the model, we aim to reproduce single-division inner-cell aggregate kinetics. It is based on experiments which analyze aggregate dynamics at short timescales, as are those studying aggregation and damage distribution for one cell-division cycle after heat or oxidative stress. Moreover, it generalizes both the confined-diffusion-based models in [1, 15] and the aggregate-creation/fusion models introduced in [14, 109].
The long-term component of our model is based on experimental studies observing aggregate-dependent aging and damage accumulation in perturbed or unperturbed WT cells over several generations. It studies consistency between single cell-division observations and longer

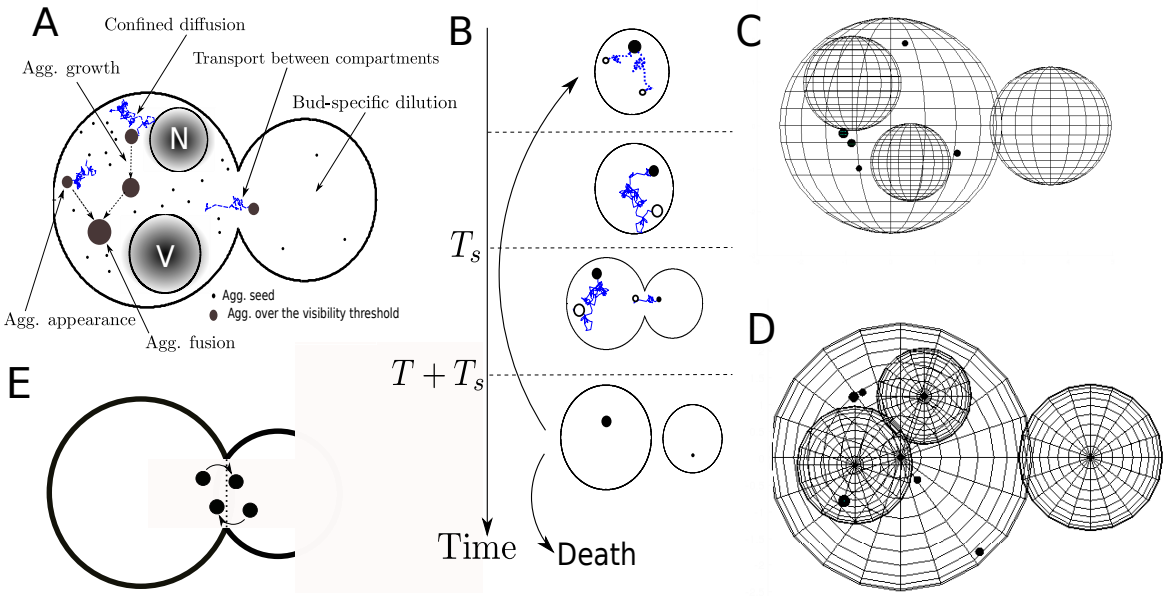

Figure II.1: The passive-only model. A,B. Schematic representations of the model's short-term and long-term components. C,D. Snapshot of the model's single-division cycle simulation. E. Example of a crossing of the neck.

timescale data such as expected divisions before senescence or death and damage accumulation/retention over several generations.

We show that while passive-only mechanisms –as introduced in existing bibliography– can reproduce the experimental data used to defend their sufficiency, notable differences remain between the results from our purely-passive model and other experimentally-quantified observables. More specifically, we observe that the rate of aggregate movement between the two compartments (in terms of the average amount of crossings) has been underestimated and in reality, in absence of active mechanisms, is nearly an order of magnitude higher than it has been measured in the experiments in [1, 14]. These differences are improved when introducing a very small (possibly undetectable) degree of aggregate-motion-bias towards the mother cell –as would be the case under an infrequent active transport [2, 102]– or confinement to regions close to organelles [105] or to the cell's membrane [16]. This result points towards the necessity of an active quality-control mechanism –enhanced by passive processes– to justify the kinetics and the degree of asymmetry in the segregation of damaged proteins observed in real life budding yeast cells.

II.2 Methods

II.2.1 The single-division-cycle, passive-only model

To study aggregate kinetics and their distribution during cytokinesis, we construct the short-term component of our passive-only model. It is schematized in Fig. II.1A together with the

key passive mechanisms that are incorporated. Namely, that aggregates follow a diffusion process [1] and may bind on collision, grow in size, appear at different rates depending on their compartment and exhibit different diffusion rates depending on their volume [14, 109].

In the three-dimensional model, aggregates are either generated at the beginning (a number N) or appear at the mother or bud compartments with constant rates $\frac{1}{\tau_m}$ and $\frac{1}{\tau_d}$. They have an initial radius r_a^i, which represents the threshold of detection; the minimum aggregate size for which experimental tracking is possible. These aggregates undergo diffusion with a rate $D(r_i(t))$ –where $r_i(t)$ is the radius of aggregate i at time t– inside a domain consisting of two spheres (mother and daughter cells) of radii r_m and $r_d(t)$ respectively, joined by a neck of length l_n. The bud's radius grows with a constant rate until it reaches its final value $r_d(T)$ at the end of cell division (which happens after a time T). For the results shown in this paper we consider the two organelles of largest size: the vacuole and the nucleus, both static and with radii r_v, r_n respectively.

Fusion occurs, upon aggregate collision, with a probability p_b. Moreover, aggregates grow (in volume) with a constant rate C_c which we take to be $\frac{4\pi}{3}(r_a^i)^3/\tau_c$ for consistency with the appearance rate (τ_c is either τ_m or τ_d depending on the compartment). Continuous aggregate growth relates to the observations in [17] showing that aggregates form and grow progressively rather than due to a collapse at advanced ages. In Section S8 in the Supporting Material, we present equivalent results for a variant of the passive-only model where the rate of growth is proportional to the surface area of the aggregate. We show that under appropriate parameter conversions the conclusions remain the same.

II.2.2 The life-cycle passive-only model

The long-term component of our passive-only model aims to reproduce aggregate-dependent aging dynamics in budding yeast over many generations. For this, we look at damage in cells throughout the entire life-cycle [315], which is composed by several divisions (all following the short-term single-division dynamics introduced above) together with a time between divisions T_s (taken from [321]) in which we just assume that aggregates grow, appear and bind with the same rates as during cytokinesis. We assume that death of cells occurs after N_{death} divisions, which we deduce from [17, 64]. The process follows the scheme presented in Figure II.1B.

II.2.3 The active-quality-control variants of the passive-only model

We also present three extensions of the passive-only model, which implement the active-quality-control mechanisms proposed in the experimental studies in [10, 16, 105]. In the first, aggregate motion has a small bias towards the mother's pole –which represents actin-driven transport. At each time step, with a probability p_s, movement in the x coordinate in the direction of the bud is reversed, so that aggregates move only in direction of the mother cell.

In the second, aggregate motion is confined when reaching the periphery of the nucleus or of the vacuole –which can account for organelle-associated confinement. When the center of the aggregate lies at a distance smaller than d_c from the boundary of the organelle, then, every minute, they are to remain confined to its surroundings with a probability p_c.

In the third, aggregates adhere to the cell membrane and remain trapped for a random time –which aims to represent adhesion to the ER. More precisely, when aggregates collide against the cell membrane, they attach with a probability p_a and remain stuck every passing minute with probability p_w.

We define the probability of confinement or attachment with respect to a minute-based timescale (in contrast to seconds or to the time-step length δt) in order to facilitate experimental measurements aiming to validate these models.

II.2.4 Model parameter values

The default parameter values that were used to obtain the results in this paper were provided by T. Nyström (personal communication with T. Nyström, Department of Cell and Molecular Biology–Microbiology, Göteborg University, Göteborg, Sweden. March 2012), deduced from [14, 109, 321], or carefully calibrated, in the case of AQC, in order to match experimental results. All parameter values and the references from which they were derived are gathered in Table S1. We take into account bud-specific dilution by assuming τ_d to be larger than τ_m by a tenfold.

II.2.5 Numerical simulations

II.2.5.1 Single-division-cycle aggregate dynamics and distribution

The numerical algorithm for the simulation of aggregate dynamics in the short-term, single-division cycle component of the passive-only model is described in Section S1.1 in the Supporting Material. In Fig. II.1C and Fig. II.1D we show two perspectives of an instant from a simulation. Throughout the simulations of aggregate kinetics during a single division cycle we keep track of statistics that can be used as a reference for experimental work; the number of aggregates, the total aggregate volume, the mean-square-displacement (MSD), and the number of cross-compartment crossings in each direction. For the latter, we only consider a crossing when the entire aggregate (not just its center) passes from one compartment to the other (Fig. II.1E).

II.2.5.2 Life cycle damage accumulation and aggregate dynamics

The simulations of the long-term component of the model –aiming to reproduce aggregate-based yeast aging patterns– are detailed in Section S1.2. After each division cycle is complete, we keep track of relevant statistics for comparison with experiments (aggregate volume, aggregate number, probability of inheritance of at least one aggregate and of the largest aggregate –if it exists– by the daughter and the number of crossing events in each direction), as well as the number of aggregates in the mother and their radii in order to start the next division cycle.

II.2.6 Mathematical analysis and validation of simulations

The work from [11, 13, 322–324] provides us with a framework to study transport between two domains analytically. Using their results, we estimate aggregate dynamics throughout the cell-division cycle with a system of ODEs. A similar mathematical model was presented recently in [15]. Here, we extend their approach to include fusion and appearance of new

aggregates.

The mathematical model designed and used is detailed in Section S2. We numerically integrate the system of ODEs in Eq. (S2) using an explicit method in order to corroborate the results of the stochastic simulations of aggregate dynamics during the single-division cycle. This is an accurate approximation of the short-term component. It could also provide an upper bound of the mother cell's aggregation levels for the long-term component over many generations.

II.3 Results

In this section we show the results obtained from our passive-only model (the short and long-term components) and from its variants, and offer direct comparison with relevant experimental data gathered from available bibliography. In the case of the single-division cycle (the short-term) component, we complement and validate some of these results with the approximations calculated from the system ODEs in Eq. (S2).

We show that the passive-only model is able to reproduce results in agreement with observables from experimental and modeling work defending the sufficiency of passive-only mechanisms. Nevertheless, we observe that the average number of cross-compartment crossings under the passive-only assumption remains substantially higher than its experimental counterpart. This result is sustained at short and long timescales and under a wide range of the relevant parameters and thus unlikely to be atypical and a consequence of the model's simplifications.

These differences can be improved when introducing basic, sporadic active-quality-control, while still remaining consistent with the rest of the experimental data used for comparison.

II.3.1 Single-division and passive-only; agreement with averaged observables from experiments supporting passive-only mechanisms and from other experimental and modeling work

II.3.1.1 Aggregate mean-square-displacement

In [1] Fig. 2, the aggregate MSD exponent α was approximated to be around 0.75 when tracking aggregate movement following heat-induced aggregation from a 30 minute TS from 30°C to 42°C.
Similarly, in our passive-only model, the degree of sub-diffusion under high aggregation rates corresponds to $\alpha \simeq 0.95$ at short timescales and $\alpha \simeq 0.71$ at intermediate timescales (Fig. II.2A) –although Eq. II.1 is not longer valid given the non-constant aggregate volumes.

Here, we provide a more precise explanation to what is referred to in [1] as diffusion with a small degree of confinement by showing the impact of both, the geometry and aggregate fusion and growth, on the MSD.

As observed in Figs. II.2A and II.2C, the MSD is slowed at intermediate and long timescales as a consequence of the confined domain. Moreover, it first stabilizes around 7.6 μm^2 before rising to 8.9 μm^2 once cross-compartment transport is no longer rare. This

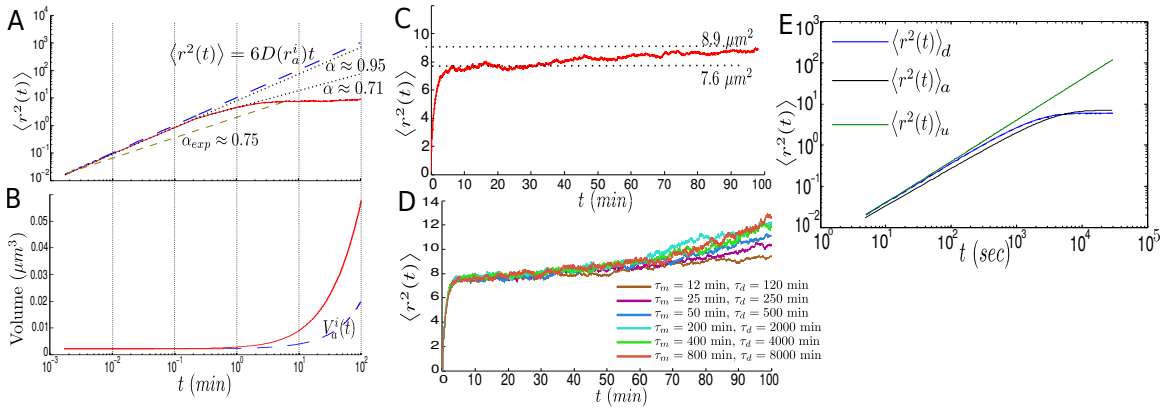

Figure II.2: MSD of aggregates in the passive-only model. A-B. Log-log plot of the MSD of one aggregate (top) and volume of the same aggregate for which the MSD was computed (bottom). Dashed lines correspond to the unconstrained MSD of an aggregate of radius r_a^i (top) and to the volume of one aggregate with initial radius r_a^i in absence of fusion events (bottom). C. Same as Fig. II.2A. D. Same as Fig. II.2C for different rates of appearance and growth of aggregates. E. Log-log plot of the MSD of a particle in 2D undergoing unconstrained diffusion $\langle r^2(t)\rangle_u$, diffusion inside an empty cell $\langle r^2(t)\rangle_d$, or diffusion inside a cell with a vacuole $\langle r^2(t)\rangle_a$. In all three cases $D = 1 \times 10^{-3}$. In Figs. A-C, $N = 5$, $\delta t = 0.1$ sec., $\tau_m = 12$ min., $\tau_d = 120$ min. In Figure D, $N = 1$, $\delta t = 0.25$ sec. All other parameters were set to the values in Table S1. Results averaged over 1024 realizations.

transition occurs after approximately 35 minutes, which is close to the mean-first-passage-time $\frac{1}{\kappa_m}$ (see Section S2) of an aggregate of radius r_a^i (approximately 32 minutes).
In Figs. II.2A-II.2B it is emphasized that not only barriers have a strong effect on the aggregates' movement but fusion and growth as well. At intermediate and large timescales, the average volume of the aggregate rises above the constant growth of volume under the absence of fusion. This effect is corroborated in Fig. II.2D, where the MSD is significantly slowed as the rate of aggregation increases. If the rate is low, so that fusion events are rare and growth is reduced, the MSD of initially equally-sized aggregates can rise to values around 13 μm^2 after 100 minutes as a result of a reduction of compartmental retention by the mother. In Fig. S1, we show the dependence of the MSD on the simulation parameter δt to emphasize that our results are not incidental.

In two dimensions, the effect of barriers and obstacles on the diffusion of particles can be studied analytically [105, 325–328]. We detail this procedure in Section S7.
Indeed, by representing the cell as a two-dimensional empty disc or as an annulus (when considering only the vacuole) we are able to examine the effect of constraints (the cell membrane and the organelles) on the MSD of the aggregates. One observes (Fig. II.2E) that sub-diffusion can appear simply as a consequence of constraints, becoming stronger (at short and intermediate timescales) when more barriers are considered.

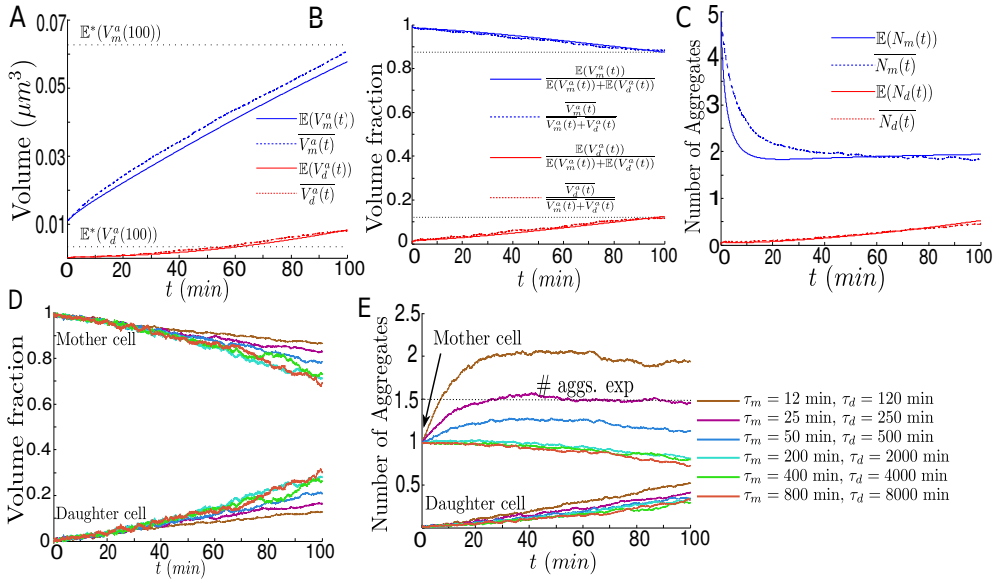

Figure II.3: Aggregate kinetics from the short-term component of the passive-only model. A-C. Total aggregate volume, fraction of the total aggregate volume and number of aggregates inside the mother (blue) and the daughter cell (red). Continuous line corresponds to the analytical prediction when numerically integrating Eq. (S2). Dotted line corresponds to the numerical average from the stochastic simulations of the short-term component of the model. D,E. Same as B,C for different rates of appearance and growth of aggregates. In Figures A-C, $N = 5$, $\delta t = 0.1$ sec., $\tau_m = 12$ min., $\tau_d = 120$ min. In Figures D,E $N = 1$, $\delta t = 0.25$ sec. All other parameters were set to the values in Table S1. Results averaged over 1024 realizations.

II.3.1.2 Asymmetric distribution of aggregate volume and aggregate concentrations during yeast cell division

We show that our passive-only model is able to reproduce the observations derived from previous modeling approaches in [1, 14, 15]. Additionally, in Section S6, we comment on possible limitations each of these models can have when on their own.

In Fig. II.3A we show the time-dependence of aggregate volume for the short-term component of the passive-only model. By comparing the slopes of both curves, it can be infered that the main drivers behind the asymmetrical distributions are the different rates of growth of existing aggregates and of appearance of new aggregates in both compartments (bud-specific dilution as proposed in [14]). Since this rate is constant, the function resembles a straight line. If the rate of growth increases in proportion of the surface of the aggregate, the shape of this function rather resembles an exponential (See Section S8). If, as in the model used in [14], we assume no compartmental crossings, at the end of cell division we would overestimate aggregate volume inside the mother cell by nearly 6% and underestimate aggregate volume inside the daughter by nearly 65%. This is shown by the values of $\mathbb{E}^*(V_m^a(100))$ and $\mathbb{E}^*(V_m^a(100))$ in Fig. II.3B, which denote the aggregate volume in each compartment under no transport (a closed neck) at the end of the division cycle when numerically integrating the system of ODEs in Eq. (S2).

Figs. II.3B and II.3D show aggregate volume concentrations in both compartments for different aggregation rates and different N. The initial number of aggregates does not impact strongly the asymmetrical distribution of volume due to the frequency of movement between compartments. On the contrary, aggregation rates (Fig. II.3D) have an important impact on the degree of asymmetry, even though their ratio among compartments is kept constant ($\tau_d = 10 \times \tau_m$). At high rates ($\tau_m = 12$ min., $\tau_m = 25$ min.), the fraction of volume inside the mother after 100 minutes is approximately 0.88, which is close to the results of the models in [1] Fig. 7B and [15] Fig. 2. The effect of variations in the diffusion coefficient is weaker under these conditions, since an increase by a tenfold or a reduction by two orders of magnitude varies the fraction of volume in the mother by a maximum of 8% (Fig. S3). At lower rates, resembling those in unperturbed cells, aggregate cross-compartment transport reduces substantially the damage asymmetry by nearly 20% (Fig. II.3D). Under these conditions, diffusion should be slowed to a fair amount (as in [1]) in order to avoid aggregate escape from the mother and to maintain a strong asymmetrical distribution of damage.

II.3.1.3 Number of aggregates during yeast cell division

In Fig. II.3C we show the time-dependence of the number of aggregates during a single cell-division cycle. The underestimation of fusion in the stochastic numerical simulations is a consequence of the discretization of time (and the time-step size $\delta t = 0.1$ sec.), given that we might overlook possible contacts. This is highlighted in Fig. S1. The discrepancy disappears at longer timescales where the number of aggregates is smaller, their size is bigger, and their diffusion coefficient decreases. Indeed, at the end of the simulation, both approaches predict that there will be approximately two aggregates in the mother cell and nearly one half in the daughter.

Fig. 2A in [16] describes how aggregate deposits in unperturbed WT cells frequently merge. Similarly, Fig. 2L in [14], shows that fusion events drop aggregate numbers from five to two in the first minutes of cell division after a TS from 30°C to 38°C. Moreover, the experimental observations in [109] suggest that not only aggregate fusion is frequent but that it is the main driver of the asymmetrical division of damage in fission yeast. Indeed, aggregate fusion in our passive-only model is very common, as attested by the sharp drop in the number of aggregates from five to two in less than 10 minutes. In Fig. II.3C, unlike Figs. 2L and 3F in [14], the average number of aggregates in the mother at the end of cell division converges to two rather than a value close to 1.5. This is a consequence of the high aggregation rate, since the average time of fusion of "newborn" aggregates with the largest aggregate is larger or equal than the average time of appearance of new aggregates. When having only one initial aggregate (and the same appearance and growth rates) this result is unaltered (Fig. II.3E for $\tau_m = 12$ min.). At lower rates, resembling those in unperturbed cells, the number of aggregates in the mother can converge to a value close to one (consistent with Fig. 2A in [16], where more than one aggregate in unperturbed cells was rare) or continuously decrease until fusion becomes rare and the number of aggregates in the mother and the daughter depend more strongly on cross-compartment movement between the two domains (Fig. II.3E for $\tau_m \geq 25$ min.).

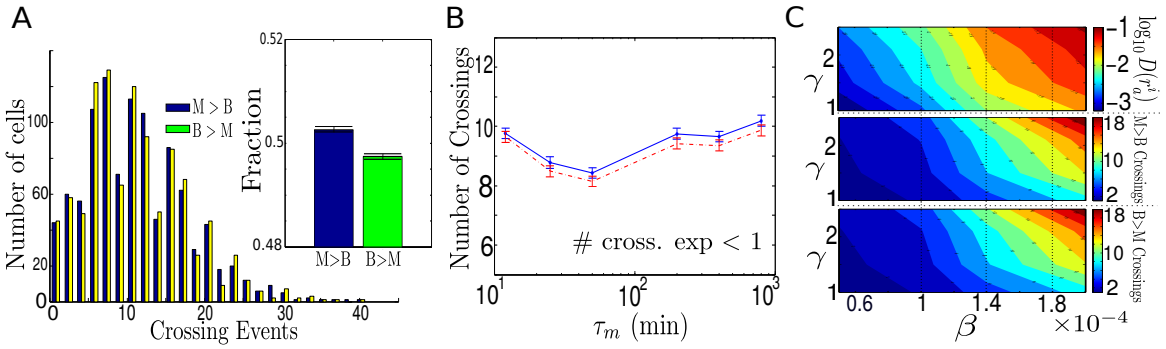

Figure II.4: Differences between the outputs of the passive-only model and experimental observations. A. Histogram of the total number of cross-compartment crossing events from mother to bud ($M > B$) and from bud to mother ($B > M$). A. Inset. Fraction of total cross-compartment events in each direction. B. Average number of crossing events $M > B$ (line) and $B > M$ (dashed line) after a cell division cycle as a function of the parameter τ_m. C. Logarithm of the diffusion rate of an aggregate with radius r_a^i (top), number of crossing events from mother to daughter (middle) and from daughter to mother (bottom) for different values of β and γ after a cell division cycle. In Fig. A, $N = 5$, $\delta t = 0.1$ sec., $\tau_m = 12$ min., $\tau_d = 120$ min. In Figures B and C, $N = 1$, $\delta t = 0.25$ sec, $\tau_m = 12$ min. (Fig C), $\tau_d = 120$ min (Fig C). All other parameters were set to the values in Table S1. Results averaged over 1024 realizations.

II.3.2 Single-division and passive-only; disagreement with experimental observables

II.3.2.1 Average number of cross-compartment crossings during a single division cycle

In [1] Fig. 1, the average number of cross-compartment crossing events per cell division cycle was measured to be close to 0.25 in the case of mother to bud and 0.15 in the case of bud to mother. These measurements were performed after a 30 minute TS from 30°C to 42°C. Likewise, in [14] Fig. S6, it is shown that only 10%-30% cell divisions exhibited bud-to-mother transport after two TS from 30°C to 38°C and from 30°C to 42°C. In our passive-only model, in a cell with initially five aggregates of small size (as in Fig. 1 in [1]) and with only two aggregates after fusion events in the first ten minutes, the average amount of crossings is two orders of magnitude higher than reported in [1] (Fig. II.4A). Indeed, the average number of crossings in each direction is 11.16 ($B > M$) and 11.27 ($M > B$) and there are runs in which they reach values over 30. Moreover, crossing events are so common that there is almost no bias with respect to the direction (Fig. II.4A inset), showing that most aggregates undergo multiple compartment exchanges during a single cell division cycle.

It was observed in [14] Fig. S6, that the amount of crossings significantly increased when the TS was raised from 38°C to 40°C to hamper polarized growth. In both cases though, the total amount of crossings remained under one event per cell division. Although temperature has a strong effect in this observable –most likely due a decreased mean-escape-time from the bud as a consequence of its smaller volume and to increased diffusion and aggregation–

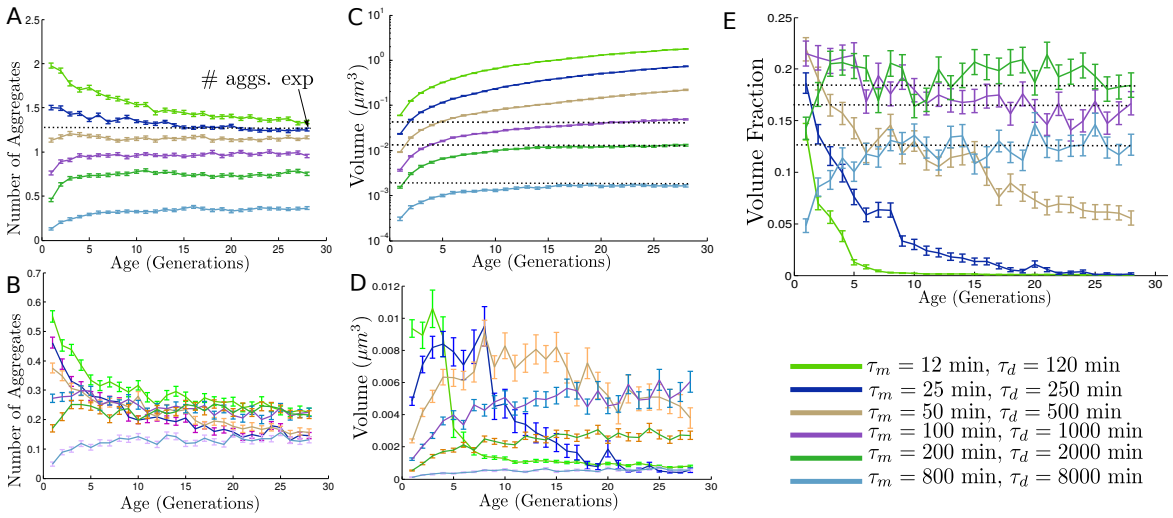

Figure II.5: Long-term dynamics of the model. A-D. Number of aggregates and total aggregate volume inside mother cell (top) and inside the daughter cell (bottom) at the end of the cell division. E. Fraction of total aggregate volume inside the daughter cell at the end of cell division. Error bars correspond to the Standard error. In all simulations $\delta t = 0.5$ sec., all other parameters were set to the values in Table S1. Results averaged over 1024 realizations.

it is unlikely that passive-only responses to variations in temperature can account for the difference between the results of the model and those from experiments. This is demonstrated in Figs. II.4A-II.4C, where the differences remains under strong variations in the initial number of aggregates and in the appearance and growth rates. Also, under variations in the diffusion coefficient, although as a default value we used the one measured in [14].
Moreover, the difference with experimental results is unaltered under reasonable values of the time-step size (see Fig. S1) –and thus is unlikely to be a consequence of multiple crossings in the event of one cross-compartment displacement.
We recall that all aggregates in the simulations have size larger or equal than the threshold of visibility $r_a^i = 0.08\ \mu m$ [1, 14] which is a conservative choice known to be larger than the experimental limitations (personal communication with T. Nyström, Department of Cell and Molecular Biology–Microbiology, Göteborg University, Göteborg, Sweden. March 2012). Hence, the difference between the amount of crossings in this work and in experiments is also not a consequence of very small aggregates which would otherwise be undetectable.

II.3.3 Long-term aggregate dynamics. Damage accumulation over a life cycle; comparison with experiments and qualitative dependence on aggregation rates

In Fig. II.5 and Fig. II.6 we show the results of the long-term component of our passive-only model –in which we track the accumulation of damage in cells over many divisions– for various appearance and growth rates $1/\tau_m$ and $1/\tau_d$. Low rates ($\tau_m = 200$ min, $\tau_m = 800$ min.) are approximations of aggregation rates in unperturbed cells ([17] Fig. 1B), while high rates ($\tau_m = 12$ min., $\tau_m = 25$ min.) approximations of aggregation rates in heat-exposed or stressed-induced cells.

II.3.3.1 Aggregate volume, concentration and numbers throughout the life cycle

In the long-term component of the passive-only model aggregate volumes, numbers and concentrations depend qualitatively on the parameter τ_m.

It has been discussed in experimental bibliography how oxidative damage gradually accumulates inside cells with passing age [17, 18] and how it generally concentrates into a single aggregate deposit [14, 16]. For small values of τ_m (under 100 min.) aggregate volume inside the mother cell grows with age at an almost constant rate (Fig. II.5B). With respect to the aggregate volume inherited by the daughter, the function rises at short ages to then drop to nearly zero ($\tau_m = 12$ min., 25 min.) or to small values ($\tau_m = 50$ min.) once a large aggregate with slower diffusion establishes (Fig. II.5A). The aggregate rarely crosses the neck and, due to its size, has a big probability of fusing with smaller aggregates before the latter pass to the bud. This is confirmed in Fig. II.5E where for small τ_m (and τ_d), the fraction of volume inherited by the daughter drops to values under 0.05 after 28 generations.

For values of τ_m over the threshold of approximately 100 minutes (which is the duration of cell division) and which resemble those in unperturbed cells, aggregate volume inside the mother cell converges to a limit value. Furthermore, both the volume and the fraction of volume inherited by the daughter cell rise in the first generations (while small aggregates accumulate), to later stabilize after the establishment of intermediate-sized aggregates. It is possible that at longer time-scales these curves will decrease again to values close to zero, after large aggregates become predominant, mimicking the behavior of their higher-rate counterparts which is best displayed by the curve for $\tau_m = 50$ min. However, this appears to be inconsistent with the number of aggregates (shown in Fig. II.5A and Fig. II.5B) –which appears to settle in both compartments to an added value smaller or equal than one– and with the total aggregate volume (in Fig. II.5C) –which converges to a limit value as well.

We can further confirm that the transition of gradual accumulation of damage versus stabilization occurs close to $\tau_m = 100$ min. by observing in Fig. II.6A that an inflection point of the curve occurs in the neighborhood of this quantity. In the case of growth proportional to the surface area the transition occurs around $\tau_m = 250$ min., which is reasonable considering that aggregate growth is exponential.

II.3.3.2 Probability of inheritance of at least one aggregate by the bud

The probability that a daughter cell inherits at least one aggregate was measured in [10] Fig. 4G to be close to 0.3 –following a TS from 30°C to 42°C– and to be around 0.10 in WT unperturbed cells ([16] Fig 3C).
In Fig. II.6C we show that for values of τ_m smaller that 100 min., the probability drops as the largest aggregate increases in size and its capacity of crossing the neck decreases. After, it stabilizes at values representing the event where small aggregates avoid collision with the largest one inside the mother and either escape to the daughter (if generated in the mother) or remain inside of it (if generated in the daughter).

For values above or equal to the threshold occurring at $\tau_m \simeq 100$ min., the functions rise as a consequence of the accumulative probability of the daughter cell creating an aggregate

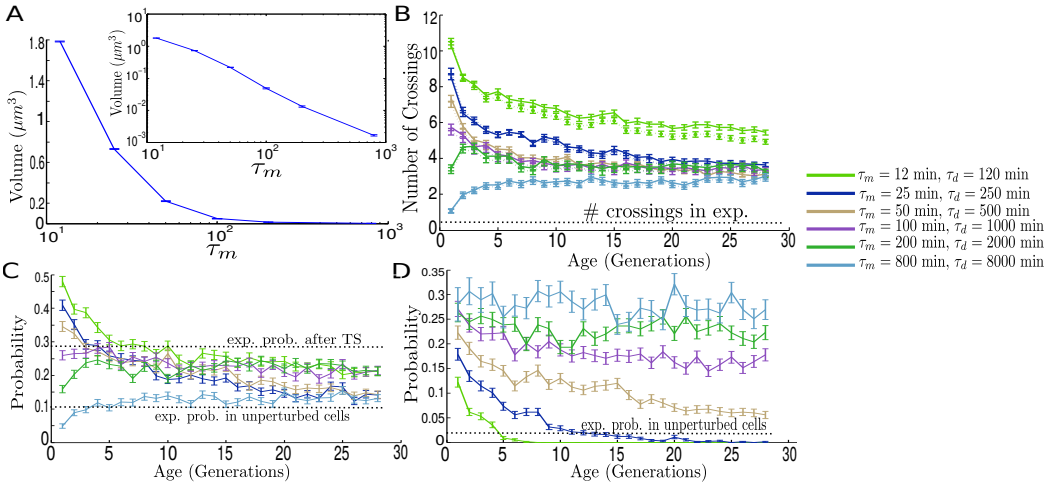

Figure II.6: Long-term aggregate dynamics. A. Total aggregate volume inside the mother cell at the end of the 28th division. Inset. Same as in Fig.II.6A but in log-log scale. B-D. Number of crossing events from mother to bud (continuous line) and from bud to mother (dotted line); probability of inheritance of at least one aggregate by the daughter cell at the end of cell division (Fig.II.6C); and probability of inheritance of the largest aggregate by the daughter cell, if it exists (Fig.II.6D), as a function of the mother's age (in generations) for different rates of appearance and growth of aggregates. Error bars correspond to the Standard error. In all simulations $\delta t = 0.5$, all other parameters were set to the values in Table S1. Results averaged over 1024 realizations.

or of inheritance of the unique aggregate (see Fig. II.5A) to later stabilize at limit values which depend on the ratio of the volumes, the ratio of the appearance rates, and of the time T. In both cases, most cells (at least 75%) are born aggregate-free and with a probable full replicative life span. Moreover, depending on the aggregation rate, the probability of a daughter cell containing at least one aggregate lies within the range 0.14-0.21 for mature mother cells (over 10 generations old). The lower bound ($\tau_m = 800$ min.) is close to the estimate in [16], while the upper bound ($\tau_m = 12$ min.) is close to the one in [10] after a TS.

II.3.3.3 Probability of inheritance of the largest aggregate by the bud

Given a positive number of aggregates, the probability that the largest one is inherited by the daughter was approximated in [16] (Fig. 3B) to be around 0.02 for unperturbed WT cells. We show in Fig. II.6D that, once more, there two different behaviors depending on the parameter τ_m. In the first (for values smaller that 100 min.), the probability drops gradually closer to zero as the largest aggregate increases in size and its capacity of crossing the neck is reduced. In contrast, for values of τ_m over the threshold, and resembling those in unperturbed cells, the probability of the existing aggregate to be in the daughter at the end of the division settles above 0.2. This is substantially higher than the experimental counterpart of 0.02 in [17].

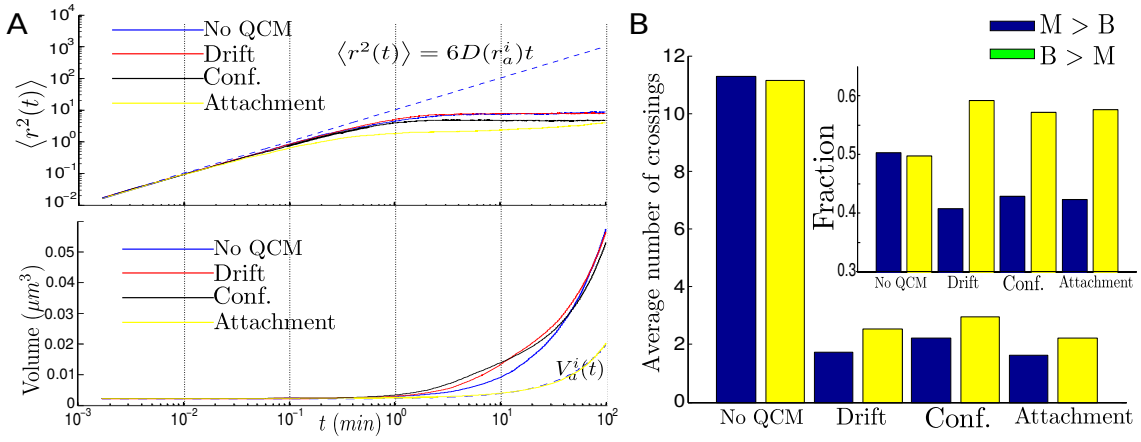

Figure II.7: Short-term results from the AQC variants of the passive-only model. A. Log-log plot the MSD of an aggregate (top) and volume of the same aggregate for which the MSD was computed (bottom). Dashed light lines correspond to the unconstrained MSD of an aggregate of radius r_a^i (top) and to the volume of one aggregate with initial radius r_a^i in absence of fusion events. B. Average number of crossing events from mother to bud ($M > B$) and from bud to mother ($B > M$). Inset. Proportion of crossing events in both directions. In both Figs. $N = 5$, $\delta t = 0.1$ sec. All other parameters were set to the values in Table S1. Results averaged over 1024 realizations.

II.3.4 Long-term aggregate dynamics, damage accumulation over a life cycle; differences with experiments

II.3.4.1 Average cross-compartment crossings throughout the life cycle

We show in Fig. II.6B, the average number of crossing events from our passive-only model as a function of the age of the mother cell. Although with age, due to the formation of larger aggregates, the number of crossing events in both directions decreases, it remains more than a 10-fold higher than in experiments ([1] Fig.1 and [14] Fig. S6) and settles around 6 crossing events, when $\tau_m = 12$ min, and 3 crossing events when τ_m is larger. These crossings are almost completely carried out by small aggregates with low mean-first-passage-time. Overall, this either suggests that experimental data in [1] relies on a mechanism of retention or that their threshold of detection was considerably above the one used in these simulations (derived from [14]), which appears unlikely after observing Figs. 1A, 1B and 1C in [1] where some aggregates have radii of approximately 0.05 μm.

II.3.5 Aggregate kinetics in cells with infrequent active-quality-control

II.3.5.1 Aggregate mean-square-displacement

We show in Fig. II.7F that sub-diffusion can also be consistent with an infrequent active mechanism of transport or with an active mechanism of retention, since the effect of the geometry combined with fusion and growth of aggregates, remains the strongest force affecting their displacement. That is, $\alpha \simeq 0.96$ and $\alpha \simeq 0.78$ at short and intermediate timescales in the case of drift (movement only towards the mother's pole with probability p_s); $\alpha \simeq 0.94$

and $\alpha \simeq 0.65$ in the case or confinement to organellar surfaces; and $\alpha \simeq 0.88$ and $\alpha \simeq 0.6$ in the case of attachment to cell membranes. In all four cases, when combining the timescales, the values of α can be considered consistent with the experimental measurements in [1].

II.3.5.2 Average number of cross-compartment crossings during a single division cycle

When introducing active-quality-control for a single cell division cycle, the number of crossings can be significantly reduced by nearly a fivefold (Fig. II.7B). Moreover, the proportion of retro and antero movement (Fig. II.7B Inset) becomes more consistent with the experimental estimations in Fig. 1A from [2].

II.3.5.3 Long-term aggregate dynamics. Damage accumulation over a life cycle; agreement with experiments

In Fig. II.8A we show that for $\tau_m = 100$ min., all of the three implemented active mechanisms can be very efficient for enhancing the accumulation of damage. After 28 divisions, the total aggregate volume inside the mother is increased by at least a threefold and does not stabilize (similarly as in [18]). Although our results indicate that confinement to organellar surfaces is less effective, this is merely a consequence of the overlapping restriction that we force on the aggregates and the organelles. After 15 generations, fusion with the largest aggregate becomes restrained since it we impose the overlapping condition with organelles. Thus, smaller aggregates escape more easily and the retention capacity of the mother cell is diminished. However, in absence of this restriction, and in line with the almost identical volume growth as under drift (Fig. II.8D top) until the 15th generation, we claim that the mother cell under this mechanism should also reach values of total aggregate volume of 0.2 μm^3, which is around a fourfold higher than the volume inside a cell in absence of any form of active-quality-control. The effect of restrained fusion with the largest aggregate under confinement to organellar surfaces is observed in Figs. II.8C-II.8F.

In Fig. II.8C we show the number of aggregates in both compartments with and without active mechanisms. Absence of quality-control, together with drift and with confinement to organelles reduces the number of aggregates in the mother cell to similar values close to one aggregate, which is consistent with the experimental quantifications for heat-induced cells in [14] Fig. 2L and for unperturbed cells in [16] Figs. 2 and 3. This is also in agreement with the observations in [10, 17]. In the case of attachment to cell membranes, as aggregate diffusion is reduced and thus their collision is less frequent, the number of aggregates is significantly higher (it can rise to around 2.5 times the value in absence of sticky membranes). This suggests that, should this mechanism be present in real life WT cells, it must be complemented with a machinery supporting aggregate assembly and fusion [16, 107].

Concerning the number of aggregates in the daughter cell, all three mechanisms reduce aggregate inheritance by the daughter cell by a fourfold. This is confirmed in Fig. II.8E displaying the probability on inheritance of at least one aggregate by the daughter. Under AQC, the probability is underestimated with respect to experimental measurements. Nevertheless, AQC outperforms passive-only assumptions.

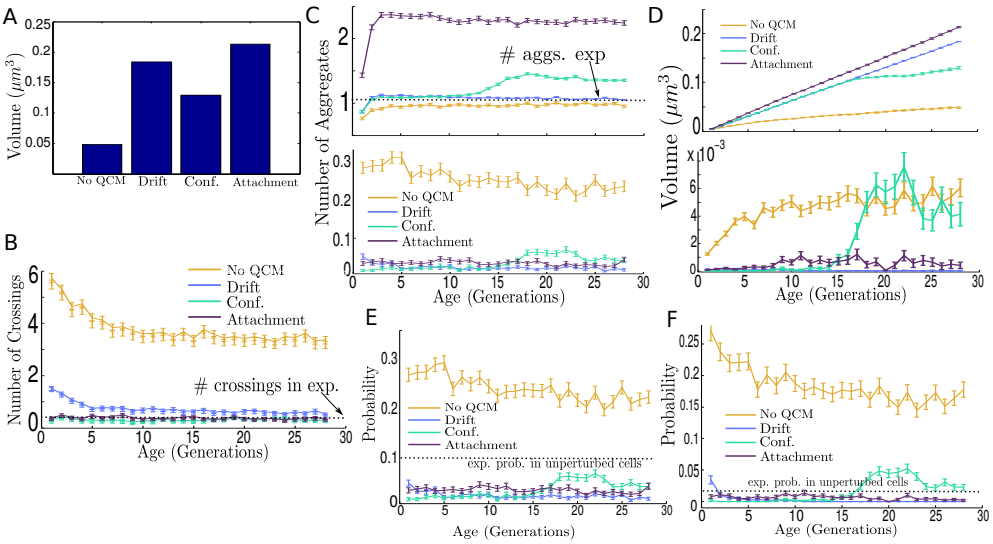

Figure II.8: Long-term results from the AQC variants of the passive-only model. A. Total aggregate volume inside the mother cell at the end of the 28th division. B. Average number of crossing events from mother to bud (continuous line) and from bud to mother (dotted line). C-D. Total number of aggregates and total aggregate volume inside the mother cell (top) and inside the daughter cell (bottom). E. Probability of inheritance of at least one aggregate by the daughter cell at the end of cell division. F. Probability of inheritance of the largest aggregate, if it exists, by the daughter cell. Error bars correspond to the Standard error. In all simulations $\delta t = 0.5$, $\tau_m = 100$ min., $\tau_d = 1000$ min., all other parameters were set to the values in Table S1. Results averaged over 1024 realizations.

The probability of inheritance of the largest aggregate by the bud remains close to 0.02 in all three variants, which is consistent with the measurements in [16] for WT cells. In absence of AQC, this probability stabilizes around 0.15 under an intermediate rate of appearance and growth close to the threshold value ($\tau_m = 100$ min.). As shown in Fig. II.6D for the passive-only model, even with $\tau_m = 50$ min. the probability can not be under 0.05 after 28 generations.

In Fig. II.8B we show the number of crossing events between compartments under the three forms of active quality-control. In all three variants of the original model, the amount of crossings are reduced to values comparable with those measured in [1] Fig. 1 and [14] Fig. S6, which are under one crossing event in each direction per cell division cycle.

II.4 Discussion

II.4.1 Single-division cycle aggregate dynamics

The results from the single-division cycle component of the passive-only model suggest that although the passive-only assumption can reproduce the experimental data used to support it, substantial differences remain between experimental observables and the predictions of

the model.

Concerning the MSD of aggregates, we show that the degree of sub-diffusion measured in [1] is consistent with the presence of passive-only mechanisms and can arise as a consequence of the geometrical effect of the dividing yeast cell and of aggregate growth and fusion. However, unless aggregates are subject to a frequent and consistent mechanism of active transport, a degree of sub-diffusion should be expected as well under active-quality-control. This suggests that an MSD consistent with sub-diffusion should not be considered a deciding argument when dismissing its presence.

With respect to aggregate kinetics and the asymmetrical accumulation of damage inside yeast cells, we observe that, although fusion of aggregates and bud-specific dilution can play a mayor role in its establishment, aggregate cross-compartment transport can have a substantial impact in the level of damage asymmetry. Indeed, similarly to the second law of thermodynamics, an open neck has a balancing effect on the appearance and growth rates of aggregates and decreases the effect of bud-specific dilution on the asymmetrical distribution of damage during cytokinesis. Moreover, rather than the case where aggregates would rarely cross the neck, as observed in [1] and as interpreted in [14], the passive-only assumption is more consistent with an interpretation where aggregate transport is frequent and where the distribution of aggregates is strongly regulated by the relation between compartmental volumes and between aggregation rates. This result suggests that models that do not incorporate either aggregate fusion, growth, and appearance –as the one in [1, 15]–, or cross-compartment transport –as that in [14]–, can potentially underestimate the role of these effects on the asymmetrical distribution of damage in real life yeast cells.

This result is corroborated by the fact that the average number of cross-compartment crossings in our passive-only model is at least an order of magnitude higher than the one observed and quantified in [1, 14]. We then suggest that it is likely that experimental observations in [1, 14] (Figs. 1 and S6 respectively) rely on an underlying mechanism of retention. Furthermore, since our active-quality-control variants of the passive-only model are able to produce results closer to the empirical estimations.

II.4.2 Long-term aggregate dynamics

The long-term component of our passive-only model, reproducing aggregate accumulation over many generations, shows a qualitative dependence on the rate of appearance and growth of aggregates. Under high rates of aggregation, resembling those after heat or oxidative stress, fusion of aggregates and bud-specific dilution can induce gradual damage accumulation in mother cells and, therefore, aggregate-dependent aging. In contrast, if the rates are low –resembling those in unperturbed cells– rather than becoming saturated with damage, cells without active quality-control have aggregate volumes which stabilize by getting rid of damage continuously and in near constant rates. Hence, although the distribution of damage remains asymmetrical between mother and daughter cells, this behavior would be more consistent with non-aging organisms. Therefore, as observed in [109] for fission yeast, depending on the rate of appearance and growth, fusion alone can or can not be the sole mechanism capable of aggregate-dependent aging in unperturbed WT cells. At low rates, resembling

those measured in experiments in [17], other (possibly active) mechanisms of retention and aggregate-compartmentalization are likely required for aggregate-dependent aging to evolve.

This is further confirmed by observing that the average number of cross-compartment crossings measured in the long-term component of the passive-only model remains an order of magnitude higher than measured in [1, 14]. This result is sustained under low and high values of the aggregation rates. Thus, results from our passive-only model suggest that although fusion indeed contributes to the asymmetrical distribution of damage, it must be accompanied by a mechanism enhancing gradual damage accumulation and retention, specially in cells that have not been exposed to stress.

When introducing active-quality-control, in all three of our variants, consistency between our results and most of the experimental data used for comparison (MSD, number of crossing events, number of aggregates in cells and probability of inheritance of largest aggregate by the daughter cell) is maintained or improved. The exception being the number of aggregates under attachment to cell walls, which we suggest must be accompanied by a mechanism enhancing aggregate fusion. Therefore, the presence of AQC in real life budding yeast cells is at least probable.

Finally, we highlight that some experimental observables can accommodate to both passive-only and AQC. Moreover, the averaged regimes of inner cell aggregate kinetics might be similar (the number of aggregates in each compartment and the MSD for instance) under both assumptions. Nevertheless, a thorough comparison with various experimentally-measured quantities is what makes the sufficiency of passive-mechanisms improbable.

II.5 Conclusion

This paper presents a computational model complemented with a mathematical approximation generalizing the works in [14, 15], aiming to study the sufficiency of passive-only mechanisms behind the asymmetric segregation of damaged proteins (Hsp104-associated aggregates) during cytokinesis and throughout the life cycle of budding yeast cells. We analyze whether aggregate kinetics and the asymmetrical distribution of damage observed in real life cells is consistent with the absence of active-quality-control as suggested in [1, 14], or as a consequence of an underlying (possibly active) mechanism that either transports or holds the aggregates inside the mother cell [10, 16, 64, 105], which can then be intensified by the mediation of passive processes.

Our results show that while some observables are reproducible under passive-only assumptions, they fail to justify the low amount of cross-compartment movement observed in experiments. Cross-compartment movement was absent in the model in [14] and was not measured in the models in [1, 15] and could be an important argument in favor of active-quality-control retention mechanisms.

Additionally, we show that aggregate fusion and bud-specific dilution can produce gradual damage accumulation with age (as suggested in [14]) only under high rates of aggregate

growth and aggregate appearance, which is the case for cells under stress but is unlikely to be the case for unperturbed cells. The rate of aggregate appearance and growth has not been exactly measured, but under low aggregation rates which resemble those approximated in WT unperturbed cells, damage accumulation (and aggregate-dependent aging) occurs in our model solely under the presence of AQC.

Last, we introduce three variants of the original passive-only model where we implement representations of active quality-control mechanisms that have been suggested in existing bibliography [10, 16, 105]. Although results rely on parameters that have no current experimental validation (which we encourage), simulation results from these alternate active versions can improve the above-mentioned differences with available experimental data.

II.6 Author Contributions

M.A-R. designed and performed the research, contributed analytic and numerical tools, analyzed results and wrote the article.

II.7 Acknowledgements

The author would like to thank Thomas Nyström for introducing him to the subject and for his contributions. He would also like to thank Khashayar Pakdaman for his invaluable guidance and Bernhard Mehlig for his counsel.

Supplemental Information and Supporting Figures

II.8 Numerical methods and dependence on numerical parameters

II.8.1 Short-term single division cycle

In the simulations of the short-term, single-division-cycle aggregate dynamics of our passive-only model we first introduce the organelles inside the mother cell as spheres centered at a random position. The centers of organelles are computed using a uniform distribution inside a sphere of radius $r_m - r_o$, where r_o is the radius of the organelle and r_m the radius of the mother cell. Organelles are not allowed to overlap with other organelles and therefore their centers must lie at a distance larger that the addition of their radii. Next, we set an initial number of aggregates N, represented by spheres with radius r_a^i, with centers computed from a uniform distribution inside a sphere of radius $r_m - r_a^i$, again with the restriction that they cannot overlap or lie inside the organelles.

Aggregates are generated randomly inside the mother and bud compartments at times taken from exponential distributions with rates $\frac{1}{\tau_m}$ and $\frac{1}{\tau_b}$ respectively. Each time this occurs, the position of the aggregate is generated randomly from a uniform distribution in each compartment –in the case of the bud, the centers are computed using a uniform distribution inside a sphere with radius $r_b(t) - r_a^i$ and which is centered at $(x_b(t), y_b(t), z_b(t))$ which denotes the bud's focus.

Aggregates undergo diffusion, with a time step of length δt (see Fig. II.9) and diffusion coefficient $D(r_i(t)) = \frac{\beta}{r_i(t)^\gamma}$, taken from [14]. As measured in [14], the values for β and γ are different from $\beta = \frac{k_B T_e}{6\pi\mu}$ and $\gamma = 1$, which correspond to the traditional Stokes-Einstein equation (T_e being the absolute temperature). Additionally we increase the radii of all aggregates following $r_i(t) = (\frac{3}{4\pi} C_c \delta t + r_i(t - \delta t)^3)^{\frac{1}{3}}$ where $C_c = \frac{4\pi (r_a^i)^3}{3\tau_m}$ or $C_c = \frac{4\pi (r_a^i)^3}{3\tau_d}$ depending on the compartment. These growth rates are chosen so that, in absence of fusion and cross-compartment crossings, aggregates will have a radius r_a^i after a time τ_c.

Upon contact of aggregates i and j (when the distance between aggregate centers is smaller that the sum of their radii), binding happens with a probability p_b. If this is the case, a new aggregate of radius $(r_i(t)^3 + r_j(t)^3)^{\frac{1}{3}}$ is generated at the intermediate position. In the case of collision against the cell walls (mother or bud) or against an organelle, the position of the aggregate is recalculated assuming a completely elastic collision against the boundary. We also considered the case where a fraction e_l of the energy was lost by setting the distance after the impact to be $l_2^* = l_2(1 - e_l)$, l_2 being the distance after a completely elastic collision, but the results were not substantially different, with the exception of a small increase in the amount of cross-compartment crossings (see Fig. II.10).

The process above is continued until a time T is reached, corresponding to the time at which the neck connecting both cells closes. Meanwhile, the radius of the daughter cell –with initial value $r_d(0) = \frac{l_n}{2} + \varepsilon$– grows progressively until it reaches its final value $r_d(T)$ at the end of the process. The value of the parameter $r_d(0)$ was chosen so that the center of the

daughter cell was at a distance larger than r_m from the center of the mother cell. In order to keep the length of the neck constant, the position of the center of the daughter cell is varied.

II.8.2 Long-term yeast life cycle

The long-term simulations of the passive-only model have the following structure. Initially, cells are born with zero aggregates. Before the first division and in-between divisions, similarly as in [14, 109], fusion of pre-existing aggregates i and j of radii $r_i(0)$, $r_j(0)$ may occur with rate:

$$K(i,j) = p_b \frac{4\pi}{V}(D(r_i(0)) + D(r_j(0)))(r_i(0) + r_j(0)),$$

where V is the volume of the domain in which they are allowed to diffuse (approximately the volume of the mother minus the volumes of organelles). Here, $r_i(0)$ is not necessarily equal to r_a^i but to the radius of aggregate i at the end of the last division. Additionally, at the end of this period of duration T_s, pre-existing aggregates' radii are increased to a value $r_i(t+T_s) = (\frac{3}{4\pi}C_m T_s + r_i(0)^3)^{\frac{1}{3}}$ and a random number of aggregates taken from a Poisson distribution with mean $\frac{T_s}{\tau_m}$ are generated with initial radii r_a^i. During this period, we generate the event times with a constant rate. The precision of this approximation becomes considerable when the rate of growth is small, as is the case for WT unperturbed cells. After the period between two consecutive division cycles, we run the single-division dynamics described in Section II.8.1.

II.8.3 Dependence on δt

In Fig. II.9 we show the dependence of the short-term simulation results when varying the parameter δt. At short and intermediate timescales the MSD is similar for all values of the time-step size. At longer timescales, for $\delta t = 1$ sec., there appears to be an overestimation of aggregate motion as shown in Fig. II.9A. Concerning aggregate numbers, for larger values of δt, fusion is underestimated as a consequence of overlooked collisions. Nevertheless, after sufficient time, for values smaller than $\delta t = 0.5$ sec. all trajectories converge to similar values after a sufficiently long time. This underestimation of aggregate collisions impacts the aggregate volume in the mother cell as well (Fig. II.9E). Indeed, for having constant rates of growth for aggregates of all sizes, two aggregates increase in volume at twice the rate of one larger aggregate. We claim that this does not impact strongly the results shown above since aggregate numbers are always low (close to 1 or 2) given the frequency of fusion and that for smaller growth rates the error becomes negligible. In the case where aggregate volume becomes significantly overestimated, we also provide a variant of the model and the mathematical approximation where aggregate growth increases with the surface area of the aggregate (Section II.15). In this case –although in general, rates must be smaller (due to the exponential growth of volume)– all the conclusions remain unvaried.

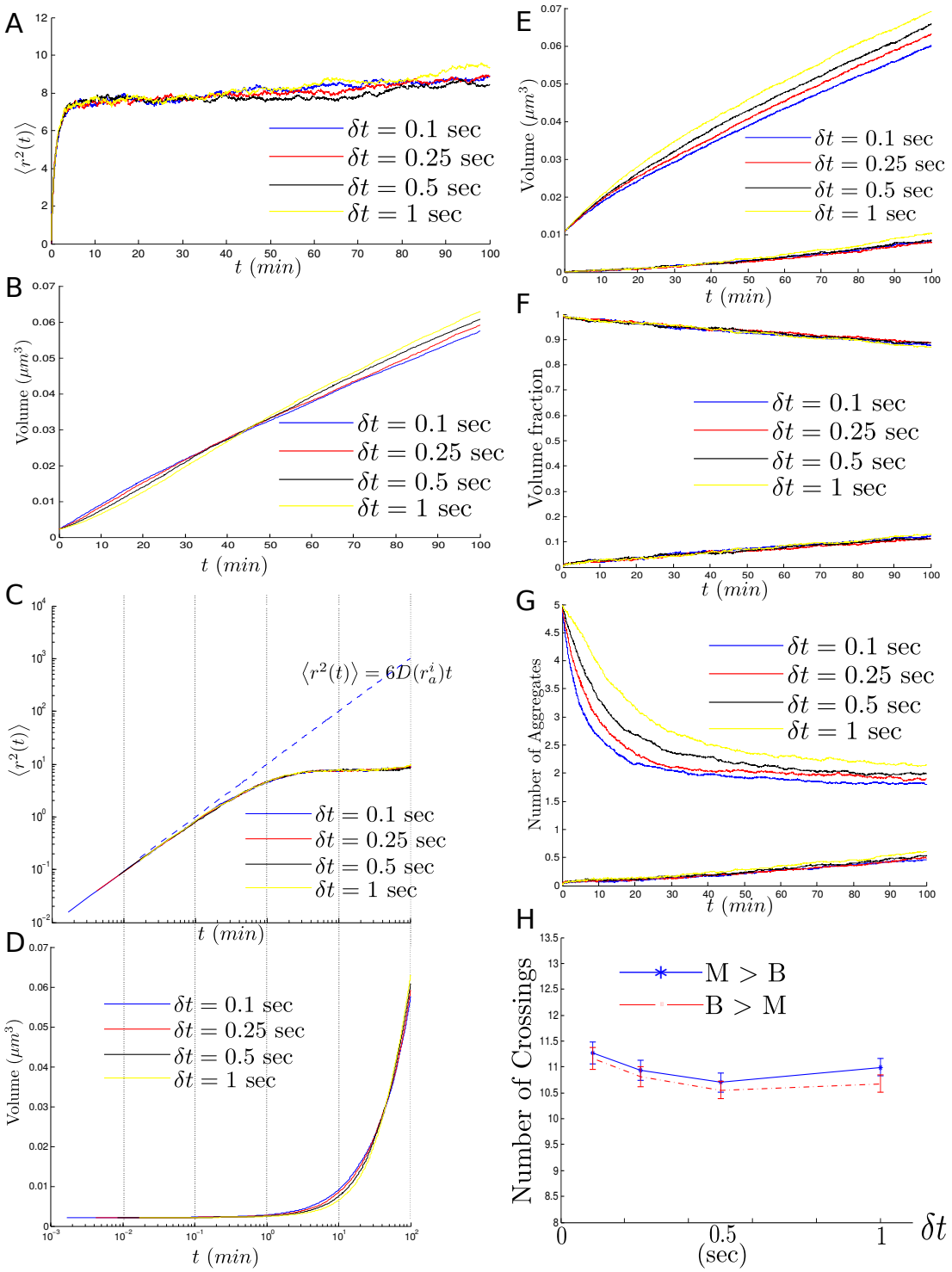

Figure II.9: Dependence on δt. A-D. MSD of one aggregate throughout the simulation of the single-division component of the model (top) and volume of the same aggregate for which the MSD was computed (bottom) for different values of δt. F-G. Log-log plot of Fig. II.9A-II.9B. Dashed lines correspond to the MSD of an aggregate of radius r_a^i. E-G. Total aggregate volume, fraction of the total aggregate volume and number of aggregates inside the mother and the daughter cell for different values of δt. H. Total number of cross-compartment events from mother to bud ($M > B$) and from bud to mother ($B > M$) as a function of δt. In all figures, $N = 5$, $\tau_m = 12$ min., $\tau_d = 120$ min. All other parameters were set to the values in Table S1. Results averaged over 1024 realizations.

II.9 Mathematical Analysis

From [11] we know that the first order approximation of the mean-first-passage-time (MFPT) of a particle undergoing diffusion in a domain of volume V follows $\mathbb{E}(\tau) = \frac{V}{2lD}(1+o(1)) \simeq \frac{V}{2lD}$, where l denotes the diameter of the disc through which particles can escape and D denotes the diffusion coefficient. Due to the possibility of recrossings at the open window where the probability of movement in both directions is equal, the rate of exit from the domain is $\kappa = \frac{1}{2\mathbb{E}(\tau)} \simeq \frac{lD}{V}$ [13]. If besides undergoing diffusion, aggregates also appear and fuse on collision, we can model inner-cell aggregate dynamics using a system of coupled differential equations. Let $V_m^a(t)$, $V_d^a(t)$ be the total aggregate volume (detected) at mother and daughter cells at a time t. In addition, let $N_m(t)$, $N_d(t)$ be the total number of aggregates in each compartment. We abuse notation by denoting $\mathbb{E}(N_m(t))$, $\mathbb{E}(N_d(t))$ by $N_m(t)$ and $N_d(t)$, and $\mathbb{E}(V_m^a(t))$, $\mathbb{E}(V_d^a(t))$ by $V_m^a(t)$, $V_d^a(t)$. Lets define $\langle V(t)\rangle_m = V_m^a(t)/N_m(t)$, $\langle V(t)\rangle_d = V_d^a(t)/N_d(t)$ as the average volume of an aggregate in the mother and the daughter cell respectively at a time t. We assume that all aggregates in the mother have radius $r_m(t) = (\frac{3\langle V(t)\rangle_m}{4\pi})^{\frac{1}{3}}$ and diffusion coefficient $D(r_m(t)) = \frac{\beta}{r_m(t)^\gamma}$. Likewise, aggregates inside the daughter all have radius equal to $r_d(t) = (\frac{3\langle V(t)\rangle_d}{4\pi})^{\frac{1}{3}}$ and diffusion coefficient $D(r_d(t)) = \frac{\beta}{r_d(t)^\gamma}$. If $V_1 = V_m - V_v - V_n$ denotes the volume of the mother cell inside which aggregates undergo diffusion and $V_2(t)$ denotes the volume of the daughter at a time t then we can model the dynamics of $N_m(t)$, $N_d(t)$, $V_m^a(t)$, $V_d^a(t)$ as:

$$\begin{cases} \frac{dN_m(t)}{dt} = \frac{1}{\tau_m} - p_b N_m(t)\max(N_m(t)-1,0)\frac{16\pi r_m(t)D(r_m(t))}{V_1} - \kappa_m(t)N_m(t) + \kappa_d(t)N_d(t) \\ \frac{dN_d(t)}{dt} = \frac{1}{\tau_d} - p_b N_d(t)\max(N_d(t)-1,0)\frac{16\pi r_d(t)D(r_d(t))}{V_2(t)} - \kappa_d(t)N_d(t) + \kappa_m(t)N_m(t) \\ \frac{dV_m^a(t)}{dt} = C_m N_m(t) - \kappa_m(t)N_m(t)\langle V(t)\rangle_m + \kappa_d(t)N_d(t)\langle V(t)\rangle_d + \frac{1}{\tau_m}V_a^i \\ \frac{dV_d^a(t)}{dt} = C_d N_d(t) - \kappa_d(t)N_d(t)\langle V(t)\rangle_d + \kappa_m(t)N_m(t)\langle V(t)\rangle_m + \frac{1}{\tau_d}V_a^i \end{cases} \tag{II.1}$$

Where $\kappa_m = \frac{(l_n - 2r_m(t))^+ D(r_m(t))}{V_1}$ is the escape rate from the mother, $\kappa_d(t) = \frac{(l_n - 2r_d(t))^+ D(r_d(t))}{V_2(t)}$ the escape rate of the daughter and V_a^i the volume of an aggregate with radius r_a^i. The second term on the right of the equality in the first two equations corresponds to rate of fusion in each one of the two domains, which was introduced in Eq. II.8.2. Here, the constant 16π is a consequence of the assumption that all aggregates in each of the compartments have equal radius and equal diffusion coefficient.

II.10 Parameter Values of the Model

The parameter values used in the simulations of the model are shown in Table S1.

Parameter	Interpretation	Value	Source	Additional comments
r_m	Radius of mother cell	2.5 μm	T.N.	
$r_d(T)$	Final radius of daughter cell	1.9 μm	T.N.	
r_v	Radius of vacuole	1.1 μm	T.N.	
r_n	Radius of nucleus	0.9 μm	T.N.	
l_n	Length of neck	1.35 μm	T.N.	
$r_{d_0} = r_d(0)$	Initial radius of daughter cell	$\frac{l_n}{2} + 0.025$ μm	-	The radius of the daughter must be larger than half the size of the neck.
T	Duration of cell division	100 min	T.N.	
r_a^i	Detection threshold (initial radius of aggregate)	0.08 μm	[14]	Estimated after a temperature shift from 30^{o}C to 38^{o}C using time-lapse microscopy to observe the fluorescence intensity of foci. Since the initial volume is $v_a^i = (0.01)(0.6\ \mu m)^3$, then $r_a^i = 0.08\ \mu m$.
T_s	Time between two cell division cycles	45 min	[16, 321]	Two successive cell divisions occur with a difference of 145 mins. Since we set $T = 100$ min we leave $T_s = 45$ min. This is consistent with Fig. 3A in [16] for WT unperturbed cells.
τ_m	Average time of appearance of aggregates in mother cell	12 min, 25 min, 50 min, 100 min, 200 min, 400 min, 800 min	[17]	Around 30% of cells form an aggregate after 1-2 divisions and thus $\tau_m \simeq 800\ min$ in WT cells and $\tau_m \ll 800\ min$ after stress.
τ_d	Average time of appearance of aggregates in daughter cell	$10 \times \tau_m$	-	
β	Constant in functional relation between diffusion coefficient and radius of aggregate	1.4×10^{-4}	[14]	Estimated after a temperature shift from 30^{o}C to 38^{o}C using time-lapse microscopy and image analysis.
γ	Power of radius of aggregate in functional description of diffusion coefficient	2.1	[14]	Same as with β.
$D(r(t))$	Diffusion coefficient for an agg. with radius $r(t)$	$D(r(t)) = \beta / r(t)^\gamma$	[14]	Same as with β and γ
N_{death}	Number of cell divisions before death	28 divisions	[17, 64]	
p_b	Probability of fusion in case of collision	0.9	[109]	The reference value used was estimated in fission yeast after wide-field fluorescence microscopy.
e_l	Proportion of energy lost in case of collision against boundary or organelles	0	-	
p_s	Probability of movement only in direction of mother cell's pole (every time step)	0.05	-	
p_c	Probability of remaining confined to organellar surfaces for every passing minute	1	-	
d_c	Maximum distance between center of the aggregate and surface of organelle for possible confinement to organellar surface	0.3 μm	-	
p_a	Probability of attachment to cell membrane in case of collision	0.5	-	
p_w	Probability of remaining attached to cell membrane after adhesion to organellar surfaces for every passing minute	0.9	-	

Table II.1: Model parameters, values and sources. T.N refers to a personal communication from Prof. Nyström, Department of Cell and Molecular Biology–Microbiology, Göteborg University, Göteborg, Sweden. March 2012.

II.11 Dependence on e_l

We show in Fig. II.10 the results of the simulations of the short-term component of our model when varying the fraction of energy lost after collision against organelles or the cell's boundary. All statistics appear to be independent of the parameter e_l, except the number of crossings which has a subtle increase for higher values of this parameter. This is likely to be a consequence of aggregates remaining close to the neck once they collide to the cell walls in its vicinity.

II.12 Dependence on the diffusion coefficient

We complement the observations concerning the dependence of the model on the diffusion rate with the results shown in Fig. II.11. For higher diffusion rates, the number of aggregates in the mother and the daughter is low as a consequence of increased fusion.
Concerning aggregate volumes, at high diffusion rates, the volume in the mother decreases as its retention capacity is diminished. This produces an increase in aggregate volumes inside the daughter. At low diffusion rates, aggregates remain inside the mother and do not cross to the bud and thus aggregate volumes are higher in the mother compartment. Nevertheless, the fraction of volume in each compartment does not change substantially. This is a consequence of the high aggregation rates and of the constant growth in volume of existing aggregates.

II.13 No cross-compartment movement and no fusion

In Fig. 3A, when comparing the slopes of both curves after 40 min., we observe that the growth rate in the mother cell is approximately 6 times higher than the growth rate in the daughter cell. Under small or non-existent cross-compartment movement, given that the rates differ in a tenfold, the ratio would be expected to be over 10 instead. Thus, cross-compartment transport reduces substantially the difference between the appearance rates, the growth rates and the initial number of aggregates between the two cells.

We show in Fig. II.12 the aggregate dynamics of the single-division component when assuming no compartmental crossings (i.e a closed neck) in our model. Under this assumption, the effect of bud-specific dilution, represented by the difference in the aggregate generation and growth rates, on the asymmetrical distribution of damage is substantially stronger, as can be confirmed in Fig. II.12C. Moreover, aggregate numbers would be overestimated in the daughter cell (Fig. II.12A) due to the lack of escape, and aggregate volume overestimated and underestimated in the mother and daughter cells respectively (Fig. II.12B).

With respect to a model without fusion or appearance of new aggregates as in [1, 15], under the diffusion rates measured in [14], asymmetrical partitioning of volume would be substantially reduced to 68%-32% (measured with equations (II.1)). This yields a probability of approximately 0.32 for each aggregate to be inherited by the bud, which is not in agreement with experimental quantifications [10].

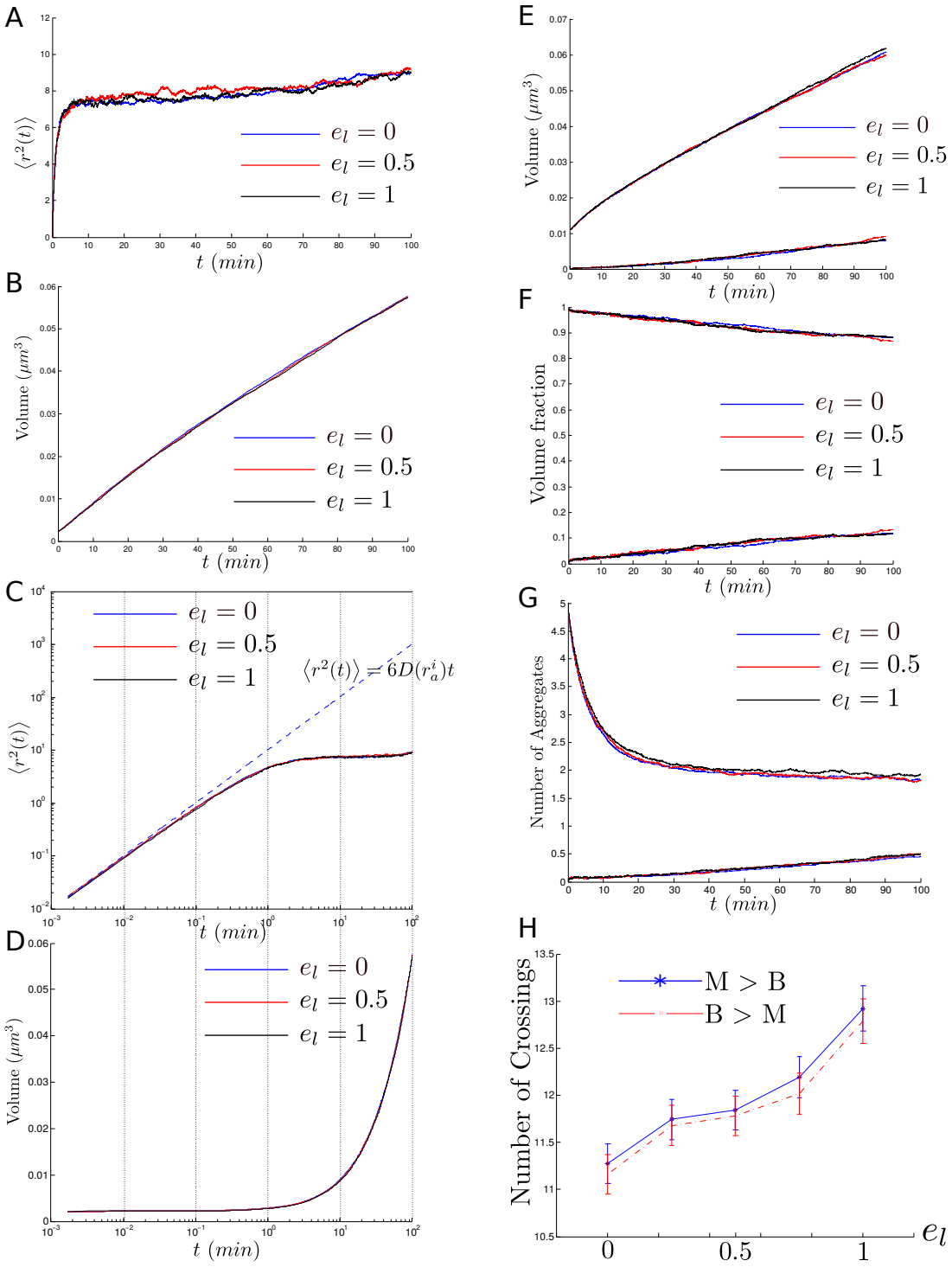

Figure II.10: Dependence on e_l. A-D. MSD of one aggregate throughout the single-division cycle simulation of the model and volume of the same aggregate for which the MSD was computed (bottom) for different values of e_l. F-G. Log-log plot of Fig. II.10A-II.10B. Dashed lines correspond to the MSD of an aggregate of radius r_a^i. E-G. Total aggregate volume, fraction of the total aggregate volume and number of aggregates inside the mother and the daughter cell for different values of e_l. H. Total number of cross-compartment events from mother to bud ($M > B$) and from bud to mother ($B > M$) as a function of e_l. In all figures, $N = 5$, $\delta t = 0.1$ sec., $\tau_m = 12$ min., $\tau_d = 120$ min. All other parameters were set to the values in Table S1. Results averaged over 1024 realizations.

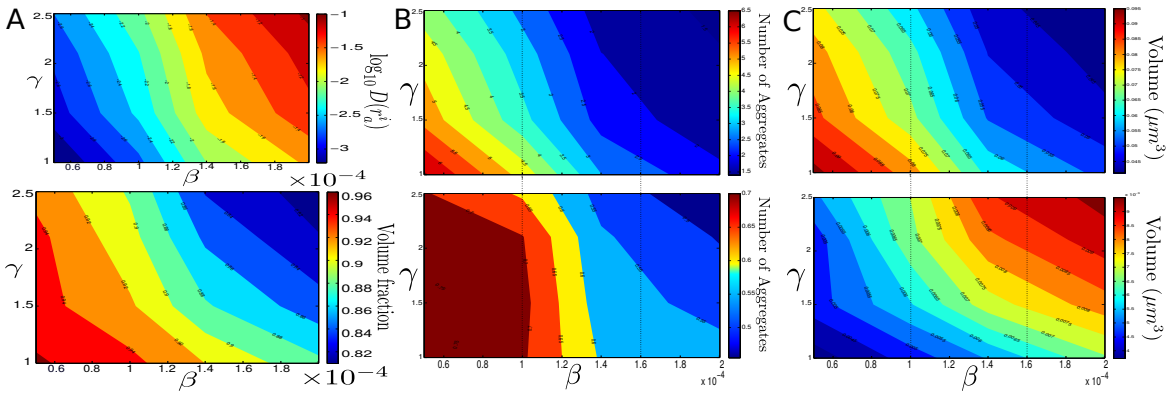

Figure II.11: Dependence on the diffusion coefficient. A. Logarithm of the diffusion rate of an aggregate with radius r_a^i (top) and fraction of volume inside the mother cells (bottom) at the end of the cell division cycle. B-C. Number of aggregates and total aggregate volume inside mother cell (top) and inside the daughter cell (bottom) at the end of the cell division for different values of β and γ. $N = 1$, $\delta t = 0.5$, $\tau_m = 12$ min., $\tau_d = 120$ min. All other parameters were set to the values in Table S1. Results averaged over 1024 realizations.

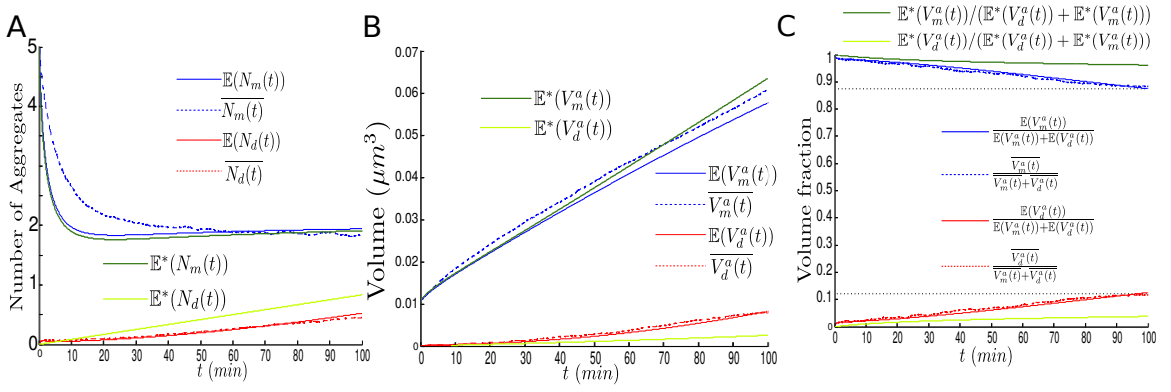

Figure II.12: Aggregate kinetics under no cross-compartment transport. A-C. Same as in Fig. 3A-3C complemented with the results from numerically integrating Eq. II.15 when assuming no cross-compartment transport. $N = 5$, $\tau_m = 12$ min., $\tau_d = 120$ min. All other parameters were set to the values in Table S1.

Hence, both bud-specific dilution and cross-compartment movement have an important role in the compartmental distribution of aggregate volumes, although their strength may vary depending on the experimental conditions (the rate $1/\tau_m$). We then suggest that both should be considered when modeling the asymmetrical distribution of aggregates in budding yeast.

II.14 Mathematical Analysis of confined diffusion in 2D

The MSD of a particle undergoing diffusion with rate D in d dimensional space follows $\langle r^2(t)\rangle_u = 2dDt$.
Anomalous Diffusion corresponds to the case where $\langle r^2(t)\rangle = 2dDt^\alpha$, with $\alpha < 1$ (sub-diffusion) of $\alpha > 1$ (super-diffusion).
In 2D space, the MSD particle undergoing diffusion inside a disk of radius a can be found to be [325–327]:

$$\left\langle r^2(t)\right\rangle_d = a^2\left(1 - 8\sum_{n\in\mathbb{Z}} \exp\left(\frac{-\beta_n^2 Dt}{a^2}\right)\frac{1}{\beta_n^2 - 1}\frac{J_0^2(\beta_n)}{J_1^2(\beta_n)}\right).$$

Where $J_i(x)$ denotes the i-th Bessel function of the first kind and the β_n's are the zeros of $J_1'(x)$.
In the case of diffusion inside an annulus with outer and inner radii a and b respectively, following the work done in [105, 327, 328], we are able to approximate $\langle r^2(t)\rangle$ at intermediate or large timescales as $\langle r^2(t)\rangle \simeq C(1 - \exp(-2\omega Dt))$, where C and ω are positive constants. As proven in [327], $C = \lim_{t\to\infty}\langle r^2(t)\rangle = 2R_G^2$, where R_G is the radius of gyration of the domain (the annulus) whereas ω is related to the degree of sub-diffusion at intermediate stages (which can be computed using curve fitting tools given its difficulty).

II.15 Growth proportional to surface area

We believe that a constant rate of growth in volume is more consistent with the period of relaxation after heat or oxidative stress since, relative to the aggregate's size, initially growth happens fast (for many aggregates) and then slow for fewer larger aggregates after fusion events. In contrast, growth proportional to the surface area could be more consistent with aggregate growth at lower rates in WT unperturbed cells. For this purpose we introduce the following model.

We modify the rate of volume growth so that it is proportional to the surface area of the aggregate. Since the surface area of a sphere of radius r is $A = 4\pi r^2$, we now let the volume of an aggregate increase according to $dV/dt = (r(t)^2/(r_a^i)^2)C_c$. Here, in order for $r(\tau_c) = r_a^i$, $C_c = C_c = \frac{4\pi(r_a^i)^3}{\tau_c}$ (so a factor of 3 larger than in the original version of the model). The mathematical approximation for the dynamics of this variant takes the following form:

$$\begin{cases} \frac{dN_m(t)}{dt} = \frac{1}{\tau_m} - p_b N_m(t) \max(N_m(t) - 1, 0) \frac{16\pi r_m(t) D(r_m(t))}{V_1} - \kappa_m(t) N_m(t) + \kappa_d(t) N_d(t) \\ \frac{dN_d(t)}{dt} = \frac{1}{\tau_d} - p_b N_d(t) \max(N_d(t) - 1, 0) \frac{16\pi r_d(t) D(r_d(t))}{V_2(t)} - \kappa_d(t) N_d(t) + \kappa_m(t) N_m(t) \\ \frac{dV_m^a(t)}{dt} = C_m(r_m(t)^2/(r_a^i)^2) N_m(t) - \kappa_m(t) N_m(t) \langle V(t) \rangle_m + \kappa_d(t) N_d(t) \langle V(t) \rangle_d + \frac{1}{\tau_m} V_a^i \\ \frac{dV_d^a(t)}{dt} = C_d(r_d(t)^2/(r_a^i)^2) N_d(t) - \kappa_d(t) N_d(t) \langle V(t) \rangle_d + \kappa_m(t) N_m(t) \langle V(t) \rangle_m + \frac{1}{\tau_d} V_a^i \end{cases}$$

As observed in Fig. II.13, the consistency between the numerical and mathematical approximations remains remarkable. Besides aggregate volume growth, which is now growing exponentially (and hence the fraction of volume in the mother increases as well), all other results and conclusions remain unvaried. Fusion remains frequent, and the MSD slows down at intermediate and long timescales. In this case, the MSD reaches a higher value and rises faster since we only consider one initial aggregate instead of five. Thus, the aggregate experiences faster diffusion at small timescales and a stronger deceleration given the increasing volume growth rate.

Concerning Fig. II.14, all results are equivalent to those in the original model –when decreasing slightly the growth rates, given that exponential growth occurs at longer timescales–, except for the number of crossings. Since, for smaller values of τ_m aggregates grow very fast, the number of crossings is significantly reduced as a function of τ_m. Nevertheless, the number of crossings remains orders of magnitude higher than the experimental observations in [1].

With respect to the the dependence on other parameters (e_l, δt and β and γ), almost all the observations above remain, with the exception of the aggregate volume growth, which is now higher for higher diffusion values (Fig. II.15B). Accumulation in the mother is favored with increased size and fusion and the appearance of larger aggregates.

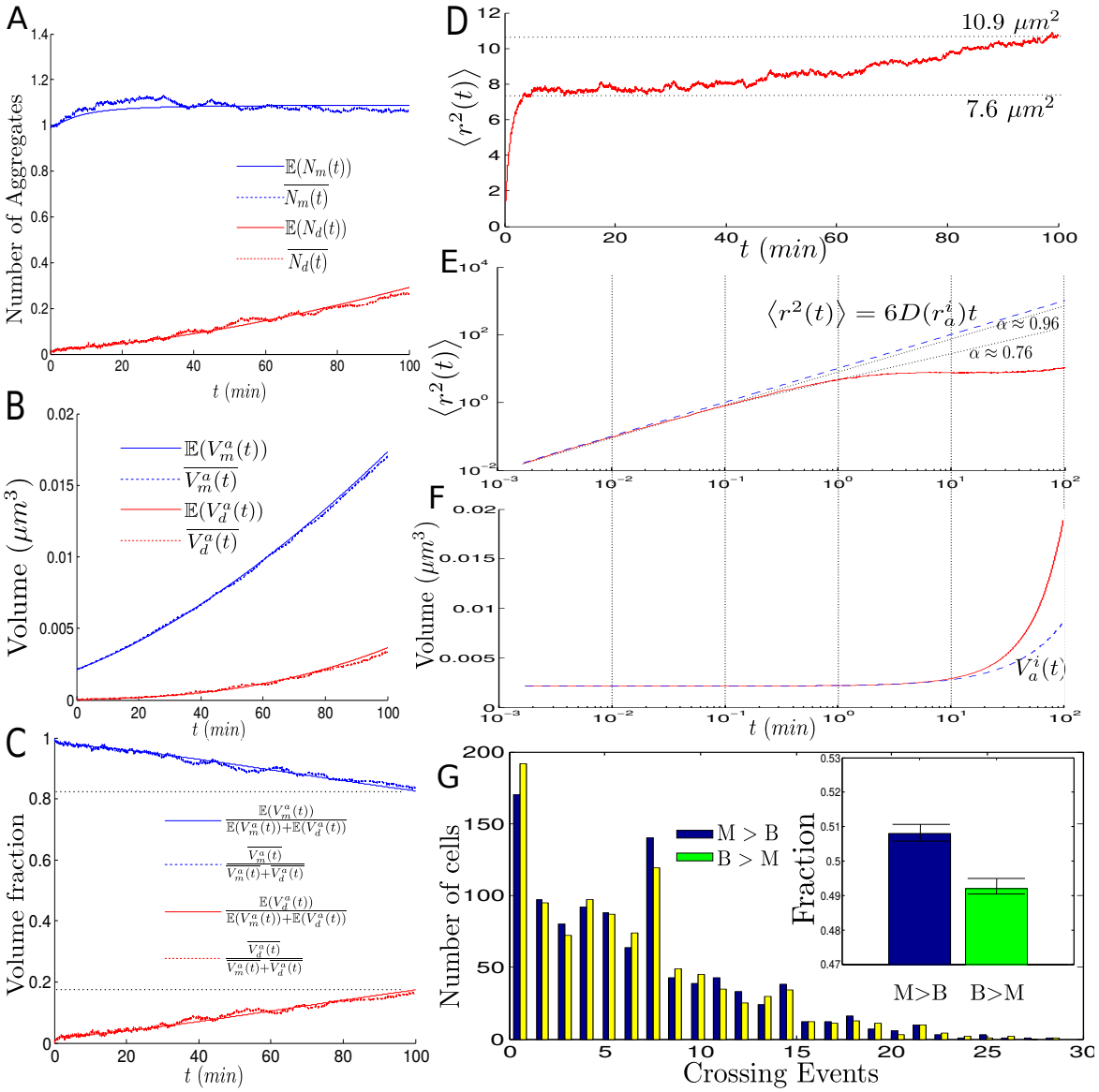

Figure II.13: Single-division aggregate dynamics of the model with aggregate growth proportional to surface area. A-C. Number of aggregates, total aggregate volume and fraction of the total aggregate volume inside the mother (blue) and the daughter cell (red). Continuous line corresponds to the analytical prediction from the mathematical model with growth proportional to the surface area when numerically integrating Eq. II.15. Dotted line corresponds to the numerical average from the simulations of the short-term aggregate dynamics. D. MSD of one aggregate throughout the short-term aggregate dynamics of the model corresponding to a single cycle of cell division. E-F. Log-log plot of Fig. II.13D (top) and volume of the same aggregate for which the MSD was computed (bottom). Dashed lines correspond to the MSD of an aggregate of radius r_a^i (top) and to the volume of one aggregate with initial radius r_a^i in absence of fusion events. G. Histogram of total number of cross-compartment events from mother to bud ($M > B$) and from bud to mother ($B > M$). H Inset. Fraction of total cross-compartment events in each direction. In all figures, $N = 1$, $\delta t = 0.1$ sec., $\tau_m = 100$ min., $\tau_d = 1000$ min. All other parameters were set to the values in Table S1. Results averaged over 1024 realizations.

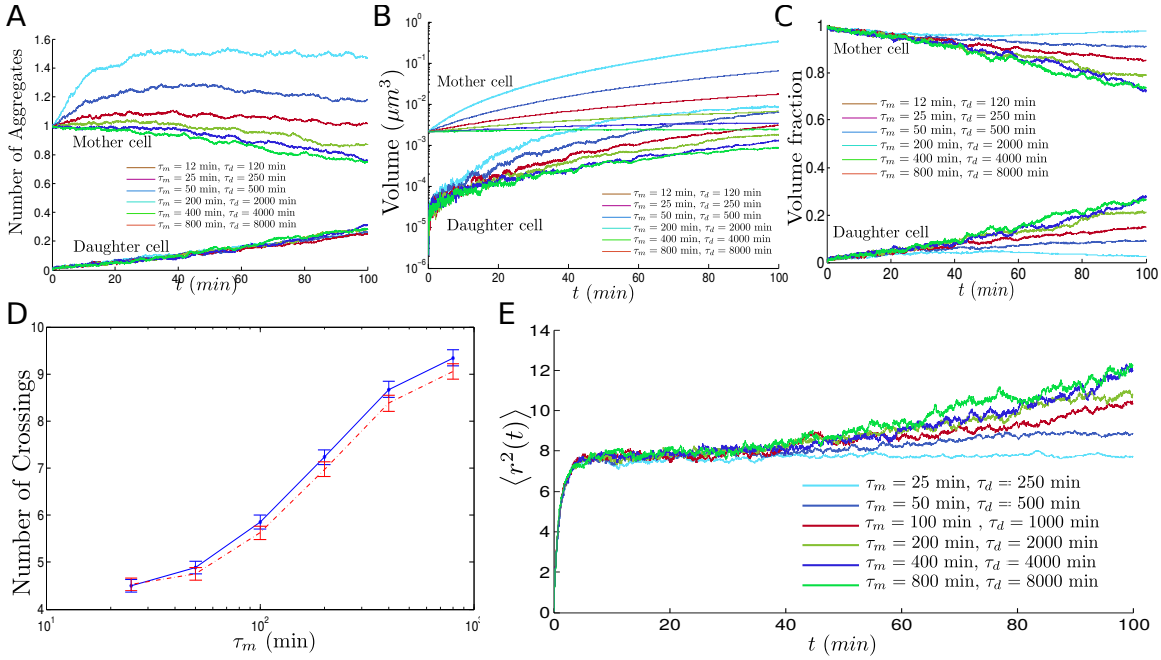

Figure II.14: Single-division aggregate dynamics; dependence on the rate of appearance and growth of aggregates when growth is proportional to surface area. A-C. Number of aggregates, total aggregate volume and fraction of the total aggregate volume inside the mother and the daughter cell. D. Number of crossing events from mother to daughter (blue line) and from daughter to mother (red dashed line). E. MSD of one aggregate throughout the short-term component of the model corresponding to a single cycle of cell division for different rates of appearance and growth of aggregates. In all figures $N = 1$, $\delta t = 0.25$ sec. All other parameters were set to the values in Table S1. Results averaged over 1024 realizations.

Finally, as observed in Fig. II.16 and Fig. II.17, all observations made in the original model regarding active-quality-control remain valid when aggregate growth is proportional to the surface area (and under smaller rates of growth). Indeed, the MSD remains consistent with sub-diffusion in all three cases, one aggregate deposit forms and is maintained in the mother cell, the number of crossings is significantly reduced to values matching experimental data, and the probability of inheritance by the bud of the largest aggregate drops to values near 0.02.

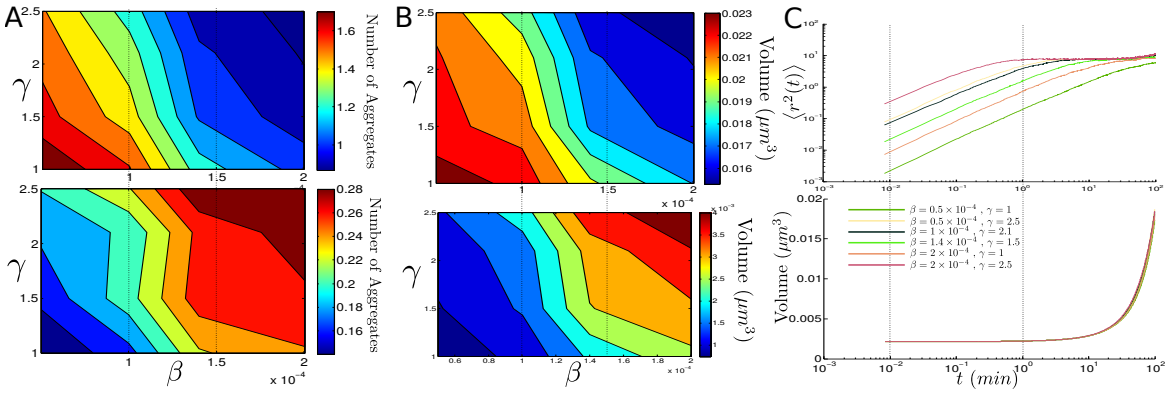

Figure II.15: Dependence on diffusion coefficient continued when growth is proportional to surface area. A-B. Number of aggregates and total aggregate volume inside mother cell (top) and inside the daughter cell (bottom) at the end of the cell division for different values of β and γ. C. MSD of one aggregate throughout the short-term component of the model corresponding to a single cycle of cell division (top) and volume of the same aggregate for which the MSD was computed (bottom) for different values of β and γ. $N = 1$, $\delta t = 0.5$, $\tau_m = 100$ min., $\tau_d = 1000$ min. All other parameters were set to the values in Table S1. Results averaged over 1024 realizations.

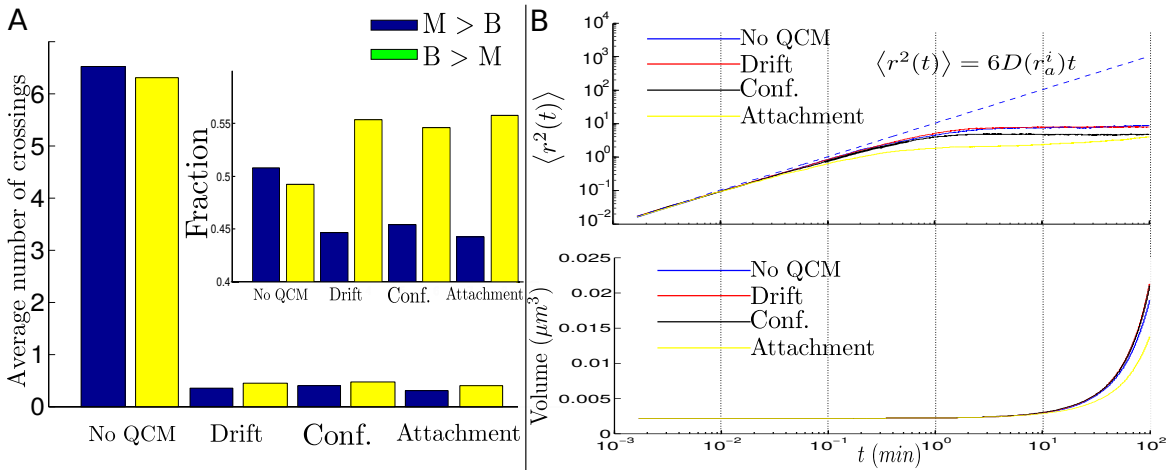

Figure II.16: Single-division aggregate dynamics; Quality-control-mechanisms with aggregate growth proportional to surface area. A. Average number of crossing events from mother to bud ($M > B$) and from bud to mother ($B > M$) under different quality control mechanisms. Inset. Proportion of crossing events in both directions under different quality control mechanisms. B. MSD of one aggregate throughout a single cycle of cell division and volume of the same aggregate for which the MSD was computed for different quality-control-mechanisms. Dashed line corresponds to the MSD of an aggregate of radius r_a^i (top). In all simulations, $N = 1$, $\delta t = 0.1$ sec., $\tau_m = 100$ min., $\tau_d = 1000$ min. All other parameters were set to the values in Table S1. Results averaged over 1024 realizations.

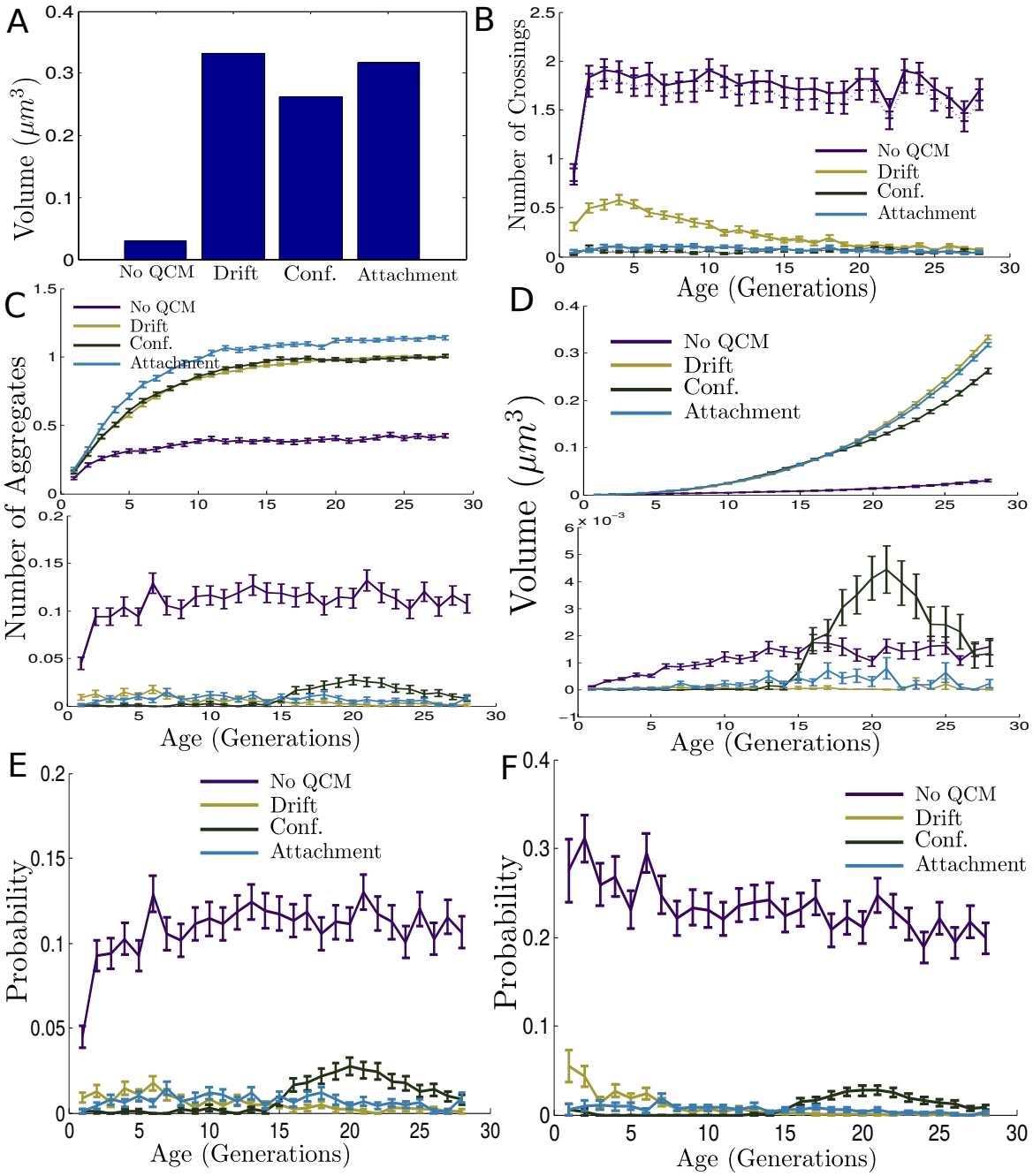

Figure II.17: Variants of the model with active-quality-control mechanisms and aggregate growth proportional to surface area. A. Total aggregate volume inside the mother cell at the end of the 28th division for different QCMs. B. Number of crossing events from mother to bud (continuous line) and from bud to mother (dotted line) as a function of the mother's age (in generations) for different QCMs. C-D. Total number of aggregates and total aggregate volume inside the mother cell (top) and inside the daughter cell (bottom) as a function of the mother's age (in generations) for different QCMs. E. Probability of inheritance of at least one aggregate by the daughter cell at the end of cell division as a function of the mother's age (in generations) for different QCMs. F. Probability of inheritance of the largest aggregate by the daughter cell, when in presence of aggregates, as a function of the mother's age (in generations) for different QCMs. Error bars correspond to the Standard error. In all simulations $\delta t = 0.5$, $\tau_m = 800$ min., $\tau_d = 8000$ min., all other parameters were set to the values in Table S1. Results averaged over 1024 realizations.

III – Modeling the Spatial Propagation of Aβ Oligomers in Alzheimer's Disease

Martín Andrade-Restrepo[1,*], Paul Lemarre[2,3,*], Laurent Pujo-Menjouet[2,3], Leon Matar-Tine[2,3], Sorin Ionel Ciuperca[2,3]

* Denotes equal contribution

[1] Institut Jacques Monod, CNRS UMR 7592, Université Paris Diderot, Paris Cité Sorbonne, F-750205, Paris, France
[2] Institut Camille Jordan, Université de Lyon, Université Claude Bernard Lyon 1, CNRS UMR 5208, 43 blvd. du 11 novembre 1918, 69622 Villeurbanne cedex, France
[3] Team Dracula, INRIA, 69603 Villeurbanne Cedex, France

Abstract

Recent advances in the study of Alzheimer's Disease and the role of Aβ amyloid formation have caused the focus of biologists to progressively shift towards the smaller protein assemblies, the oligomers. These appear early on in the disease progression and seem to be the most infectious species for the neurons. We suggest a model of spatial propagation of Aβ oligomers in the vicinity of a few neurons, without considering the formation of large fibrils or plaques. We also include a simple representation of the oligomers neurotoxic effect. A numerical study reveals that the oligomer spatial dynamics are very sensitive to the balance between their diffusion and their replication, and that the outcome in terms of the progression of AD strongly depends on it.

Introduction

Biological background: Alzheimer's Disease and Aβ aggregation

Alzheimer's disease (AD) is the most common of neurodegenerative diseases, a group also including Parkinson's disease, Huntington disease, Creutzfeldt-Jakob disease, transmissible spongiform encephalopathies. As is the case for these other diseases, AD is associated with the misconformation, aggregation and propagation of different proteins in the neural system [66], namely the proteins Aβ and tau. The distinct characteristic of these proteins is their ability to adopt different stable **conformations**. Misshapen conformations often lead to **aggregation** and accumulation of the proteins into assemblies of different structure, stability and activity.

Biologists identify two different types of structures. On one hand the proteins can assemble into long linear **fibrils**. These fibrils in turn coalesce into large and amorphous tangles, that constitute the visible **plaques** observed in most late-stage AD patients. On the other hand, they can also assemble into smaller oligomeric species. These **oligomers** are soluble, and thus more difficult to detect, but their role in AD propagation and pathology is believed to be essential [4, 147]. In fact, in the last decade it has become clear that plaques are mostly inactive by-products of polymerization, but oligomers are the active species both for propagation inside the brain and destruction of the neurons. The interaction between fibrils and oligomers is unclear, but it has been shown that oligomers appear early on during the onset of Alzheimer's disease, while fibrils and plaques become detectable much later [147].

The generally accepted mechanism for the onset of AD is the so-called **cascade hypothesis** [5, 147]. The first appearance of oligomers is a rare and highly stochastic event, possibly favored by mutations or co-factors. Monomers can spontaneously change conformation and assemble into small proto-oligomers, this process is termed primary nucleation. Once the process has started and a seed has appeared, the oligomers replicate very fast [5, 126, 329, 330]. This second step is usually referred to as secondary nucleation. Although the precise phenomenon that allows oligomers to replicate is not known, it can be described as a prion-like propagation. A combination of propagation in the brain through diffusion, recruitment of healthy Aβ monomers, and though other mechanisms such as exosomes [331]. In the later stages, fibrils and plaques accumulate in the brain.

It is of particular interest for biologists and physicians to understand the precise mechanisms of propagation and replication of Aβ oligomers, especially in the early stages of AD. Insight into the phenomena could indeed help develop therapeutical strategies [147, 332], favor early diagnosis and predict the prognosis of the pathology. This is precisely where our focus lies, at the very early stages of the disease when a seed has been produced and oligomers start replicating.

Previous mathematical work

Amyloid formation and propagation has drawn strong attention among scientists and has been the subject of numerous interdisciplinary research studies. In particular, numerical and mathematical modeling, both stochastic and deterministic has aimed to shed light on

the subject. Early modeling work used systems of ordinary or partial differential equations to study the dynamics of prion aggregates [131, 333, 334] in the context of transmissible spongiform encephalopathies (TSE). The dynamics of Aβ oligomers and prion aggregates are similar, however different microscopic processes distinguish the two.

A more recent discovery is that Aβ oligomers interact with the prion protein (PrP) to induce neurotoxicity, and different models of joint PrP-Aβ dynamics have been introduced [136, 137, 335]. These models propose an elaborate description of the degenerative effect oligomers have on the neurons, but they do not analyze the effects of their spatial spreading. In [136, 335], a size-continuous description of the aggregates is used, and while the latter can be a good approximation for very large aggregates it is less relevant for small oligomers. The relation between continuous and discrete protein sizes has been studied rigorously in [142, 333, 336]. In [137], the size of the oligomers, fibrils and plaques is discrete. Overall, the molecular dynamics of oligomers have been investigated in the context of general models where fibrils and plaques were also present, and with a complex description of neurotoxicity involving the prion protein.

The spatial dynamics of aggregated species have been analyzed for Alzheimer's Disease [144], and for prion propagation in other neurodegenerative disorders [337]. In [144] a comprehensive model of amyloid spatial propagation in the form of Aβ monomers, oligomers, fibrils (and plaques) was introduced. While this model achieves some interesting results in the qualitative dynamics of macroscopic biomarkers (deposits and brain atrophy), some of the parameters and hypotheses remain unjustified biologically. In particular, the extrapolation of microscopic molecular dynamics to a macroscopic scale is delicate, because different biological processes have to be taken into account at the macroscopic scale (*e.g.* the recycling of cerebrospinal fluid).

In this work we intend to develop a model similar to the one proposed in [137], with a special focus on Aβ oligomers and their spatial propagation. The scope of this model is the early stages of AD propagation, when fibrils and plaques are most likely not yet present and the dynamics are driven by oligomers. As studied in [144] we include diffusion of the different molecular species, but we restrict the study to the mesoscopic scale (a few neurons), which is also relevant with the early stages of the disease. This ensures that our hypothesis of absence of fibrils or plaques is valid. To simplify even further the model, the neurotoxicity of the oligomers is considered independently of any other protein. These hypotheses allow us to build a simpler model, at the cost of restricting the scope, but with a stronger biological basis.

In the first section, we introduce the biological model as well as its mathematical formulation. This formulation is presented as a partial differential equation problem and its variational formulation. The second section describes some obtained theoretical results. The third section discusses the parameter choice, before showing simulation results.

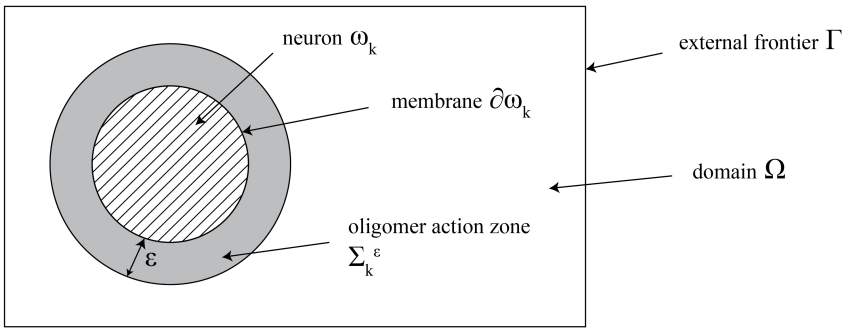

Figure III.1: Representation of the modeling domain (with only one neuron represented)

III.1 A spatial model of Aβ oligomers

III.1.1 Model hypotheses and formulation

We investigate a simplified model of the propagation of Aβ oligomers in the brain. We do not aim at modeling the spontaneous appearance of oligomers in the brain. This sporadic event is highly stochastic and rare, but once it is seeded, the proliferation of oligomers becomes very fast and deterministic. We aim here at describing the evolution of a small initial number of oligomers in the vicinity of a few neurons (mesoscopic scale) using partial differential equations. Fibrils and plaques are not considered yet, since they are not believed to appear until a later stage of the disease.

III.1.1.1 Molecular scale

First we describe the chemical processes that we consider at the molecular scale. We consider a domain Ω with a boundary Γ, where $N \in \mathbb{N}$ **neurons** $\omega_1, \omega_2, ..., \omega_N$ are represented by disks. Fig. III.1 shows a representation of one neuron in the domain Ω. The neurons actively produce **Aβ monomers** with a rate λ at their membrane $\partial\omega_k$, $k = 1, 2, ..., N$. The Aβ monomer production rate is homogeneous along the membrane of one neuron but depends on its activity. The significance and the evolution of this activity will be described later on. The Aβ monomers inside Ω are constantly evacuated or degraded by the cerebro-spinal fluid with a rate δ.

The Aβ monomers assemble first into **proto-oligomers**, and then **oligomers**. Proto-oligomers are small unstable polymers that grow by addition of monomers - **polymerization** - with a rate r_i (for size i), and that lose monomers through **depolymerization** with a rate b. The polymerization rate is supposed to be size dependent, whereas the depolymerization rate is not. Proto-oligomers can also **fragment** into smaller pieces. The fragmentation rate of a size i proto-oligomer is given by $\beta \times (i-1)$, representing the assumption that each bond in the chain is equally likely to break. The usual assumptions are made on the fragmentation kernel $\kappa(i, j)$ (probability of obtaining a size i aggregate from a size j aggregate) [333].

- Symmetry: $\kappa(i,j) = \kappa(j-i,j)$
- Probability kernel: $\sum_{i=1}^{j-1} \kappa(i,j) = 1$ (which implies $\kappa(i,j) = 0$ for $i \geq j$)
- Mass conservation: $2\sum_{i=1}^{j-1} i\kappa(i,j) = j$ (the factor 2 comes from the symmetry property)

The simplest kernel verifying these assumptions is the uniform kernel, where every configuration is equally likely. This writes as $\kappa(i,j) = \frac{1}{j-1}\mathbb{1}_{[1\leq i\leq j-1]}$ (it does not depend on i). One can easily check that it verifies the previous assumptions. Using this kernel greatly simplifies the fragmentation equation. Indeed, expressing the speed of fragmentation from size j to size i gives $2\beta(j)\kappa(i,j) = 2\beta$ for $1 \leq i \leq j-1$ (the factor 2 once again comes from the symmetry of the kernel). This model is the classical polymerization-fragmentation equation, see [131, 334] for further developments.

Once proto-oligomers reach the critical size i_0, they become oligomers. The oligomers are very stable units that do not exchange monomers with the system, as suggested in previous models [137]. This means that they neither depolymerize nor fragment. We assume that they are the main toxic elements for the neurons.

The above assumptions are illustrated in Figure III.2. They are also summarized into the following set of chemical reactions, where m is the local density of monomers, μ_i is the local density of size i proto-oligomers ($\mu_1 = m$ by convention), and μ_{i_0} that of oligomers.

$$\begin{aligned}
&\forall k \in \{1,\dots,N\}, \forall x \in \partial\omega_k, && \emptyset \xrightarrow{\lambda_k} m,\\
&\forall x \in \Omega, && m \xrightarrow{\delta} \emptyset,\\
&\forall x \in \Omega, \forall i \in \{2,\dots,i_0-2\}, && \mu_i + m \underset{b}{\overset{r_i}{\rightleftharpoons}} \mu_{i+1},\\
&\forall x \in \Omega, && \mu_{i_0-1} + m \xrightarrow{r_{i_0-1}} \mu_{i_0},\\
&\forall x \in \Omega, \forall j \in \{2,\dots,i_0-1\}, \forall i \in \{1,\dots,j-1\}, && \mu_j \xrightarrow{\beta\times(j-1)} \mu_i + \mu_{j-i}.
\end{aligned}$$

III.1.1.2 Mesoscopic scale

We now describe the interactions between the different molecular elements at the mesoscopic scale. Naturally, we are interested in studying more than one neuron. The objective here is to describe how the polymerization reaction propagates from neuron to neuron via diffusion and induces progressive neurodegeneration.

On the scale of a few neurons, we consider spatial diffusion of all the molecular components described before, in two dimensions. Each species is associated with a specific diffusion coefficient depending on its size, from D_1 (for $A\beta$ monomers) to D_{i_0} for oligomers. We assume that the smaller the species, the faster it is diffused. The specific choice of the diffusion coefficients and their scaling with size will be described later on.

Oligomers are supposed to be the toxic species. Their effect on the neurons relies on their presence in the action perimeter Σ_k^ε of radius ε around ω_k (see Figure III.1). To model

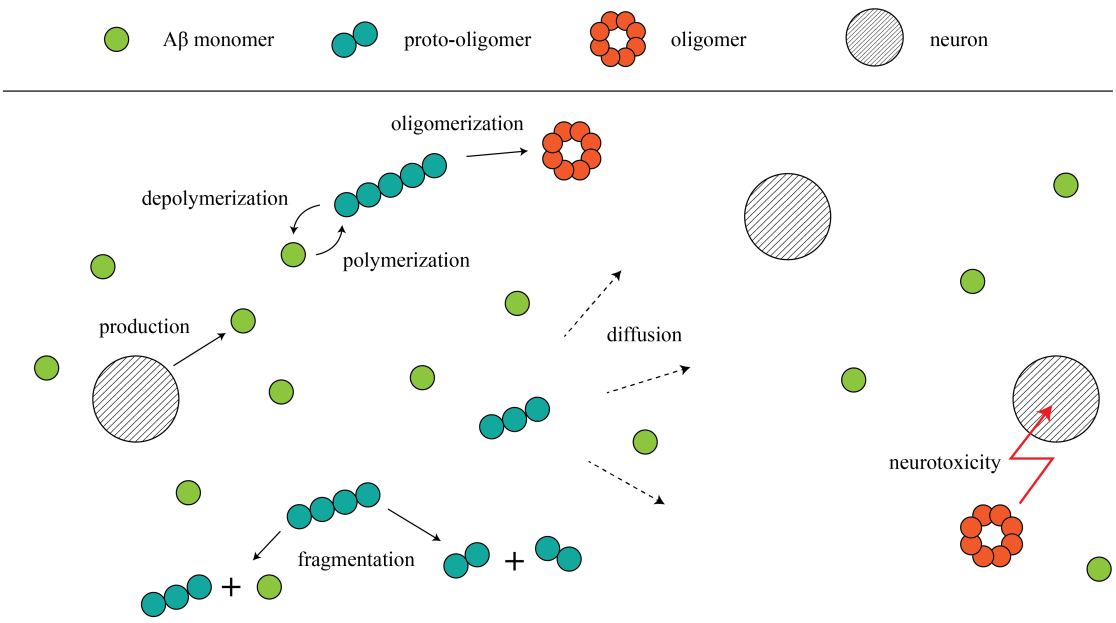

Figure III.2: Representation of the different processes and agents at play in the model

the fact that oligomers progressively kill the neurons, we use an equation to describe their production rate. A healthy neuron produces $A\beta$ monomers at maximum rate λ_0, and a dead neuron has a production rate of 0. We suggest that this production decreases with a rate proportional to the number of oligomers in the ring Σ_k^ε. A simple model to describe this is

$$\frac{\mathrm{d}\lambda_k}{\mathrm{d}t} = -\tau\lambda_k \int_{\Sigma_k^\varepsilon} \mu_{i_0}(x,t)\,\mathrm{d}x.$$

Here τ represents the lethal efficiency of the oligomers on the neurons. As said previously, the production of Aβ happens only at the surface membrane of the neurons $\partial\omega_k$. This gives the boundary condition for monomers on these surfaces, via a non-homogeneous Neumann condition. For the other species (proto-oligomers and oligomers), we consider a simple non-flux boundary condition.

On the sides of the domain Ω, different choices are possible. To model isolation from other neurons, we can use absorbing conditions on the external boundary, but we could also consider periodical boundary conditions to reflect the effect of a crowded brain region. For the moment, we choose an absorbing condition.

III.1.2 Mathematical formulation

III.1.2.1 System of partial differential equations

We now introduce the mathematical problem corresponding to the model, first the local equations, then the boundary conditions and finally the initial condition. Our goal here is

to discuss the hypotheses made in the formulation of the model, and not provide general theoretical results. For this reason we do not specify the formal and general mathematical problem in this work. It will be done as part of a subsequent theoretical study.

The local densities of the different elements verify the following system of partial differential equations for $x \in \Omega$ and $t > 0$

$$\begin{aligned}
\frac{\partial m}{\partial t}(x,t) =& D_1 \Delta m + \sum_{j=3}^{i_0-1} b\mu_j - \sum_{j=2}^{i_0-1} r_j \mu_j m + 2\beta \sum_{j=2}^{i_0-1} \mu_j - \delta m, \\
\frac{\partial \mu_2}{\partial t}(x,t) =& D_2 \Delta \mu_2 + b\mu_3 - r_2 \mu_2 m - \beta \mu_2 + 2\beta \sum_{j=3}^{i_0-1} \mu_j, \\
\forall i \in \{3, \dots, i_0 - 2\}, \frac{\partial \mu_i}{\partial t}(x,t) =& D_i \Delta \mu_i + b\mu_{i+1} - b\mu_i + r_{i-1}\mu_{i-1} m - r_i \mu_i m - \beta(i-1)\mu_i + 2\beta \sum_{j=i+1}^{i_0-1} \mu_j, \\
\frac{\partial \mu_{i_0-1}}{\partial t}(x,t) =& D_{i_0-1} \Delta \mu_{i_0-1} - b\mu_{i_0-1} + r_{i_0-2}\mu_{i_0-2} m - r_{i_0-1}\mu_{i_0-1} m - \beta(i_0-2)\mu_{i_0-1}, \\
\frac{\partial \mu_{i_0}}{\partial t}(x,t) =& D_{i_0} \Delta \mu_{i_0} + r_{i_0-1}\mu_{i_0-1} m.
\end{aligned} \tag{III.1}$$

The initial conditions are chosen in the space $X = \{v \in \mathrm{L}^2(\Omega) | v(x) \geq 0, \ a.e.\ x \in \Omega, \}$.

$$\begin{aligned}
&a.e. x \in \Omega, m(x,0) = m^0(x), \mu_2(x,0) = \mu_2^0(x), \dots, \mu_{i_0}(x,0) = \mu_{i_0}^0(x), \\
&\{m^0, \mu_2^0, \dots, \mu_{i_0}^0\} \in X^{i_0}.
\end{aligned}$$

All the boundary conditions we define are Neumann conditions, imposed upon the fluxes of particles. The unitary normal vectors used for these definitions are pointing outwards (relative to the domain Ω), denoted $\vec{n}|_\Gamma$ on the exterior boundary Γ and $\vec{n}|_{\partial\omega_k}$ on the neurons membrane.

On the exterior frontier, we impose an absorbing condition with a proportion γ. This gives, for any variable $\xi = m, \mu_2, \dots, \mu_{i_0}$

$$D_\xi \nabla \xi \cdot \vec{n}|_\Gamma = -\gamma \xi.$$

On the neurons membrane $\partial\omega_k$ for $k \in \{1, \dots, N\}$, we have a zero-flux condition for $\xi = \mu_2, \dots, \mu_{i_0}$ and a source term for m

$$\begin{aligned}
D_\xi \nabla \xi \cdot \vec{n}|_{\partial\omega_k} =& 0, \\
D_1 \nabla m \cdot \vec{n}|_{\partial\omega_k} =& \lambda_k(t).
\end{aligned}$$

The source term λ_k of the neuron k follows the differential equation

$$\begin{aligned}
\frac{\mathrm{d}\lambda_k}{\mathrm{d}t}(t) =& -\tau \lambda_k \int_{\Sigma_k^\varepsilon} \mu_{i_0}(x,t)\, \mathrm{d}x, \\
\lambda_k(0) =& \lambda_0.
\end{aligned}$$

The initial condition for System (III.1) is a perturbation of the disease-free solution. The disease-free solution corresponds to the case when no proto-oligomers or oligomers are

present, and the neurons are healthy. The monomer density thus verifies the boundary-condition problem

$$\begin{aligned} D_1\Delta m =&\delta m, \\ D_1\nabla m\cdot\vec{n}|_\Gamma =&-\gamma m, \\ \forall k\in\{1,\dots,N\}, D_1\nabla m\cdot\vec{n}|_{\partial\omega_k} =&\lambda_0. \end{aligned} \tag{III.2}$$

The initial condition for m is chosen to be the solution to System (III.2). The initial condition for proto-oligomers and oligomers is a local Gaussian distribution, both in space and in size of assemblies. This represents the fact that the stochastic process of spontaneous misfolding and oligomerization has already occurred, and a seed is now present to catalyze the reaction.

III.1.2.2 Variational formulation

To run numerical simulations of this system of equations, we use the finite elements method. The first step is to express the problem under a variational form. The calculations that follow are formal, and we assume sufficient regularity for all the functions studied. The theoretical setting will be detailed in future work.

We rewrite System (III.1) as a system of reaction-diffusion equations (where by convention $\mu_1 = m$)

$$\begin{cases} \forall i\in\{1,\dots,i_0\}, \dfrac{\partial\mu_i}{\partial t} =D_i\Delta\mu_i + F_i(\mu_1,\dots,\mu_{i_0}), \\ \forall i\in\{1,\dots,i_0\}, D_i\nabla\mu_i\cdot\vec{n}|_\Gamma =-\gamma\mu_i, \\ \forall i\in\{2,\dots,i_0\}, D_i\nabla\mu_i\cdot\vec{n}|_{\partial\omega_k} =0, \text{ and } D_1\nabla\mu_1\cdot\vec{n}|_{\partial\omega_k} = \lambda_k(t). \end{cases}$$

The reaction terms are explicitly given by

$$\begin{cases} F_1(\mu_1,\dots,\mu_{i_0}) =-\delta\mu_1 + b\displaystyle\sum_{j=3}^{i_0-1}\mu_j + 2\beta\sum_{j=2}^{i_0-1}\mu_j - \sum_{j=2}^{i_0-1} r_j\mu_j\mu_1, \\ F_2(\mu_1,\dots,\mu_{i_0}) =b\mu_3 - r_2\mu_2\mu_1 - \beta\mu_2 + 2\beta\displaystyle\sum_{j=3}^{i_0-1}\mu_j, \\ F_i(\mu_1,\dots,\mu_{i_0}) =b\mu_{i+1} - b\mu_i + r_{i-1}\mu_{i-1}\mu_1 - r_i\mu_i\mu_1 - \beta(i-1)\mu_i + 2\beta\displaystyle\sum_{j=i+1}^{i_0-1}\mu_j, \\ F_{i_0-1}(\mu_1,\dots,\mu_{i_0}) =-b\mu_{i_0-1} + r_{i_0-2}\mu_{i_0-2}\mu_1 - r_{i_0-1}\mu_{i_0-1}\mu_1 - \beta(i_0-2)\mu_{i_0-1}, \\ F_{i_0}(\mu_1,\dots,\mu_{i_0}) =r_{i_0-1}\mu_{i_0-1}\mu_1. \end{cases}$$

To discretize this system in time, we use an Euler scheme with implicit diffusion and explicit reaction. For a pace δ_t and at step n, it writes

$$\frac{\mu_i^{n+1}-\mu_i^n}{\delta_t} = D_i\Delta\mu_i^{n+1} + F_i(\mu_1^n,\dots,\mu_{i_0}^n).$$

By multiplying with a suitable test function, and integrating over the whole domain we get

$$\int_\Omega(\mu_i^{n+1}v - \mu_i^n v)\,\mathrm{d}x - \int_\Omega \delta_t D_i\Delta\mu_i^{n+1}v\,\mathrm{d}x - \int_\Omega \delta_t F_i(\mu_1^n,\dots,\mu_{i_0}^n)v\,\mathrm{d}x = 0.$$

By the divergence theorem we are left with

$$\int_\Omega (\mu_i^{n+1} v + \delta_t D_i \nabla \mu_i^{n+1} \cdot \nabla v)\,\mathrm{d}x - \int_\Gamma \delta_t D_i (\nabla \mu_i^{n+1} \cdot \vec{n}) v\,\mathrm{d}x - \sum_k \int_{\partial\omega_k} \delta_t D_i (\nabla \mu_i^{n+1} \cdot \vec{n}) v\,\mathrm{d}x - \int_\Omega \mu_i^n v\,\mathrm{d}x - \int_\Omega \delta_t F_i(\mu_1^n, \ldots, \mu_{i_0}^n) v\,\mathrm{d}x = 0.$$

The boundary conditions give us the variational formulation for each variable $i = 2, \ldots, i_0$

$$\int_\Omega (\mu_i^{n+1} v + \delta_t D_i \nabla \mu_i^{n+1} \cdot \nabla v)\,\mathrm{d}x + \int_\Gamma \delta_t \gamma \mu_i^{n+1} v\,\mathrm{d}x - \int_\Omega \mu_i^n v\,\mathrm{d}x - \int_\Omega \delta_t F_i(\mu_1^n, \ldots, \mu_{i_0}^n) v\,\mathrm{d}x = 0,$$

and for the monomers

$$\int_\Omega (\mu_1^{n+1} v + \delta_t D_1 \nabla \mu_1^{n+1} \cdot \nabla v)\,\mathrm{d}x + \int_\Gamma \delta_t \gamma \mu_1^{n+1} v\,\mathrm{d}x - \sum_{k=1}^{N} \int_{\partial\omega_k} \delta_t \lambda_k^{n+1} v\,\mathrm{d}x - \int_\Omega \mu_1^n v\,\mathrm{d}x - \int_\Omega \delta_t F_1(\mu_1^n, \ldots, \mu_{i_0}^n) v\,\mathrm{d}x = 0.$$

Note that since diffusion is implicit, the source term in the boundary condition is also implicit (λ_k^{n+1}). We evaluate it with a forward Euler scheme, requiring the equation on the monomers to be solved last. In this case we can directly solve

$$\lambda_k^{n+1} - \lambda_k^n = -\delta_t \tau \lambda_k^{n+1} \int_{\Sigma_k^\varepsilon} \mu_{i_0}^{n+1}\,\mathrm{d}x.$$

III.2 Theoretical results

The theoretical background allowing for the study of this model will not be formally proved in this work. Further work will provide existence, uniqueness and positivity of solutions.

III.2.1 Analytic solution for the healthy state

Before the spontaneous appearance of the first oligomers (proto-oligomers of size two) in the brain, the system is assumed to rest at a disease-free equilibrium state where only ordinary monomers are present. This configuration is used in the numerical simulations as an initial condition for the distribution of monomers. We hereby present a detailed study of this specific case.

We consider a system composed of one neuron only and assume enough distance between susceptible neuron cells, so that the disease-free resting state of the system for multiple neurons can be computed by the superposition of the multiple solutions for each individual neuron. Moreover, for simplicity in the computation of solutions using polar coordinates we assume the domain Ω to be circular with radius r_Γ. Let Σ be the annular domain between the exterior boundary Γ of radius r_Γ and a circle ω of radius r_N (representing the neuron cell) both centered at the point $(0, 0)$. Let $m(x, t)$ denote the monomer concentration at time t at the point $x \in \Omega$.

In absence of proto-oligomers and oligomers and from the system of equations in Eq. (III.1), the monomer dynamics follow Eq. (III.3) given by

$$\frac{\partial m(x,t)}{\partial t} = D_1 \Delta m(x,t) - \delta m(x,t). \tag{III.3}$$

The corresponding boundary conditions are

$$D_1 \nabla m \cdot \vec{n}|_\Gamma = -\gamma m,$$

at the outer boundary and

$$D_1 \nabla m \cdot \vec{n}|_{\partial\omega} = \lambda_0.$$

In polar coordinates, Eq. (III.3) becomes

$$\frac{\partial m(x,t)}{\partial t} = D_1 \left(\frac{\partial^2 m(r,\theta,t)}{\partial r^2} + \frac{1}{r}\frac{\partial m(r,\theta,t)}{\partial r} + \frac{1}{r^2}\frac{\partial^2 m(r,\theta,t)}{\partial \theta^2} \right) - \delta m(r,\theta,t),$$

with Neumann boundary conditions

$$\begin{aligned} D_1 \frac{\partial m(r_\Gamma,\theta,t)}{\partial r} &= -\gamma m(r_\Gamma,\theta,t), \\ D_1 \frac{\partial m(r_N,\theta,t)}{\partial r} &= -\lambda_0. \end{aligned}$$

with $0 < r_N \leq r \leq r_\Gamma$. Notice that the normal vector is pointing out of Ω so the sign is reversed in r_N $(-\lambda_0)$.

The problem is symmetrical by rotation around $(0,0)$ thanks to the choice of concentrical circles for the different boundaries, so as long as the initial condition does not depend on θ (in polar coordinates), the solution will keep this symmetry at all times. Using this assumption on the initial condition, we drop the dependency on θ in the following and write $m(x,t) = m(r,t)$. The partial differential equation becomes

$$\frac{\partial m(r,t)}{\partial t} = D_1 \left(\frac{\partial^2 m(r,t)}{\partial r^2} + \frac{1}{r}\frac{\partial m(r,t)}{\partial r} \right) - \delta m(r,t),$$

with the new boundary conditions

$$\begin{aligned} D_1 \frac{\partial m(r_\Gamma,t)}{\partial r} &= -\gamma m(r_\Gamma,t), \\ D_1 \frac{\partial m(r_N,t)}{\partial r} &= -\lambda_0. \end{aligned}$$

To find the equilibrium solution $m_0(r)$ we set

$$D_1 \left(m_0''(r) + \frac{1}{r} m_0'(r) \right) - \delta m_0(r) = 0,$$

with

$$\begin{aligned} D_1 m_0'(r_\Gamma) + \gamma m_0(r_\Gamma) &= 0, \\ D_1 m_0'(r_N) + \lambda_0 &= 0. \end{aligned}$$

This equation can then be written in the form of an Emden-Fowler equation or a Sturm-Liouville equation [338]

$$\frac{\mathrm{d}}{dr}\left(r\frac{dm_0}{\mathrm{d}r}(r)\right) - r\frac{\delta m_0(r)}{D_1} = 0.$$

Its solution exists and has the form [339, 340]

$$m_0(r) = c_1 J_0\left(\frac{\mathrm{i}\sqrt{\delta}r}{\sqrt{D_1}}\right) + c_2 Y_0\left(-\frac{\mathrm{i}\sqrt{\delta}r}{\sqrt{D_1}}\right)$$

with c_1 and c_2 constants depending on the boundary conditions and J_0 and Y_0 Bessel functions of the first and second kind respectively. In practice, this steady-state problem will be solved numerically in order to determine the initial condition for the evolution problem. This theoretical study provides the possibility of comparison with the numerical solution, as well as qualitative analysis of the various parameters on the disease-free solution.

III.3 Numerical results

III.3.1 Parameter choice and model scaling

III.3.1.1 Non-dimensional equations

To ease the numerical simulation, we nondimensionalize the model. First we specify the unit system we use. In the following we consider SI units. In particular, we express lengths in meters and time in seconds. For concentrations we use the molar concentration unit M ($1M = 1\ mol.L^{-1}$). We can now define the scales.

- Spatial scale: we define L the characteristic length of the domain. Typically L is about 100 μm.
- Time scale: the characteristic time is T, it is about 100 s.
- Concentration scales: the characteristic concentration is C_0, around $10^{-9}M$.

Using these scales we can nondimensionalize the model. In the rest of this section, a superscript $*$ will indicate nondimensional variables. We define

$$t^* = \frac{t}{T}, x^* = \frac{x}{L}, y^* = \frac{y}{L}, \xi^* = \frac{\xi}{C_0}, \xi = \mu_1 \dots \mu_{i_0}.$$

The non-dimensional operators are given by

$$\begin{aligned} \frac{\partial}{\partial t} &= \frac{1}{T}\frac{\partial}{\partial t^*}, \\ \nabla &= \frac{1}{L}\nabla^*, \\ \Delta &= \frac{1}{L^2}\Delta^*. \end{aligned}$$

Now using the equations of the model, we obtain the nondimensional model. The equations are the same as (III.1), replacing the operators by the non-dimensional operators and modifying the coefficients as follows

$$D^* = D\frac{T}{L^2},\ r_i^* = r_i C_0 T,\ b^* = bT,\ \beta^* = \beta T,\ \delta^* = \delta T,\ \gamma^* = \gamma\frac{T}{L},\ \lambda_k^* = \lambda_k\frac{T}{LC_0},\ \tau^* = \tau C_0 T.$$

III.3.1.2 Parameter choices

To be consistent with biology we need to choose the coefficients appropriately. We know from anatomy that neurons have a size of a few μm and are separated by around 10 μm in the brain. Accordingly, the characteristic spatial scale will be $L = 100\ \mu m$.

For specific data on Aβ, we refer to [341]. The diffusion coefficients will be chosen using the Stokes-Einstein relation

$$D = \frac{k_b T}{6\pi\mu r_h},$$

where k_b is the Boltzmann constant ($k_b = 1.38.10^{-23}\ m^2 kg s^{-2} K^{-1}$), T the temperature, μ the dynamical viscosity of the fluid, and r_h the hydrodynamic radius of the particle considered. In the case of Aβ particles in the cerebrospinal fluid we have (in SI units) $T = 310\ K(37°C)$, $\mu = 10^{-3}\ kgm^{-1}s^{-1}$ [342]. The hydrodynamic radius of monomers is $r_h = 1\ nm$ [343]. For oligomeric species, the hydrodynamic radius grows with the size and we suggest it scales as $i^{1/3}$ where i is the size of the oligomers (to represent 3D rearrangement of the particle as it grows in size). This ultimately gives $D_1 = 2.27.10^{-10}\ m^2 s^{-1}$, and $D_i = \frac{D_1}{i^{1/3}}$. This value is of the same order as measured by [341]. However when we use this value for the diffusion coefficient in the simulations, the distribution of Aβ monomers in the spatial scale $L \approx 100\ \mu m$ is almost homogeneous. To obtain a significant variation of the monomer distribution on this scale, the diffusion coefficient has to be reduced to $D \approx 10^{-14}\ m^2.s^{-1}$. This in turn corresponds to a displacement of 1 μm in approximately 10 s. To justify the use of a diffusion coefficient 4 orders of magnitude than the one suggested by the Stokes-Einstein formula, we first suggest that the cerebrospinal fluid is very crowded by other proteins and assemblies, which impairs the diffusion of molecules. Furthermore, the spatial spreading of the neurons could be increased in the model, because *in vivo* not all the neurons produce Aβ. Without more detailed data, we choose to use $D \approx 10^{-14}\ m^2.s^{-1}$.

For the production and degradation of monomers, we have some suggestions from literature [341, 343]. The disease-free equilibrium concentration of Aβ monomers in the cerebrospinal fluid is of about $C_b = 10\ ng.mL^{-1}$ [344]. The molecular weight of Aβ is 4514 $g.mol^{-1}$, so this concentration amounts to about $C_b = 2.10^{-9}\ M$. The half-life of Aβ monomers is a few hours, which corresponds to a degradation rate δ of about $10^{-4}\ s^{-1}$. The total production rate of a disease-free neuron (integrated over its surface) is $\lambda_0 \pi R^2_{\text{neuron}}$. If we consider that the measured concentration in the cerebrospinal fluid is equivalent to that of a single neuron in a domain of volume $V_{\text{neuron}} = 20\ \mu m^3$, the equilibrium between production and degradation gives us the relation $\lambda_0 \pi R^2_{\text{neuron}}/V = C_b\delta = 2.10^{-13}\ M.s^{-1}$, from which we evaluate λ_0.

The polymerization-depolymerization reaction is estimated to occur at rates $r_0 = 100\ M^{-1}s^{-1}$ and $b = 10^{-3}\ s^{-1}$. The fragmentation rate is more difficult to evaluate, it will be adjusted using the simulations. The same goes for γ and τ. The parameter choices are summarized in Table III.1.

Table III.1: Parameter values used for the simulations (unless specified otherwise). See the main text for a detailed justification of the parameter choice.

Parameter	Value	Unit	Description
T	50000	s	Time scale
L	100	μm	Length scale
C_0	10^{-9}	M	Concentration scale
i_0	20	-	Size of oligomers
D_i	$D_1/i^{1/3}$	$m^2.s^{-1}$	Diffusion coefficient of size i
D_1	$2.2.10^{-14}$	$m^2.s^{-1}$	Diffusion coefficient of monomers
δ	5.10^{-4}	s^{-1}	Degradation coefficient of monomers
γ	1	$m.s^{-1}$	Surface absorption rate
r_i	r_0	$M^{-1}s^{-1}$	Polymerization rate of size i
r_0	10^7	$M^{-1}s^{-1}$	Basal poplymerization rate
b	10^{-3}	s^{-1}	Depolymerization rate
β	10^{-4}	s^{-1}	Fragmentation rate
$\lambda_0 \times \pi R^2_{\text{neuron}}/V_{\text{neuron}}$	2.10^{-13}	$M.s^{-1}$	Monomer production rate of a neuron
τ	10^{10}	$M^{-1}.s^{-1}$	Infectivity rate
R_{neuron}	2	μm	Radius of a neuron
V_{neuron}	20	μm^3	Apparent volume of isolation for a neuron
ε	2	μm	Radius of activity for oligomers

III.3.2 Simulation results

The numerical resolution of the model is conducted using Freefem++ [345], and visualized in Paraview [346]. The default parameter values are presented in Table III.1, and the initial configuration for all the simulations is presented in Figure III.3.

Figure III.4 shows the results of the simulation with the default parameters (see Table III.1). We observe the successive attacks of oligomers first on the left neuron, then the right neuron. Their monomer production is progressively brought to 0 and after about 20000 s, both of the neurons are completely inactive. The balance between diffusion and replication of the proto-oligomers plays a critical role in the observed dynamics. The spatial distribution of the oligomers is strongly impacted, and their neurotoxic action is also affected. It appears that there is an optimal value for the rate of fragmentation β that induces the fastest neuron inactivation. With extremely high fragmentation rates ($\beta > 5.10^{-3}\ s^{-1}$), the oligomers reach both neurons, but their concentration does not reach sufficiently high levels to completely inactivate them in less than 50000 s, as shown in Figure III.5. With extremely low fragmentation rates ($\beta < 10^{-5}\ s^{-1}$) the proto-oligomer distribution is shifted towards larger, so they diffuse more slowly. In this case, the first neuron is inactivated ef-

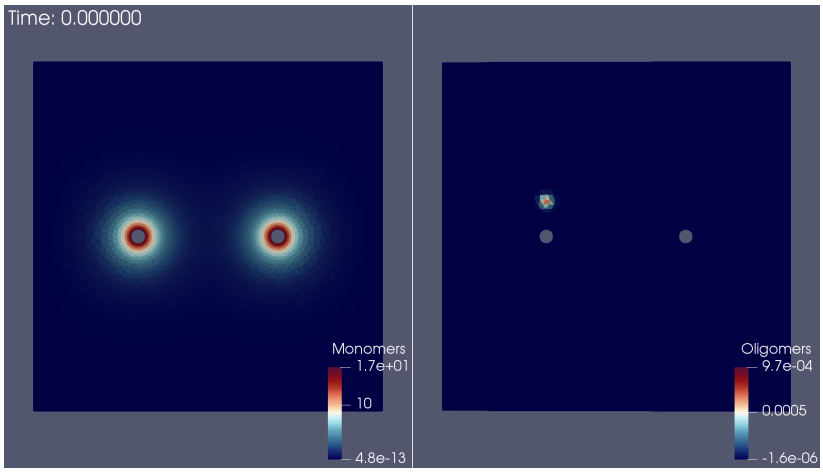

Figure III.3: Initial configuration used for the simulation. Left panel: Aβ monomer distribution. Right panel: Aβ oligomers (of size i_0) distribution.

ficiently enough, but the second is still producing at half the maximum rate after 50000 s, see Figure III.6.

III.4 Conclusion and perspectives

This work has allowed us to build a promising model to study the spatial propagation Aβ oligomers during the early stages of AD. The model is very restrictive, because it focuses on the scale of a few neurons and a few hours. These limitations lead to a simpler model than suggested by previous work [144]. Nevertheless, despite its simplicity, it already exhibits some complex behavior and non-trivial parameter dependence. In particular, the fragmentation rate of proto-oligomers appears to be critical in determining the dynamics of oligomers and their efficiency at inactivating neurons. Further study of this model is planned; first by establishing a theoretical framework (existence, uniqueness, positivity of the solutions), and by extending the simulations to more complex cases, *e.g.* adding more neurons to the domain. Also, investigating thoroughly the influence of the parameters (including, but not limited to, the fragmentation rate), as well as that of the initial conditions. Moreover, including a more detailed description of the neurotoxicity of the oligomers and extending this model to a multi-scale model of the propagation of AD, taking into account fibrils, plaques and macroscopical processes.

III.5 Acknowledgements

We express our thanks to the organizing team of CEMRACS 2018 and SMAI for the opportunity to participate in this event and to start this project. We also thank Human Rezaei (INRA, Jouy-en-Josas) for fruitful discussions and his great help in the choice of the parameters.

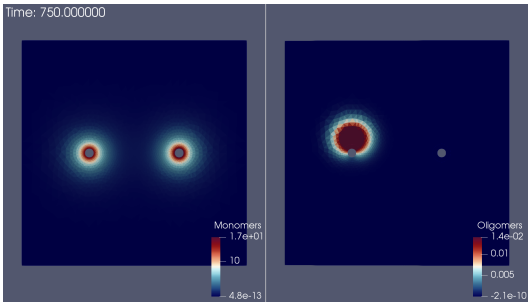

(a) $t = 750\ s$

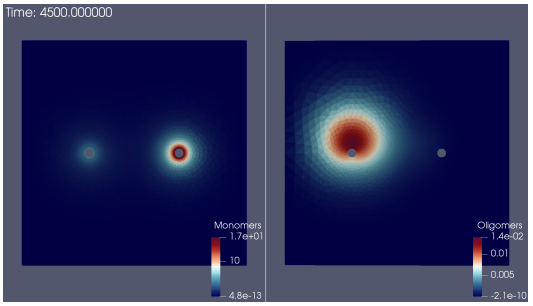

(b) $t = 4500\ s$

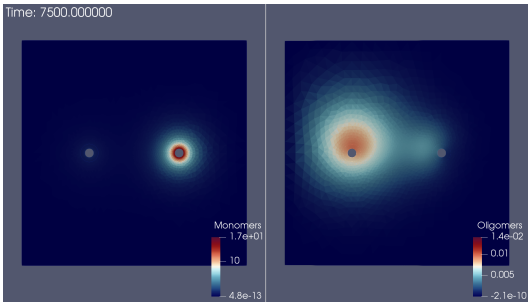

(c) $t = 7500\ s$

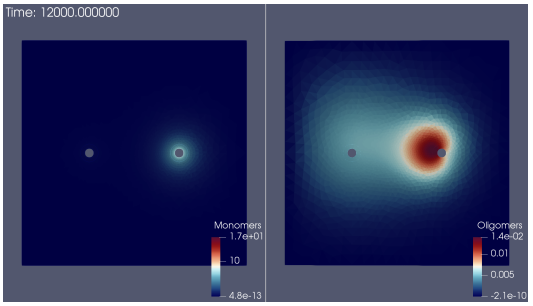

(d) $t = 12000\ s$

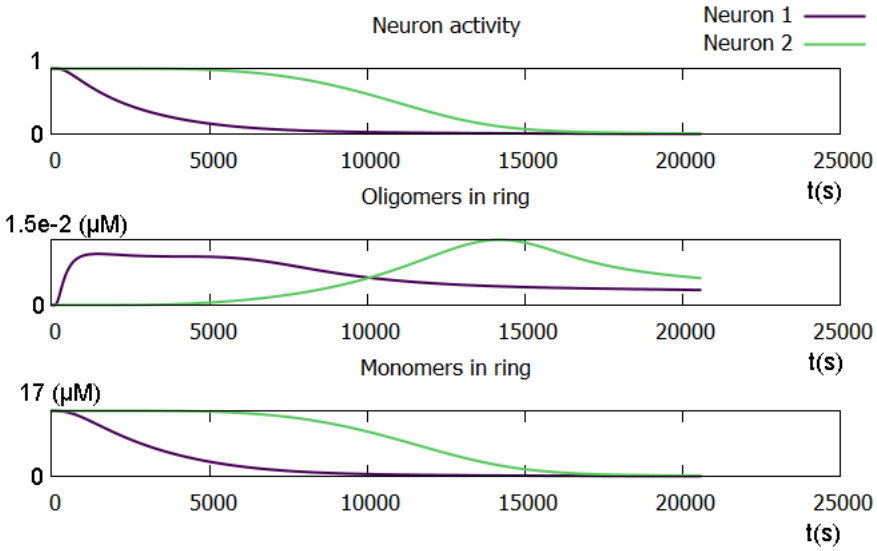

(e) Evolution of monomer production normalized by the maximum λ_0 (top), oligomer concentration in activity ring (middle) and monomer concentration in ring (bottom) for each neuron and over time.

Figure III.4: Simulation results for the default parameters (see Table III.1). For panels (a),(b),(c) and (d), the monomer distribution is on the left, and the oligomer distribution is on the right.

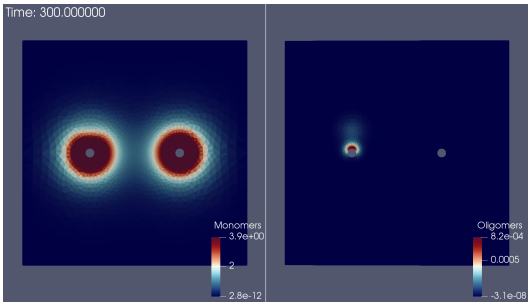

(a) $t = 300\ s$

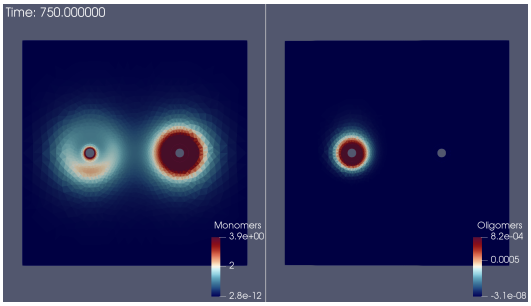

(b) $t = 750\ s$

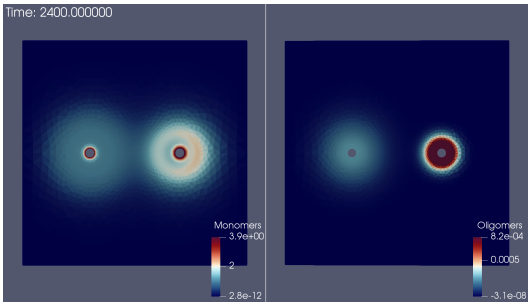

(c) $t = 2400\ s$

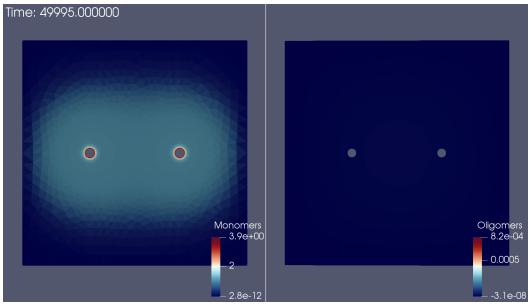

(d) $t = 49995\ s$

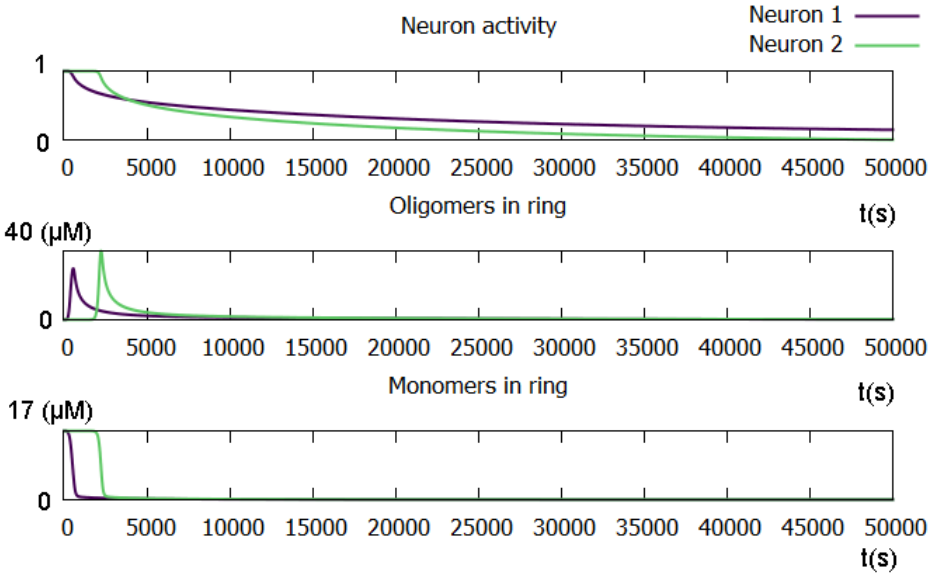

(e) Evolution of monomer production normalized by the maximum λ_0 (top), oligomer concentration in activity ring (middle) and monomer concentration in ring (bottom) for each neuron and over time.

Figure III.5: Simulation results for $\beta = 5.10^{-3}\ s^{-1}$ (see Table III.1 for the other paramters). For panels (a),(b),(c) and (d), the monomer distribution is on the left, and the oligomer distribution is on the right.

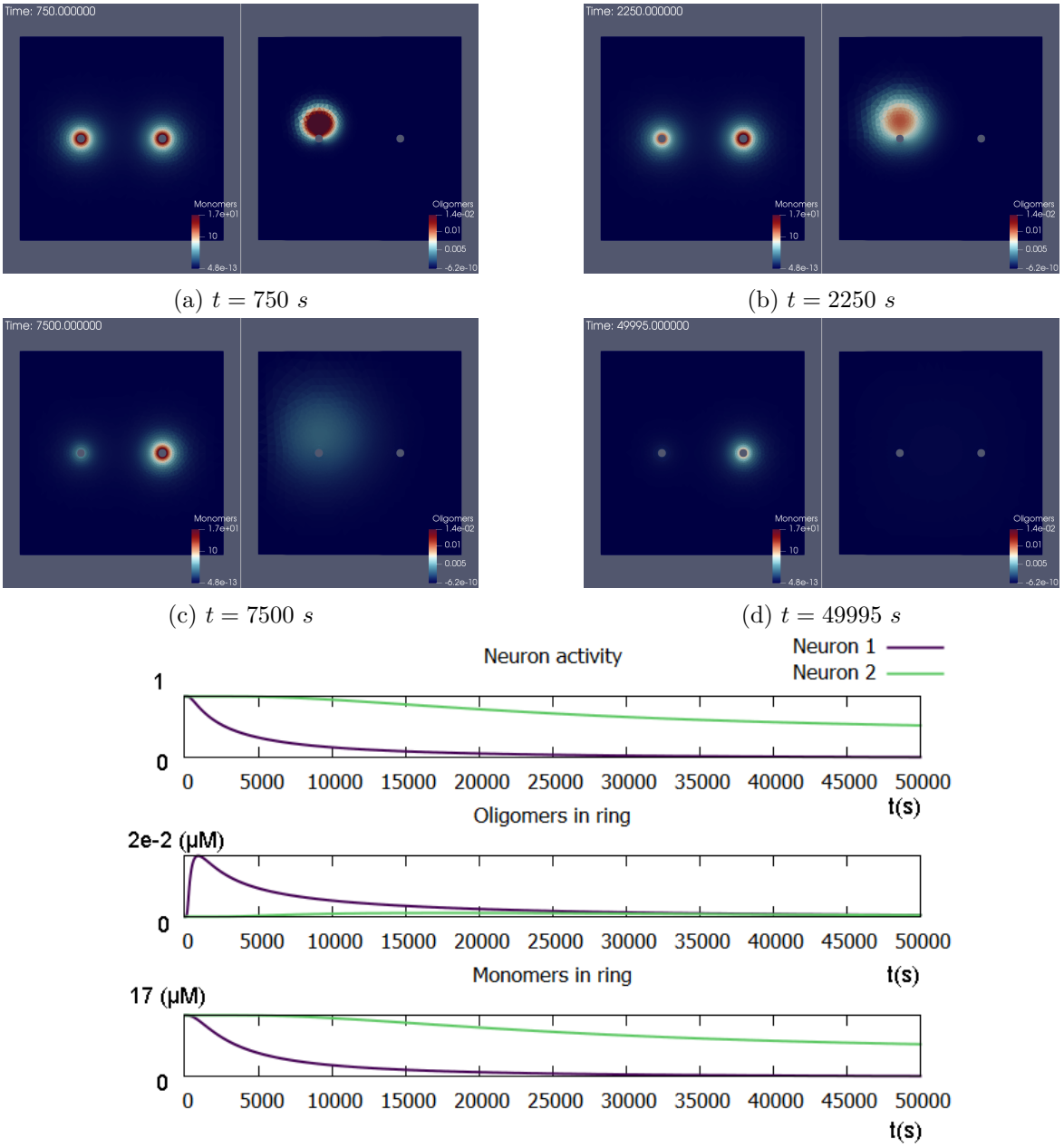

(a) $t = 750\ s$ (b) $t = 2250\ s$

(c) $t = 7500\ s$ (d) $t = 49995\ s$

(e) Evolution of monomer production normalized by the maximum λ_0 (top), oligomer concentration in activity ring (middle) and monomer concentration in ring (bottom) for each neuron and over time.

Figure III.6: Simulation results for $\beta = 1.10^{-5}\ s^{-1}$ (see Table III.1 for the other paramters). For panels (a),(b),(c) and (d), the monomer distribution is on the left, and the oligomer distribution is on the right.

IV – Local Adaptation, Dispersal Evolution, and the Spatial Eco-Evolutionary Dynamics of Invasion

Martín Andrade-Restrepo[1], Nicolas Champagnat[2,3], Régis Ferrière[4,5,6]

[1] Institut Jacques Monod, CNRS UMR 7592,
Université Paris Diderot, Paris Cité Sorbonne, F-750205, Paris, France
[2] IECL, CNRS UMR 7502, Université de Lorraine, Vandœuvre-lès-Nancy, F-54506, France
[3] Inria, TOSCA team, Villers-lès-Nancy, F-54600, France
[4] Institut de Biologie de l'ENS, CNRS UMR 8197, INSERM U 1043, Ecole Normale Supérieure, Paris Sciences & Lettres University
[5] Department of Ecology and Evolutionary Biology, University of Arizona
[6] Interdisciplinary Global Environmental Studies (iGLOBES), CNRS UMI 3157, Ecole Normale Supérieure, Paris Sciences & Lettres University

Abstract

Local adaptation and dispersal evolution are key evolutionary processes shaping the invasion dynamics of populations colonizing new environments. Yet their interaction is largely unresolved. Using a single-species population model along a one-dimensional environmental gradient, we show how local competition and dispersal jointly shape the eco-evolutionary dynamics and speed of invasion. From a focal introduction site, the generic pattern predicted by our model features a temporal transition from wave-like to pulsed invasion. Each regime is driven primarily by local adaptation, while the transition is caused by eco-evolutionary feedbacks mediated by dispersal. The interaction range and cost of dispersal arise as key factors of the duration and speed of each phase. Our results demonstrate that spatial eco-evolutionary feedbacks along environmental gradients can drive strong temporal variation in the rate and structure of population spread, and must be considered to better understand and forecast invasion rates and range dynamics.

Keywords: Spatially structured population, Adaptive evolution, Environmental gradient, Range expansion, Population clustering.

IV.1 Introduction

In the current era of human-mediated climate, landscape and ecosystem changes, the conservation and management of biodiversity makes it crucial to understand what governs the growth and spread of populations colonizing novel environments. To this end, we need quantitative models that describe invasion mechanistically as the outcome of local growth and dispersal [46, 268, 347, 348].

Mechanistic models of invasion are rooted in ecological models of population dynamics in uniform continuous environments, in which invasion patterns are captured by traveling wavefronts moving at constant velocity, or 'invasion speed' [48, 274, 275]. However, the prediction of invasion continuous waves and constant invasion speed does not square with all biological data [273, 349]. Suspected causes of discrepancy include spatial and/or temporal variation in the abiotic environment, environmental and demographic stochasticity, non-Brownian dispersal, Allee effects, and interspecific interactions [49, 50, 269, 270, 350–354]. Here, we examine the hypothesis that rapid local adaptation and dispersal evolution can, through eco-evolutionary feedbacks [156, 158, 161, 355], play a significant role in shaping the dynamics of population expansion and variation in invasion speed.

Rapid evolution has been demonstrated empirically in colonizing populations, including local adaptation to new habitats [356, 357], the evolution of geographic clines along climatic gradients [358, 359], and the evolution of dispersal ability [360, 361]. To investigate the causal role of evolution in population expansion, theory has been developed to address local adaptation on the one hand, and dispersal evolution on the other. In temporally constant environments, quantitative genetics models of local adaptation along environmental gradients [271] predict wave-like patterns of continuous expansion at a constant speed. Given the environmental gradient steepness, dispersal reduces invasion speed due to a negative interaction with local adaptation through gene flow at the expansion edges [362, 363]. This 'standing load' is potentially aggravated by the 'expansion load' created by deleterious alleles 'surfing' at high frequency at the expansion edge [364–366].

Dispersal, however, fuels genetic variation and numerical abundance at the expansion edge [367, 368], thus alleviating some of the maladaptive effects that limit population spread [349, 369–372]. Individual variation in dispersal may also result in the 'spatial sorting' of high-dispersal individuals at the edge of expansion, which can accelerate invasion [276, 373, 374]. The effect of dispersal variation on invasion speed will be further modulated by the individual fitness cost of dispersal [375–378] and the response of dispersal to selection, which is expected to vary from the core to the moving edge of the expansion [379, 380].

Given their multiple and conflicting effects on population expansion, the joint influence of local adaptation and dispersal variation on invasion dynamics remains poorly understood [372, 380]. This raises the need to extend current theory of species' range and invasion dynamics and take into account the reciprocity between ecological processes and evolutionary change [380]. Specifically, we construct an eco-evolutionary model of invasion dynamics that integrate local adaptation with key factors of dispersal evolution [375, 378, 381–383]. Our baseline model is derived from [7] eco-evolutionary model of local adaptation, that

we extend to include the evolution of dispersal. The original model (without dispersal evolution) predicted the long-term population spatial distribution to be of one of two kinds, either continuous, or clustered [7, 228]. Population clustering refers to individuals forming high-density groups interspersed with low density areas [237–241]. Here we examine how the continuous/clustering dichotomy affects the transient regime of population spread. We show that dispersal evolution interacting with local adaptation drives a generic pattern of invasion shaped by both continuous expansion and population clustering. This pattern is also associated with strong temporal variation in invasion speed, with invasion pulses occurring as a consequence of eco-evolutionary feedbacks between local adaptation and dispersal on the invasion front.

IV.2 Materials and Methods

IV.2.1 Models

We use an individual-based stochastic model of spatial eco-evolutionary dynamics which was first introduced in [7]. The model describes a population living on a spatial linear environmental gradient; in its baseline form, only one dimension of space is considered. Each individual is characterized by its physical location x and two quantitative phenotypic traits: a niche position trait along the environmental gradient, u, and a trait measuring individual mobility (or dispersal), w. Individuals give birth asexually at a rate which depends on how adapted they are to their local environment; the difference between the niche position trait and the local optimum measures the degree of maladaptation. We refer to the local optimum as the niche position trait for which the birth rate is highest. With proper rescaling we can assume that this trait value is equal to the geographic coordinate, x. Mobility is modeled as a diffusion (random walk) along the spatial axis of environmental variation. Individuals die at a rate which increases with the intensity of local competition and the cost of dispersal. Offspring inherit their parent's traits, unless a mutation occurs, with constant probability and independently between traits. Mutations are assumed to have small effects, which may alter the niche trait or dispersal. For simplicity, our model assumes equal mutation probability and mutational variance for both traits.

More precisely, the birth rate B of an individual with niche position u at location x, is given by: $B(x,u) = \max\{b_0 - b_1(x-u)^2; 0\}$. The smooth continuous variation of the maximum birth rate along the line $x = u$ represents the environmental gradient. For instance, if the physical axis represents oceanic depth [245], $x > u$ corresponds to individuals with niche position u being adapted to shallower waters than their current depth x. Individual dispersal is measured by $D_m w$, where D_m is the intrinsic (constant) dispersal rate and w is the evolving investment in mobility. The death rate of an individual is given by the sum of a density-independent component, equal to $d_0(1+w)^\theta$ where θ scales the cost of dispersal, and the cumulative (additive) competition effect resulting from interaction with all individuals within a distance δ, the 'interaction range', irrespective of their phenotype.

By taking a large-population limit on the individual-based stochastic model, we obtain the following deterministic approximation, which takes the form of an integro-partial differential equation [7]:

$$\frac{\partial\, n(x,u,w,t)}{\partial\, t} = D_m w \frac{\partial^2\, n(x,u,w,t)}{\partial\, x^2} + n(x,u,w,t)\times \left((1-2\gamma)B(x,u) - d_0(1+w)^\theta - \int_{\mathcal{X}}\int_{\mathcal{U}}\int_{\mathcal{W}} \mathbb{1}_{|x-y|<\delta} n(y,a,b,t)db\ da\ dy\right) + \gamma \int_{\mathcal{U}} n(x,a,w,t)B(x,a)\frac{1}{\sqrt{2\pi}\sigma}\exp\left(-\frac{(u-a)^2}{2\sigma^2}\right)da + \gamma \int_{\mathcal{W}} n(x,u,b,t)B(x,u)\frac{1}{\sqrt{2\pi}\sigma}\exp\left(-\frac{(w-b)^2}{2\sigma^2}\right)db, \tag{IV.1}$$

where (heuristically) $n(x,u,w,t)$ is the density of the population of individuals with niche trait u and dispersal trait w located at x at time t. $\mathcal{U}$, $\mathcal{W}$ and $\mathcal{X}$ denote the ranges of variation of trait u, dispersal w, and location x. Parameters γ and σ^2 are the mutation probability and mutational variance, respectively. In Section IV.5 of the Supporting Information, we provide more details about the individual-based stochastic process (simulation algorithm) and the deterministic model (boundary conditions, numerical solving scheme).

IV.3 Results

The deterministic model provides a good approximation of the invasion dynamics generated by the individual-based stochastic process (Section IV.5.2). In the absence of genetic variation in the niche trait, population expansion is prevented altogether, due to the inability of the species to maintain viable populations in geographic areas where optimal conditions are too different from its original niche (see Section IV.7). With genetic variation in the niche trait, invasion occurs. As anticipated from [228], spatial expansion does not necessarily develop as a continuous wave. Local adaptation can shape invasion through the formation of population clusters (Figs IV.1 and IV.2).

At low dispersal (Figs. IV.1A, IV.2A), population expansion is 'pulled' by clusters forming sequentially, in both spatial and niche trait space, with new clusters adapting gradually to the newly colonized environment (Figs. IV.1A, IV.2E). Each new cluster is seeded predominantly by dispersers from previous outer clusters, at the edge of the distribution. (See Sections IV.6 and IV.10.3 for the effect of interaction range, mutational variance, gradient steepness and spatial spread of the initial population on cluster formation.)

If dispersal is above a 'clustering threshold', invasion proceeds as pushed by an expanding wave (Figs. IV.1B-IV.1C, IV.2B-IV.2C). Edge adaptation to the optimum niche is initially poor and gradually improves (Fig. IV.2F, IV.2G). For dispersal above but close to the clustering threshold, the wave is unstable and the distribution breaks out into clusters (Figs. IV.1B, IV.2B). Here the model shows that it is possible for organisms to invade in continuous waves and yet develop patchy distributions as they spread more broadly.

For dispersal further above the clustering threshold (Figs. IV.1C, IV.2C), wave-like invasion leads to a continuous distribution (Section IV.6), but adaptation lagging behind spatial

spread results in peaks of abundance whose relative position moves during invasion: initially located at the introduction focus, relatively far from the expansion edge (Fig. IV.1C, $T = 40$); then moving progressively towards the edge (Fig. IV.1C, $T = 60, 80$). Thus, peaks of invaders' abundance move outward within the population distribution during expansion, in contrast with non-monotonous waves of invasion with invaders consistently concentrated at the front (*e.g.* [384]).

Finally, for very high dispersal (Figs. IV.1D, IV.2D), colonization of the whole available space is possible, in a wave-like pattern, even without significant local adaptation during the invasion process. Thus, high dispersal from a focal population well adapted to the introduction site makes spatial spread very rapid, even though most of the population remains maladapted during expansion.

Invasion speed can vary dramatically in the course of population expansion. At low dispersal (Figs. IV.2A, IV.2E, IV.2I), there is a first, latent phase of invasion during which the population focus spreads only locally and local maladaptation remains low. This is followed by the first invasion pulse, which corresponds to the establishment and growth of the first cluster; at that point invasion stops (Fig. IV.2I) while the cluster adapts (Fig. IV.2E). As local adaptation increases, the cluster grows locally and generate enough pioneer dispersers to reach areas of low competition, thus triggering the formation of the next cluster. The process of cluster formation repeats itself, and invasion speed fluctuates between a constant high value and zero.

For higher dispersal (Figs. IV.2B, IV.2F, IV.2J and IV.2C, IV.2G, IV.2K), dispersal is responsible for a first phase of rapid invasion, which turns out to be the fastest (Fig. IV.2B, IV.2J and IV.2C, IV.2K). Strong maladaptation at the population edge builds up rapidly during this initial phase (Fig. IV.2F, IV.2G), which causes invasion speed to drop (Fig. IV.2J, IV.2K). Once the population edge is sufficiently adapted, invasion resumes. Invasion speed rapidly reaches a plateau in the case of continuous expansion (Fig. IV.2C, IV.2K) or increases gradually in the case of expanding waves breaking down in clusters. At very high dispersal (Fig. IV.2D, IV.2H, IV.2L), expansion into the whole spatial domain occurs very rapidly; local adaptation is much slower (Fig. IV.2D, IV.2H), and eventually results in the divergence of niche traits toward extreme values (Fig. IV.2D).

We can gain further insights into the cluster formation regime by using a Hamilton-Jacobi approximation approach [41], valid for populations with low dispersal and small mutational variance of the niche trait. We find that the inter-cluster distance is closely approximated by the competition range (Section IV.9.2). Remarkably, clusters influence one another as they grow and adapt. As a new cluster establishes at the edge, adaptation of the previous front cluster slows down (Fig. IV.3, blue curve when red cluster appears). This is due to the fact that the formerly front cluster now receives a flow of locally maladapted dispersers from the core and the (new) edge of the range. When combined with sufficient dispersal, these large scale, inter-cluster effects contribute to fluctuation (and possibly increase) of invasion speed found in the case of a fragmenting expansion wave (Fig. IV.2B, IV.2J). We also note that for not too small dispersal, where cluster formation occurs yet the Hamilton-Jacobi approximation may not apply, multi-stability is possible (Sections IV.6 and IV.8.1). Thus, we expect

some quantitative differences in invasion dynamics resulting from the dynamical uncertainty.

We now turn to the case where niche and dispersal evolve jointly. Increasing the cost of dispersal results in a lower clustering threshold on dispersal (Fig. IV.4). Thus, clustering always occurs, irrespective of the cost of dispersal, provided dispersal is low enough; and in populations experiencing a relatively low cost of dispersal, clustering occurs over a broad range of dispersal rates.

With both niche and dispersal traits evolving, mean dispersal always tends to decrease (Fig. IV.5A-IV.5C). However, if the dispersal rate of ancestral colonizers is far enough (above or below) from the clustering threshold, the selection gradient against dispersal is weak (Fig. IV.5B). Thus, three alternate patterns of spatial expansion and invasion dynamics emerge. If ancestral dispersal is below the clustering threshold, the population expands through cluster formation (Fig. IV.5A, IV.5D, IV.5G, IV.5J). If ancestral dispersal is far above the clustering threshold, the population expands as a continuous wave (Fig. IV.5B, IV.5E, IV.5H, IV.5K). For intermediate dispersal values, the evolution of dispersal drives the population across the clustering threshold, causing the invasion regime to shift from continuous to clustering (Fig. IV.5C, IV.5F, IV.5I, IV.5L). For colonizing populations of highly mobile individuals introduced in a new environment that is sufficiently vast, the latter scenario is expected generically.

A broad range of dispersal trait values evolve in the course of the invasion (Fig. IV.5A-IV.5C). In spite of dispersal being selected against, even at the invasion front (Fig. IV.5G-IV.5I), there is always 'spatial sorting' [374] at the population edge (Fig. IV.5D-IV.5F). In addition, in the case of clustering expansion, mean dispersal and the degree of local (mal)adaptation, both measured in the front cluster, vary through time (Fig. IV.5G, green curve for dispersal, blue curve for local maladaptation). Every time a new cluster forms, mean dispersal reaches a higher value (because of high-dispersal individuals coming from inner clusters further away from the edge) while local maladaptation is reset to a relatively constant level; as the new cluster grows, both mean dispersal and the degree of local maladaptation drop lower than they did in the previous front cluster.

Dramatic variation of invasion speed can occur (Fig. IV.5J, IV.5K, IV.5L). Dispersal evolution driving invasion from wave-like to clustering causes an abrupt shift in invasion speed, from being relatively constant to fluctuating widely (Fig. IV.5L). In the clustering regime of invasion, invasion speed tends to increase between consecutive pulses of expansion (Fig. IV.5J). This means that each new front cluster grows faster than the previous one. This is somewhat unexpected given that mean dispersal in the front cluster increases (Fig. IV.5G, green curve), hence a larger demographic cost, while the level of maladaptation remains about the same across new front clusters (Fig. IV.5G, blue curve). In fact, a new front cluster is a mix of individuals that come potentially from all inner clusters. Those individuals that come from near clusters have relatively low dispersal rates (hence a low cost of dispersal) and are less maladapted as they move up front; their birth rate is therefore relatively high. Every time a new front cluster forms, the former front cluster is less maladapted than the previous one (*cf.* blue curve dropping deeper in Fig. IV.5G). As a consequence, individuals that move from the former front cluster, have higher fitness compared to individuals that made similar moves on a previous event of front cluster formation, hence the increase in invasion speed.

The inclusion of Allee effects does not change the overall pattern: cycles of accelerating-decelerating invasion, existence of a clustering threshold on dispersal, and selection against dispersal that drives a rapid transition from wave-like to clustered invasion (Fig. IV.6, Sections IV.5.3, IV.10.4 and IV.10.5). Allee effects also favor clustering (lower clustering threshold, for any given cost of dispersal). In agreement with existing theory, Allee effects tend to slow down invasion, and in the wave-like regime of population with expansion (Figs. IV.6B), the invading wave is 'pushed' rather than 'pulled'. As a consequence, mean dispersal on the front is lower than in the rest of the range (Figs. IV.6E). In contrast, in the clustering regime of invasion, expansion is pulled by new clusters, where spatial sorting of high-dispersal individuals followed by selection against dispersal occur (Figs. IV.6G), as in the case without Allee effects.

IV.4 Discussion

Local adaptation and dispersal evolution are key evolutionary processes shaping the invasion dynamics of populations colonizing new environments [356, 357, 360, 385, 386]. To resolve their interaction, we use a simple eco-evolutionary model of a single-species population along a one-dimensional resource gradient. The predicted long-term spatial distribution of the population (continuous or clustered) has major consequences on the invasion dynamics. Below a threshold (*clustering threshold*) on the dispersal rate of initial colonizers, invasion develops in pulses, driven by bouts of spatial sorting and local adaptation. For colonizers with dispersal above the threshold, the generic pattern of invasion begins with a phase of acceleration-deceleration, continues as a wave traveling at constant speed, until selection against dispersal drives an abrupt transition into the pulsed regime of invasion. Whereas our model constraints spatial dynamics to one dimension of environmental variation, similar dynamics occur if we unfold a second spatial dimension and let dispersal occur in both directions (Section IV.10.1).

The finding of long-term population spatial distribution being either continuous (for dispersal above a threshold) or clustered (for dispersal below a threshold) is similar to [228], but our model differs in three ways: First, rather than limiting individual mobility to dispersal at birth, we assume that individuals can change location throughout their life. Intuitively, this favors mixing and sets a priori more restrictive conditions for cluster formation. Second, we use competition kernels that are box-shaped rather than Gaussian. This removes spurious effects of Gaussian competition kernels [182, 228, 250, 251]. Third, we exclude fitness frequency-dependence from our assumptions, by assuming that competition intensity does not depend on relative trait values. Even though we define competition with respect to physical location, the interplay between competition with neighbors and local adaptation results in a correlation between physical location and trait, which can lead to fragmentation in both dimensions [228]. Compared to [228], we found a broader range of dispersal and other parameter values for which clustering is expected, which is explained by our stability analysis accounting for perturbations in both space and trait dimensions. Allee effects further enlarge the range of conditions for clustering. Similarly to [228] we find that population clustering is promoted by intermediate gradient steepness. Recent mathematical work backs up the gen-

erality of long-term clustering as an outcome of competition within neighborhoods [387, 388].

Dispersal evolution plays a key role in driving the invasion regime from wave to clusters. In general, dispersal evolution is shaped by a set of costs and benefits (reviewed *e.g.* in [375, 389]). Costs of dispersal include intrinsic costs, and environmentally-mediated costs (how risky movement is, and the fitness loss due to moving away from areas to which the population is adapted or into habitats of low quality). Benefits of dispersal include the potential to found new population where competition is released, avoidance of kin competition, and in sexual organisms, inbreeding avoidance. In temporally constant, spatially heterogeneous environments, dispersal is generally selected against [390–394], unless there are mechanisms to counter the risk of fitness loss due to spatial heterogeneity, such as conditional dispersal [395] or local adaptation [396, 397]. The organisms' life cycle is also a strong influence of selection on dispersal; evolution of dispersal in the adult stage (as in our model) generally involves more stringent conditions on environmental structure and variation [398].

Costs and benefits of dispersal can vary across a species' range, and may be particularly large at the range margins, where dispersers can reach previously unoccupied areas but face Allee effects and genetic drift [364, 368, 379]. Previous theory has explored the evolution of dispersal as a population expands across a spatially homogeneous environment (*e.g.* [399, 400]) or across an environmental gradient [401]. How selection acts on dispersal during periods of range expansion can be very different from selection on dispersal in stationary populations [400]. On an expanding front, dispersal may be strongly favored because of spatial sorting and selection [374, 399, 402], despite spatial heterogeneity acting against dispersal on average across the range [400, 403]. Spatial sorting refers to the fact that the best dispersers tend to be disproportionately represented on the population front; competition release experienced by these individuals may result in larger reproductive success, hence selection for increased dispersal.

In addition to spatial sorting and selection, kin competition may also be a strong agent of selection on dispersal at the population front, because founder effects driving invasion result in locally high relatedness [404, 405]. For invasion occurring along spatial gradients of resources, kin selection for dispersal may counter the cost of maladaptation incurred by dispersers [396, 406]. [397] analysis suggests that the balance of kin selection and maladaptation is determined by the strength of intraspecific competition and the intrinsic cost of dispersal (which influence local population size), and the gradient steepness (which influences the spatial variance in selection on resource use).

In our model, several selective agents act against dispersal: the intrinsic mortality cost; spatial heterogeneity manifested in the gradient of resources, and enhanced by population self-structuring when dispersal is close to or below the clustering threshold; and the cost of maladaptation. Selection against dispersal is particularly strong around the clustering threshold. If the ancestral phenotype is above the threshold, the eco-evolutionary feedback on dispersal can drive a macroscopic transition from wave-like to pulsed invasion: as spatial population heterogeneity develops when dispersal becomes sufficiently close to the threshold, selection against dispersal intensifies; lower dispersal enhances spatial variation in population density, thus selecting even more strongly against dispersal, which eventually crosses

the clustering threshold.

We found that spatial sorting generally occurs, but not spatial selection. High-dispersal individuals tend to be assorted at the range margin (front cluster or wave front), but the benefit of low density (reduced competition) and kin selection appear to be too weak to counter maladaptation, resulting in selection against dispersal ('suppressed spatial selection' [407]). In the wave-like invasion regime, suppressed spatial selection leads to invasion occurring at constant speed (past the initial phase of acceleration-deceleration), rather than accelerating [408].

In the clustered invasion regime, the consequences of suppressed spatial selection for invasion dynamics are germane to the phenomenon of 'elastic' range expansion [368, 401], whereby a population invasion progresses in alternating bouts of expansion and contraction. In our model of clustered invasion, the rapid formation of new front clusters by spatial sorting is followed by a phase of local adaptation and selection against dispersal within clusters. This results in a dynamical pattern of alternating range expansion and pause, rather than contraction. In addition, the speed of expansion bouts tend to increase, reflecting the more rapid growth of newly formed clusters. The accelerating growth of new clusters is driven by a positive feedback with local adaptation in the 'source' clusters: colonizers will be less maladapted to their new location on the invasion front, and therefore establish faster-growing populations that will send even less maladapted individuals to form the next front cluster.

Data-model fitting and model selection for the cane toads case [360, 408] has provided strong support for spatial selection on dispersal causing an accelerating invasion [407]. However, the scope of the mechanism remains to be determined. Mathematical analyses of 'cane toad equations' have assumed homogeneous environments, no cost of dispersal, and 'point local' competition [276, 409], which limits their relevance to real systems. Fitness costs of dispersal [377] influence the dynamics of range expansion ([376]; this work), as the form and spatial structure of density regulation does too ([410]; this work). Recent experimental work on laboratory systems sought out to evaluate the effect of spatial evolutionary processes on invasion [277, 384, 411, 412]. For populations exposed to a novel environment, [277] showed that expansion and invasion speed were strongly influenced by local adaptation, whereas spatial evolutionary processes acting at the edge contributed less, which is consistent with our predictions. Specific predictions from our model, such as changes in expansion regime and concurrent variation in invasion speed, could be tested by setting up microcosm experiments on environmental gradients and artificially varying interaction range and gradient steepness.

From a genetic point of view, range expansion usually leads to decreasing genetic diversity, either affecting adaptation [413] or dispersal [414]. The dynamics of genetic diversity at the margins of an expanding range can differ markedly between pulled *vs.* pushed waves [415, 416]. In pulled waves, competition is relaxed on the front, where 'pioneer' individuals filtered by spatial sorting can establish growing populations. Thus, the wave travels through recurrent founding events, and genetic diversity is consistently low on the front. With Allee effects, pioneer individuals are less likely to establish front populations that pull the wave; instead the wave is pushed by the growth of populations at the back of the front, and no genetic diversity is lost on the front [415]. In our model, the same effect is predicted in the

case of wave-like invasion (Fig. IV.5B, E; Fig. IV.6E). The model predictions differ when clustering occurs. In this case, invasion is pulled by new clusters even when Allee effects operate (Fig. IV.6A, D, G). In contrast, Allee effects prevent new clusters to form from the population low-density 'nose' ahead of the core even though competition is relaxed. Instead, new clusters must form through spatial sorting of high-dispersal individuals, causing a founder effect. Thus genetic diversity is reduced, but eventually rebuilds by mutation, which fuels local adaptation of the newly formed cluster. How fast genetic variance of both dispersal and niche traits builds up depends on the mutation rates, which thus appear as key parameters of the invasion dynamics in the clustering regime.

IV.4.1 Conclusions

In contrast with long-standing theory predicting that, under a wide range of conditions, a population will asymptotically spread with a constant velocity [48, 274], there has been growing empirical evidence that invasion speed can be variable [412, 417–420]. Empirical studies often attributed temporal variation in invasion speed to differences in the environments encountered by the invading population [273, 421], while models pointed to potential endogenous factors, such as demographic stoshasticity causing time lags in population expansion [422–424], and long-distance dispersal [425, 426] or Allee effects [351, 352, 417, 427] driving pulsed invasion.

Our model offers an alternate mechanism for lags in expansion and pulsed invasion, based on the interaction of dispersal evolution and local adaptation along an environmental resource gradient. For dispersal below the clustering threshold, invasion accelerates when high-dispersal individuals are spatially sorted on the population front, and pauses as the front clusters adapts to the newly colonized habitat. Selection driving dispersal across the clustering threshold will cause an abrupt transition from wave-like invasion at constant speed to the clustering regime of pulsed invasion. The interaction range, cost of dispersal, and genetic variance of niche and dispersal traits, thus arise as key factors of the dynamics of invasion, in addition to gradient steepness [228, 372].

How often and to what extent do eco-evolutionary processes affect invasion dynamics in nature, given the pervasive influences of environmental heterogeneity and demographic stochasticity and their roles in invasion variability? To begin to answer this question, we suggest that coupling models and empirical data, as was done in [407], is a promising approach. The power of model-data integration will be enhanced by further theoretical developments to address other important factors of population spread, including resource-consumer interactions [380, 384, 428], conditional dispersal [49, 50, 400, 429], and selection on multiple life-history traits [376, 407, 430].

Competing interests

We declare we have no competing interests.

Acknowledgments

We thank four anonymous reviewers for their insightful comments that greatly improved the manuscript, and Feng Gao for discussion and comments on an initial version of the manuscript.

Martin Andrade Restrepo is grateful to Khashayar Pakdaman, the CNRS, and the Administrative Department of Science, Technology and Innovation of Colombia *Colciencias* for advice and support.

Nicolas Champagnat benefited from the support of the Chair "Modélisation Mathématique et Biodiversité" of Veolia Environnement - École Polytechnique - Muséum National d'Histoire Naturelle - Fondation X and from the support of the French National Research Agency for the project ANR-14-CE25-0013, "Propagation phenomena and nonlocal equations" (ANR NONLOCAL).

Regis Ferriere acknowledges support from FACE *Partner University Fund*, CNRS *Mission pour l'Interdisciplinarité*, LabEx MemoLife, PSL University (IRIS OCAV and PSL-University of Arizona Mobility Program), and NSF *Dimensions of Biodiversity* (DEB-1831493).

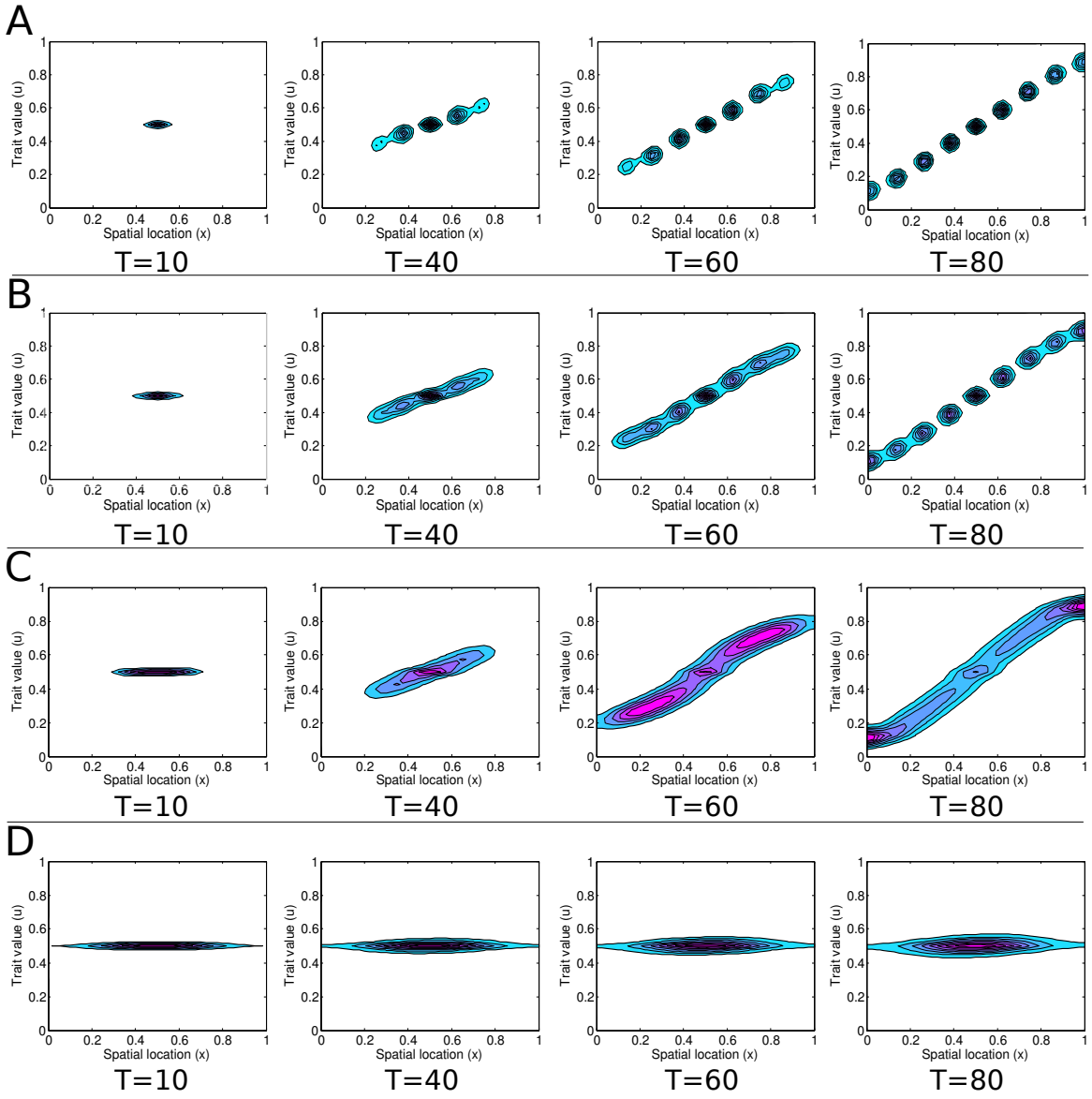

Figure IV.1: Spatial eco-evolutionary dynamics of invasion with local adaptation and constant dispersal. Time-evolution of the population distribution. A. $D_m = 5 \times 10^{-5}$. B. $D_m = 8 \times 10^{-5}$. C. $D_m = 5 \times 10^{-4}$. D. $D_m = 2 \times 10^{-2}$. At $T = 0$ the distribution is Gaussian with standard deviation $\sigma_0 = 0.1$ (in both dimensions) centered at $(0.5, 0.5)$. Large-population model given by Eq. (IV.3), parameters set to the default clustering values in Table IV.2. In all panels cyan represents the lowest density and magenta the highest. Density is negligible in white areas.

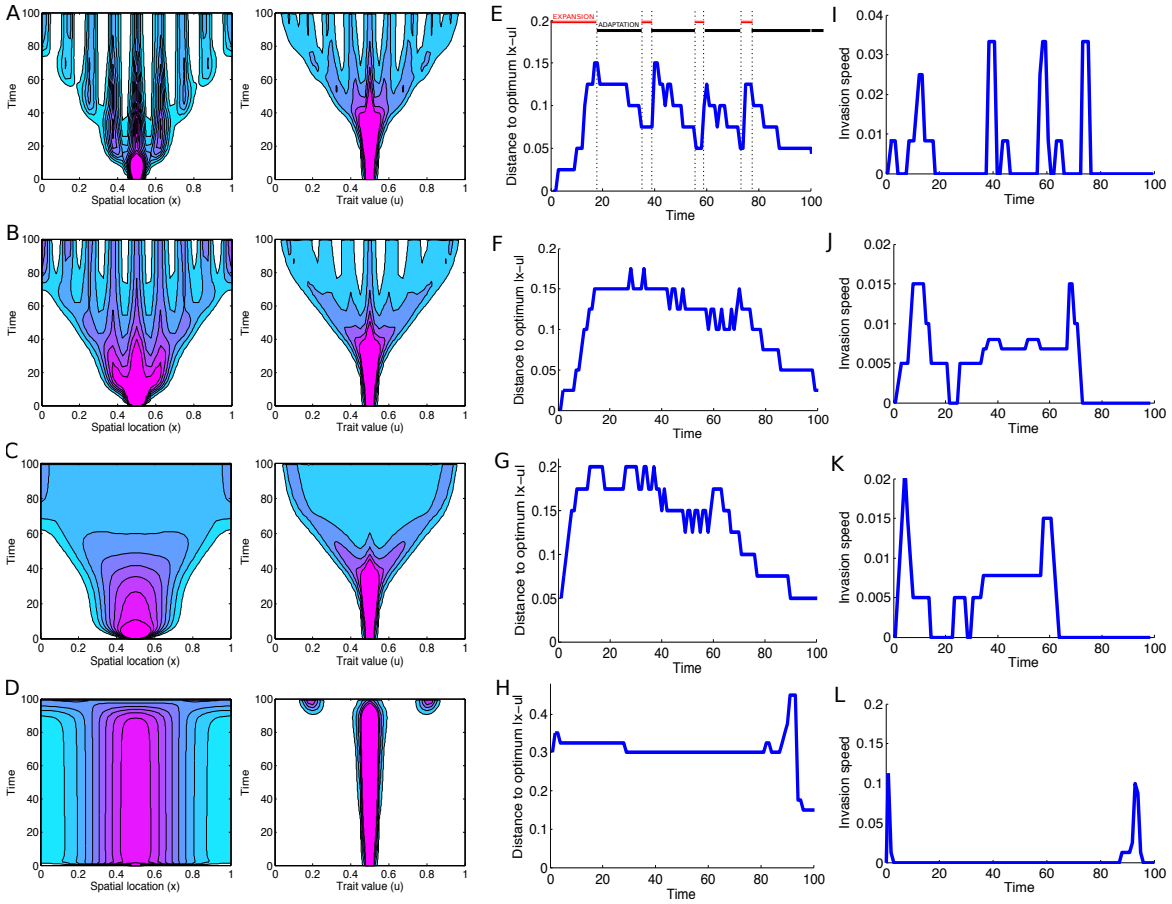

Figure IV.2: Spatial eco-evolutionary dynamics of invasion with local adaptation and constant dispersal. Time-evolution of spatial and niche-trait distributions for $D_m = 5 \times 10^{-5}$ (Panel A), $D_m = 8 \times 10^{-5}$ (Panel B), $D_m = 5 \times 10^{-4}$ (Panel C), $D_m = 2 \times 10^{-2}$ (Panel D). Time-evolution of local maladaptation, measured by the distance between the local optimum and physical location ($|x - u|$) at the population front for $D_m = 5 \times 10^{-5}$ (Panel E), $D_m = 8 \times 10^{-5}$ (Panel F), $D_m = 5 \times 10^{-4}$ (Panel G), $D_m = 2 \times 10^{-2}$ (Panel H). Front invasion speed for $D_m = 5 \times 10^{-5}$ (Panel I), $D_m = 8 \times 10^{-5}$ (Panel J) , $D_m = 5 \times 10^{-4}$ (Panel K) , $D_m = 2 \times 10^{-2}$ (Panel L). At $T = 0$ the population distribution is Gaussian with standard deviation $\sigma_0 = 0.1$ (in both dimensions) centered at $(0.5, 0.5)$. Large-population model given by Eq. (IV.3), other parameters set to the default clustering values in Table IV.2. In all panels cyan represents the lowest density and magenta the highest. Density is negligible in white areas.

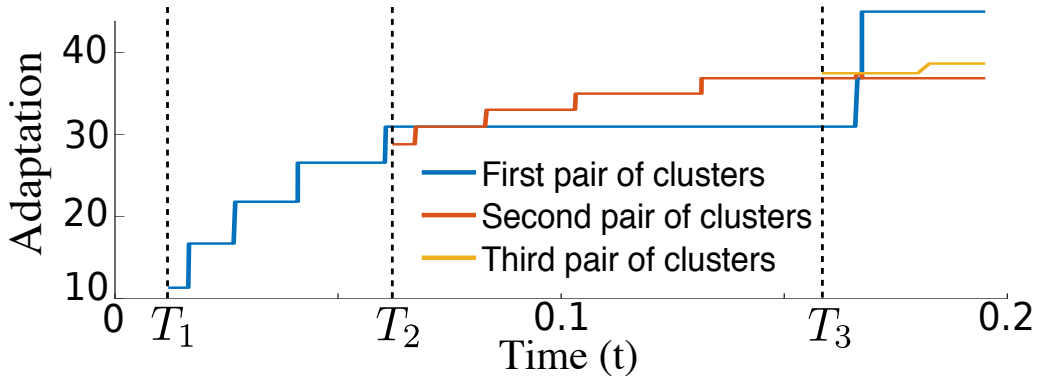

Figure IV.3: Spatial eco-evolutionary dynamics of invasion with local adaptation and constant dispersal: dynamics of cluster emergence and adaptation. Simulation based on the Hamilton-Jacobi equation Eq. (IV.15). Time-evolution of adaptation, measured by angular degree between the cluster alignment and gradient (cf. Fig IV.21). T_i, $i = 1, 2, 3$, indicate times at which new clusters emerge. Parameters set to the default clustering values in Table IV.2.

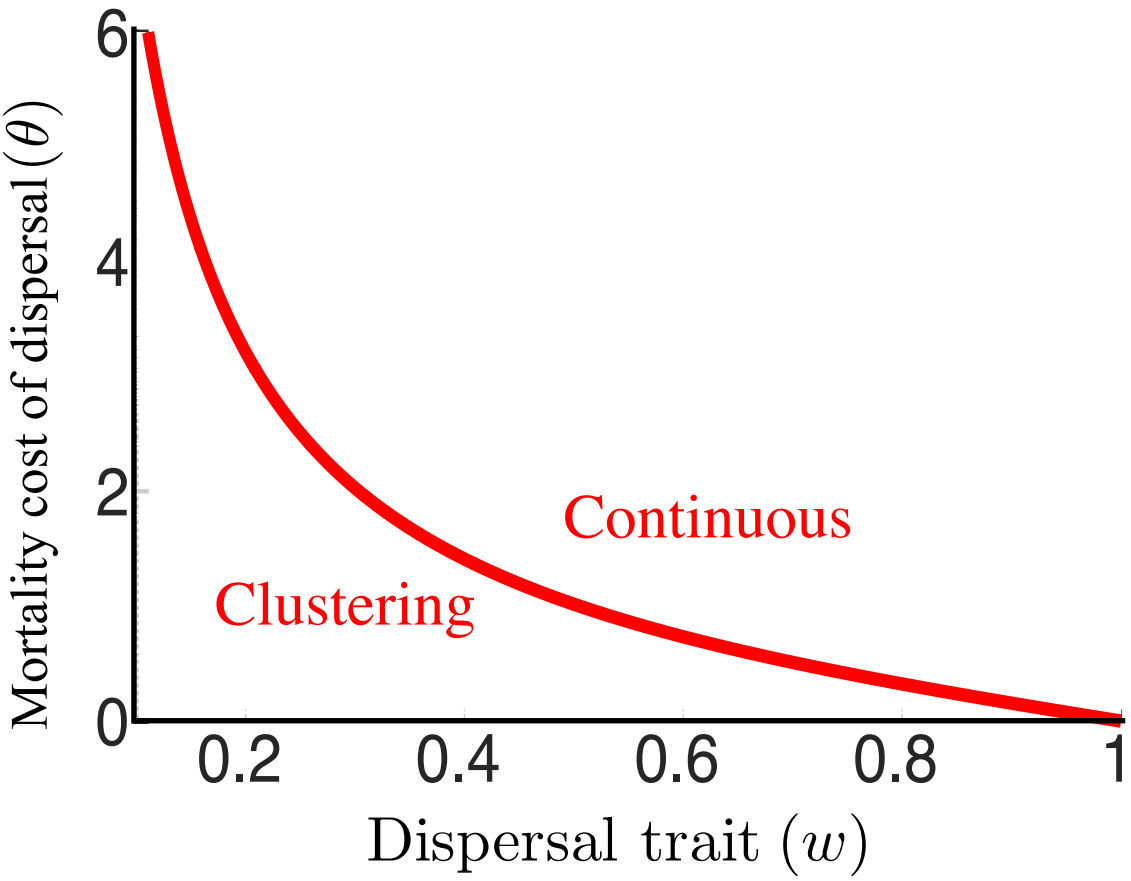

Figure IV.4: Influence of dispersal value and cost on long-term spatial population structure. The bifurcation line between clustering and continuous spread is computed as the zero contour of the Lyapunov exponent given by Eq. (IV.7). Large-population model given by Eq. (IV.1). Other parameter values are set to the default parameter values in Table IV.1.

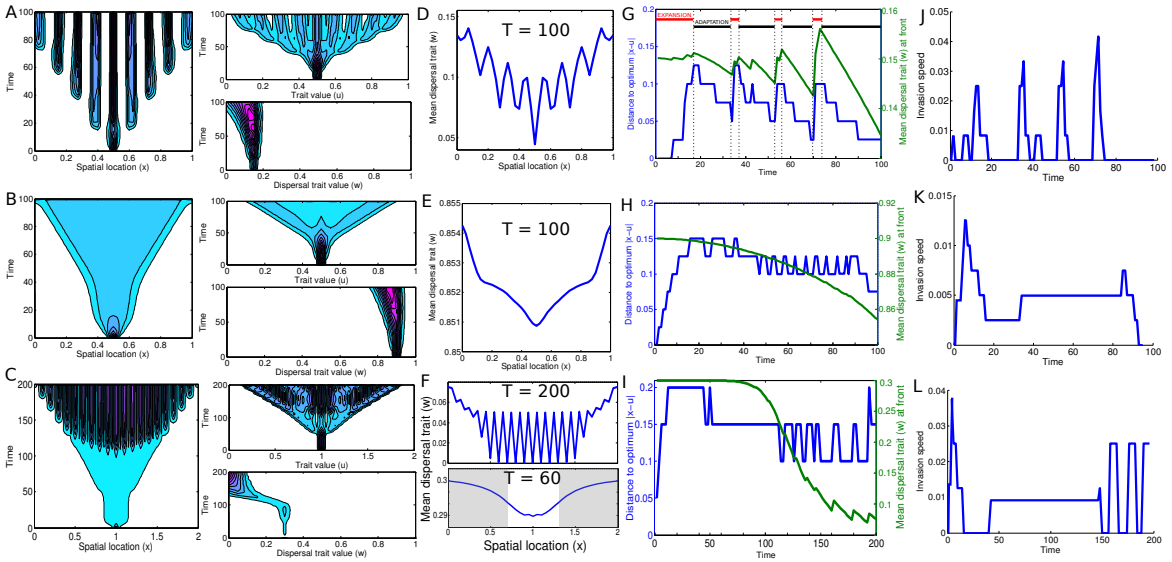

Figure IV.5: Spatial eco-evolutionary dynamics of invasion with local adaptation and evolving dispersal. (A-C) Time-evolution of spatial, niche-trait and dispersal-trait distributions. (D-F) Local mean dispersal as a function of spatial location. (G-I) Time-evolution of local maladaptation at the population front, measured by the distance between the local optimum and physical location ($|x - u|$), and mean dispersal at the population front. (J-L) Time-evolution of invasion speed. Large-population model given by Eq. (IV.1). At $T = 0$ the population distribution is Gaussian with standard deviation $\sigma_0 = 0.1$ (in the three dimensions) centered at $(0.5, 0.5, w_0)$. Parameter values: $w_0 = 0.15$ and $\theta = 0.75$ in A, D, G, J; $w_0 = 0.9$ and $\theta = 0.75$ in B, E, H, K; $w_0 = 0.3$ and $\theta = 1.75$ in C, F, I, L. Other parameters set to the default values in Table IV.1. In Panels A,B and C, cyan represents the lowest density and magenta the highest. Density is negligible in white areas.

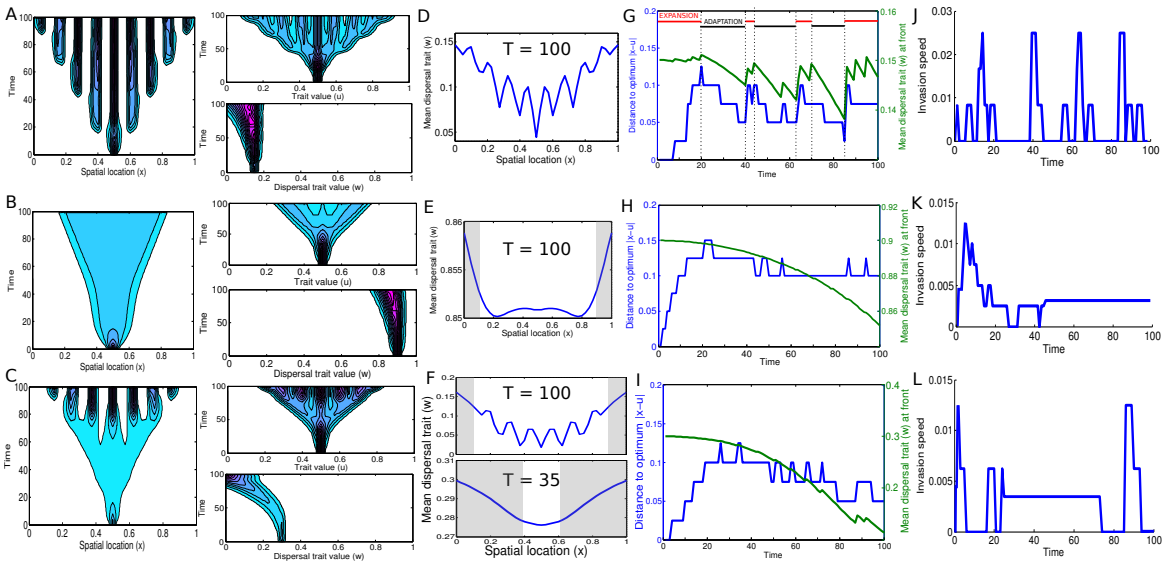

Figure IV.6: Spatial eco-evolutionary dynamics of invasion with local adaptation, evolving dispersal, and Allee effect (Section IV.5.3). Large-population model given by Eq. (IV.1). See Fig. IV.5 for panel labeling and other details.

Supporting Information

IV.5 Stochastic model and large-population approximation

We use an individual-based stochastic model of spatial eco-evolutionary dynamics which extends a model first introduced in [7] to include evolving dispersal. We then take a large-population limit (as in [7]), to derive the deterministic model in Eq. (IV.1).

IV.5.1 Individual-based stochastic model with evolving dispersal

Given three smooth domains (open, connected) $\mathcal{X} \subseteq \mathbb{R}^d$ (spatial domain), $\mathcal{U} \subseteq \mathbb{R}^k$ (first phenotypic domain) and $\mathcal{W} \subseteq \mathbb{R}^l$ (second phenotypic domain), we consider an asexual population where each individual is characterized by its physical location $x \in \overline{\mathcal{X}}$ and its two phenotypic traits $u \in \mathcal{U}$ and $w \in \mathcal{W}$. The first trait relates to the individual's niche and the second trait to dispersal. Individuals give birth at a rate which depends on how adapted they are to their local environment; the degree of (mal)adaptation is measured by the difference between the individual niche trait and the local optimum. Individuals die at a rate which increases with the intensity of local competition and with higher dispersal. Offspring inherit their parent's traits, unless a mutation occurs (independently on each trait); the mutation probability is denoted by γ and is assumed to be equal in both traits. Individuals' mobility is modeled as spatial diffusion (with diffusion coefficients dependent on the dispersal-related trait) reflected at the boundary of $\mathcal{X}$. Unless specified otherwise, we take $\mathcal{X} = \mathcal{U} = \mathcal{W} = (0, 1)$.

More precisely, the birth rate B of an individual with niche trait u and dispersal trait w located at position x is given by

$$B(x, u) = \max\left\{b_0 - b_1(x - u)^2; 0\right\},$$

where $b_0 > 0$ and $b_1 > 0$. The smooth continuous variation of the optimum along the line $x = u$ represents the environmental gradient. The death rate of an individual at (x, u, w) in a population of N_t individuals at positions $x_1, \ldots, x_{N_t}$ and traits $u_1, \ldots, u_{N_t}$, $w_1, \ldots, w_{N_t}$ is given by

$$d_0(1 + w)^\theta + d_1 \sum_{i=1}^{N_t} \mathbb{1}_{|x - x_i| < \delta},$$

where d_0 measures the minimal natural death rate, θ determines the degree of increased mortality of higher mobility and d_1 scales the mortality effect of competition. Applying the appropriate time-scaling, we assume $d_1 = 1$ without loss of generality.

The distribution of mutational effects on the niche trait from an individual at position (x, u, w) is Gaussian centered at u (and independent of x) with variance σ^2, conditioned to remain within $\mathcal{U} = (0, 1)$. The same occurs for mutational effects on the dispersal trait w. The spatial diffusion coefficient (mobility rate) has value $D_m(w)$.

The algorithm used to simulate the individual-based model is based on [7]. Nevertheless, we use a slightly different acceptance/rejection procedure in order to avoid costly numerical

computations of the exact jump rates in the process. This procedure consists on simulating more frequent potential jump times and then deciding whether the jumps actually occur at these times based on a given probability. This implies the probabilities of births or deaths do not sum up to 1 since the complementary probability is that of a rejection of the potential jump time (i.e. no jump occurs). We proceed as in this reference by constructing recursively sequences N_k, T_k, X_k, U_k, W_k respectively of integers, positive real numbers, N_k-dimensional vectors in $\bar{\mathcal{X}}$ and N_k-dimensional vectors in $\mathcal{U}$ and in $\mathcal{W}$, which represent respectively the number of individual in the k-th step of the algorithm, the end time of the k-th step and the vectors of positions and ecological (niche) and dispersal traits of the N_k living individuals at the end of the k-th step. We set the potential event rate to $C_{tot} := N_{k-1}(b_0 + 2d_0 + N_{k-1}/K)$ (K being the carrying capacity) and then decide, based on a parameter θ_k (a uniformly distributed random variable on $[0, C_{tot}]$), which event can potentially occur at time $T_k = T_{k-1} + E_{k-1}$, where E_{k-1} is an exponential random variable with parameter C_{tot}. If $\theta_k < N_{k-1}b_0$, we randomly select an individual $I_k = i$, which will give birth (to a clone or a mutant) with probability $\frac{B(X^i_{T_k}, U^i_{T_k-1})}{b_0}$. If, instead, $N_{k-1}b_0 \leq \theta_k \leq N_{k-1}b_0 + 2N_{k-1}d_0$, a randomly selected individual $I_k = i$ will die with probability $\frac{d_0(1+W^i_{T_k-1})^2}{2d_0}$ no matter its position and niche trait (since the rate of natural death only depends on the dispersal-related trait). Finally, if $\theta \geq N_{k-1}b_0 + 2N_{k-1}d_0$, two individuals $I_k = i$, $J_k = j$ are selected randomly. If the distance among them at time T_k is smaller than δ, then individual i dies. Otherwise nothing happens.

IV.5.2 Large-population approximation model

Taking a large-population limit on the individual-based simulation model yields the following deterministic approximation [7]:

$$
\begin{aligned}
\frac{\partial\, n(x,u,w,t)}{\partial\, t} = {} & D_m(w)\frac{\partial^2\, n(x,u,w,t)}{\partial\, x^2} + n(x,u,w,t)\times \\
& \left((1-\gamma)^2 B(x,u) - d_0(1+w)^\theta - \int_{\mathcal{X}}\int_{\mathcal{U}}\int_{\mathcal{W}} \mathbb{1}_{|x-y|<\delta} n(y,a,b,t)db\ da\ dy\right) \\
& + \gamma \int_{\mathcal{U}} n(x,a,w,t)B(x,a)\frac{1}{\sqrt{2\pi}\sigma}\exp\left(-\frac{(u-a)^2}{2\sigma^2}\right)da \\
& + \gamma \int_{\mathcal{W}} n(x,u,b,t)B(x,u)\frac{1}{\sqrt{2\pi}\sigma}\exp\left(-\frac{(w-b)^2}{2\sigma^2}\right)db \\
& + \gamma^2 \int_{\mathcal{U}}\int_{\mathcal{W}} n(x,a,b,t)B(x,a)\frac{1}{\sqrt{2\pi}\sigma}\exp\left(-\frac{(w-b)^2}{2\sigma^2}\right)\frac{1}{\sqrt{2\pi}\sigma}\exp\left(-\frac{(u-a)^2}{2\sigma^2}\right)db\ da,
\end{aligned}
\tag{IV.2}
$$

$$
\begin{aligned}
&\left.\frac{\partial\, n(x,u,w,t)}{\partial\, x}\right|_{x=0} = \left.\frac{\partial n(x,u,w,t)}{\partial x}\right|_{x=1} = 0, \\
&n(x,0,w,t) = n(x,1,w,t) = 0, \quad x \in \overline{\mathcal{X}}, w \in \mathcal{W} \quad t \geq 0, \\
&n(x,u,0,t) = n(x,u,1,t) = 0, \quad x \in \overline{\mathcal{X}}, u \in \mathcal{U} \quad t \geq 0.
\end{aligned}
$$

where

$$B(x,u) = \max\{b_0 - b_1(x-u)^2, 0\}.$$

Note that the Neumann boundary condition in physical space corresponds to reflection of spatial motion at the boundary of $\mathcal{X}$, and the Dirichlet boundary condition in phenotype space indicates that individuals die when their trait exits from $\mathcal{U}$ or $\mathcal{W}$.

To understand the death by competition term in Eq. (IV.2), it is convenient to introduce the population counting process from the stochastic individual-based model:

$$f_t = \sum_{j=1}^{N_t} \delta_{(x_j,u_j,w_j)}$$

which is the sum of Dirac delta functions at the points where individuals are located at time t. The death rate for the individual-based-model can then be written as

$$D(x,u,w,f_t) := d_0(1+w)^\theta + \int_{\mathcal{X}\times\mathcal{U}\times\mathcal{W}} \mathbb{1}_{|x-y|<\delta} f_t(dy,da,db).$$

The approximation of the individual-based model by Equation (IV.2) can be formally justified in the limit of large population as follows: when assuming a fixed amount of total resources, a large system composed of the order of N individuals may be sustained if the biomass of each individual scales as $\frac{1}{N}$; the intensity of competition must scale as $\frac{1}{N}$ as well. Using the martingale properties of the individual-level stochastic process, [7] proved that in the limit of large N the renormalized population process converges to a macroscopic deterministic limit, in which the local population density is a weak solution to Eq. (IV.2).

To simulate the dynamics of the infinite population-size limit of the model we compute $n(x,u,w,t)$ according to Eq. (IV.2) using an explicit scheme where $n(x,u,w,0)$ has the form of a Gaussian centered at $(0.5, 0.5, w_0)$ with standard deviation σ_0 (in each dimension). We use Euler's method with a step size $\Delta_x = \Delta_u = \Delta_w = 2.5 \times 10^{-2}$ and a time-step size $\Delta_t = 1 \times 10^{-3}$. For numerical purposes we assume that the last term in Eq. (IV.2) (the event of a double mutation) is equal to zero since mutations on niche position or dispersal occur independently and are rare. This changes the proportion of births without mutations from $(1-\gamma)^2$ to $(1-2\gamma)$.

To calculate the invasion speed we compute the (spatial) time derivative (using Euler's method) of the location of the front. We compute the spatial location and niche trait of the front as the extreme values $x_{\min}$ and $x_{\max}$ and $u_{\min}$ and $u_{\max}$ (lowest and highest x and u) where the cumulative density over $\mathcal{W}$ satisfies the condition:

$$n_{x,u}(x,u,t) := \int_{\mathcal{W}} n(x,u,w,t)\, dw \;\geq 0.5 \times \max_{x\in\mathcal{X},u\in\mathcal{U}} n_{x,u}(x,u,t), \quad t \geq 0.$$

When the front has been computed we also calculate the difference ($|x-u|$) as $|x_{\max} - u_{\max}|$. Due to the symmetry in the initial conditions, this is the same as computing $|x_{\min} - u_{\min}|$.

IV.5.3 Inclusion of Allee effects

We extend our model to include Allee effects. Local adaptation (u compared to x) determines the reproductive potential of an individual, and nearby density (of identical or of all phenotypes) determines whether this potential is realized or not.
More precisely,

$$B(x,u,n) = \max\left\{(b_0 - b_1(x-u)^2) \times \frac{\int_{\mathcal{X}} \mathbb{1}_{|x-y|<\delta} \times n(y,u,t)dy}{c_1 + \int_{\mathcal{X}} \mathbb{1}_{|x-y|<\delta} \times n(y,u,t)dy}; 0\right\},$$

where the range of interaction (of distance δ) with nearby neighbors is the same as in the death-by-competition term. The parameter $c_1 \geq 0$ scales the impact Allee effects have on local reproduction. If c_1 is too large the population goes extinct. If c_1 is too small the results of the variant resemble from those of model in Section IV.5.1. If c_1 is intermediate, when the density of neighbor individuals is low, the birth rate is close to zero and the reproductive potential is hardly expressed. When density is high, the ratio in birth rate is close to 1, and the reproductive potential is realized fully.

We also consider the case where:

$$B(x,u,n) = \max\left\{(b_0 - b_1(x-u)^2) \times \frac{\int_{\mathcal{X}}\int_{\mathcal{U}} \mathbb{1}_{|x-y|<\delta} \times n(y,w,t)dw\ dy}{c_2 + \int_{\mathcal{X}}\int_{\mathcal{U}} \mathbb{1}_{|x-y|<\delta} \times n(y,w,t)dw\ dy}; 0\right\}.$$

but find that results are equivalent after appropriate re-scalings of the parameters c_1 and c_2 ($c_1 \simeq c_2^2$).

IV.5.4 Model parameters and values

The parameters of the model and their description, together with the default values are presented in Table IV.1. The value of D_m is the threshold value at which the clustering pattern loses stability in the model with no dispersal evolution and other parameters set to the default values in Table IV.2.

Parameter	Description	Default value
b_0	Maximal birth rate	$b_0 = 2$
c_1	Scaling of Allee effects from identical individuals	$c_1 = 1 \times 10^{-4}$
c_2	Scaling of Allee effects from all individuals	$c_2 = 1 \times 10^{-2}$
b_1	Quadratic coefficient in the rate of decay in the birth rate	$b_1 = 20$
d_0	Minimal natural death rate	$d_0 = 1$
θ	Degree of mortality cost of dispersal	$\theta = 0.75$
D_m	Spatial diffusion constant	$D_m = 1.62 \times 10^{-4}$
δ	Spatial competition range	$\delta = 0.1$
σ	Standard deviation of mutation transition measure	$\sigma = 1 \times 10^{-2}$
γ	Mutation probability	$\gamma = 0.1$

Table IV.1: Model parameters, description and default values.

IV.5.5 Individual-based stochastic model in absence of evolving dispersal

To facilitate part of the mathematical and numerical analysis we partially work on a simplified version of the model in which the dispersal rate (mobility rate) is fixed and constant for all individuals. We later generalize our results (when possible) to the extended model introduced in Section IV.5.1.

The model was introduced in [7] and results from removing the dispersal-associated trait in the model introduced in Section IV.5.1. Each individual is characterized by its physical location $x \in \overline{\mathcal{X}}$ and its phenotypic trait $u \in \mathcal{U}$ ($\mathcal{X} \subseteq \mathbb{R}^d$ and $\mathcal{U} \subseteq \mathbb{R}^k$ are open and connected). Individuals give birth at the rate $B(x,u)$ introduced in Section IV.5.1. Individuals die at a rate which increases with the intensity of local competition. The death rate of an individual at (x,u) in a population of N_t individuals at positions $x_1,\dots,x_{N_t}$ and traits $u_1,\dots,u_{N_t}$ is given by

$$d_0 + d_1 \sum_{i=1}^{N_t} \mathbb{1}_{|x-x_i|<\delta},$$

where d_0 measures the natural death rate, and d_1 scales the mortality effect of competition. Again, we assume $d_1 = 1$ without loss of generality.

Offspring inherit their parent's trait, unless a mutation occurs. The distribution of mutational effects from an individual at position (x,u) is Gaussian centered at u (and independent of x) with variance σ^2, conditioned to remain within $\mathcal{U} = (0,1)$. Individuals' mobility is modeled as spatial diffusion reflected at the boundary of $\mathcal{X}$. The spatial diffusion coefficient (mobility rate) is assumed constant with value D_m. Unless specified otherwise, we take $\mathcal{X} = \mathcal{U} = (0,1)$.

The algorithm used to simulate the individual-based model is based on [7]. As before, we construct recursively sequences N_k, T_k, X_k, U_k, which represent respectively the number of individual in the k-th step of the algorithm, the end time of the k-th step and the vector of positions and traits of the N_k living individuals at the end of the k-th step. We set the potential event rate to $C_{tot} := N_{k-1}(b_0 + d_0 + N_{k-1}/K)$ and then decide, based on θ_k (a uniformly distributed random variable on $[0, C_{tot}]$), which event can potentially occur at time $T_k = T_{k-1} + E_{k-1}$, where E_{k-1} is an exponential random variable with parameter C_{tot}. If $\theta_k < N_{k-1}b_0$, we randomly select an individual $I_k = i$, which will give birth (to a clone or a mutant) with probability $\frac{B(X^i_{T_k}, U^i_{T_k-1})}{b_0}$. If, instead, $N_{k-1}b_0 \le \theta_k \le N_{k-1}b_0 + N_{k-1}d_0$, a randomly selected individual $I_k = i$ dies no matter its position and trait (since the rate of natural death is the same for all individuals). Finally, if $\theta \ge N_{k-1}b_0 + N_{k-1}d_0$, two individuals $I_k = i$, $J_k = j$ are selected randomly. If the distance among them at time T_k is smaller than δ, then individual i dies. Otherwise nothing happens.

IV.5.6 Large-population approximation model in absence of evolving dispersal

In the large-population limit, the distribution of the population in the model behaves according to [7]:

$$\begin{aligned}\frac{\partial n(x,u,t)}{\partial t} &= D_m \frac{\partial^2 n(x,u,t)}{\partial x^2} + n(x,u,t)\times \\ &\quad \left((1-\gamma)B(x,u) - d_0 - \int_{\mathcal{X}}\int_{\mathcal{U}} \mathbb{1}_{|x-y|<\delta} n(y,w,t)dwdy\right) \\ &\quad + \gamma \int_{\mathcal{U}} n(x,w,t)B(x,w)\frac{1}{\sqrt{2\pi}\sigma}\exp\left(-\frac{(u-w)^2}{2\sigma^2}\right)dw, \\ \left.\frac{\partial n(x,u,t)}{\partial x}\right|_{x=0} &= \left.\frac{\partial n(x,u,t)}{\partial x}\right|_{x=1} = 0, \\ n(x,0,t) &= n(x,1,t) = 0, \quad x \in \overline{\mathcal{X}}, \quad t \geq 0.\end{aligned} \tag{IV.3}$$

We simulate the dynamics of the model in Eq. (IV.3) using an explicit scheme where $n(x,u,0)$ has the form of a Gaussian centered at $(0.5, 0.5)$ with standard deviation σ_0 (in each dimension).

IV.5.7 Model parameters and values in absence of evolving dispersal

The parameters of the model and their description, together with the default clustering values are presented in Table IV.2.

Parameter	Description	Default value
b_0	Maximal birth rate	$b_0 = 2$
b_1	Quadratic coefficient in the rate of decay in the birth rate	$b_1 = 20$
d_0	Natural death rate	$d_0 = 1$
D_m	Spatial diffusion coefficient	$D_m = 5 \times 10^{-5}$
δ	Spatial competition range	$\delta = 0.1$
σ	Standard deviation of mutation transition measure	$\sigma = 1 \times 10^{-2}$
γ	Mutation probability	$\gamma = 0.1$

Table IV.2: Model parameters, description and default clustering values.

IV.6 Population expansion in absence of evolving dispersal

We examine the effect of parameters δ (spatial range of competition), D_m (spatial motion), and σ (mutation range) on the spatial eco-evolutionary dynamics when the dispersal (mobility) rate is equal for all individuals. We also address the influence of the initial distribution. Figs. IV.7A and IV.7B show the formation of clusters in the stochastic individual-based model with an initial population concentrated at a single space-phenotype position. An expanding wave of clusters propagates the population across the space-phenotype domain. Here, new clusters are established by individuals that colonize competition-free areas. Even though competition is defined with respect to physical location, the interplay between spatial competition and local adaptation results in a correlation between physical location and trait, which leads to fragmentation in both dimensions.

Simulations of the deterministic approximation model Eq. (IV.3) give results that are remarkably consistent (Fig. IV.7C) with the individual-based stochastic model (Figs. IV.7A and IV.7B). The deterministic model clearly highlights the dichotomy between clustering patterns versus cline-like states which can be defined [228] as symmetrical distributions with respect to the line $x = u$, of the form $n(u, x, t) = \varphi(x - u)$. Comparing the stochastic and deterministic models shows that the domain boundaries and edge effects do not invalidate the cluster dynamics and population spread predicted by the deterministic model, even though deterministic diffusion creates non-zero density across the whole domain from the time of introduction. Boundary conditions may affect the long-term population state, but the transient dynamics of cluster formation and range expansion are robust to them.

Fig. IV.8 illustrates the influence of parameter variation on cluster formation and dynamics. Snapshots shown for the longest simulation times represent the stationary state of the system. Three main effects are apparent. First (Fig. IV.8A), clustering may evolve in phenotypic space and not in geographic space, as a consequence of a larger mobility rate. Thus, individual mobility can spread the population out geographically, without preventing phenotypic differentiation in distinct trait clusters. In this case, the population distribution is geographically continuous, but distinct ranges of phenotypes evolve in different geographic areas.

Second (Fig. IV.8B), the interaction (competition) range δ is a critical determinant of population clustering. Populations with relatively short competition range evolve a cline-like pattern. Third, Fig. IV.8C shows the effect of increasing the mutation range σ. Genetic variation fuels the process of local adaptation, with effects potentially conflicting with individual mobility, as alleles are exported to spatial neighborhoods where they may be poorly adapted. Larger mutational effects tend to blur phenotypic clustering without altering geographic clustering. This response is essentially opposite to the effect of increased mobility, with the difference that even very large mutation ranges may not completely offset phenotypic clustering. Considering very small mutation ranges, the stationary clustering pattern appears unaffected; only the time of cluster formation and population spread is changed, increasing as mutational variance decreases. In the limit of zero mutational variance, i.e. in the absence of genetic variation, range expansion is prevented altogether, due to the inability of the species to maintain viable populations in geographic areas where optimal conditions

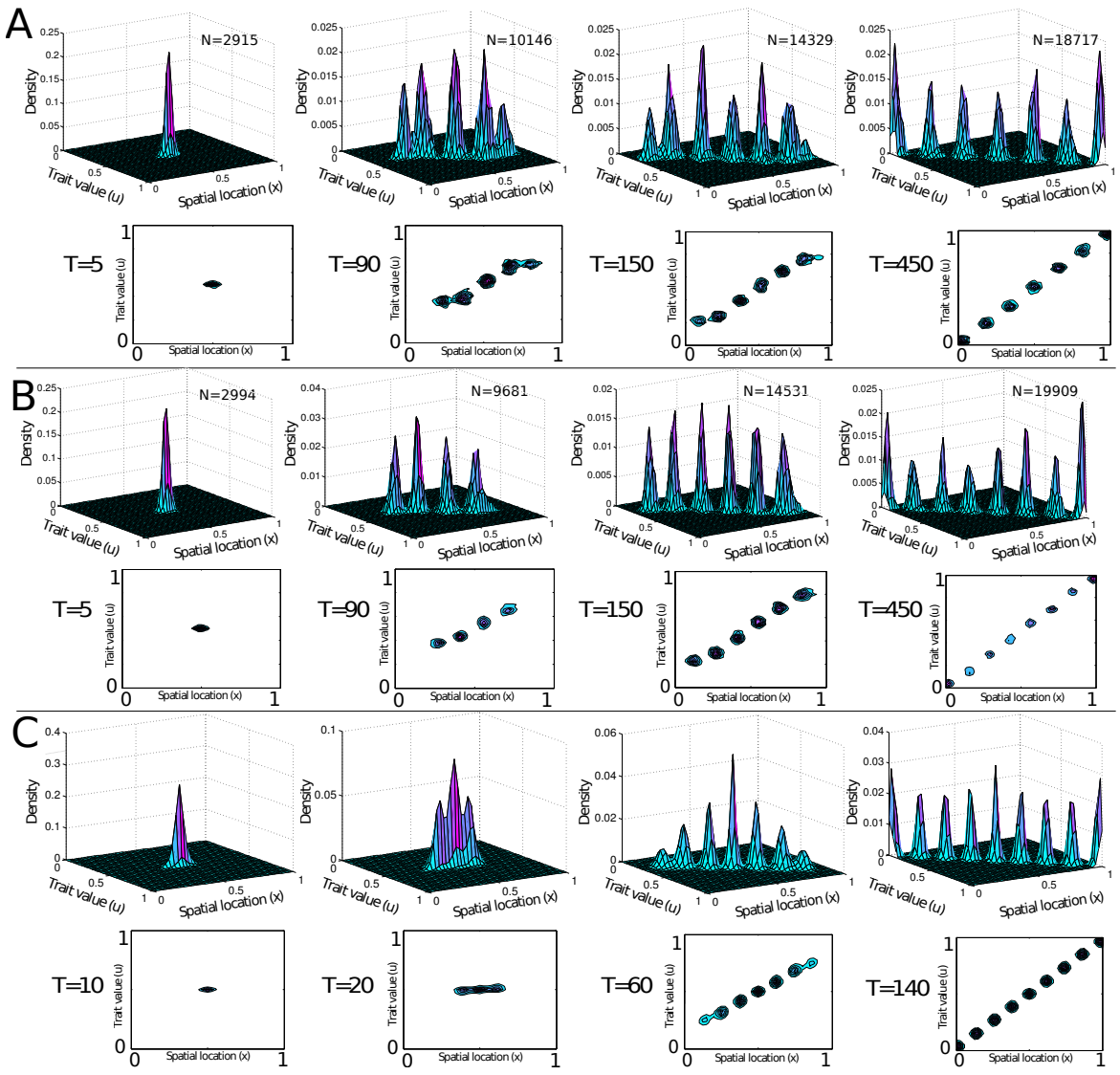

Figure IV.7: Spatial eco-evolutionary dynamics in the individual-based stochastic model (A,B) and the deterministic large population limit (C). A and B. Initially, a population of $N = 3000$ is concentrated at the point $(0.5, 0.5)$. B. At $T = 0$ the distribution is a Gaussian with standard deviation $\sigma_0 = 0.1$ (in both dimensions) centered at $(0.5, 0.5)$. Parameters set to the default clustering values (Table IV.2). In all panels, cyan represents the lowest density and magenta the highest. Density is negligible in white areas.

are too different from its original niche (See Section IV.7).

Fig. IV.9 further documents the effect of large mobility rates. Large mobility rates drive fast expansion of the population across the spatial domain, in the form of two geographically broad but phenotypically narrow and diverging clusters. Each cluster is structured into a 'hot spot' of adaptation at the center, and 'cold spots' at the margins. Throughout the

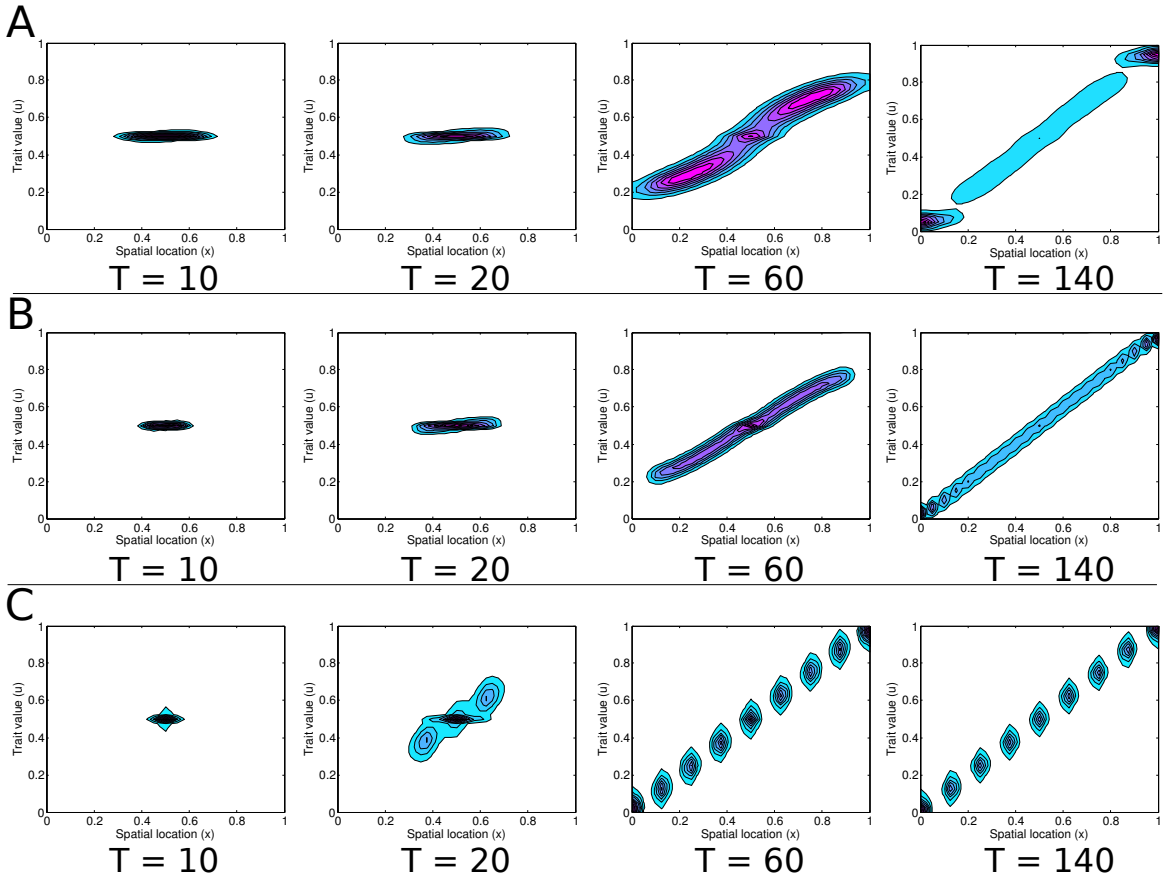

Figure IV.8: Effect of mobility, competition, and mutation in the deterministic large population-size limit. A. Increased diffusion rate: $D_m = 5 \times 10^{-4}$. B. Reduced interaction range: $\delta = 0.05$. C. Increased mutation variance $\sigma = 0.25$. At $T = 0$ the distribution has the form of a Gaussian with standard deviation $\sigma_0 = 0.1$ (in both dimensions) centered at $(0.5, 0.5)$. Other parameters set to the default clustering values in Table IV.2. In all panels, cyan represents the lowest density and magenta the highest. Density is negligible in white areas.

process of population spread, the adaptation hot spot of each cluster acts as a population source fueling the highly maladapted geographic margins. The spatial spread of each cluster is established early in the process of expansion from the site of introduction, and within each cluster, the adaptation hot spot moves along the environmental gradient from the site of introduction (early on) to asymptotic trait values that are close to, but distinct from the edges of the gradient. The long-term pattern is one of relatively uniform spatial distribution, with three (Fig. IV.9A) or only two (Fig. IV.9B) phenotypic clusters –a pattern known from models of sexually reproducing organisms, to promote parapatric speciation [22].

Finally, Fig. IV.10 documents the effect of the initial spread of the population on its spatial dynamics. In large populations well approximated by the deterministic model (Fig. IV.10), a broad initial range can cause the population to invade as a traveling wave. Local

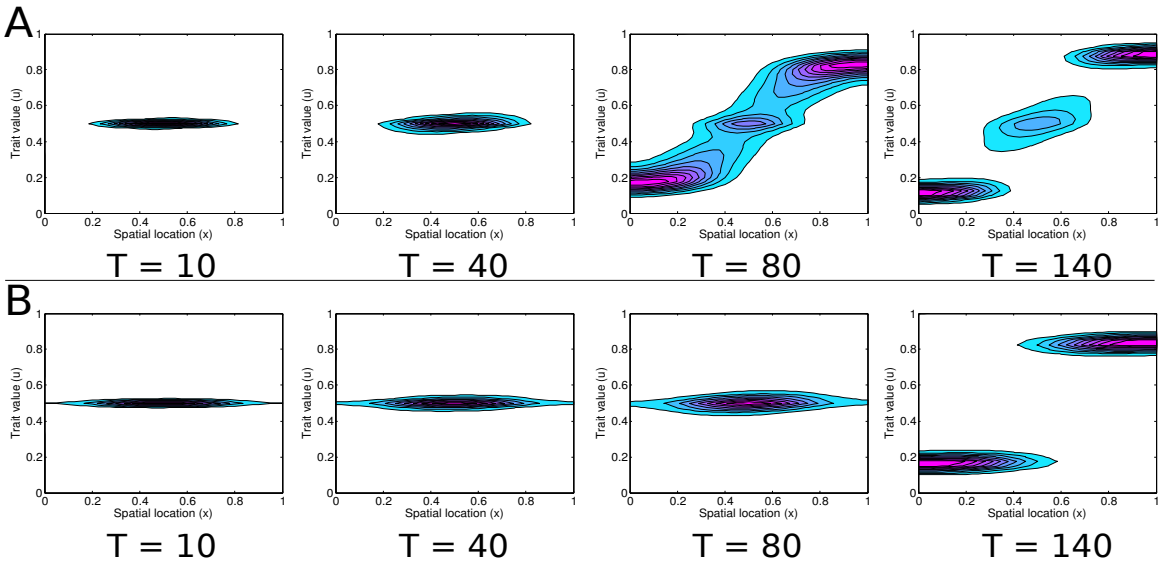

Figure IV.9: Effect of mobility in the deterministic large population limit. A. $D_m = 5\times10^{-3}$. B. $D_m = 2\times10^{-2}$. At $T = 0$ the distribution is a Gaussian with standard deviation $\sigma_0 = 0.1$ (in both dimensions) centered at $(0.5, 0.5)$. Other parameters set to the default clustering values (Table IV.2). In all panels, cyan represents the lowest density and magenta the highest. Density is negligible in white areas.

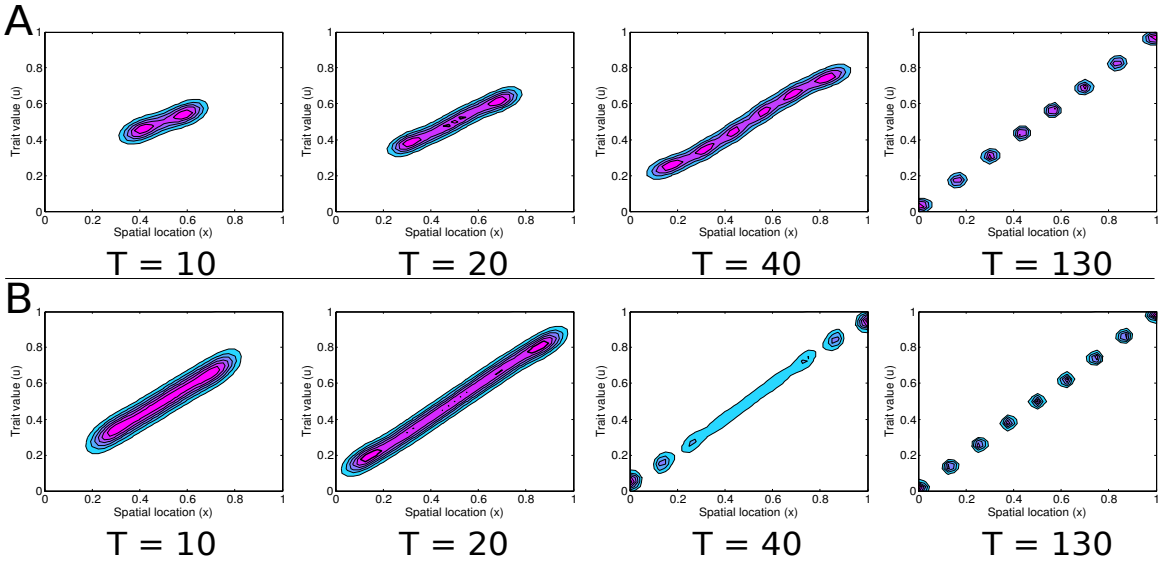

Figure IV.10: Cluster formation in the deterministic large population limit. At $T = 0$ the distribution has the form of a Gaussian with standard deviations $\sigma_0 = 0.04$ (panel A) and $\sigma_0 = 0.1$ (panel B) in both dimensions centered at $(0.5, 0.5)$. Parameters set to the default clustering values (Table IV.2). In all panels, cyan represents the lowest density and magenta the highest. Density is negligible in white areas.

competition and adaptation tend to create variation in density (Fig. IV.10A), but clusters do not separate until the population reaches the edges of the domain, where complete isolation of clusters initiate and propagates back toward the center of the gradient (Fig. IV.10B). Thus, with sufficiently broad initial conditions, the spatial eco-evolutionary dynamics drive a continuous range expansion, followed by cluster patterning once the environmental gradient has been fully invaded.

Simulations reported in Figs. IV.7, IV.10 and IV.13 indicate the the number of clusters evolving asymptotically may vary. This suggests that the spatial eco-evolutionary dynamics may be multi-stable, with slightly different initial conditions leading to alternate attractors.

Figs. IV.11, IV.12 and IV.13 show equivalent results as in Figs. IV.8, IV.9 and IV.10 for the stochastic individual-based model.

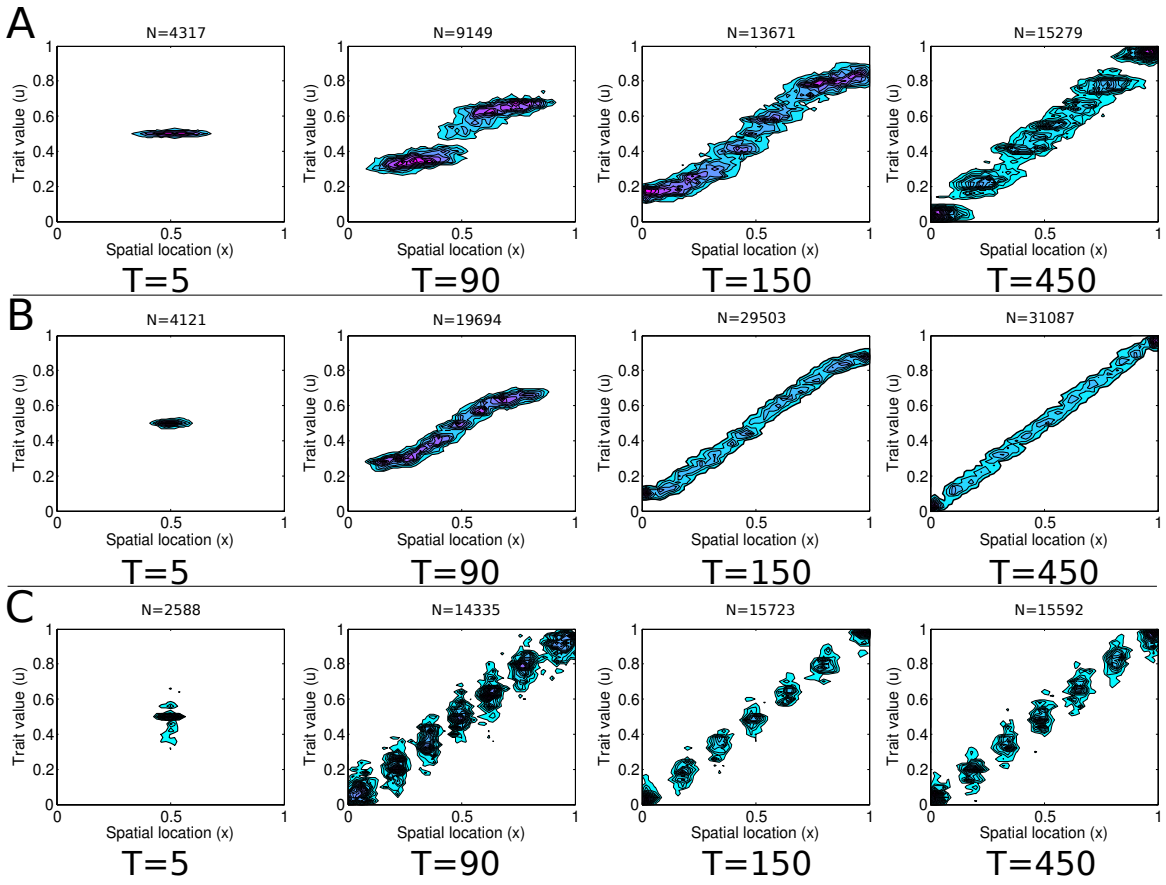

Figure IV.11: Effect of mobility, competition, and mutation in the individual-based stochastic model. A. Increased mobility rate: $D_m = 5 \times 10^{-4}$. The final population size is $N = 15279$. B. Reduced interaction range: $\delta = 0.05$. The final population size is $N = 31087$. C. Increased mutation variance $\sigma = 0.25$. The final population size is $N = 15592$. Initially, a population of $N = 3000$ is concentrated at the point $(0.5, 0.5)$. Other parameters set to the default clustering values in Table IV.2. In all panels, cyan represents the lowest density and magenta the highest. Density is negligible in white areas.

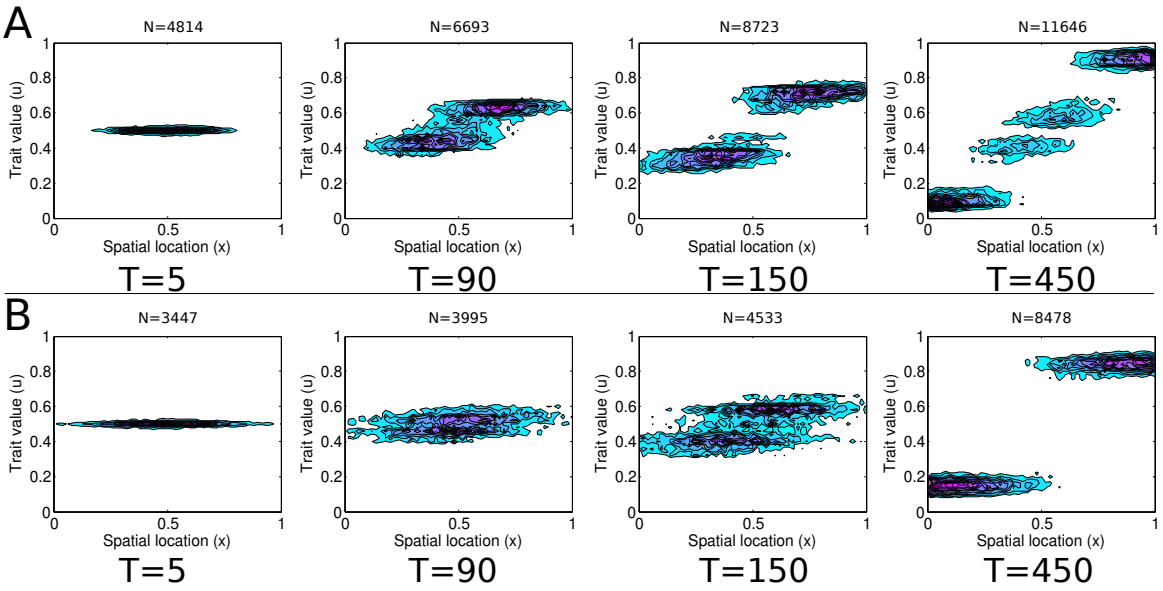

Figure IV.12: Effect of mobility in the individual-based stochastic model. A. $D_m = 5 \times 10^{-3}$. B. $D_m = 2 \times 10^{-2}$. Initially, a population of $N = 3000$ is concentrated at the point $(0.5, 0.5)$. The final population size is $N = 11646$ (panel A) and $N = 8478$ (panel B). Other parameters set to the default clustering values in Table IV.2. In all panels, cyan represents the lowest density and magenta the highest. Density is negligible in white areas.

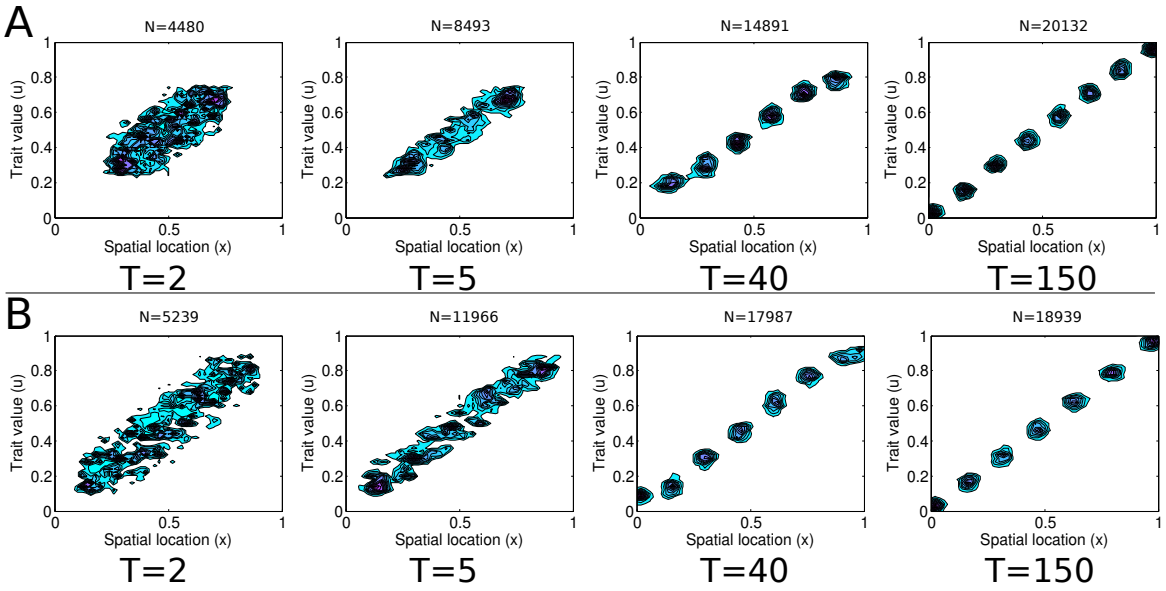

Figure IV.13: Effect of initial conditions on cluster formation and dynamics in the individual-based stochastic model. Initially, a population of $N = 3000$ is uniformly distributed in the range $[0.25, 0.75]$ (panel A) or in the range $[0.1, 0.9]$ (panel B) in both dimensions. The final population size is $N = 20132$ (panel A) and $N = 18939$ (panel B). Parameters set to the default clustering values (Table IV.2). In all panels, cyan represents the lowest density and magenta the highest. Density is negligible in white areas.

IV.7 Dynamics of population expansion in the absence of evolution

IV.7.1 Clustering in the individual-based stochastic model and deterministic large-population limit in the absence of evolution

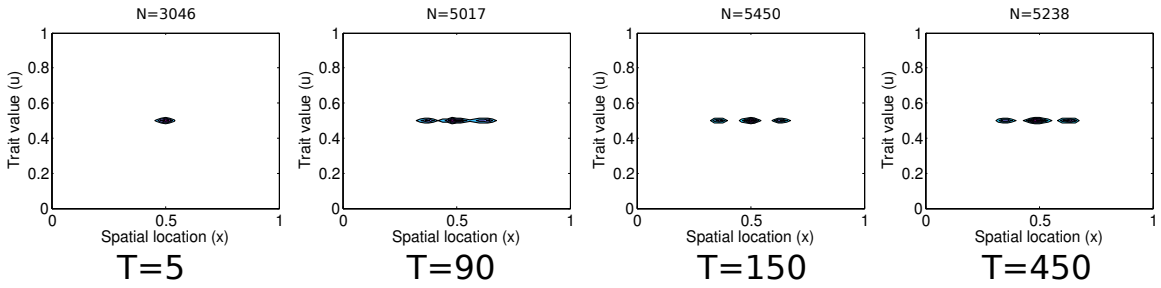

Figure IV.14: Cluster formation in the simulations of the individual-based stochastic model in the absence of evolution ($\gamma = 0$). The final population size is $N = 5238$. Initially, a population of $N = 3000$ is concentrated at the point $(0.5, 0.5)$. Parameter values set to the default clustering parameter values in Table IV.2. In all panels, cyan represents the lowest density and magenta the highest. Density is negligible in white areas.

We analyze the dynamics of the individual-based stochastic model and its deterministic large population-size limit in the absence of evolution in both the niche trait and the dispersal-related trait to study the dependence of clustering and adaptive diversification on phenotypic mutations in niche traits when competition is only spatial. As observed in Figs. IV.14 and IV.15, clustering occurs—in both cases—in the form of a multimodal distribution under the default clustering parameter values. Complete separation of clusters does not occur, however, due to the adaptation constraints.

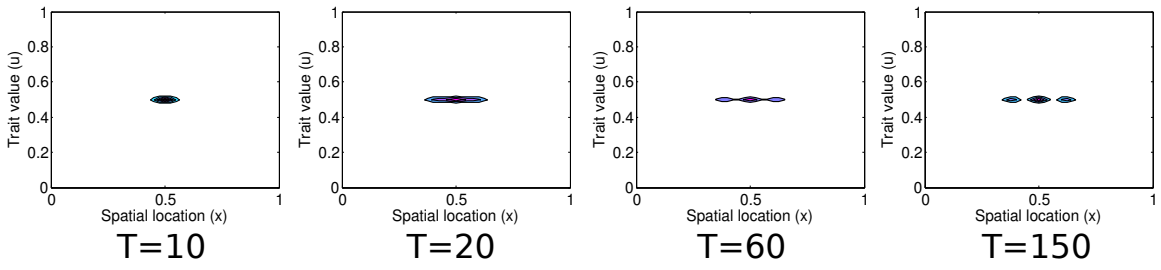

Figure IV.15: Cluster formation in the simulations of the deterministic large population-size limit in the absence of evolution ($\gamma = 0$). At $T = 0$ the distribution has the form of a Gaussian with standard deviation $\sigma_0 = 1 \times 10^{-2}$ (in the spatial direction) centered at $(0.5, 0.5)$. Parameter values set to the default clustering parameter values in Table IV.2. In all panels, cyan represents the lowest density and magenta the highest. Density is negligible in white areas.

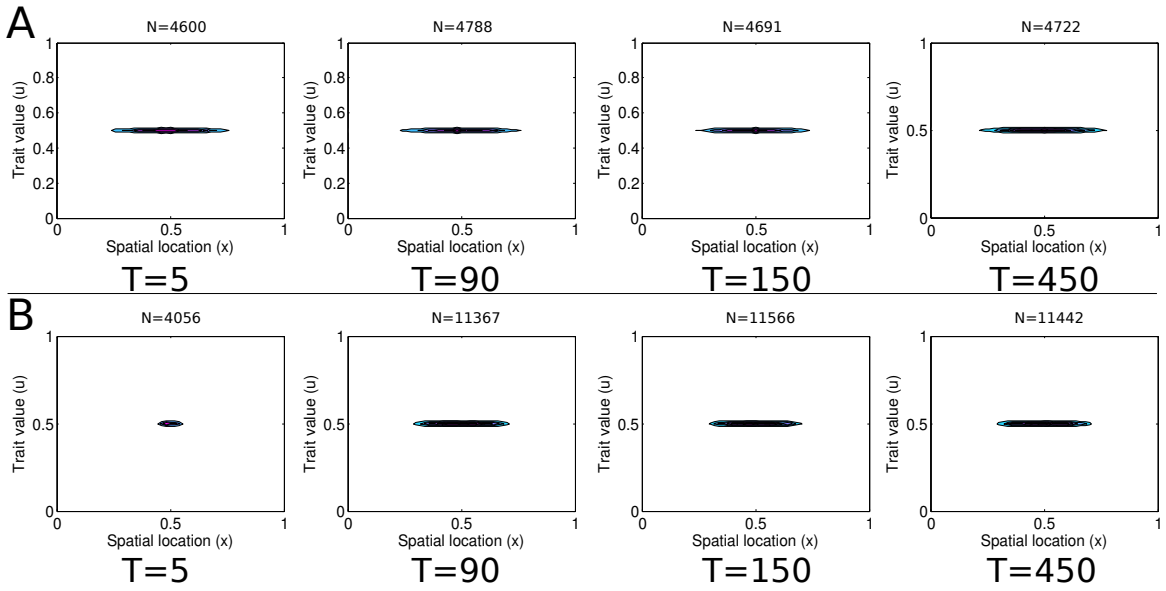

Figure IV.16: Parameter dependence in the simulations of the individual-based stochastic model in the absence of evolution ($\gamma = 0$). A. Increased diffusion rate: $D_m = 5 \times 10^{-4}$. B. Reduced interaction range: $\delta = 0.05$. The final population size is $N = 4722$ (panel A) and $N = 11442$ (panel B). Initially, a population of $N = 3000$ is concentrated at the point $(0.5, 0.5)$. Other parameter values set to the default clustering parameter values in Table IV.2. In all panels, cyan represents the lowest density and magenta the highest. Density is negligible in white areas.

IV.7.2 Effect of parameters in the absence of evolution

As observed in Figs. IV.16 and IV.17 for both the stochastic individual-based model and its deterministic limit and similarly as in the original model, both an increase in the diffusion rate and a reduction in the interaction range hinder clustering and multimodality in the absence of evolution. In both cases there is a transition to unimodality (with respect to Figs. IV.14 and IV.15) with a larger range in the case of faster spatial motion (the transition occurs at a lower value of D_m^*) as emphasized in Section IV.7.3.

IV.7.3 Importance of niche trait evolution in the appearance of clustering

To emphasize the role of phenotypic evolution in ecological (resource-use or niche) traits in the appearance of clustering along environmental gradients we show an example where phenotypic mutations are essential for the appearance and evolution of clustering.

In Section IV.8.1 we show that there is an interval where perturbations only at the spatial component would predict stability of the cline-like equilibrium while perturbations in both dimensions would instead predict instability. This is done to show that the stability analysis in [228] may have misestimated the ranges of stability of cline-like equilibria. For a value of D_m in this interval, clustering occurs in presence but not in absence of phenotypic evolution (Figs. IV.18 and IV.19). In the case of the individual-based stochastic model,

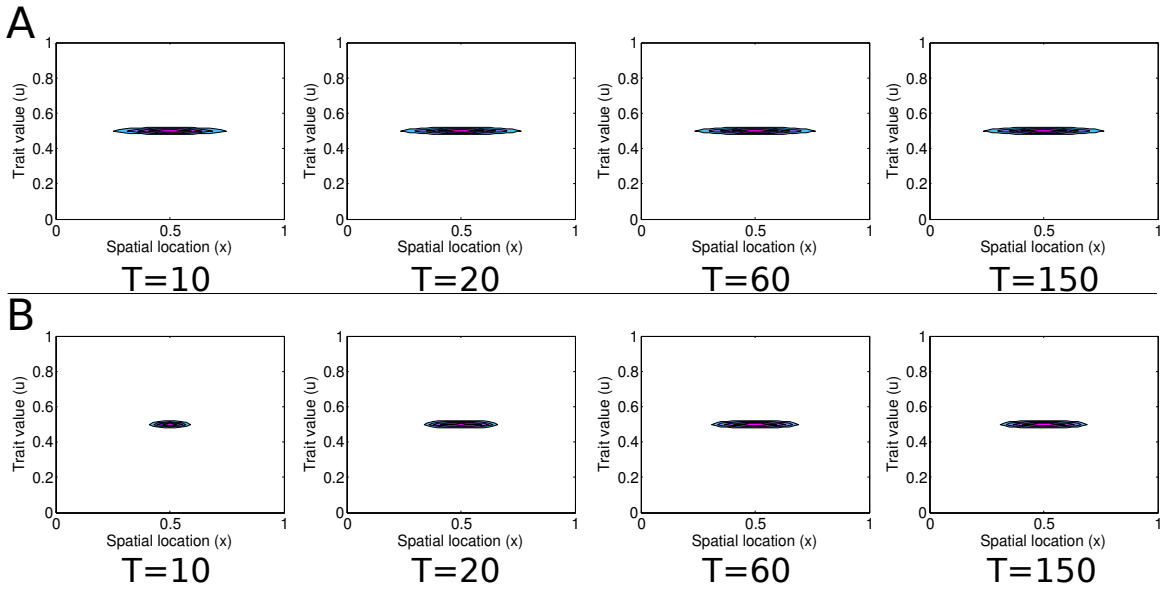

Figure IV.17: Parameter dependence in the simulations of the deterministic large population-size limit in the absence of evolution ($\gamma = 0$). A. Increased diffusion rate: $D_m = 5 \times 10^{-4}$. B. Reduced interaction range: $\delta = 0.05$. At $T = 0$ the distribution has the form of a Gaussian with standard deviation $\sigma_0 = 0.1$ (in the spatial dimension) centered at $(0.5, 0.5)$. Other parameter values set to the default clustering parameter values in Table IV.2. In all panels, cyan represents the lowest density and magenta the highest. Density is negligible in white areas.

although unimodality is not as stable as in Fig. IV.16, the distribution does not show a clear multimodality as in Fig. IV.14.

In the deterministic large population-size limit (Fig. IV.19), the difference is more visible. While clustering occurs in presence of evolution –although the convergence time is much larger than in Fig. IV.7 (the distribution has not yet fully converged to a clustering pattern at $T = 150$) and the dynamics are dependent on the boundary conditions– clustering does not occur in absence of phenotypic mutations and the unimodality of the distribution is stable. The cluster formation dynamics are as those in Fig. IV.10B.

These results show that multimodality in the population's distribution and clustering is facilitated and occurs under a wider range of spatially dependent parameters when phenotypic evolution occurs, even under the assumption that competition is only spatial. Phenotypic evolution becomes essential in some cases as a consequence of the interplay and the appearing correlation between selection (which is spatial and phenotype dependent) and competition.

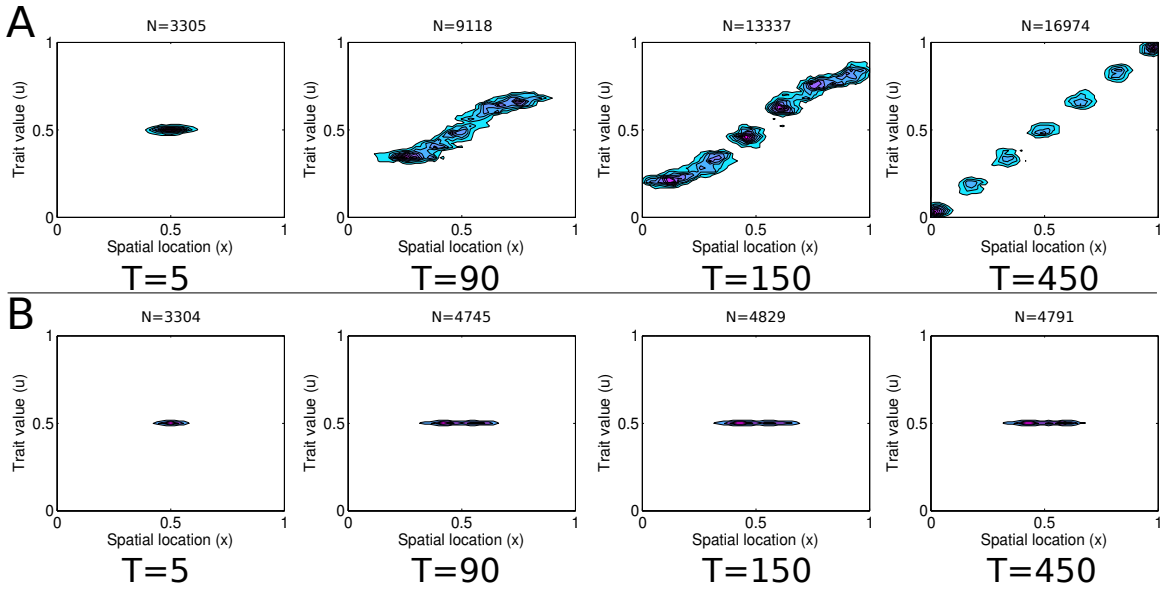

Figure IV.18: Clustering in presence of evolution (panel A) and no clustering in the absence of evolution (panel B with $\gamma = 0$) in the individual-based stochastic model. In both cases $D_m = 1.35 \times 10^{-4}$. The final population size is $N = 16974$ (panel A) and $N = 4791$ (panel B). Initially, a population of $N = 3000$ is concentrated at the point $(0.5, 0.5)$. Other parameter values set to the default clustering parameter values in Table IV.2. In all panels, cyan represents the lowest density and magenta the highest. Density is negligible in white areas.

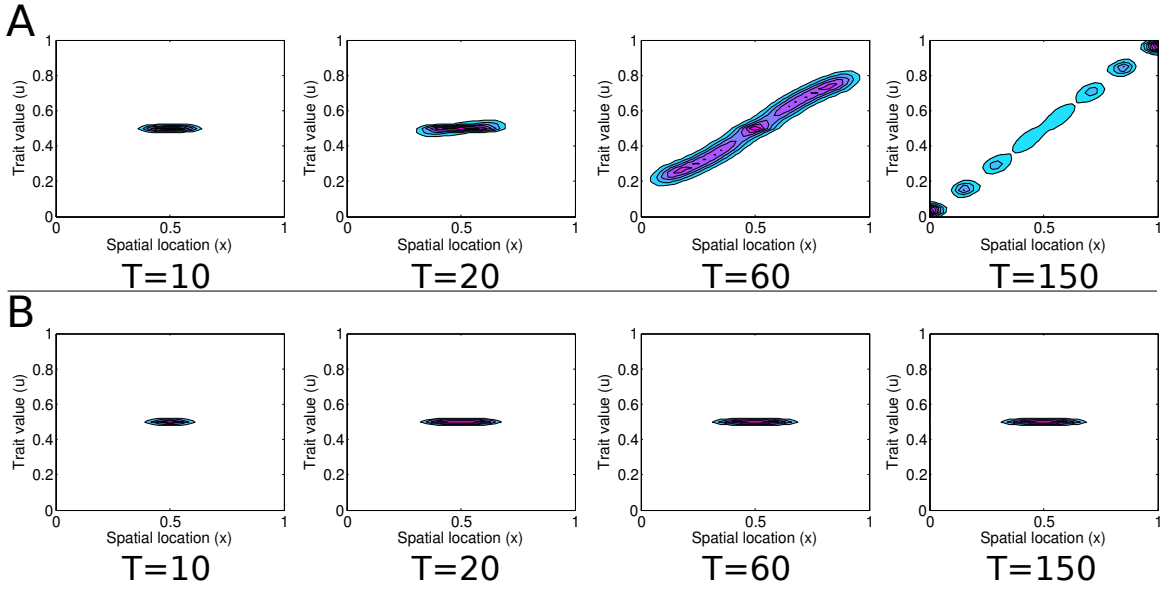

Figure IV.19: Clustering in presence of evolution (panel A) and no clustering in the absence of evolution (panel B with $\gamma = 0$) in the the deterministic large population-size limit. In both cases $D_m = 1.35 \times 10^{-4}$. Other parameter values set to the default clustering parameter values in Table IV.2. In all panels, cyan represents the lowest density and magenta the highest. Density is negligible in white areas.

IV.8 Conditions for continuous vs. clustering population expansion

IV.8.1 Turing stability analysis

We use Turing's method for pattern formation analysis [431] to study the conditions under which the spatial eco-evolutionary dynamics converge to a clustering pattern or a cline-like pattern in absence of evolving dispersal. We then use this result to extend to the case where dispersal evolves to predict when expansion and invasion occurs through the formation of clusters of through continuous-front expansion.

To avoid artifactual boundary effects, we change the boundary conditions from Neumann and Dirichlet to periodic boundary conditions. In this case, our models are translation invariant both in space and trait. Turing's method consists in determining a cline-like invariant solution of (IV.3), of the form $n(t,x,u) = \rho(x-u)$, and analyzing, either numerically or analytically, the stability of perturbations of the stationary solution $\rho(x-u)$. Note that, contrary to [228] where the state space is assumed unbounded, the fact that our domain is bounded imposes to consider periodic perturbations on $[0,1]^2$, and so restricts the set of possible perturbations of the model. By the decomposition of periodic functions in Fourier series and because the model is translation invariant, it is enough to consider perturbations of the form:

$$n(0,x,u) = [1+\varepsilon\cos(2\pi m_1 u + 2\pi m_2 x)]\rho(x-u) \tag{IV.4}$$

for small $\varepsilon > 0$ and for any nonnegative integers m_1, m_2, usually called *frequencies*. If the perturbation does not grow for any couple of integers (m_1, m_2), then the cline-like solution is stable. If, for a certain (m_1, m_2), the perturbation grows, then one expects the attracting state of the system (if it exists) to be distributed among approximately $m_1 + m_2 + 1$ clusters, and their distance along the line $x = u$ can be expected to be close to multiples of $1/(m_1+m_2)$, where $(m_1, m_2) \neq (0,0)$ are the frequencies with higher growth rate of the perturbation (Fig. IV.20B and Fig. IV.20C). Hence, our analysis allows to characterize cases where the population stabilizes at cline-like or clustered equilibria and also provides an estimate of the number of clusters.

Note that the analysis of [228] was performed only for such perturbations with $m_1 = 0$ (Fig. IV.20C) but for any real value of m_2 due to the lack of boundary conditions. Hence, their stability analysis may have missed perturbations acting both in space and trait directions –as suggested from the results in IV.7.3–, which could make the cline-like solution unstable in cases where they would predict it to be stable.

Our analysis, detailed hereafter, shows the existence of the cline-like invariant solution in the torus. We also show that the Lyapunov exponent (i.e. the rate of exponential growth or decay of the perturbation) of a perturbation of the form (IV.4) can be approximated by:

$$\lambda_{m_1,m_2} = -4\pi^2(D_m m_2^2 + D_\gamma m_1^2) - \frac{b_0 - d_0 - \sqrt{b_1(D_m+D_\gamma)}}{2\pi\delta(m_1+m_2)} \exp\left(-2\pi^2 m_1^2 \sqrt{\frac{D_m+D_\gamma}{b_1}}\right) \sin(2\pi\delta(m_1+m_2)), \tag{IV.5}$$

where $D_\gamma = \frac{b_0\gamma\sigma^2}{2}$. This equation should provide a decomposition of the dynamics in terms of the parameter space.

In the case of perturbation in the space direction only ($m_1 = 0$), the Lyapunov exponent takes the form:

$$\lambda_{0,m_2} = -4\pi^2 D_m m_2^2 - \frac{b_0 - d_0 - \sqrt{b_1(D_m + D_\gamma)}}{2\pi\delta m_2}\sin(2\pi\delta m_2). \tag{IV.6}$$

We generalize Eq. IV.5 to predict when invasion occurs through cluster formation or through continuous-front expansion. We claim the transition between the two occurs approximately when the generalized Lyapunov exponent changes sign (for the values of m_1 and m_2 for which it is maximal):

$$\lambda_{m_1,m_2} = -4\pi^2(D_m(w)m_2^2 + D_\gamma m_1^2) - \frac{b_0 - d_0(1+w)^\theta - \sqrt{b_1(D_m(w) + D_\gamma)}}{2\pi\delta(m_1+m_2)}\exp\left(-2\pi^2 m_1^2\sqrt{\frac{D_m(w)+D_\gamma}{b_1}}\right)\sin(2\pi\delta(m_1+m_2)). \tag{IV.7}$$

Here, w is the dispersal-associated trait at the fronts of population.

To obtain these results, our first step is to construct an approximate model for which explicit computations are possible. If we consider σ^2 to be small, and (x, u) to be near the line $x = u$ where the birth rate is b_0, by making a second order expansion of the function

$$M(u) = \gamma\left(\int_{\mathcal{U}} n(x,w,t)B(x,w)\frac{1}{\sqrt{2\pi}\sigma}\exp\left(-\frac{(u-w)^2}{2\sigma^2}\right)dw - B(x,u)n(x,u,t)\right)$$

while assuming that mutations occur at a constant rate (independent of (x, u)), we can approximate the function $M(u)$ with a diffusion equation with rate $D_\gamma = \frac{b_0\gamma\sigma^2}{2}$. Thus we can replace equation (IV.3) by the simpler reaction-diffusion equation:

$$\begin{aligned}\frac{\partial n(x,u,t)}{\partial t} &= n(x,u,t)\times \\ &\left(B(x,u) - d_0 - \int_{\mathcal{X}}\int_{\mathcal{U}} \mathbb{1}_{|x-y|<\delta} \times n(y,w,t)dwdy\right) + \\ &D_m\frac{\partial^2 n(x,u,t)}{\partial x^2} + D_\gamma\frac{\partial^2 n(x,u,t)}{\partial u^2}.\end{aligned} \tag{IV.8}$$

Since we are interested in studying time-constant cline-like solutions, we will modify the boundary conditions in order to make competition uniform along the line $x = u$. Let $\bar{\mathcal{X}} = \mathcal{U} = T^1$ and remove the Neumann and Dirichlet boundary conditions. Here we denote by T^1 the one-dimensional torus of length 1. From this point on, all operations on x or u will be defined on T^1. Hence, we will impose the condition $\delta < 0.5$ and redefine $B(x, u)$ as

$$B(x,u) = \max\{b_0 - b_1 \times d(x,u)^2, 0\}$$

where $d(x,u) := \min\{|x-u|, 1-|x-u|\}$ is the distance function in T^1.

Suppose then that $n(x,u,t)$ is a cline-like distribution, that is of the form $n(\beta,t)$, $\beta := d(x,u) \in [0,\frac{1}{2}]$. We wish to write equation (IV.8) in terms of the new parameter β. We proceed by analysing the equation term by term. First, $B(x,u)$ can be substituted by $B(\beta)$ by simply redefining (with a slight abuse of notation) $B : [0,\frac{1}{2}] \to [0,b_0]$ as $B(\beta) = \max\{b_0 - b_1(\beta)^2, 0\}$. Consider now the term in Eq. (IV.8) representing death by competition. Let $D_c(x,n) := \int_{\mathcal{X}}\int_{\mathcal{U}} \mathbb{1}_{d(x-y)<\delta} \times n(y,w,t)dwdy$. We want to show that if $n(x,u,t)$ is of the form $n(\beta,t)$, $D_c(x,n)$ is independent of x. Let $x_1 \le x_2$, $x_1, x_2 \in [0,1)$. Because of the new boundary conditions and the symmetry of n with respect to x and u, one has that $n(x_2,u,t) = n(x_1+\alpha,u,t) = n(x_1,u-\alpha,t)$ for $\alpha = x_2 - x_1$. Thus $\int_{\mathcal{U}} n(x_2,u,t)du = \int_{\mathcal{U}} n(x_1,w,t)dw$. Hence, $\int_{\mathcal{U}} n(y,w,t)dw$ is constant for all $y \in [0,1)$. Denoting this constant value by C we can deduce that

$$\begin{aligned} D_c(x,n) &= \int_{\mathcal{X}}\int_{\mathcal{U}} \mathbb{1}_{|x-y|<\delta} \times n(y,w,t)dwdy \\ &= \left|\int_{x-\delta}^{x+\delta} \mathbb{1}_{|x-y|<\delta} \times C dy\right| = 2\delta C, \end{aligned}$$

which has no dependence on x. Finally, for the diffusion terms in equation (IV.8), one obtains that $\frac{\partial^2 n(x,u,t)}{\partial x^2} = \frac{\partial^2 n(x,u,t)}{\partial u^2} = \frac{\partial^2 n(x,u,t)}{\partial \beta^2}$ for a cline-like solution $n(x,u,t) = n(\beta,t)$.

Hence, for a cline-like distribution $n(\beta,t)$, observing that $\int_{T_1} n(\beta)d\beta = 2\int_0^{1/2} n(\beta)d\beta$, for all $\beta \in [0,1/2]$,

$$\frac{\partial n(\beta,t)}{\partial t} = n(\beta,t)\left(B(\beta) - d_0 - 4\delta\int_0^{1/2} n(a,t)da\right) + (D_m + D_\gamma)\frac{\partial^2 n(\beta,t)}{\partial \beta^2}.$$

Since we are interested in proving the existence of a cline-like stationary solution, we wish to study the solvability of the second order differential equation given by

$$n(\beta)\left(B(\beta) - d_0 - 4\delta\int_0^{1/2} n(a)da\right) + (D_m + D_\gamma)n''(\beta) = 0 \tag{IV.9}$$

with appropriate boundary conditions: due to the form of the birth rate function and the symmetry of the torus, $n(\beta)$ must be minimum at $\beta = \frac{1}{2}$ and a maximum at $\beta = 0$, thus we have the boundary conditions $n'(0) = n'(\frac{1}{2}) = 0$.

Let $\rho = d_0 + 4\delta\int_0^{1/2} n(a)da$ (an unknown quantity) and $M = D_m + D_\gamma$. We can rewrite equation (IV.9) as

$$Mn''(\beta) + n(\beta)B(\beta) = +\rho n(\beta), \quad \forall \beta \in [0,1/2]. \tag{IV.10}$$

With the boundary conditions $n'(0) = n'(1/2) = 0$, this is a Sturm-Liouville (S–L) regular problem [432–434], which means that it is solvable for countably many values of ρ, $\rho_0 < \rho_1 < \ldots$ and that the linear space of solutions associated to ρ_n has dimension 1 and is generated by a function ψ_n having exactly n zeroes on $[0,1/2]$. In particular, we can assume without loss of generality that $\psi_0 > 0$, and the only biologically relevant solutions are of the form $a\psi_0$ for some $a > 0$. In order to recover a solution of (IV.9), a needs to be chosen such that $\rho_0 = d_0 + 4\delta a\int_0^{1/2}\psi_0(\beta)d\beta$. This is only possible if $\rho_0 > d_0$, hence for sufficiently small

death rate. Note also that ρ_0 depends in a non-trivial way on the birth rate B and hence on b_0 and b_1.

In order to make more precise the corresponding assumptions on b_0, b_1 and d_0, let us first integrate (IV.10) over $[0, 1/2]$. We obtain $\int_0^{1/2} \psi_0(\beta) B(\beta) d\beta = \rho_0 \int_0^{1/2} \psi_0(\beta) d\beta$, from which we deduce that $\rho_0 \in (0, b_0)$. Note also that, if the positive part in the definition of B is removed, the principal eigenvalue problem (IV.10) on $[0, +\infty)$ with boundary conditions $n'(0) = 0$ and $n(+\infty) = 0$ becomes explicitly solvable, with eigenvalue $\bar{\rho}_0 = b_0 - \sqrt{b_1 M}$ and eigenfunction

$$\bar{\psi}_0(\beta) = \bar{\psi}_0(0) \exp\left(-\frac{\beta^2}{2\sqrt{M/b_1}}\right).$$

This gives a particular solution of (IV.10) with $\rho = \bar{\rho}_0$ and $n'(0) = 0$

$$n(\beta) = \begin{cases} n(0) \exp\left(-\frac{\beta^2}{2\sqrt{M/b_1}}\right) & \text{if } \beta \le \sqrt{b_0/b_1} \\ n(0) \exp\left(-\frac{b_0}{2\sqrt{Mb_1}}\right) \cos\left(\sqrt{\frac{\bar{\rho}_0}{M}}\beta + \bar{\varphi}_0\right) & \text{if } \sqrt{b_0/b_1} \le \beta \le 1/2, \end{cases}$$

where $\bar{\varphi}_0$ is a solution to

$$\sin\left(\sqrt{\frac{\bar{\rho}_0 b_0}{Mb_1}} + \bar{\varphi}_0\right) = \left(1 - \frac{\sqrt{Mb_1}}{b_0}\right)^{-1/2}.$$

Hence, assuming $\frac{b_0}{\sqrt{Mb_1}} \gg 1$, the previous function satisfies $n'(1/2) \simeq 0$ and hence is a good approximation to a solution of the Sturm-Liouville problem (IV.10). This function is not positive but may take very small negative values for β close to $\frac{1}{2}$. Therefore, a biologically consistent approximation of n is given by the previous formula truncated below zero. Therefore, $\rho_0 \simeq \bar{\rho}_0$ and $\psi_0 \simeq \bar{\psi}_0$. This leads to the equation

$$\begin{aligned} b_0 - \sqrt{b_1 M} \simeq \rho_0 \simeq d_0 + 4\delta \int_0^{1/2} \bar{\psi}_0(\beta) d\beta \simeq d_0 + 4\delta \int_0^{\infty} \bar{\psi}_0(\beta) d\beta \\ = d_0 + 2\delta \bar{\psi}_0(0) \sqrt{2\pi\sqrt{M/b_1}}. \end{aligned}$$

Under the assumptions $d_0 < b_0 - \sqrt{Mb_1}$ and $b_0 \gg \sqrt{Mb_1}$, we obtain the following approximation of the cline-like stationary solution of (IV.8):

$$n_0(\beta) \simeq \frac{b_0 - d_0 - \sqrt{b_1 M}}{2\delta\sqrt{2\pi\sqrt{M/b_1}}} \exp\left(-\frac{\beta^2}{2\sqrt{M/b_1}}\right).$$

We will write this in the form:

$$n_0(\beta) = C \frac{1}{\sqrt{2\pi\sigma_0^2}} \exp\left(-\frac{\beta^2}{2\sigma_0^2}\right), \tag{IV.11}$$

with $C = \frac{b_0 - d_0 - \sqrt{b_1 M}}{2\delta}$ and $\sigma_0^2 = \sqrt{M/b_1}$. Notice that C is the same as above when $M \ll b_1$.

Now, consider a perturbation of $n_0(x,u)$ of the form

$$\hat{n}_0(x,u) = (1+\varepsilon\mu(x,u))n_0(x,u),$$

where $\varepsilon \ll 1$ and $\mu(x,u) = \mu(m_1u + m_2x)$. Here, $\mu(x,u)$ is a periodic function on the torus $(T^1)^2$. This requires $\mu(m_1(u+1)+m_2x) = \mu(m_1u+m_2x) = \mu(m_1u+m_2(x+1))$ for all $x,u \in T^1$, i.e. $m_1, m_2 \in \mathbb{Z}$. Fourier analysis tells us that any periodic function on $(T^1)^2$ is a linear combination of such functions, so it is enough to study each perturbation with $m_1, m_2 \in \mathbb{Z}$. By symmetry, we can restrict to $m_1, m_2 \in \mathbb{N}$. We will study the dynamics of $\nu(x,u,t) = \hat{n}(x,u,t) - n_0(x,u)$ when $\hat{n}(x,u,0) = \hat{n}_0(x,u)$. Furthermore, by local linearization of the PDE it is enough to look at solutions of the form $\nu(x,u,t) = \exp(\lambda t)\nu(x,u,0) = \exp(\lambda t)(\varepsilon\mu(x,u)n_0(x,u))$. Turing's stability method consists in computing the value of λ and looking for values that satisfy $\lambda > 0$. Since, $\frac{\partial\nu(x,u,t)}{\partial t} = \frac{\partial\hat{n}(x,u,t)}{\partial t}$, we get:

$$\begin{aligned}\frac{\partial\nu(x,u,t)}{\partial t} &= \nu(x,u,t)\times\left(B(x,u) - d_0 - \int_{\mathcal{X}}\int_{\mathcal{U}} \mathbb{1}_{d(x,y)<\delta}\times n_0(y,w)dwdy\right)\\ &+ D_m\frac{\partial^2\nu(x,u,t)}{\partial x^2} + D_\gamma\frac{\partial^2\nu(x,u,t)}{\partial u^2} - \hat{n}(x,u,t)\int_{\mathcal{X}}\int_{\mathcal{U}}\mathbb{1}_{d(x,y)<\delta}\times\nu(y,w,t)dwdy.\end{aligned}$$

Hence, simplifying by $\varepsilon\exp(\lambda t)$ and considering $\varepsilon \ll 1$ we have

$$\begin{aligned}&\lambda\mu(x,u)n_0(x,u) = \mu(x,u)n_0(x,u)(B(x,u) - d_0 - 2\delta C) +\\ &\quad D_m\left(\frac{\partial^2\mu(x,u)}{\partial x^2}n_0(x,u) + 2\frac{\partial\mu(x,u)}{\partial x}\frac{\partial n_0(x,u)}{\partial x} + \mu(x,u)\frac{\partial^2 n_0(x,u)}{\partial x^2}\right) +\\ &\quad D_\gamma\left(\frac{\partial^2\mu(x,u)}{\partial u^2}n_0(x,u) + 2\frac{\partial\mu(x,u)}{\partial u}\frac{\partial n_0(x,u)}{\partial u} + \mu(x,u)\frac{\partial^2 n_0(x,u)}{\partial u^2}\right) -\\ &\quad \hat{n}(x,u,t)\int_{\mathcal{X}}\mathbb{1}_{d(x,y)<\delta}\int_{\mathcal{U}}\mu(y,w)n_0(y,w)dwdy.\end{aligned}$$

Since $\varepsilon \ll 1$, we substitute the last term in the previous equation with:

$$n_0(x,u)\int_{x-\delta}^{x+\delta}\int_{\mathcal{U}}\mu(y,w)n_0(y,w)dwdy$$

Setting $u = x$ ($\beta = 0$) and abusing notation by denoting $n_0(x,u)$ as $n_0(\beta)$ we obtain

$$\begin{aligned}\lambda\mu((m_1+m_2)x) &= (D_m m_2^2 + D_\gamma m_1^2)\mu''((m_1+m_2)x) -\\ &\int_{x-\delta}^{x+\delta}\int_{\mathcal{U}}\mu(y,w)n_0(y,w)dwdy.\end{aligned} \tag{IV.12}$$

Suppose $\mu(m_1u+m_2x) = \cos(2\pi(m_1u+m_2x))$. Using (IV.11), we can compute

$$\begin{aligned}&\int_{x-\delta}^{x+\delta}\int_{-\infty}^{\infty}\cos(2\pi(m_1w+m_2y))n_0(y,w)dwdy =\\ &\quad\frac{C}{\pi(m_1+m_2)}\exp(-2\pi^2\sigma_0^2m_1^2)\sin(2\pi(m_1+m_2)\delta)\cos(2\pi(m_1+m_2)x).\end{aligned}$$

Hence, $\mu(m_1u + m_2x) = \cos(2\pi(m_1u + m_2x))$ is a solution of equation (IV.12) if and only if

$$\lambda = -4\pi^2(D_m m_2^2 + D_\gamma m_1^2) - \frac{C}{\pi(m_1+m_2)} \exp(-2\pi^2\sigma_0^2 m_1^2)\sin(2\pi\delta(m_1+m_2)).$$

Furthermore, since the Fourier decomposition of periodic functions is unique we argue that every periodic solution of equation (IV.12) is a linear combination functions of the form $\mu(m_1u + m_2x) = \cos(2\pi(m_1u + m_2x))$ with m_1, $m_2 \in \mathbb{Z}$ giving identical values of λ.

Using the expressions of C and σ_0, we finally obtain

$$\lambda = -4\pi^2(D_m m_2^2 + D_\gamma m_1^2) - \frac{b_0 - d_0 - \sqrt{b_1(D_m + D_\gamma)}}{2\pi\delta(m_1+m_2)} \exp\left(-2\pi^2 m_1^2\sqrt{\frac{D_m + D_\gamma}{b_1}}\right)\sin(2\pi\delta(m_1+m_2)).$$

Replacing D_m by $D_m(w)$ and d_0 by $d_0(1+w)^\theta$ we have:

$$\lambda_{m_1,m_2} = -4\pi^2(D_m(w) m_2^2 + D_\gamma m_1^2) - \frac{b_0 - d_0(1+w)^\theta - \sqrt{b_1(D_m(w) + D_\gamma)}}{2\pi\delta(m_1+m_2)} \exp\left(-2\pi^2 m_1^2\sqrt{\frac{D_m(w) + D_\gamma}{b_1}}\right)\sin(2\pi\delta(m_1+m_2)).$$

In Fig. IV.20A, we show the dependence of λ_{m_1,m_2} on the values of m_1 and m_2 in $\mathbb{Z}$, for the default parameters presented in Table IV.2 (the parameters used in the simulations from Fig. IV.7). Instability of the cline-like solution can be predicted as a consequence of the existence of positive values of λ_{m_1,m_2} for multiple pairs (m_1, m_2) of perturbations in the form of equation (IV.4). Larger ranges of values of m_1 and m_2 are unnecessary since λ_{m_1,m_2} decreases when m_1 and m_2 become too large due to the boundness of the exponential and the sine and the unboundness of the first term in equation (IV.5). In this case, the highest values of λ_{m_1,m_2} occur for $|m_1 + m_2| = 7$, thus suggesting an attracting distribution for the original system fragmented into 8 clusters at a distance $1/7$ from each other, as observed in Fig. IV.7. In the torus only 7 clusters form since the ones at the boundary merge into a single one. Nevertheless, λ_{m_1,m_2} can also be positive for $|m_1 + m_2| = 6$ and $|m_1 + m_2| = 8$ suggesting that a distribution fragmented into 7 or 9 clusters is also possible when varying characteristics not considered here (for instance, the initial coverage of the population). However, these distributions grow slower for a population close to the cline-like equilibrium. Furthermore, the maxima of λ_{m_1,m_2} occur for non-zero values of m_1 at the points $(m_1, m_2) = (2, 5)$ and $(m_1, m_2) = (-2, -5)$, thus showing that the effect is strongest when periodic perturbations are made as in Fig. IV.20B instead of as in Fig. IV.20C. This is corroborated in Fig. IV.20D and Fig. IV.20E, where values of D_m and δ exist for which a perturbation only in the spatial direction would not predict instability on the cline-like equilibrium. Indeed, between $D_m \simeq 1 \times 10^{-4}$ and $D_m \simeq 1.62 \times 10^{-4}$ and in the small range between $\delta \simeq 0.076$ and $\delta \simeq 0.08$, only perturbations with $(m_1, m_2) = (2, 5)$ and $(m_1, m_2) = (-2, -5)$ would predict instability. In Section IV.7, we investigate this region and compare the analysis in [228] with ours for $D_m = 1.3 \times 10^{-4}$. In addition, we show how in the absence of evolution, clustering would occur under smaller parameter ranges.

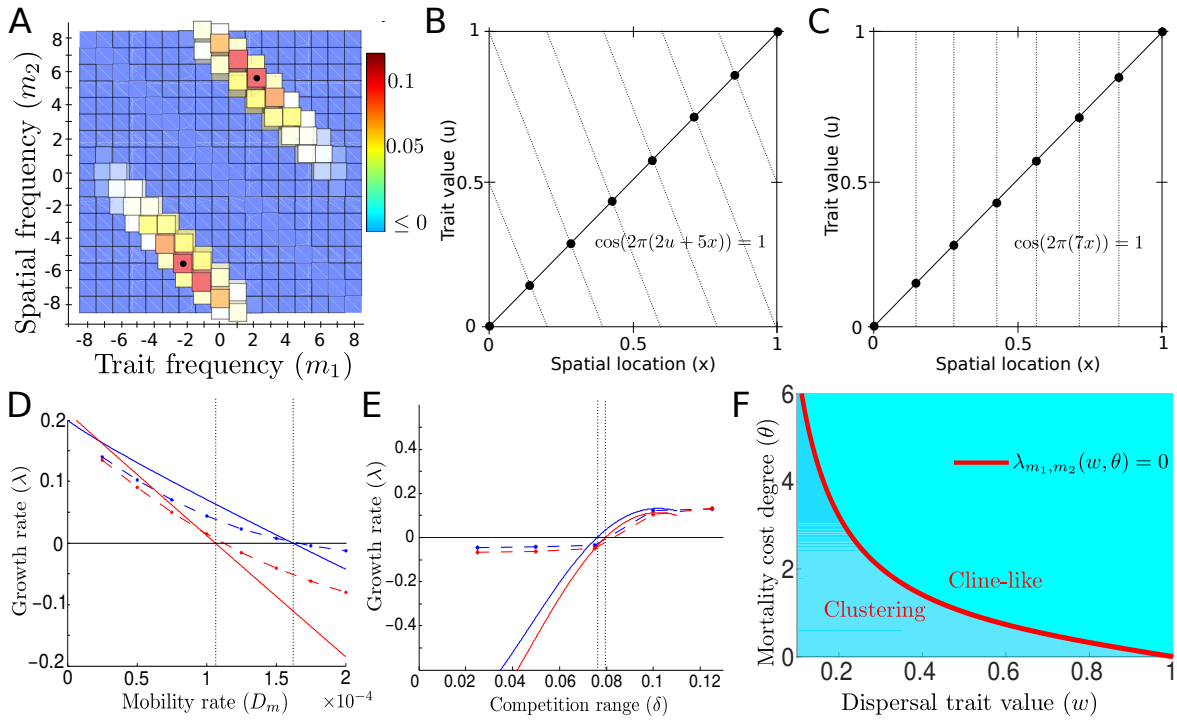

Figure IV.20: Bifurcations between clustering and cline-like stable patterns and multistability. A. The exponent λ_{m_1,m_2} in equation (IV.5) as a function of the integer frequencies m_1 and m_2. The black dots denote the maxima: $(m_1, m_2) = (2, 5)$ and $(m_1, m_2) = (-2, -5)$. Parameter values set to the default clustering parameter values in Table IV.2. B. Dashed line: maxima of a perturbation in the form of equation (IV.4) of $\rho(x-u)$ on the torus $[0,1]^2$ with $m_1 = 2$ and $m_2 = 5$. Black line: line $x = u$. Black points denote the peaks of $n(0, x, u)$.. C Dashed line: maxima of a perturbation in the form of equation (IV.4) of $\rho(x-u)$ on the torus $[0,1]^2$ with $m_1 = 0$ and $m_2 = 7$. Black line: line $x = u$. Black points denote the peaks of $n(0, x, u)$. The growth exponents λ_{m_1,m_2} (continuous line) and λ_{num} (dashed line) are shown as functions of D_m (panel D) and δ (panel E) for perturbations with $(m_1, m_2) = (0, 7)$ (red) and $(m_1, m_2) = (2, 5)$ (blue). In the computation of λ_{num}, $\varepsilon = 1 \times 10^{-3}$. F. The transition line from clustering to continuous front expansion ($\lambda_{m_1,m_2} = 0$) as a function of the dispersal trait w and the degree of mortality of dispersal θ when $(m_1, m_2) = (2, 5)$ computed from Eq. (IV.7). In Figs. IV.20A, IV.20D and IV.20E the other parameter values are set to the default clustering parameter values in Table IV.2. In Fig. IV.20F the other parameter values are set to the default parameter values in Table IV.1.

From Fig. IV.20 we can predict that the cline-like equilibrium distribution becomes stable for $D_m > D_m^* \simeq 1.62 \times 10^{-4}$ when all other parameters remain at their default values (Table IV.2). Therefore, the transition from the attractor observed in Fig. IV.7B to the one in Fig. IV.8A must occur close to this value. Contrary to D_m, an increase in δ above the threshold value $\delta^* \simeq 0.076$ causes the cline-like equilibrium to become unstable. It is expected that the dynamics will then converge towards a clustering pattern. We thus argue that the transition observed in Fig. IV.8B occurs close to this threshold value δ^*.

IV.8.2 Numerical validation of the Turing stability analysis

We now present the numerical scheme used for validating the results derived in this section with respect to the exponent λ_{m_1,m_2}. The numerical growth exponent λ_{num} obtained with this scheme is shown in Fig. IV.20. Both approaches yield similar values of mobility rate and competition range at which the cline-like equilibrium loses stability. The agreement between λ_{m_1,m_2} and λ_{num} is satisfactory only for values λ_{m_1,m_2} which are not too negative.

To construct our numerical scheme, we set periodic boundary conditions ($\bar{\mathcal{X}} \times \mathcal{U} = T^1 \times T^1$) and start from the cline-like equilibrium's approximation computed in the previous subsection. Since this is only an approximation of the cline-like equilibrium, we simulate the dynamics of this system for a time T_c to correct for imperfections. Due to the periodic boundary conditions and the constant value of the distribution along the diagonal lines, this will not cause an infringement of the cline-like condition (a distribution only dependent on $\beta = |x - u|$). We set the time T_c to be the minimum time that satisfies that the maximum difference between two consecutive time steps at all points is less than a threshold value we set to be equal to the time step size Δ_t. Based on the simulations, we observe that normally $T_c \sim 1$.

The obtained population distribution becomes the approximation of the cline-like equilibrium used to compute numerically the Lyapunov exponents of perturbations. Since the cline-like equilibrium may be unstable this might introduce errors. More precisely, since the approximate cline-like solution is actually a small perturbation of the exact cline-like solution, it has a Lyapunov exponent $\bar{\lambda}$ which might be positive. In particular, the Lyapunov exponent of a perturbation of the approximate equilibrium is not close to λ_{m_1,m_2}, but should rather be close to $\max\{\lambda_{m_1,m_2}, \bar{\lambda}\}$, hence introducing a threshold effect in the numerical computations. This threshold effect is indeed observed for small values of λ_{m_1,m_2} in Fig. IV.20E. Note also that we cannot use the clever method of computation of the cline-like equilibrium as done in [228] since, because of our boundary conditions, we are unable to reduce the spatial window of numerical resolution of the PDE so that possible perturbations have very strong frequencies and do not destabilize the equilibrium. Nevertheless, the approximation was good enough so that the dynamics always converged towards a distribution that only depends on values of $|x - u|$.

After we retrieve an approximation of the cline-like equilibrium distribution $n_0(x, u) = n_0(|x - u|)$, we introduce a perturbation of the form:

$$\hat{n}_0(x, u) = (1 + \varepsilon \cos(2(m_1 u + m_2 x)))n_0(x, u), \tag{IV.13}$$

$\varepsilon \ll 1$, for several integer values of m_1 and m_2. Next, we simulate the dynamics of $\hat{n}(x, u, t)$, $\hat{n}(x, u, 0) = \hat{n}_0(x, u)$ and measure the growth or decay of the perturbation by calculating the exponent:

$$\lambda_{num} = \max_{i \in I} \left\{ \left\langle \frac{\log(|n_0(x_i, u_i) - \hat{n}(x_i, u_i, n\delta t)|/|n_0(x_i, u_i) - \hat{n}_0(x_i, u_i)|)}{n\delta t} \right\rangle_{n\delta t \leq T_p} \right\}.$$

where δt is the time step size and I is an enumeration of the points along the line $x = u$ of the grid on which we simulate the dynamics of the system. Again —although λ_{num} is not

necessarily equal to λ_{m_1,m_2}— if λ_{num} is positive, the cline-like equilibrium is unstable for perturbations of the form in equation (IV.13). If this is the case for at least one pair (m_1, m_2) it is expected that the attracting state of the system will be distributed among isolated clusters.

In Fig. IV.20 we show the computation of λ_{num} when varying D_m and δ for perturbations with $(m_1, m_2) = (0, 7)$ and $(m_1, m_2) = (2, 5)$, this last pair resulted in the highest registered value of λ_{num} in the considered ranges of both parameters. As observed, results in figure Fig. IV.20D show an almost perfect consistency with their analytical counterpart when approximating the transition value D_m^* of D_m for both pairs (m_1, m_2) considered. Thus we corroborate that when increasing the dispersal rate D_m, the transition from the clustering attractor to the to cline-like one occurs at a threshold value $D_m^* \simeq 1.6 \times 10^{-4}$. Again this value would have been miscalculated if only perturbations along the spatial component had been considered.

The numerical simulations for determining λ_{num} as function of δ are harder due to practical issues. More precisely, the spatial discretization of space as cells of width Δ_x needs to be chosen so that δ/Δ_x is an integer. Given Δ_x, for values of δ such that δ/Δ_x is an integer, the numerical scheme is exactly the same as for $\delta' = \Delta_x \lfloor \delta/\Delta_x \rfloor$ and so the computed values of λ are the same. Hence, to have a precise estimate of λ as a function of δ, we need to take very small Δ_x. However, this is impractical in terms of numerical cost since the stability condition of explicit finite difference scheme requires to take time-steps Δ_t even smaller. Therefore, our numerical validation for the dependence with respect to δ has been validated for $\Delta_x = 0.025$, and hence for the values $\delta = 0.025,\ 0.05,\ 0.075,\ 0.1,\ 0.125$, shown in Fig. IV.20E. Of course, these five values are not sufficient to determine precisely the location of the transition from cline-like to clustering patterns, predicted to be close to $\delta^* \simeq 0.076$ from the analytical approximation (IV.6). Nevertheless, results are consistent, indicating that the transition occurs at a value larger but close to $\delta = 0.075$ and that λ_{num} is smaller when $(m_1, m_2) = (0, 7)$ than when $(m_1, m_2) = (2, 5)$.

In the simulations we use an explicit scheme before and after introducing the perturbation. In both cases we considered a step size $\Delta_x = \Delta_u = 2.5 \times 10^{-2}$ and a time-step size $\Delta_t = 1 \times 10^{-3}$.

IV.9 Dynamics and asymptotics under low mobility and small mutations

Here we present a Hamilton-Jacobi approach (following the work in [41]) to analyze the dynamics and asymptotics of clustering in the PDE model for low individual mobility and small mutations when mobility does not evolve. A similar analysis can be performed for the generalized model with evolving dispersal. However, results would be analogous given that one of the assumptions is low individual mobility (only expansion through formation of clusters).

The method is based on a concentration approximation of the population as a sum of Dirac delta functions. These distribution functions are characterized by: (1) having value zero everywhere except at one point and (2) having a positive integral over the entire domain. The approximation method allows to derive a Hamilton-Jacobi equation whose solution $\varphi(x,u,t)$ is non-positive and has its zeros exactly at the points where the population is concentrated, therefore allowing to mathematically identify the positions of the clusters where the population aggregates.

IV.9.1 Derivation of the Hamilton-Jacobi equation

Hereafter we prove that in a periodic, invariant solution $\varphi(x,u)$ of (IV.15) which is not identically 0 along the line $x=u$, the zeros of φ along the line $x=u$ are necessary separated by a distance δ/n for some $n\in\mathbb{N}^*$. We also show that this invariant solution is stable only if its zeros are at a distance δ. This suggest that, in cases where clustering occurs (as discussed above), provided individual mobility is low and mutations are small, the clusters are spaced by a distance close to δ. This is consistent with the simulations of Fig. IV.7.

We take $\mathcal{X}=\mathcal{U}=\mathbb{R}$ to make competition uniform along $\mathcal{X}\times\mathcal{U}$ and to remove boundary effects from our analysis. Let $\varepsilon>0$. In order to concentrate the population's distribution into Dirac delta functions (by letting $\varepsilon\to 0$), we will redefine the diffusion coefficient as $D_m\varepsilon^2$ and the standard deviation of the mutation transition measure as $\varepsilon\sigma$. In this case, the appropriate time scaling to observe a limit process in the limit of small mutations and slow motion is $\tau=\frac{t}{\varepsilon}$. Hereafter we will simplify notations and use t for τ. Let $n^\varepsilon(x,u,t)$ represent the approximation of $n(x,u,t)$ according to this rescaling and $\varphi^\varepsilon(x,u,t):=\varepsilon\log(n^\varepsilon(x,u,t))$.One has that

$$\begin{aligned}\varepsilon\frac{\partial}{\partial t}n^\varepsilon(x,u,t)&=\varepsilon^2D_m\Delta_x n^\varepsilon(x,u,t)+n^\varepsilon(x,u,t)\times\\&\left((1-\gamma)B(x,u)-d_0-\int_{\mathcal{X}}\int_{\mathcal{U}}\mathbb{1}_{|x-y|<\delta}\times n^\varepsilon(y,w,t)dwdy\right)\\&+\gamma\int_{\mathcal{U}}B(x,w)n^\varepsilon(x,w,t)\Pi^\varepsilon(w\to u)dw.\end{aligned}$$

Where

$$\Pi^\varepsilon(w\to u)=\frac{1}{\varepsilon\sigma\sqrt{2\pi}}\exp\left(-\frac{(u-w)^2}{2\sigma^2\varepsilon^2}\right)$$

denotes the rescaled mutation-transition measure concentrating mutation events in a neighborhood of size ε around w. Multiplying on both sides of the equation by $\frac{1}{n^\varepsilon(x,u,t)}$ yields

$$\begin{aligned}\frac{\varepsilon}{n^\varepsilon(x,u,t)}\frac{\partial}{\partial t}n^\varepsilon(x,u,t) &= (1-\gamma)B(x,u) - d_0 - \\ &\int_{\mathcal{X}}\int_{\mathcal{U}} \mathbb{1}_{|x-y|<\delta} \times n^\varepsilon(y,w,t)dwdy + \frac{\varepsilon^2 D_m \Delta_x n^\varepsilon(x,u,t)}{n^\varepsilon(x,u,t)} + \\ &\frac{\gamma}{n^\varepsilon(x,u,t)} \times \int_{\mathcal{U}} B(x,w)n^\varepsilon(x,w,t)\frac{1}{\varepsilon\sigma\sqrt{2\pi}}\exp\left(-\frac{(u-w)^2}{2\sigma^2\varepsilon^2}\right)dw. \qquad \text{(IV.14)}\end{aligned}$$

Consider now the substitution $\varphi^\varepsilon(x,u,t) := \varepsilon\log(n^\varepsilon(x,u,t))$, or, expressed differently, $n^\varepsilon(x,u,t) = \exp\left(\frac{\varphi^\varepsilon(x,u,t)}{\varepsilon}\right)$. Intuitively, what we aim for is that, when setting $\varepsilon \to 0$, $\varphi^\varepsilon(x,u,t)$ will converge to a function $\varphi(x,u,t)$ which will be negative at the points where $n^\varepsilon(x,u,t)$ converges to 0, and that will never be positive as this would make $n^\varepsilon(x,u,t)$ blow up. Thus, assuming that $\int_{\mathcal{X}}\int_{\mathcal{U}} n^\varepsilon(y,w,t)dwdy$ is strictly positive and bounded from above (both conditions independent of ε), we will have that, as $\varepsilon \to 0$, $n^\varepsilon(x,u,t)$ will concentrate in Dirac delta functions at the points where $\varphi^\varepsilon(x,u,t) \to \varphi(x,u,t) = 0$. As anticipated, making the substitution in (IV.14) and introducing the change of variable $z = \frac{u-w}{\varepsilon}$ we obtain

$$\begin{aligned}\frac{\partial}{\partial t}\varphi^\varepsilon(x,u,t) &= (1-\gamma)B(x,u) - d_0 - \int_{\mathcal{X}}\int_{\mathcal{U}} \mathbb{1}_{|x-y|<\delta} \times \exp\left(\frac{\varphi^\varepsilon(y,w,t)}{\varepsilon}\right)dwdy \\ &+ \varepsilon D_m \Delta_x \varphi^\varepsilon(x,u,t) + D_m\left|\frac{\partial}{\partial x}\varphi^\varepsilon(x,u,t)\right|^2 \\ &- \gamma\int_{\frac{u}{\varepsilon}}^{\frac{u-1}{\varepsilon}} B(x,u+z\varepsilon)\exp\left(-\frac{(\varphi^\varepsilon(x,u,t)-\varphi^\varepsilon(x,u+z\varepsilon,t))}{\varepsilon}\right)\frac{1}{\sigma\sqrt{2\pi}}\exp\left(-\frac{z^2}{2\sigma^2}\right)dz.\end{aligned}$$

Let $\mu_t(dy,dw)$ be the weak limit of $n^\varepsilon(x,u,t) = \exp(\frac{\varphi^\varepsilon(y,w,t)}{\varepsilon})dwdy$ when ε approaches zero. Assuming ε small suggests that $\varphi^\varepsilon(x,u,t)$ converges to a function $\varphi(x,u,t)$ satisfying the Hamilton–Jacobi equation (of first order with a Hamiltonian non-linearity in $(\frac{\partial\varphi(x,u,t)}{\partial x}, \frac{\partial\varphi(x,u,t)}{\partial u})$):

$$\begin{aligned}\frac{\partial}{\partial t}\varphi(x,u,t) &= B(x,u) - d_0 - \int_{\mathcal{X}}\int_{\mathcal{U}} \mathbb{1}_{|x-y|<\delta} \times \mu_t(dy,dw) \\ &+ D_m\left|\frac{\partial}{\partial x}\varphi(x,u,t)\right|^2 + \gamma B(x,u)H\left(\frac{\partial\varphi(x,u,t)}{\partial u}\right), \qquad \text{(IV.15)}\end{aligned}$$

where

$$H\left(\frac{\partial\varphi(x,u,t)}{\partial u}\right) := \int_{-\infty}^{\infty}\left(\exp\left(-\frac{\partial\varphi(x,u,t)}{\partial u}z\right)-1\right)\frac{1}{\sigma\sqrt{2\pi}}\exp\left(-\frac{z^2}{2\sigma^2}\right)dz.$$

Since the mutation kernel is a Gaussian we can simplify the function $H\left(\frac{\partial\varphi(x,u,t)}{\partial u}\right)$ to be:

$$H\left(\frac{\partial\varphi(x,u,t)}{\partial u}\right) = \exp\left(\frac{\sigma^2}{2}\left(\frac{\partial\varphi(x,u,t)}{\partial u}\right)^2\right) - 1. \qquad \text{(IV.16)}$$

Since $\varphi^\varepsilon(x,u,t) = \varepsilon \log(n^\varepsilon(x,u,t))$, $\varphi^\varepsilon(x,u,t) \to \varphi(x,u,t)$ implies that $\mu_t(dy,dw)$ should be concentrated at the zeros of φ at a time t, set which we denote by Ω_t. Hence, the distance between two successive zeros of φ at time t can be interpreted as the distance between two consecutive clusters. In general, the proof of $\varphi^\varepsilon(x,u,t) \to \varphi(x,u,t)$ and $\exp(\frac{\varphi^\varepsilon(y,w,t)}{\varepsilon})dwdy \to \mu_t(dy,dw)$ is difficult and has only been obtained for a few models [225, 226, 435–439]; here, we assume that convergence holds and focus on the limiting equation.

Assuming convergence $\varphi^\varepsilon(x,u,t) \to \varphi(x,u,t)$ and $\exp(\frac{\varphi^\varepsilon(y,w,t)}{\varepsilon})dwdy \to \mu_t(dy,dw)$, we have that $\varphi(x,u,t)$ must satisfy the following conditions:

$$
\begin{aligned}
&(i)\ \varphi(x,u) \le 0 \quad \forall (x,u) \in \mathcal{X}\times\mathcal{U},\\
&(ii)\ \sup_{(x,u)\in\mathcal{X}\times\mathcal{U}} \varphi(x,u,t) = 0,\\
&(iii)\ Supp(\mu) \subseteq \Omega_t := \{(x,u) : \varphi(x,u,t) = 0\},\\
&(iv)\ \forall (x,u) \in \Omega_t, \quad (1-\gamma)B(x,u) - d_0 -\\
&\qquad \int_{\mathcal{X}}\int_{\mathcal{U}} \mathbb{1}_{|x-y|<\delta}\mu_t(dy,dw) \le 0,\\
&(v)\ \forall (x,u) \in Supp(\mu_t), \quad \{(1-\gamma)B(x,u) - d_0\\
&\qquad - \int_{\mathcal{X}}\int_{\mathcal{U}} \mathbb{1}_{|x-y|<\delta}\mu_t(dy,dw)\} = 0,
\end{aligned}
$$

where *(i)* is needed to prevent the solution u_ε to explode as $\varepsilon \to 0$, *(ii)* follows from the fact that $\int_{\mathcal{X}\times\mathcal{U}} u_\varepsilon(t,x,u)dx\,du$ cannot vanish when $\varepsilon \to 0$, and *(iii)* is due to the fact that μ_t cannot give mass at points where φ is negative. Conditions *(iv)*, *(v)* are consequences of the elements of Ω_t being local extrema of φ and indicates that μ_t is a quasi-equilibrium for the dynamics without mutation for all $t \ge 0$ (see [438]). In particular, when $\Omega_t = \{(x_i,u_i); i \in I_t\}$ with I_t finite or countable, condition *(iii)* implies that $\mu_t(dy,dw)$ has the form

$$
\mu_t(dy,dw) = \sum_{i\in I_t} \alpha_i \delta_{(x_i,u_i)}dwdy \tag{IV.17}
$$

for some appropriate weights $(\alpha_i)_{i\in I_t}$. Thus, the distance between two successive zeros of φ at time t can be interpreted as the distance between clusters.

In the model of evolving dispersal an analogous equation to Eq. IV.15 can be derived. This equation is:

$$
\begin{aligned}
\frac{\partial}{\partial t}\varphi(x,u,w,t) &= (1+\gamma)B(x,u) - d_0(1+w)^\theta - \int_{\mathcal{X}}\int_{\mathcal{U}}\int_{\mathcal{W}} \mathbb{1}_{|x-y|<\delta} \times \mu_t(dy,da,db)\\
&+ D_m(1+w)\left|\frac{\partial}{\partial x}\varphi(x,u,w,t)\right|^2 + \gamma B(x,u)\left(H\left(\frac{\partial\varphi(x,u,w,t)}{\partial u}\right) + H\left(\frac{\partial\varphi(x,u,w,t)}{\partial w}\right)\right),
\end{aligned}
$$

With

$$
H\left(\frac{\partial\varphi(x,u,w,t)}{\partial u}\right) = \exp\left(\frac{\sigma^2}{2}\left(\frac{\partial\varphi(x,u,w,t)}{\partial u}\right)^2\right) - 1,
$$

and

$$
H\left(\frac{\partial\varphi(x,u,w,t)}{\partial w}\right) = \exp\left(\frac{\sigma^2}{2}\left(\frac{\partial\varphi(x,u,w,t)}{\partial w}\right)^2\right) - 1.
$$

As was noted, in the limit of low individual mobility (very low w), expansion only occurs through the formation of clusters. Hence, the subsequent analysis is analogous to a model of evolving dispersal (with $w \simeq 0$).

IV.9.2 Distance between clusters and stability of periodic asymptotic solutions

Suppose we have an invariant solution $\hat{\varphi}(x,u)$ to equation (IV.15). Since selection is strongest along the line $x=u$, we will assume that the points for which $\hat{\varphi}(x,u)=0$ are located along this line i.e that $u_i = x_i$ $i \in \mathcal{I}$. We will try to determine the characteristics of this solution (the number of clusters and their spacing). To do this, let us first remove the boundary conditions ($\mathcal{X} = \mathcal{U} = \mathbb{R}$) and suppose, without loss of generality, that $\hat{\varphi}(0,0) = 0$ (i.e that the population is concentrated in a Dirac delta at $(0,0)$). Since we are interested in solutions exhibiting periodic clustering patterns we make the assumption of constant positive spacing between clusters (supported by simulations). Hence, Ω_t is countable and there exists $T>0$ minimal for which $\hat{\varphi}(x,u) = \hat{\varphi}(x+T, u+T)$. Combining both conditions we have, $\Omega_t = \{(nT, nT),\ n \in \mathbb{Z}\}$. Notice that the value of T is the distance between the Dirac delta peaks and hence the distance between clusters. Since we are interested in the behaviour along the line $x=u$, when imposing this condition, equation (IV.15) for $\hat{\varphi}(x,x)$, which we denote by $\hat{\varphi}(x)$, becomes

$$0 = b_0 - d_0 - \sum_{n\in\mathbb{Z}} \alpha_n \mathbb{1}_{|x-nT|<\delta} + D_m \left| \frac{\partial \hat{\varphi}}{\partial x}(x,x) \right|^2 + \gamma b_0\ H\left(\frac{\partial \hat{\varphi}}{\partial u}(x,x) \right). \tag{IV.18}$$

Since the points in Ω_t are local maxima, we have that, for all $n \in \mathbb{Z}$, $\frac{\partial \hat{\varphi}(x,u)}{\partial u}|_{(nT,nT)} = \frac{\partial \hat{\varphi}(x,u)}{\partial x}|_{(nT,nT)} = 0$. This last property requires some care, since actually, due to the singularity of the competition kernel, the function $\hat{\varphi}$ may not admit derivatives at its local maxima. However, we can approximate the competition kernel $\mathbb{1}_{[-\delta,\delta]}$ by a sequence of smooth kernels $(K_k)_{k\geq 1}$ and argue that the corresponding solution φ_k converges to $\hat{\varphi}$, and $\frac{\partial \varphi_k(x,u)}{\partial u}|_{(nT,nT)} = \frac{\partial \varphi_k(x,u)}{\partial x}|_{(nT,nT)} = 0$ for all $k \geq 1$. To make this rigorous, one would need to use stability properties of the Hamilton-Jacobi problem with constraints (i) to (v). However, this is not known in general since for such equations, even the problem of uniqueness is difficult [440, 441]. If we leave aside this difficulty, we obtain that, for $(x,u) \in \Omega_t$,

$$b_0 - d_0 - \sum_{n\in\mathbb{Z}} \alpha_n \mathbb{1}_{|x-nT|<\delta} = 0.$$

Suppose now that $T > \delta$. Consider the point $(0,0)$. Because of the condition stated above and the fact that all other $(x_i,u_i) \in \Omega_t$ satisfy $|x - x_i| > \delta$, one has that

$$b_0 - d_0 - \alpha_0 = 0.$$

Now, let $0 < \varepsilon < T - \delta$. By evaluating equation (IV.18) at the point $(\varepsilon,\varepsilon)$, one has that

$$\begin{aligned} 0 &= b_0 - d_0 - \alpha_0 + D_m \left| \frac{\partial \hat{\varphi}}{\partial x}(\varepsilon,\varepsilon) \right|^2 + \gamma b_0\, H\left(\frac{\partial \hat{\varphi}}{\partial u}(\varepsilon,\varepsilon) \right) \\ &= D_m \left| \frac{\partial \hat{\varphi}}{\partial x}(\varepsilon,\varepsilon) \right|^2 + \gamma b_0\, H\left(\frac{\partial \hat{\varphi}}{\partial u}(\varepsilon,\varepsilon) \right). \end{aligned} \tag{IV.19}$$

We observe that, by Jensen's inequality

$$H(p) = \mathbb{E}(\exp(pG) - 1) \geq \exp(p\mathbb{E}(G)) - 1 = 0$$

The inequality is strict unless $p = 0$. Therefore, equation (IV.19) implies $\frac{\partial \hat{\varphi}}{\partial u}(\varepsilon, \varepsilon) = \frac{\partial \hat{\varphi}}{\partial x}(\varepsilon, \varepsilon) = 0$. Since ε was arbitrary, we have that for every $\kappa \in [0, T - \delta)$, $\frac{\partial}{\partial u}\hat{\varphi}(\kappa, \kappa) = \frac{\partial}{\partial x}\hat{\varphi}(\kappa, \kappa) = 0$. Hence, $\hat{\varphi}(\kappa, \kappa) = 0 \; \forall \kappa \in [0, T-\delta)$ which is a contradiction since Ω_t was taken to be countable.

Suppose now that $T < \delta$, and that $\frac{\delta}{T} \notin \mathbb{N}$. Then, again for $(0, 0)$ one has

$$b_0 - d_0 - \sum_{n \in \mathbb{Z},\ |n|T < \delta} \alpha_n \mathbb{1}_{|x - nT| < \delta} = b_0 - d_0 - \sum_{n=-\lfloor \frac{\delta}{T} \rfloor}^{\lfloor \frac{\delta}{T} \rfloor} \alpha_n = 0.$$

Letting $0 < \varepsilon < \delta - \lfloor \frac{\delta}{T} \rfloor \times T$ and using the same analysis as in the previous case one can arrive to the same contradictions. This proves that $T \leq \delta$ and that $\frac{\delta}{T} \in \mathbb{N}$.

We denote a solution with period $T = \frac{\delta}{m}$, $m \in \mathbb{N}^*$ along the axis $x = u$ by $\hat{\varphi}_m$. We now prove that solutions $\hat{\varphi}_m$ with $m > 1$ are unstable. We prove this result only for $\hat{\varphi}_2$, the proof is analogous for all $m > 2$. We suppose without loss of generality that the zeros of $\hat{\varphi}_2$ are located at the points $\left(\frac{n\delta}{2}, \frac{n\delta}{2}\right)$, $n \in \mathbb{Z}$, associated each with a weight α_n. The stability condition (v) implies that, for all $k \in \mathbb{Z}$,

$$b_0 - d_0 = \alpha_{k-1} + \alpha_k + \alpha_{k+1}.$$

In particular, this imples that the sequence $(\alpha_k)_{k \in \mathbb{Z}}$ is 3-periodic. Let $\hat{\varphi}_2^*$ be a small perturbation of $\hat{\varphi}_2$ where the only modification with respect to $\hat{\varphi}_2$ is that it is modified on a small ball of radius $\eta > 0$ centered at $(0, 0)$ such that the point $(0, 0)$ is still a local maximum but with a value slightly below zero. Hence the measure $\mu(dx, du)$ associated to $\hat{\varphi}_2^*$ satisfying conditions (i)–(v) has no Dirac mass close to $(0, 0)$. We denote the new weights at the zeros of $\hat{\varphi}_2^*$ located at the points $\left(n\frac{\delta}{2}, n\frac{\delta}{2}\right)$, $n \in \mathbb{Z}$, $n \neq 1$, by α_n^*. As above, these weights satisfy

$$b_0 - d_0 = \alpha_{k-1}^* + \alpha_k^* + \alpha_{k+1}^*, \tag{IV.20}$$

for all $k \in \mathbb{Z}$ with $k \neq 0$, with the convention that $\alpha_0^* = 0$. Again, the sequence $(\alpha_k^*)_{k \in \mathbb{Z}}$ is 3-periodic and hence $\alpha_{3k}^* = 0$ for all $k \in \mathbb{Z}$ and $\alpha_1^* + \alpha_2^* = b_0 - d_0$. In particular, (IV.20) is also true for $k = 0$. Since $\alpha_0 > 0$, the fact that $\alpha_1^* + \alpha_2^* = b_0 - d_0$ implies that we either have $\alpha_1^* > \alpha_1$ or $\alpha_2^* > \alpha_2$ (maybe both). Let us assume (without loss of generality) that $\alpha_1^* > \alpha_1$.

We can now consider the solution $\hat{\varphi}_2^*(x, u, t)$ of (IV.15) with initial condition $\hat{\varphi}_2^*$ (with a slight abuse of notation). For all $x \in \mathbb{R}$ such that $|x| > \eta$ and $x \in (k\delta/2, (k+1)\delta/2)$ for some

$k \in \mathbb{Z}$,

$$\begin{aligned}\frac{\partial \hat\varphi_2^*}{\partial t}(x,x,0) &= b_0 - d_0 - \alpha_{k-1}^* - \alpha_k^* - \alpha_{k+1}^* - \alpha_{k+2}^* \\ &\quad + D_m \left|\frac{\partial \hat\varphi_2^*}{\partial x}(x,x,0)\right|^2 + \gamma b_0 H\left(\frac{\partial \hat\varphi_2^*}{\partial x}(x,x,0)\right) \\ &= b_0 - d_0 - \alpha_{k-1}^* - \alpha_k^* - \alpha_{k+1}^* - \alpha_{k+2}^* \\ &\quad + D_m \left|\frac{\partial \hat\varphi_2}{\partial x}(x,x)\right|^2 + \gamma b_0 H\left(\frac{\partial \hat\varphi_2}{\partial x}(x,x)\right) \\ &= \alpha_{k-1} + \alpha_k + \alpha_{k+1} + \alpha_{k+2} - \alpha_{k-1}^* - \alpha_k^* - \alpha_{k+1}^* - \alpha_{k+2}^* \\ &= \alpha_{k-1} - \alpha_{k-1}^*,\end{aligned}$$

where we used in the third equality that $\hat\varphi_2$ is a stationary solution of (IV.15). Hence we have proved that $\frac{\partial \hat\varphi_2^*}{\partial t}(x,x,0) < 0$ for all $|x| > \eta$ such that $x \in (k\delta/2, (k+1)\delta/2)$ for some $k \in 3\mathbb{Z}+2$. In particular, the perturbation does not converge back to $\hat\varphi_2$, which is hence unstable.

To conclude we need to check that the solution $\hat\varphi_1$ with period $T = \delta$ is stable. This is a non-trivial problem, and we will only check a weak form of stability, assuming only specific perturbations of $\hat\varphi_1$. We assume without loss of generality that the zeroes of $\hat\varphi_1$ are located at the points $(n\delta, n\delta)$. Suppose a perturbation is made in such a way that the new function $\hat\varphi_1^*$ is different from the original solution only in a small ball of radius $\eta > 0$ centered at $(0,0)$ (this point is arbitrary) such that $\hat\varphi_1^*(0,0) = -\varepsilon < 0$ is a local maximum. Hence the measure μ associated to $\hat\varphi_1^*$ loses a Dirac mass at $(0,0)$. In this case, $\alpha_k^* = \alpha_k = b_0 - d_0$ for all $k \neq 1$, so that $\frac{\partial \hat\varphi_1^*}{\partial t}(x,u,0) = 0$ for all (x,u) at a distance larger than δ from $(0,0)$ and

$$\left.\frac{\partial \hat\varphi_1^*(x,u,t)}{\partial t}\right|_{t=x=u=0} = b_0 - d_0 > 0,$$

since there are no neighboring maxima located at a distance smaller than δ. Hence the solution has an initial tendency to approach $\hat\varphi_1$. However, the dynamics becomes more complicated after time 0 since the local maxima initially at $(n\delta, n\delta)$ for $n \neq 0$ might move. Of course, this is not sufficient to prove stability, but this strongly suggests that stability should hold true.

IV.9.3 Transient dynamics of clusters

Eq. (IV.15) also provides information on the transient dynamics of clusters – on their formation times, location, motion, and shape. As discussed in [442], one has to be cautious about the conclusions regarding time scales since the speed of evolution in the Hamilton-Jacobi model is very sensitive to the initial condition away from zero. However, the location of clusters in the Hamilton-Jacobi equation brings interesting biological insights, as illustrated by the simulation of Fig. IV.21. In this simulation, the dynamics of φ are studied numerically by integrating equation (IV.15). The algorithm built for this purpose is non trivial and is described in the next subsection. We consider parameter values that yield clustering. For the initial population density we take $n^\varepsilon(x,u,0) = \exp(-\frac{2(x-0.5)^2}{\varepsilon} - \frac{2(u-0.5)^2}{\varepsilon})$, i.e. an initial population close to the Dirac peak at $(0.5, 0.5)$. This choice for a Gaussian distribution in the original model translates into an initial condition where φ is quadratic and non-positive

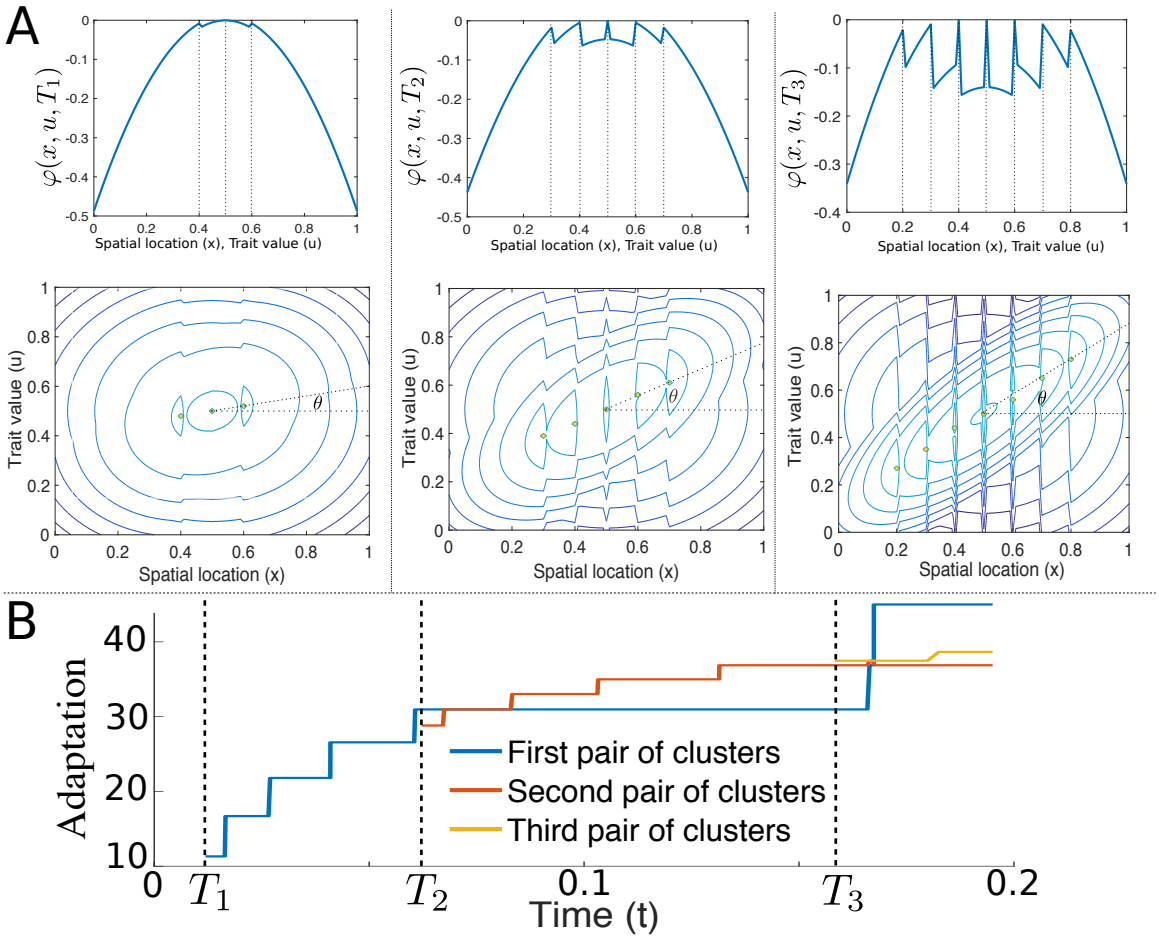

Figure IV.21: Simulations of the Hamilton-Jacobi equation. A. Snapshots of two different profiles of $\varphi(x,u,T_i)$, $i=1,2,3$ at the times where φ develops a new pair of zeros (the times where new clusters emerge). Top: $\varphi(x,u,T_i)$ along the line $x=u$. Bottom: Contour plot of $\varphi(x,u,T_i)$ and position of its local maxima in yellow. B. Time-evolution of the angle (in degrees) between each pair of clusters and the midpoint of the domain. Parameters set to the default clustering values (Table IV.2).

with one zero at $(0.5,0.5)$.

Fig. IV.21A shows snapshots of the simulation at the times where new pairs of clusters emerge (when new zeros of φ appear). The irregular shape of the function φ is due to the fact that the interaction kernel is not continuous. Otherwise, one would expect φ to be smoother, except at local minima of φ, where singularities are expected in Hamilton-Jacobi equations. Fig. IV.21 confirms that, when the population is initially concentrated at the mid-point of the 2-dimensional domain, and the dynamics converge to clustering patterns, the expected distance between the clusters (in physical space) will be δ. In addition, the rate at which zeros appear (which is equivalent to the rate at which new clusters form) is not constant: the time between two consecutive clustering events increases. Even though time has been re-scaled, properties such as the ratio of clustering times are left unaffected.

We also observe that spatial clustering occurs faster than phenotypical clustering since the local speed of diffusion $D_m = 5 \times 10^{-5}$ is larger than the local maximal speed of trait motion $b_0\gamma\sigma^2/2 = 0.00001$, obtained by a local expansion of $\exp(-\frac{\partial\varphi}{\partial u}z)$ in the mutation term in (IV.15) (valid since σ^2 is small). This is shown in Fig. IV.21B, where clusters first occur away from the diagonal, and then slowly shift towards the line $x = u$ as the local populations adapt. Because our rescaling of motion was the same both in the spatial and phenotypic directions, clusters in the original system are expected to behave similarly.

IV.9.4 Numerical integration of the Hamilton–Jacobi equation

We take as initial condition $\varphi(x, u, 0) = -(x - 0.5)^2 - (u - 0.5)^2$ and we compute the dynamics of φ according to the Hamilton–Jacobi equation (IV.15) using an explicit scheme. In order to always satisfy condition *(i)* we need to use a scheme with variable time-step where the time step is set to Δt unless the condition of negativity is violated for at least one point. In this case, we take the minimum time step for which the nonpositivity condition is maintained and used it instead. We then obtain a function $\varphi(x, u, t + \Delta t')$ admitting at least one more zero that $\varphi(x, u, t)$. In the next time step, some of the zeroes might disappear if $\partial_t\varphi(x, u, t + \Delta t') < 0$ at some of these points. To compute the Hamiltonian function $H\left(\frac{\partial\varphi(x,u,t)}{\partial u}\right)$, we use the expression in Eq. (IV.16).

To compute the values of the α_i's in the density function $\mu(dy, dw, t)$ (introduced in equation (IV.17)) which satisfy conditions *(iv), (v)*, we use the following scheme. If there is just one pair (x, u) satisfying $\varphi(x, u, t) = 0$, i.e $|\Omega_t| = 1$, we set its respective coefficient α to the unique value satisfying condition *(v)*.

Consider now the case when $|\Omega_t| \geq 2$. Let $(x_i, u_i) \in \Omega_t$, $1 \leq i \leq m := |\Omega_t|$ denote the elements of Ω_t. In order to find the appropriate values of the α_i's we first divide the set Ω_t into smaller sets A_k constructed inductively by using the following method. Initially we construct A_1 as the set containing the first element (x_1, u_1) of Ω_t. Then, for every $1 < i \leq m$, the pair (x_i, u_i) is added to a set A_k if there exists a pair $(x_j, u_j) \in A_k$ such that $|x_i - x_j| < \delta$. If there exists more than one A_k satisfying this condition, then A_k will be redefined as the union of such sets. One can picture the sets A_k as sets containing the pairs (x_i, u_i) with correlated values of α_i's in the sense that elements of different sets do not compete among them. Likewise, in the end, no elements from two different sets will be at a distance less than δ. Once this is done, in each subset A_k we verify whether conditions *(iv), (v)* can be satisfied when setting one of the values of the α_i's to the value imposed by condition *(v)* and setting the values of the other α_j's to zero. If this is the case for at least one element (x_i, u_i) in each A_k, we take such values of the α's to be coefficients of $\mu(dy, dw, t)$. Otherwise, if this conditions are not satisfied we compute numerically the values of the α_i's as the solutions of

the system appearing from imposing condition *(v)* to every element in $|\Omega_t|$;

$$\begin{aligned} b_0 - b_1(x_1 - u_1)^2 - d_0 - \sum_{i \leq m} \mathbb{1}_{|x_1 - x_i| < \delta} \alpha_i = 0, \\ b_0 - b_1(x_2 - u_2)^2 - d_0 - \sum_{i \leq m} \mathbb{1}_{|x_2 - x_i| < \delta} \alpha_i = 0, \\ \vdots \\ b_0 - b_1(x_m - u_m)^2 - d_0 - \sum_{i \leq m} \mathbb{1}_{|x_m - x_i| < \delta} \alpha_i = 0. \end{aligned}$$

In principle we should look for other solutions for which the subset S_k of elements $(x_i, u_i)_k$ associated to non-zero α's in each set A_k has size 2, then 3 and so on. In practice, however, we only look at cases where $|S_k| = 1$ or $|\cup_k S_k| = m$ and these ones were enough at short time scales like the ones we use in our simulations.

IV.10 Extensions to the model with no evolving dispersal

IV.10.1 Two-Dimensional spatial domain and one-dimensional spatial adaptation

In this section we consider an extension of the deterministic, infinite population size model with no evolving dispersal where the physical domain $\overline{\mathcal{X}} \times \overline{\mathcal{Y}} \subset \mathbb{R}^2$ is two-dimensional ($\overline{\mathcal{Y}} = \overline{\mathcal{X}}$).

Individuals are characterized by a vector (x, y, u) with spatial components $x \in \overline{\mathcal{X}}$ and $y \in \overline{\mathcal{Y}}$ and a trait $u \in \mathcal{U}$. Spatial movement is two-dimensional but the birth rate, which depends on how adapted individuals are to their local environment only varies along one of the spatial dimensions. As in the original one-dimensional spatial model, the degree of (mal)adaptation is measured by the difference between the individual trait and the local optima. Competition is two-dimensional with a range δ in both dimensions. For the sake of simplicity in the numerical simulations we take a boxed shaped competition range of distance δ in each dimension (the competition range is a square of side 2δ) instead of the euclidean two dimensional distance.

More precisely, the birth rate of an individual at (x, y, u) in a population of N_t individuals located at (x_i, y_i, u_i), $i = 1, ..., N_t$ remains

$$B(x, u) = \max\left\{b_0 - b_1(x - u)^2; 0\right\},$$

while the death rate becomes

$$d_0 + d_1 \sum_{i=1}^{N_t} \mathbb{1}_{|x-x_i|<\delta} \times \mathbb{1}_{|y-y_i|<\delta},$$

Mutation events are identical as in the one-dimensional spatial model. Meanwhile, individuals undergo diffusion with mobility rates (diffusion coefficients) D_x and D_y in the first and second spatial dimensions respectively.

The deterministic approximation of this two-dimensional spatial model is:

$$\begin{aligned}
\frac{\partial n(x,y,u,t)}{\partial t} = {} & D_x \frac{\partial^2 n(x,y,u,t)}{\partial x^2} + D_y \frac{\partial^2 n(x,y,u,t)}{\partial y^2} + n(x,y,u,t)\times \\
& \left((1-\gamma)B(x,u) - d_0 - \int_{\mathcal{X}}\int_{\mathcal{Y}}\int_{\mathcal{U}} \mathbb{1}_{|x-a|<\delta}\mathbb{1}_{|y-b|<\delta} \times n(a,b,w,t)dwdbda\right) \\
& + \gamma \int_{\mathcal{U}} n(x,y,w,t)B(x,w)\frac{1}{\sqrt{2\pi}\sigma}\exp\left(-\frac{(u-w)^2}{2\sigma^2}\right)dw, \\
\left.\frac{\partial n(x,y,u,t)}{\partial x}\right|_{x=0} = {} & \left.\frac{\partial n(x,y,u,t)}{\partial x}\right|_{x=1} = 0, \\
\left.\frac{\partial n(x,y,u,t)}{\partial y}\right|_{y=0} = {} & \left.\frac{\partial n(x,y,u,t)}{\partial y}\right|_{y=1} = 0, \\
n(x,y,0,t) = {} & n(x,y,1,t) = 0, \quad x \in \overline{\mathcal{X}}, y \in \overline{\mathcal{Y}}, \quad t \geq 0.
\end{aligned} \tag{IV.21}$$

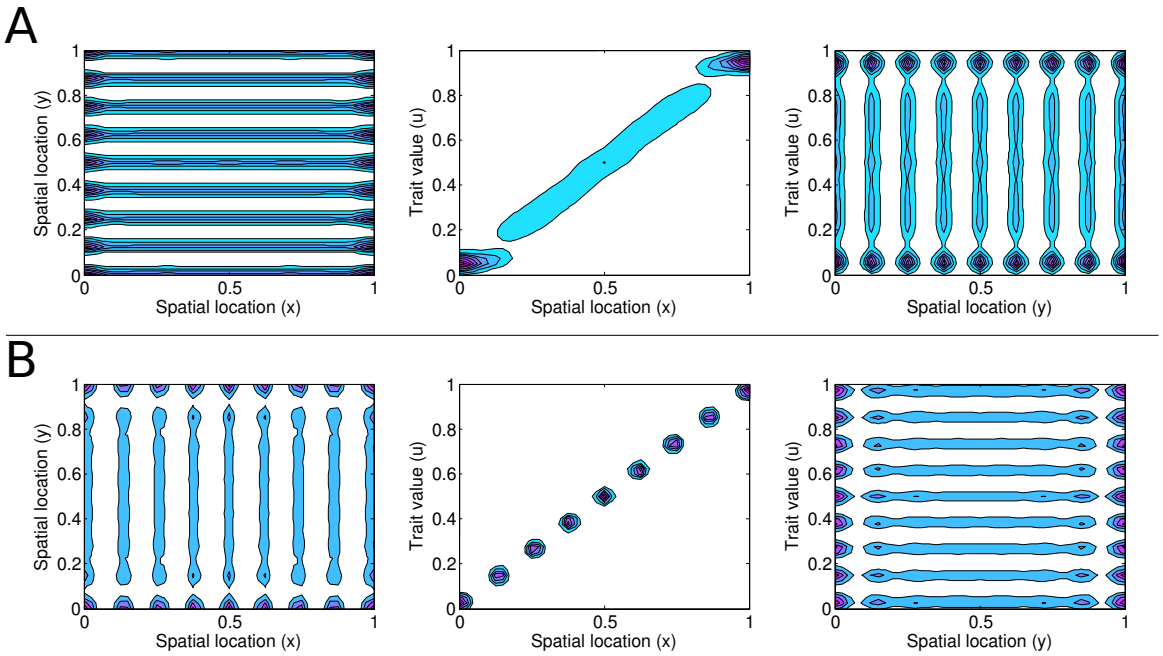

Figure IV.22: Two-dimensional physical space. A. Cline-like distribution along $\overline{\mathcal{X}}$ and clustered distribution along $\overline{\mathcal{Y}}$. Contour plot of the final concentration density after a time $T = 150$. Diffusion rates are $D_x = 5 \times 10^{-4}$ and $D_y = 5 \times 10^{-5}$. B. Almost cline-like distribution along $\overline{\mathcal{Y}}$ and clustered distribution along $\overline{\mathcal{X}}$. Contour plot of the final concentration density after a time $T = 150$. Diffusion rates are $D_x = 5 \times 10^{-5}$ and $D_y = 1.35 \times 10^{-4}$. At $T = 0$ the distribution has the form of a Gaussian with standard deviation $\sigma_0 = 1 \times 10^{-2}$ in all three dimensions and centered at $(0.5, 0.5, 0.5)$. Other parameter values set to the default clustering parameter values in Table IV.2. In all panels, cyan represents the lowest density and magenta the highest. Density is negligible in white areas.

Simulations of this variant show that the spatial dynamics on each one of the spatial dimensions appear to be independent. In each spatial direction either clustering or cline-like propagation (as a continuous front) occurs depending on D_x and D_y respectively. Similarly, the attractor can be a clustering or a cline-like (constant) pattern in both, either or neither dimension depending on their mobility rates. Clustering in trait space occurs only through clustering in the spatial dimension $\overline{\mathcal{X}}$.

Fig. IV.22 shows the long-term concentrations of the population in physical xy space, and in the physical-trait spaces xu and yu after two simulations. As in the one-dimensional spatial model we use an explicit finite difference scheme to simulate the dynamics of the normalized population according to Eq. (IV.21). As shown, clustering in the spatial direction $\overline{\mathcal{X}}$ can occur simultaneous to cline-like (constant) distributions on the spatial direction $\overline{\mathcal{X}}$ if diffusion is slow in the first and fast in the second (and on the contrary). When clustering occurs in both spatial dimensions, the number of clusters in two-dimensional physical space is $n_C^x \times n_C^y$ clusters wheren_C^x are the number of clusters in $\overline{\mathcal{X}}$ and $\overline{\mathcal{Y}}$ respectively.

Notably, and in consistency with the results in the one-dimensional spatial model derived in Section IV.8.1, multistability is also present and the exact transition values values of D_x and D_y where the model jumps between attractors –although similar– vary. More precisely, clustering occurs under wider parameter conditions when space and trait space interact through selection (physical dimension $\overline{\mathcal{X}}$ and trait space $\mathcal{U}$). That is: $D_x^* > D_y^*$ (see Fig. IV.22A).

The derivation of the Hamilton-Jacobi equation associated to this variant in the limit of small mutations and slow motion is analogous to the analysis in IV.9.1. Here, the function $\varphi^\varepsilon(x,y,u,t)$ is suggested to converge to $\varphi(x,y,u,t)$ satisfying the equation:

$$\frac{\partial}{\partial t}\varphi(x,y,u,t) = B(x,u) - d_0 - \int_{\mathcal{X}}\int_{\mathcal{Y}}\int_{\mathcal{U}} \mathbb{1}_{|x-a|<\delta}\mathbb{1}_{|x-b|<\delta} \times \mu_t(da,db,dw) + D_x\left|\frac{\partial}{\partial x}\varphi(x,y,u,t)\right|^2 + D_y\left|\frac{\partial}{\partial y}\varphi(x,y,u,t)\right|^2 + \gamma B(x,u) H\left(\frac{\partial\varphi(x,y,u,t)}{\partial u}\right),$$

where $H\left(\frac{\partial\varphi(x,y,u,t)}{\partial u}\right)$ was defined in Eq. (IV.16).

IV.10.2Two-Dimensional spatial domain and two-dimensional spatial adaptation

We consider another variant of a model where physical space is two-dimensional and where adaptation to the local environment varies on both physical dimensions $\overline{\mathcal{X}}$ and $\overline{\mathcal{Y}}$. The model is identical to the one in the previous section with the exception of the birth rate which becomes

$$B(x,y,u) = \max\left\{b_0 - b_1(x-u)^2(y-u)^2; 0\right\}.$$

Without the loss of generality and due to rescaling we can assume the same form of dependence in the optimal trait with respect to local optimum along both spatial dimensions. The deterministic approximation of this variant becomes:

$$\begin{aligned}\frac{\partial n(x,y,u,t)}{\partial t} = {} & D_x\frac{\partial^2 n(x,y,u,t)}{\partial x^2} + D_y\frac{\partial^2 n(x,y,u,t)}{\partial y^2} + n(x,y,u,t)\times \\ & \left((1-\gamma)B(x,y,u) - d_0 - \int_{\mathcal{X}}\int_{\mathcal{Y}}\int_{\mathcal{U}} \mathbb{1}_{|x-a|<\delta}\mathbb{1}_{|y-b|<\delta} \times n(a,b,w,t)dwdbda\right) \\ & + \gamma\int_{\mathcal{U}} n(x,y,w,t)B(x,y,w)\frac{1}{\sqrt{2\pi}\sigma}\exp\left(-\frac{(u-w)^2}{2\sigma^2}\right)dw,\end{aligned} \tag{IV.22}$$

$$\left.\frac{\partial n(x,y,u,t)}{\partial x}\right|_{x=0} = \left.\frac{\partial n(x,y,u,t)}{\partial x}\right|_{x=1} = 0,$$

$$\left.\frac{\partial n(x,y,u,t)}{\partial y}\right|_{y=0} = \left.\frac{\partial n(x,y,u,t)}{\partial y}\right|_{y=1} = 0,$$

$$n(x,y,0,t) = n(x,y,1,t) = 0, \quad x\in\overline{\mathcal{X}}, y\in\overline{\mathcal{Y}}, \quad t\geq 0.$$

Numerical simulations of Eq. (IV.22) show qualitative differences with the original one-dimensional spatial model and with the first two-dimensional spatial variant. Although the

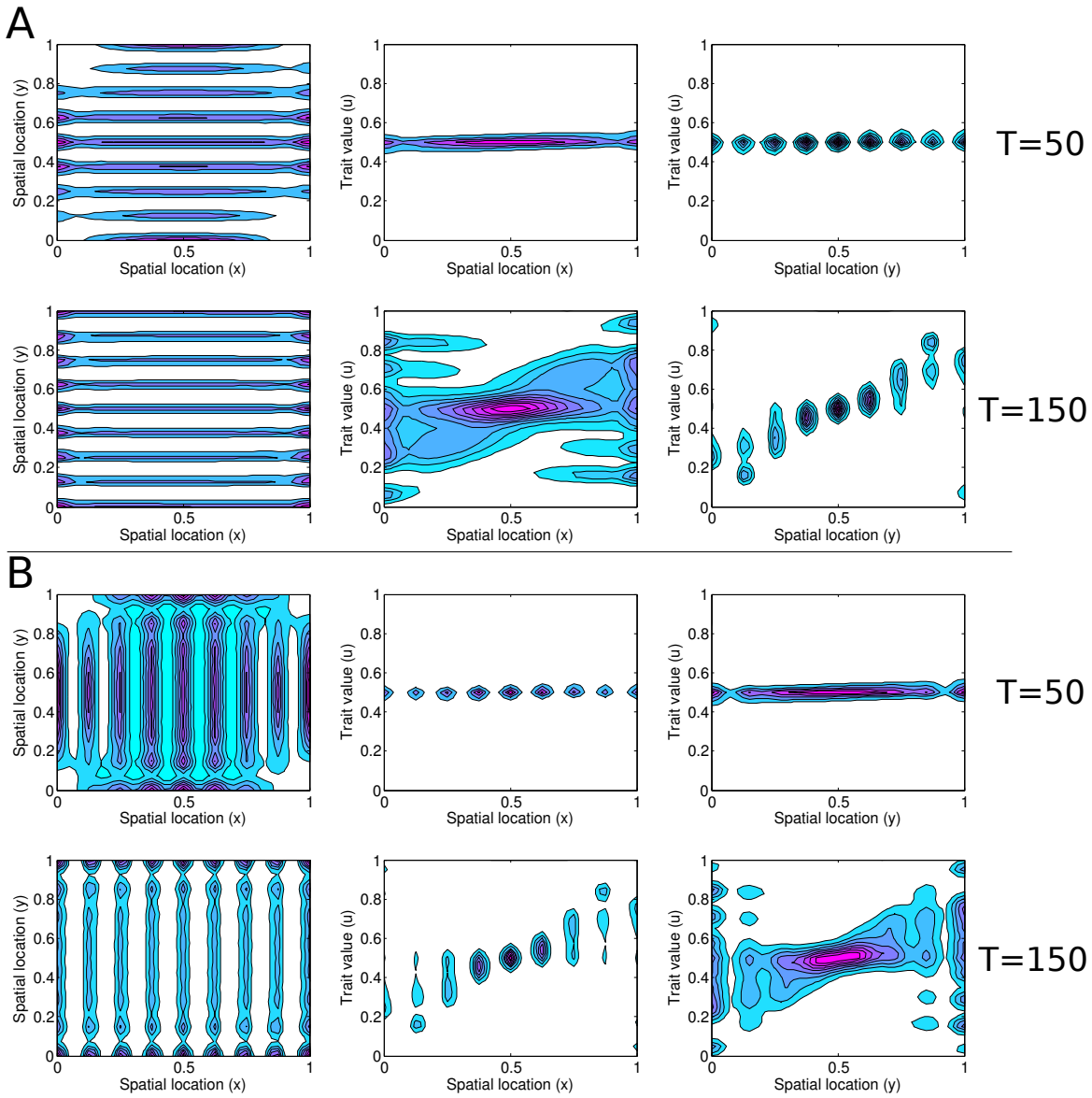

Figure IV.23: Two-dimensional physical space and two-dimensional spatial adaptation. A. Contour plot of the concentration density after a time $T = 50$ (top) and $T = 150$ (bottom). Diffusion rates are $D_x = 5 \times 10^{-4}$ and $D_y = 5 \times 10^{-5}$. B. Contour plot of the concentration density after a time $T = 50$ (top) and $T = 150$ (bottom). Diffusion rates are $D_x = 5 \times 10^{-5}$ and $D_y = 1.35 \times 10^{-4}$. At $T = 0$ the distribution has the form of a Gaussian with standard deviation $\sigma_0 = 1 \times 10^{-2}$ in all three dimensions and centered at $(0.5, 0.5, 0.5)$. Other parameter values set to the default clustering parameter values in Table IV.2. In all panels, cyan represents the lowest density and magenta the highest. Density is negligible in white areas.

model requires further exploration, considering its rich and complex dynamics, it can observed (see Fig. IV.23) that mutation and phenotypic spread is substantially more limited. Since the decay in the birth rate is stronger for mutants located further away from the local optimum (although slightly), their invasion capacity is hindered which limits density growth for other trait values. However, at longer temporal scales, once the population has invaded physical space through cluster propagation or cline-like wave-fronts (depending on D_x and D_y respectively), mutational effects accumulate, translating distribution along $\overline{\mathcal{X}}$ and $\overline{\mathcal{Y}}$ (concentrated at the initial central value $u = 0.5$) to the optimal line $x = y = u$. As in the other two-dimensional variant, multistability is also present and clustering and constant patterns can simultaneously occur on each spatial projection depending on the coefficients D_x and D_y. Nevertheless, the transition values D_x^*, D_y^* are different from those in the original one-dimensional spatial model.

The transient dynamics of the system on the spatio-phenotypic projections during the translation along trait-space of the (initially) clustered or constant distributions to the line $x = y = u$ are interesting and complex, as are the long-term distributions of the population. In the original one-dimensional spatial model and the first two-dimensional spatial variant, the distribution in trait space inherits its structure from the distribution in the associated spatial dimension (through selection in the birth rate). Here, since trait interacts with both spatial dimensions, the distribution along the two space-trait projections exhibits a mixed behavior between both physical regimes. This is seen in Figs. IV.23A and IV.23B at $T = 150$, where the population distribution along $\mathcal{U}$ propagates in what appears as a combination of cline-like wave fronts and clustering patterns. Moreover, meta-clusters (or clusters of clusters) can also be present due to the possibility of multiple optimal evolutionary strategies for a trait value u located and (x, y) with $x \neq y$.

As in the previous section. The derivation of the Hamilton-Jacobi equation associated to this variant in the limit of small mutations and slow motion is analogous to the analysis in IV.9.1. Here, the function $\varphi^\varepsilon(x, y, u, t)$ is suggested to converge to $\varphi(x, y, u, t)$ satisfying the equation:

$$\frac{\partial}{\partial t}\varphi(x,y,u,t) = B(x,y,u) - d_0 - \int_{\mathcal{X}}\int_{\mathcal{Y}}\int_{\mathcal{U}} \mathbb{1}_{|x-a|<\delta}\mathbb{1}_{|x-b|<\delta} \times \mu_t(da,db,dw) + D_x\left|\frac{\partial}{\partial x}\varphi(x,y,u,t)\right|^2 + D_y\left|\frac{\partial}{\partial y}\varphi(x,y,u,t)\right|^2 + \gamma B(x,y,u) H\left(\frac{\partial\varphi(x,y,u,t)}{\partial u}\right),$$

where $H\left(\frac{\partial\varphi(x,y,u,t)}{\partial u}\right)$ was defined in Eq. (IV.16).

IV.10.3Effect of environmental gradient steepness

Here we show that results from the original model are robust to different steepness of the environmental gradient. We modify the birth rate so that (mal)adaptation declines with a slope $g > 0$. That is

$$B(x,u) = \max\left\{b_0 - b_1(x-gu)^2; 0\right\},$$

with the partial differential equation for this variant being identical to Eq. (IV.3). We verify with simulations that results from the paper hold under appropriate scalings of mutation

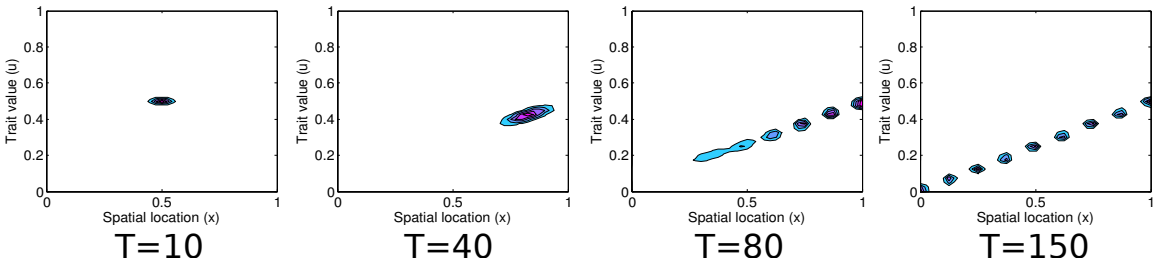

Figure IV.24: Clustering under steeper environmental gradients. Contour plot of the concentration density at four different stages of the simulation. At $T = 0$ the distribution has the form of a Gaussian with standard deviation $\sigma_0 = 1 \times 10^{-2}$ in all three dimensions and centered at $(0.5, 0.5)$. Other parameter values set to the default clustering parameter values in Table IV.2. In all panels, cyan represents the lowest density and magenta the highest. Density is negligible in white areas.

related parameters. That is, clustering and cline-like equilibria can occur, multistability is also present and Hamilton-Jacobi equations are possible to derive. We show one example of a simulation with a gradient steepness $g = 2$ in Fig. IV.24. Since the initial spatial location is far away from the optimal position (for the initial trait value), the population migrates in space to then spread through the formation of clusters analogously to the simulations of the original model in Fig. IV.7B.

Since the partial differential equation for this variant is identical to Eq. (IV.3), the Hamilton-Jacobi equation –suggested to be associated with the model– is the same as Eq. (IV.15).

IV.10.4Allee effect from nearby identical population's density

We consider two variants of the model in which we incorporate Allee effects. In both, we aim to capture the biological fact that local adaptation (u compared to x) determines the reproductive potential of an individual, and then nearby density (of identical or of all phenotypes) determines whether this potential is realized or not.

In the first Allee effect variant we take

$$B(x,u,n) = \max\left\{(b_0 - b_1(x-u)^2) \times \frac{\int_{\mathcal{X}} \mathbb{1}_{|x-y|<\delta} \times n(y,u,t)dy}{c_1 + \int_{\mathcal{X}} \mathbb{1}_{|x-y|<\delta} \times n(y,u,t)dy}; 0\right\},$$

where the range of interaction (of distance δ) with nearby neighbors is the same as in the death-by-competition term. The parameter $c_1 \geq 0$ needs to be chosen carefully in relation with the integral. If c_1 is too large the population goes extinct since the birth rate is low. If c_1 is too small the results of the variant are indistinguishable from those of original model. If c_1 is intermediate, when the density of neighbor identical individuals is very low, the birth rate is close to zero and the reproductive potential is hardly expressed. When density is very high, the ratio in birth rate is close to 1, and the reproductive potential is realized fully.

Fig. IV.25 shows the density of the population at different times from two simulations converging to clustering and cline-like patterns respectively. As in the original model, the

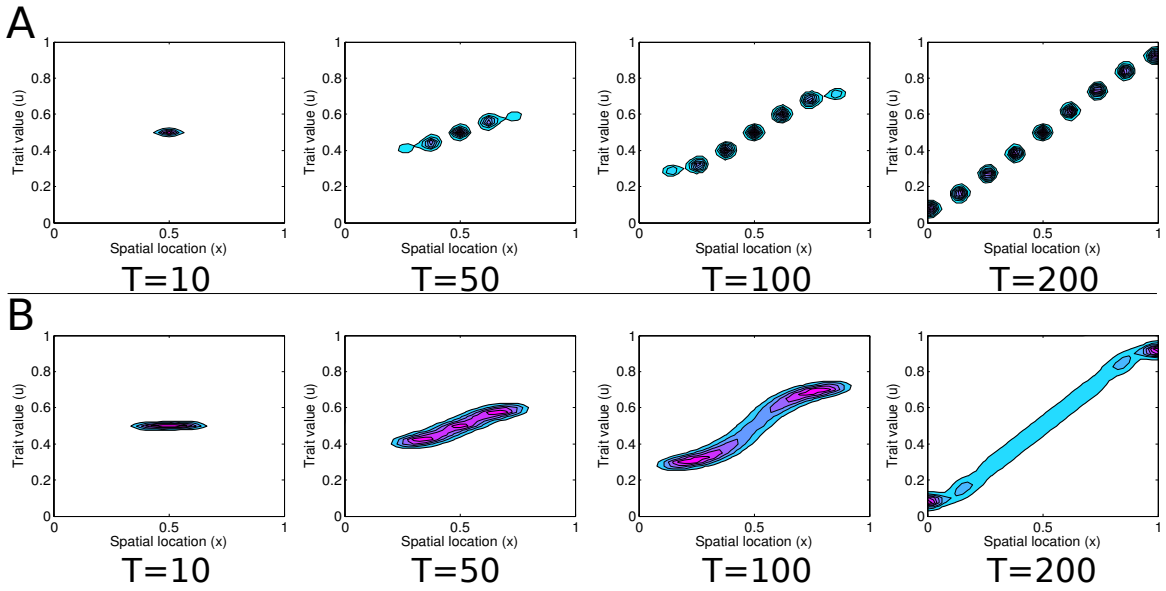

Figure IV.25: Clustering and cline-like density patterns after the inclusion of Allee Effects from identical individuals. A. Clustering attractor. Contour plot of the concentration density at four different stages of a simulation with $D_m = 5 \times 10^{-5}$. B. Cline-like attractor. Contour plot of the concentration density at four different stages of the simulation with $D_m = 2 \times 10^{-4}$. At $T = 0$ the distribution has the form of a Gaussian with standard deviation $\sigma_0 = 1 \times 10^{-2}$ in all three dimensions and centered at $(0.5, 0.5)$. In both simulations $c_1 = 1 \times 10^{-3}$. Other parameter values set to the default clustering parameter values in Table IV.2. In all panels, cyan represents the lowest density and magenta the highest. Density is negligible in white areas.

population spreads through the formation of clusters and converges to a clustering pattern if the diffusion rate is low. When spatial mobility is increased, the population spreads as a continuous front (where the density of individuals at the extremes is higher than in the original model) and converges to a cline-like pattern with high accumulation at the edges due to decreased competition.

In general –for intermediate and small values of c_1– the incorporation of Allee effects (from identical individuals) to the original model does not affect qualitatively the dynamics. Aggregation of similar individuals (and hence clustering) appears to be slightly favored (clustering can occur for mobility rates moderately higher than D_m^*) due to the increase in the birth rate. The aggregation of individuals in Fig. IV.25B in the center and at the borders is higher than in the original model. Furthermore, and depending on the parameter c_1, the expansion dynamics can be significantly slowed down (to the point of extinction), as shown in Fig. IV.25 where after $T = 100$ the population is yet to reach the boundaries of the domain. Moreover, even under a fourfold increase in D_m (Fig. IV.25B with respect to Fig. IV.25A), the spatial ranges of the population appear to be the same at all times. This suggests, that under intermediate values of c_1, it is mutation that dominates the speed of spatial invasion of the population. Since birth rates are decreased due to lower population

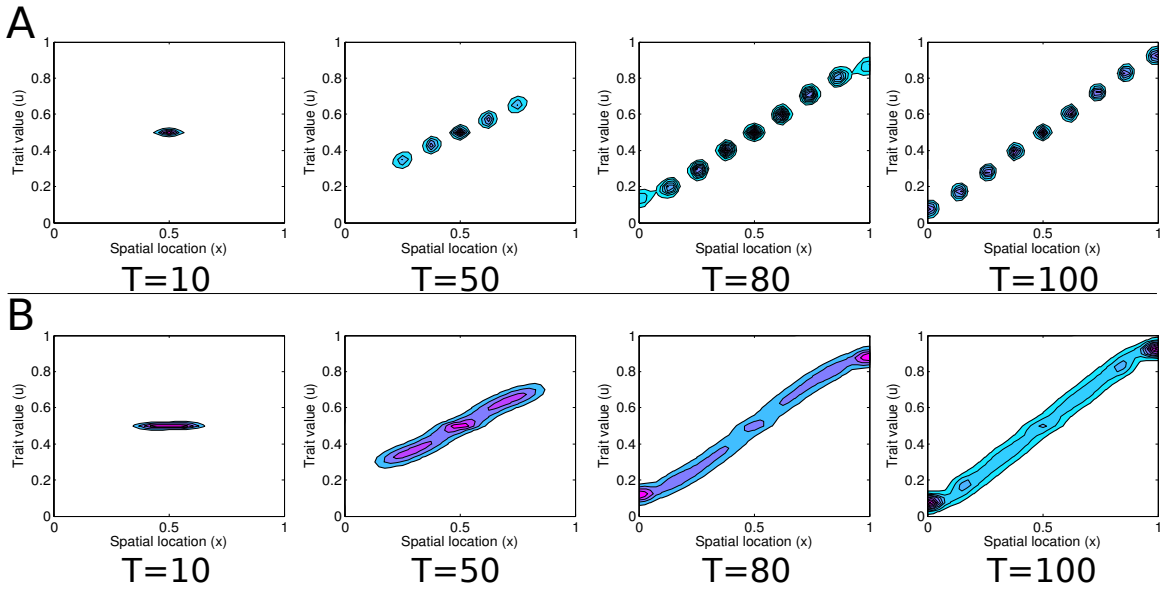

Figure IV.26: Clustering and cline-like density patterns after the inclusion of Allee Effects. A. Clustering attractor. Contour plot of the concentration density at four different stages of a simulation with $D_m = 5 \times 10^{-5}$. B. Cline-like attractor. Contour plot of the concentration density at four different stages of the simulation with $D_m = 2 \times 10^{-4}$. At $T = 0$ the distribution has the form of a Gaussian with standard deviation $\sigma_0 = 1 \times 10^{-2}$ in all three dimensions and centered at $(0.5, 0.5)$. In both simulations $c_2 = 1 \times 10^{-3}$. Other parameter values set to the default clustering parameter values in Table IV.2. In all panels, cyan represents the lowest density and magenta the highest. Density is negligible in white areas.

density, there is an increase in the impact of adaptation on the survival and prosperity of invading populations.

IV.10.5Allee effect from nearby population's density

We consider a second variant of the model incorporating Allee Effects where the reproductive potential of an individual depends on the nearby density of all phenotypes. The birth rate has the form

$$B(x,u,n) = \max\left\{(b_0 - b_1(x-u)^2) \times \frac{\int_{\mathcal{X}}\int_{\mathcal{U}} \mathbb{1}_{|x-y|<\delta} \times n(y,w,t)dwdy}{c_2 + \int_{\mathcal{X}}\int_{\mathcal{U}} \mathbb{1}_{|x-y|<\delta} \times n(y,w,t)dwdy}; 0\right\}.$$

Again, there is a qualitative and quantitative dependence on the parameter $c_2 \geq 0$. High c_2 results in population extinction. Small and intermediate values of c_2 yield equivalent or slowed versions of the original model which converge in the long term to either clustering of cline-like distributions (Fig. IV.26). As shown in Fig. IV.26, for c_2 equal to the value of c_1 used in the simulations in Fig. IV.25, the population expansion on both phenotypic and spatial dimensions is faster (at $T = 80$ it has reached both boundaries). Since the reproductive potential is achieved through the nearby density of all individuals, invasion is facilitated.

Both forms of Allee effects show equivalent results after a proper scaling of the parameter c_1. More precisely, results are equivalent for $c_1 = c_2^2$.

We note that observations from the original model are sustained under the inclusion of both forms of Allee effects depending on c_1 and c_2. When this occurs, the exact transition (critical) parameter values where the population changes between attractors change and depend on the parameter. Their approximation can be computed in analogous fashion as in IV.8.1.

In contrast, the derivation of Hamilton-Jacobi equations for the two variants is not analogous to the original model and non-trivial since the local birth rate depends on the population's distribution.

IV.11 Evolving dispersal and Allee effects from identical individuals

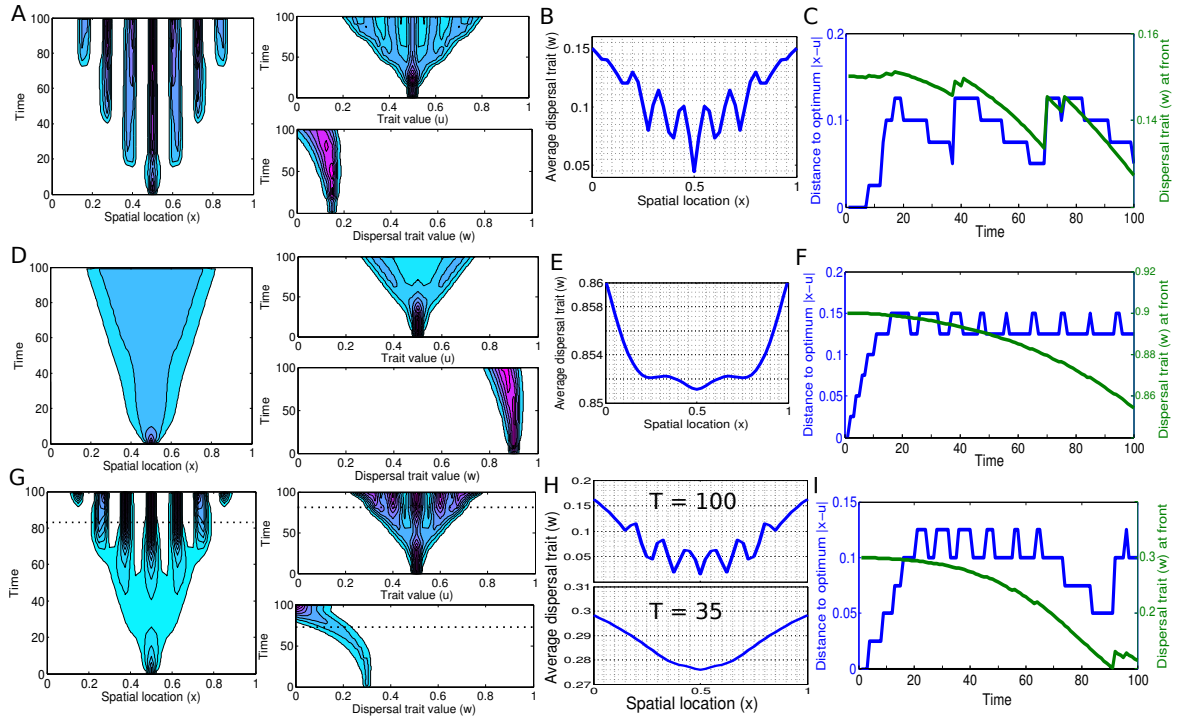

Figure IV.27: Dynamics of invasion in physical, and trait spaces in the model of evolving dispersal with Allee effects from nearby identical individuals. Adaptational and expansion regimes, dispersal traits and invasion speed at front. Time-evolution of spatial, niche trait and dispersal trait distributions when $w_0 = 0.15$ and $\theta = 0.75$ (Panel A), $w_0 = 0.9$ and $\theta = 0.75$ (Panel D), $w_0 = 0.3$ and $\theta = 1.75$ (Panel G). Average dispersal trait at each spatial location at $T = 100$ when $w_0 = 0.15$ and $\theta = 0.75$ (Panel B), $w_0 = 0.9$ and $\theta = 0.75$ (Panel E). Average dispersal trait at each spatial location at $T = 100$ (top) and $T = 35$ (bottom) when $w_0 = 0.3$ and $\theta = 1.75$ (Panel H). Time-evolution of the distance between local optimal niche trait and the physical location ($|x-u|$) and of dispersal traits at the front of the population when $w_0 = 0.15$ and $\theta = 0.75$ (Panel C), $w_0 = 0.9$ and $\theta = 0.75$ (Panel F), $w_0 = 0.3$ and $\theta = 1.75$ (Panel I). At $T = 0$ the distribution has the form of a Gaussian with standard deviation $\sigma_0 = 0.1$ (in the three dimensions) centered at $(0.5, 0.5, w_0)$. Other parameters set to the default values in Table IV.1. In all panels, cyan represents the lowest density and magenta the highest. Density is negligible in white areas.

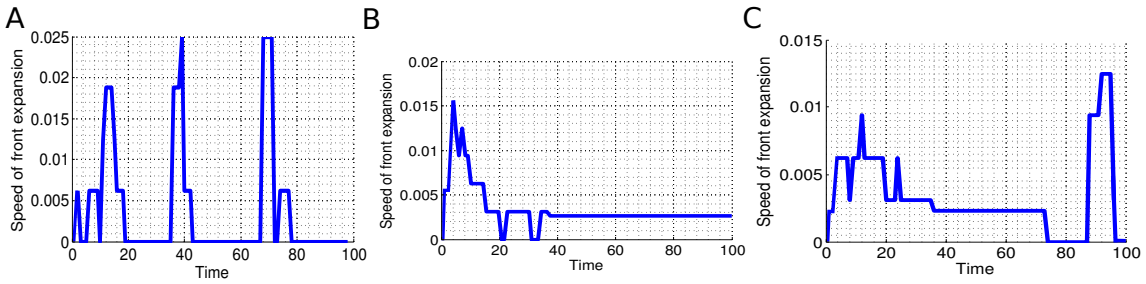

Figure IV.28: Invasion speeds in the model of evolving dispersal with Allee effects from nearby identical individuals. Spatial invasion speed when $w_0 = 0.15$ and $\theta = 0.75$ (Panel A), $w_0 = 0.9$ and $\theta = 0.75$ (Panel B), $w_0 = 0.3$ and $\theta = 1.75$ (Panel C). At $T = 0$ the distribution has the form of a Gaussian with standard deviation $\sigma_0 = 0.1$ (in the three dimensions) centered at $(0.5, 0.5, w_0)$. Other parameters set to the default values in Table IV.1.

V – Equation-free analysis of equilibria and multi-stability in spatially-explicit eco-evolutionary dynamics of a population along a one-dimensional resource gradient

Martín Andrade-Restrepo[1], Jens Starke[2]

[1] Institut Jacques Monod, CNRS UMR 7592,
Université Paris Diderot, Paris Cité Sorbonne, F-750205, Paris, France
[2] Institute of Mathematics, Scientific Computing Group, University of Rostock, D-18057,
Rostock, Germany

Abstract

We present an equation-free approach to analyze equilibria (stable and unstable) and of multi-stability in the stochastic dynamical system appearing when studying the evolution of a population along a one-dimensional environmental gradient. In this system, continuous or clustering patterns (with different number of clusters) emerge from local ecological interactions between the individuals. These patterns have distinct eco-evolutionary interpretations related to the evolution of diversity in absence of strong geographical barriers. More specifically, concerning speciation or adaptive diversification through the formation of spatially isolated clusters. We analyze the microscopic high-dimensional dynamics of a stochastic individual–based model through a low dimensional restriction (at the slow manifold) which is able to capture information such as existing equilibria (stable and unstable) and the bifurcations occurring in terms of one its ecological parameters. Obtained results show that the system is multi-stable with a strong presence of hysteresis due to the potential presence of successive saddle node bifurcations. Our method can be extended to other individual-based-models of eco-evolutionary dynamics for which a mathematical analysis is unfeasible or impractical or to multi-scale models exhibiting substantial noise.

V.1 Introduction

Speciation events and diversification in biological populations occurring as a consequence of geographic isolation between subpopulations has been well documented in empirical [24, 25] and experimental work [443] and is well understood from a theoretical perspective [23, 444, 445]. When subpopulations are not geographically isolated, diversification clashes with the principles of natural selection (*i.e* of 'survival of the fittest') and with some of the principles of population genetics (*e.g* gene-flow) [445, 446] and hence remains an issue of controversy for both its feasibility and its frequency.

Contributing to this debate, recent seminal empirical studies have found monophyletic populations which have diverged in conditions where geographic isolation seems unlikely [27–34, 169, 174, 175]. These studies have been reinforced by increasing evidence from experimental work supporting the idea that ecological interactions can frequently generate environments favoring the emergence and stability of phenotypically and genetically diverse populations [36–40]. Moreover, theoretical analysis has demonstrated that diversification in quantitative-trait models can occur as a consequence of disruptive selection [164], an outcome of the 'eco-evolutionary feedback', where ecological and evolutionary changes exert reciprocal influences on one another [156, 160, 162].

Mathematical models have shown how eco-evolutionary feedbacks alter population and evolutionary dynamics and species interactions [164, 186, 447, 448] mainly in non-spatial domains. However, although ecological interactions are tied to spatial constraints, the spatial aspect of eco-evolutionary dynamics remains poorly understood [449, 450].

The work from Doebeli and Dieckmann 2003 [22], on spatially-explicit eco-evolutionary dynamics extends earlier theory on species coexistence [250–253, 451] in non-spatial models. It predicted the emergence of clustering (a collective phenomenon emerging from local interactions in which individuals form high-density groups interspersed with low density areas [237–241]) along geographic and phenotypic space in a single-species inhabiting a one-dimensional environmental gradient as a consequence of spatially-dependent eco-evolutionary feedbacks. Clustering stands in contrast of smooth distributions across the space-phenotype domain [21, 242–244]. This was consistent with the prediction that space favors the emergence and stability of diversity[20, 21] but was a shift from the paradigm of local adaptation along environmental gradients resulting in gradual and smooth variation in the average value of a trait (cline-like phenotypic distributions [246–249]). Moreover, it might provide a mechanism for evolutionary processes of diversification in absence of geographic isolation such as parapatric speciation [176–178] and/or speciation along environmental gradients [452].

Although recent work has contributed to the understanding spatial eco-evolutionary dynamics –*e.g* concerning boundary conditions and competition kernels and their effect on the emergence of clustering [7, 227, 228]– the current theory on this topic leaves questions unanswered. First, a qualitative and quantitative understanding of the conditions required for cluster formation and persistence is still incomplete. More specifically, concerning the way in which spatially-intrinsic individual-level factors affect cluster formation and key characteristics of the emerging population structure, such as the number of clusters and their distance.

Furthermore, it was reported recently that spatial eco-evolutionary dynamics exhibit multi-stability [8, 9], hence small variations in initial conditions can lead to different attractors and disturbances may cause a population to switch rapidly between alternate spatial distribution and phenotypic compositions. However, whether multi-stability is ubiquitous or not, and in the case of the latter, under what conditions it is present remains elusive.

Here, we address these questions by using and 'equation-free' approach [51–53] (also referred to as coarse-analysis) based on a 'microscopic' individual-based (IB), stochastic model of spatial eco-evolutionary dynamics introduced in [7] and used recently in [8, 9]. Equation-free analysis is used to study complex multi-scale systems where descriptions come at microscopic scales and the interest lies on macroscopic collective behavior and where equations are unavailable or their analysis is impractical. It is particularly useful for analyzing equilibria (stable and unstable) and for bifurcation analysis and numerical continuation (as done in [293]). The methodology relies on successive shifts between microscopic and macroscopic scales through appropriately constructed operators combined with short simulations of the microscopic system.

In our case, although a macroscopic deterministic (PDE-approximation) model is available –as shown in [7, 185, 255]– its mathematical analysis, in particular concerning equilibria and stability, is substantially difficult and challenging. Moreover, its simulation can be computationally prohibitive specially when concerning its dependence on spatial parameters requiring very fine multi-dimensional grid representations of the domain. Also, coarse-analysis, in relation to direct simulations, is less vulnerable to misinterpret transient regimes and can detect the presence of equilibria regardless of their nature.

Other reasons to justify our choice of equation-free analysis (rather than other methods) include its versatility to changes, generalizations or extensions (these can refer to boundary conditions, different competition kernels, incorporation of Allee effects or other ecological situations) and its needlessness for some assumptions concerning boundaries or special scalings [41, 45, 228]. Additionally, the possibility of reducing the analysis to a low dimensional space which allows for a graphic visualization of the equilibria and the bifurcations occurring between them. Moreover, we base the analysis on the IB stochastic model to study potential finite size-effects which can result in mixed states simultaneously displaying combinations of the multi-stable patterns.

In this work we analyze asymptotic population structures and relate them to an individual-level, spatially-implicit parameter, specifically the competition spatial range of competition experienced by each individual. We report on this relation both qualitatively and quantitatively by performing a bifurcation analysis on the different transitions exhibited by the system when changing from continuous cline-like distributions to clustering structures and among clustering patterns showing different numbers of clusters. We find strong hysteresis which we predict are a consequence of successive saddle node bifurcations where stable branches can co-occur hence explaining multi-stability. Furthermore, we extend the current methodology to perform equation-free analysis on a highly stochastic systems. This methodology can be extended to other stochastic models exhibiting substantial noise.

V.2 The Model

We present the microscopic stochastic individual-based model and the equation-free methods we use in order to study the behavior of the stochastic dynamical system in terms of the ecologically relevant parameters.

V.2.1 Individual-based stochastic model of phenotypic evolution

We use an individual-based stochastic model introduced in [7]. We characterize each individual from an asexual population by a position and a quantitative phenotype (a trait).

New offspring appears with rates dependent on the local adaptation of the progenitors. The local optimal phenotype varies gradually and smoothly with space, hence representing the environmental gradient. At birth events, progeny appears at the spatial location of the parent. Mutations on the phenotype occur with a given probability and the new trait is selected with a transition measure.

We implement two types of death events. The first occur at a fixed rate (for each individual) and correspond to natural deaths. The second are deaths by competition and occur at rates which depend on the strength of competition from nearby individuals.

Throughout their lives, individuals undergo diffusion inside the spatial domain.

Mathematical formulation

Let $\mathcal{X} \subseteq \mathbb{R}^d$ (spatial domain) and $\mathcal{U} \subseteq \mathbb{R}^k$ (phenotypes domain) be open, connected sets. Individuals are characterized by their spatial location $x \in \overline{\mathcal{X}}$ and their phenotype value $u \in \mathcal{U}$.

Let $(x_1, \ldots, x_{N_t})^T \in \overline{\mathcal{X}}^{N_t}$ be the spatial locations and $(u_1, \ldots, u_{N_t})^T \in \mathcal{U}^{N_t}$ be the phenotype values of a population composed of N_t individuals at a time $t \geq 0$.

An individual i, $i = 1, \ldots, N_t$ at position $x_i \in \overline{\mathcal{X}}$ and with phenotype $u_i \in \mathcal{U}$ reproduces asexually with a rate:

$$B(x_i, u_i) = \max\left\{b_0 - b_1(x_i - u_i)^2; 0\right\},$$

where $b_0 > 0$ is the maximal birth rate and $b_1 > 0$ scales the decline in the reproductive rate for individuals away from their optimal spatial location.

The maximal rate occurs along the line $x = u$, representing the environmental gradient, and the width of the region where it is positive is $\sqrt{b_0/b_1}$.

New offspring appearing on birth events has the trait of the parent with probability $1-\gamma$. Otherwise, the new trait is chosen according to a Gaussian centered at u (and independent of x) and with variance σ^2.

The death rate of individual i is:

$$d_0 + d_1 \sum_{i=j}^{N_t} \mathbb{1}_{|x_i - x_j| < \delta},$$

where $d_0 \geq 0$ is the rate of natural death, and $d_1 \leq 0$ the scaling for death due to pair competition. We can (and will) assume that $d_1 = 1$ without loss of generality due to an appropriate time-scaling. The parameter δ represents the range of interaction (competition) experienced by each individual.

We can rewrite the death rate as

$$D(x_i, u_i, f_t) := d_0 + \int_{\mathcal{X}\times\mathcal{U}} \mathbb{1}_{|x_i - y| < \delta} f_t(dy, dw).$$

with

$$f_t = \sum_{j=1}^{N_t} \delta_{(x_j, u_j)}$$

being the population counting process with Dirac delta functions located at the populations' positions (at time t).

Individuals undergo diffusion -independent from each other- in the spatial domain $\overline{\mathcal{X}}$ with a constant diffusion coefficient D_m.

For an initial condition $f_0 = \sum_{j=1}^{N_0} \delta_{(x_j, u_j)}$, we denote the microscopic state at the system after a time t by $\Phi(f_0, t)$.

Boundary conditions

The impact of boundary conditions on the emergence of clustering *v.s* continuous (cline-like) patterns along environmental gradients has been an issue of controversy since the phenomenon was first reported [22, 227] and has remained relevant in more recent works [8, 228]. While initially a debate on whether clustering was artifactual or not [22, 227], it was later proved that it is robust to open and closed boundaries [8, 228] and, albeit being enforced or hindered by them, occurs due to other forces.

The original model [7] incorporates reflection of spatial motion at the boundary of $\mathcal{X}$ and restricts mutations to remain within $\mathcal{U}$, otherwise discarting the mutated offspring. In other words, the boundary is reflecting on $\mathcal{X}$ and absorbing in $\mathcal{U}$ where $\mathcal{X} = \mathcal{U} = (0, 1) \subseteq \mathbb{R}$.

Due to asymmetric competition near the boundaries, increased aggregation of individuals is observed close to the edges (see Figs. 1 and S1 in [9]). This contributes to a disruption of continuous distributions due to a propagated effect -from the edges and towards the center of the domain- of unequal competition. Moreover, it alters the presence and nature of equilibria in general for the complete microscopic system. For this reason, and to facilitate our analysis by studying more regular patterns, we modify the boundary conditions so that they are periodic in both dimensions or $\mathcal{X} = \mathcal{U} = S^1$. Our complete domain is then the torus $S^1 \times S^1$.

To perform an equation-free analysis we need to construct a macroscopic variable able to capture the macroscopic transitions in the microscopic system by reducing the dynamics to a low-dimensional space. To calculate such variable we require a frame of reference in the new domain (the torus). We find that the most appropriate one which facilitates this construction corresponds to the coordinate system where origin (which is both $(0,0)$ and $(1,1)$) is placed at the point where the populationś density distribution has its maximum. That is, the position in which the population is most aggregated after a discretization of the domain into $L \times L$ squares. This fixes the position of the other clusters in such a way that they are -in general- equally spaced and uniformly located along the diagonal in $[0,1)\times[0,1)$.

Model parameters and values

All the parameters of the model and their descriptions are presented in Table V.1.

Parameter	Description	Default value
b_0	Maximal birth rate	$b_0 = 2$
b_1	Quadratic coefficient in the rate of decay in the birth rate	$b_1 = 20$
d_0	Natural death rate	$d_0 = 1$
D_m	Spatial diffusion coefficient	$D_m = 5 \times 10^{-5}$
δ	Spatial competition range	$\delta = 0.1$
σ	Standard deviation of mutation transition measure (Gaussian)	$\sigma = 0.01$
γ	Mutation probability	$\gamma = 0.1$

Table V.1: Model parameters, description and default values.

In the forthcoming analysis we will focus on the effect of the parameter δ (the competition range distance) on the macroscopic patterns. This parameter has been observed to have the a substantial and qualitative impact on the distributions of the population and has been analyzed in simpler models (*e.g.* [45]). Other parameters like σ, γ, d_0, b_0 and b_1 have mainly quantitative effects (see Supporting Material from [9]) with the exception of extreme values which cause either fast extinction or massive population growth. In contrast, the dependence on D_m will be the subject of future work.

V.3 Methods

Equation-free analysis has its grounds in the *lift-evolve-restrict* scheme which relies on continuous shifts between microscopic and macroscopic scales.

In this section we present the numerical and mathematical methods used at the different scales which make part of our equation-free methodology.

V.3.1 Numerical simulations of the individual-based stochastic model. The microscopic time-stepper

We use an algorithm based on [7] –which was described in detail and used in [8]– to simulate the individual-based model. We refer to this as the microscopic time-stepper $\mathcal{M}$.

The algorithm uses an acceptance/rejection scheme. It constructs sequences N_k, T_k, X_k, U_k with $N_k \in \mathbb{N}^*$, $T_k \in \mathbb{R}$, $X_k \in \overline{\mathcal{X}}^{N_k}$ and $U_k \in \mathcal{U}^{N_k}$. These sequences represent the number of individuals, the time, the vector of spatial locations and the vector of phenotype values of the N_k living individuals at the time of the end of k-th time step.

The potential event rate at each step is $C_{tot} := N_{k-1}(b_0 + d_0 + N_{k-1}/K)$, where K is the carrying capacity. We chose, based on a parameter θ_k (a uniformly distributed random variable on $[0, C_{tot}]$), an event which can potentially occur at the time $T_k = T_{k-1} + E_{k-1}$, with E_{k-1} being an exponentially generated random variable with parameter C_{tot}.

If $\theta_k < N_{k-1}b_0$, an individual $I_k = i$, $1 \leq i \leq N_{k-1}$, is randomly selected to give birth (to a clone or a mutant) with a probability $\frac{B(X^i_{T_k}, U^i_{T_k-1})}{b_0}$. In the event of mutation (which occurs with probability γ), the new trait is selected using a Gaussian centered at $U^i_{T_k-1}$ with variance σ^2. If, instead, $N_{k-1}b_0 \leq \theta_k \leq N_{k-1}b_0 + N_{k-1}d_0$, an event of natural death occurs and an individual $I_k = i$, $1 \leq i \leq N_{k-1}$, is erased no matter its position and trait. Finally, if $\theta \geq N_{k-1}b_0 + N_{k-1}d_0$, two individuals $I_k = i$, $J_k = j$, $1 \leq i, j \leq N_{k-1}$ are selected randomly. If the distance among them at time T_k is smaller than δ, then individual i dies. Otherwise nothing happens.

Spatial locations are updated for selected individuals in the acceptance/rejection scheme before the event occurs. Otherwise, they are updated for all individuals every time step of length T_{aff}. To simulate spatial diffusion we use the method presented in [453]. Nevertheless, other methods [454] are equally capable of producing equivalent results.

V.3.2 Construction of Restriction Operator and computation of the macroscopic macro-variable

Simulations of the individual-based stochastic model show a strong dependence in the leap from continuous to clustering patterns and between clustering patterns which display differences in the number of clusters, on the system's parameters. In particular on δ (the competition range) and D_m (the spatial diffusion coefficient). This issue was reported in [8, 9], where the transition between continuous and clustering patterns –and their characteristics– was studied using Turing's method for pattern formation analysis [431] and a Hamilton-Jacobi approach based on [41]. These analyses rely on different assumptions (*e.g* boundary conditions, mutation jumps, spatial diffusion, and the shape of perturbations) and only focus on the gain or loss of stability of the cline-like equilibrium.

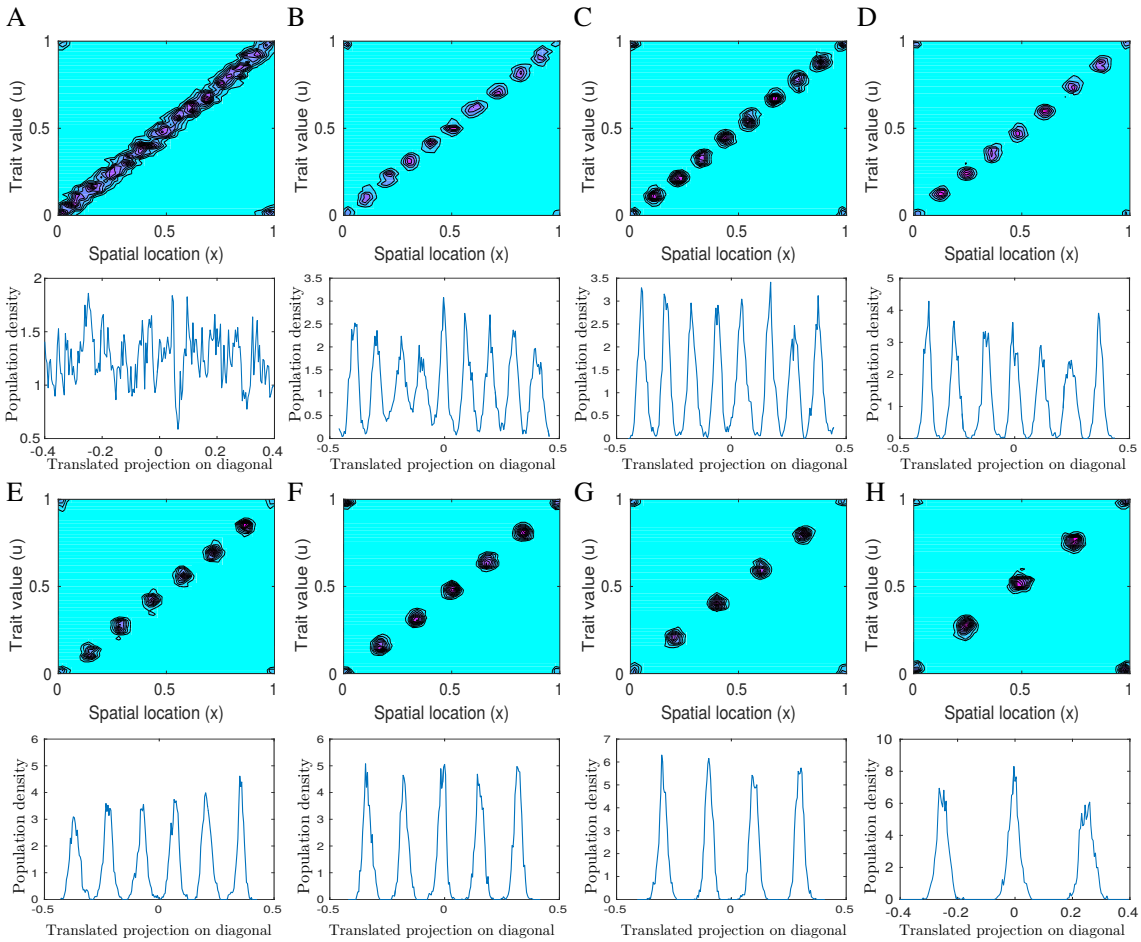

Figure V.1: Microscopic distributions and dependence on the competition range δ. Density contour maps of the microscopic state (top) and density of the (translated) projections onto the line $x = u$ (bottom) after a time T_{end} for $\delta = 0.05$ (panel A), $\delta = 0.07$ (panel B), $\delta = 0.08$ (panel C), $\delta = 0.095$ (panel D) $\delta = 0.11$ (panel E), $\delta = 0.13$ (panel F), $\delta = 0.16$ (panel G), and $\delta = 0.19$ (panel H). In all contour plots, magenta represents the highest density. Density is negligible in cyan areas. See Section V.4.1 and Tables V.1 and V.2 for details on the numerical methods and the parameters used.

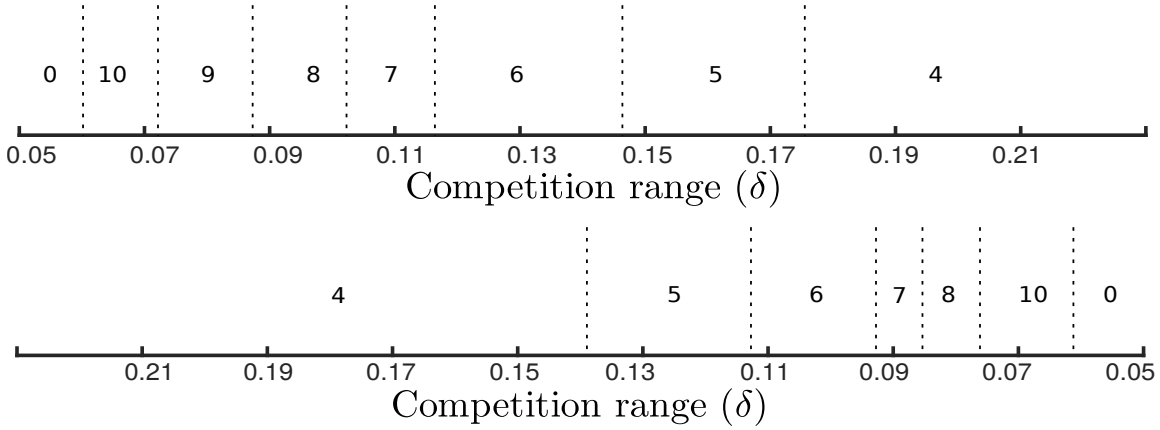

Figure V.2: Dependence of the number of clusters on the competition range δ. Number of clusters of the long-term microscopic patterns after a time T_{end} when increasing (top) and decreasing the competition range δ (bottom). See Section V.4.1 and Tables V.1 and V.2 for details on the numerical methods and the parameters used.

In the top figures of each panel from Fig. V.1 we show contour plots of the long-term distributions observed while gradually changing the parameter δ. As observed, the macroscopic patterns go from a nearly-continuous, "cline-like" distributions, to distributions fragmented into a number of clusters which decreases as δ becomes greater. The way in which the long-term number of clusters depends on δ when gradually increasing or decreasing this parameter (with an initial condition equal to the final microscopic distribution of the earlier simulation) is shown in Fig. V.2.

With the purpose of analyzing the macroscopic bifurcations and the behavior of these macroscopic equilibria we search for a low dimensional macroscopic variable which is able to: (i) capture the convergence of the microscopic system to the slow manifold and to the macroscopic attractors, (ii) distinguish between these attractors and their respective basins of attraction/repulsion and (iii) show the presence of -stable or unstable- equilibria (if any) and of multi-stability in the microscopic system.

Classical measures of clustering of a data-set normally require iterative methods for their computation and/or specific inputs such as the number of clusters in which the population should be distributed [455–461]. These involves extensive numerical computations and additional manual inputs (which can affect negatively the analysis given the uncertainty concerning the number of clusters) and overall makes their use inconvenient.

Initially, we chose to look at the moments of the distribution, either on one of its dimensions or along the diagonal where the population aggregates. The motivation for this choice was the moment-generating function which uniquely defines a distribution as the probability density or cumulative distribution functions do. Alas, although initially promising, the dynamics could not be properly analyzed in one dimension, given that time-trajectories often crossed through known equilibria.

Other natural candidates to analyze the macroscopic patterns observed are functions of the Fourier coefficients a_n and b_n of the distribution when projecting along the diagonal or along one of the dimensions. This dimensionality reduction is effective even though –and as will be described below– it requires individually isolating the different bifurcations (each one corresponding to a macroscopic transition). This is, since each one of them (corresponding to the appearance of a macroscopic pattern with a determined number of clusters) requires a different macroscopic variable (corresponding to a given frequency). In order to facilitate the visualization of the system's dynamics we overlap all the analyses into a single one where all equilibria can be simultaneously observed.

Macroscopic variables for the Equation-free analysis on the parameter δ

We analyze separately the bifurcations occurring with respect to macroscopic equilibria corresponding to distributions fragmented into n clusters ($n = 10, 9, 8, 7, 6, 5, 4$).

Clustering and continuous patterns generally differ by their number of clusters (0 in the case of cline-like distributions), their inter-cluster distance, their amplitude (when normalized) and their cluster-width among other characteristics (see Fig. V.1). However, they all are (nearly) symmetric with respect to mid-point of the domain and concentrated along the diagonal line $x = u$ due to the functional form in which natural selection is incorporated (the function $B(x, u)$). We take advantage of both properties and do the following procedure for all values of n. First, if $X_t = (x_1, \ldots, x_{N(t)})^T \in \mathcal{X}^{N_t}$ denotes the vector of spatial positions and $U_t = (u_1, \ldots, u_{N(t)})^T \in \mathcal{U}^{N_t}$ the vector of trait values (both according to the frame of reference described before) of the microscopic state with N_t individuals at a time t, we take the single component of the orthogonal projection of each pair $(x_i, u_i)^T$ along the diagonal line:

$$h_i = \frac{1}{\sqrt{2}}(x_i, u_i)^T \bullet \left(\frac{1}{\sqrt{2}}, \frac{1}{\sqrt{2}}\right)^T,$$

to construct a new vector of data points $H_t = (h_1, \ldots, h_{N(t)})^T \in [0, 1)$. Due to the boundary conditions and the frame of reference considered, the largest cluster is divided into four parts, each aggregated near one of the corners of the domain (see the top figures of each panel of Fig. V.1). The positions of the individuals aggregated near the edges $(0, 1)$ and $(1, 0)$ are projected to values close to $(0.5, 0.5)$, and not to $(0, 0)$ nor $(1, 1)$. This introduces a small error, where the number of individuals at the center is overestimated. To correct this, we remove the edge cluster from the analysis and hence, only consider the individuals located at positions $(x_i, u_i)^T$ with $c_n \leq x_i, u_i \leq C_n$. We find that the best estimation of c_n and C_n such that the edge cluster is removed is $c_n = 0.1 - (n - 4) \times 0.01$ and $C_n = 0.9 + (n - 4) \times 0.01$. Once, this condition has been imposed, we translate this new set of data points to be symmetrical about 0 by subtracting 0.5 to each of the components of H_t. Next, we approximate the (normalized) distribution's density function numerically (using MATLAB's function *histogram*) to arrive at a function f_n as the ones represented at the bottom of each panel of Fig. V.1. By definition this function has an integral equal to 1 over the range $(c_n - 0.5, C_n - 0, 5)$. Since the edge cluster has been previously removed, these functions have $n - 1$ peaks, from which we observe that the natural candidate for a

macro-variable is a function of the $n-1$ Fourier coefficients

$$a_{n-1} = \frac{1}{L_n}\int_{c_n-0.5}^{C_n-0.5} f_n(\tau)\cos\left(\frac{(n-1)\pi\tau}{L_n}\right)d\tau,$$

$$b_{n-1} = \frac{1}{L_n}\int_{c_n-0.5}^{C_n-0.5} f_n(\tau)\sin\left(\frac{(n-1)\pi\tau}{L_n}\right)d\tau$$

where $L_n = (C_n - c_n)/2$. Since the f_n's are symmetrical with respect to 0 we define our macro-variable as $\Lambda_n = (a_{n-1})^2$. Hence, the Restriction Operators $\mathcal{R}_n$ are such that for a microscopic state $(X_t, U_t) \in \mathcal{X}^{N_t} \times \mathcal{U}^{N_t}$, $\mathcal{R}_n((X_t, U_t)) = \Lambda_n(f_n) = (a_{n-1})^2$ when constructing f_n by following the scheme above.

As shown in Fig. V.3, the macroscopic variable Λ_n is effective in recognizing macroscopic patterns with n clusters, for which it rises from values close to zero to positive quantities.

V.3.3 Construction of the Lifting Operators

The construction of the Lifting Operators $\mathcal{L}_n$ is not trivial; it requires the identification of an appropriate map from a low dimensional space, namely $\mathbb{R}$, to a space with multiple dimensions $\mathcal{X}^{N_0} \times \mathcal{U}^{N_0}$ of microscopic states of the stochastic system with N_0 individuals. As before, we construct different Lifting Operators for each case considered, *i.e* $n = 10, 9, 8, 7, 6, 5, 4$.

Fist, the initial number of individuals N_0 is chosen based on the relation observed between the long-term microscopic patterns and the parameter δ (see Fig. V.4), where using curve fitting tools we find that it generally obeys a power-law.

The analysis of macroscopic equilibria requires the computation of the time derivatives $\frac{d\Lambda_n}{dt}$ by using short simulation bursts of the microscopic time stepper. Hence, a 'discrete' Lifting Operator, which only maps ranges of macroscopic variables to distributions with n-modes (or 0 modes) is insufficient. In contrast, one desires to identify a characteristic of the microscopic state which varies gradually (and hopefully in a one-to-one correspondence) with the macro-variable. We observe that clusters are generally equally spaced (see Fig. V.1) so we do not consider any measurement based on the position of the clusters. Conversely, a measure of spread of the distribution of each cluster presents as a natural candidate as it relates directly with the Fourier coefficients.

We generated by sampling a substantial number of microscopic states with n clusters centered at the positions $(\frac{m}{n}, \frac{m}{n})$, $m = 0, 1, \ldots, n-1$ and with variance σ_c^2 (in both $\mathcal{X}$ and $\mathcal{U}$). It is assumed that each cluster has initially a Gaussian distribution (with equal variance in both dimensions), however, as explained in Section V.3.4, we run the microscopic dynamics for a short 'healing-time' with which we aim to correct potential errors bound to this assumption. We observed a one-to-one exponential relation (in the range of interest) between σ_c and Λ_n where:

$$\Lambda_n(\sigma_c) = \alpha_1 \exp\left(-\left(\frac{\sigma_c - \alpha_2}{\alpha_3}\right)^2\right).$$

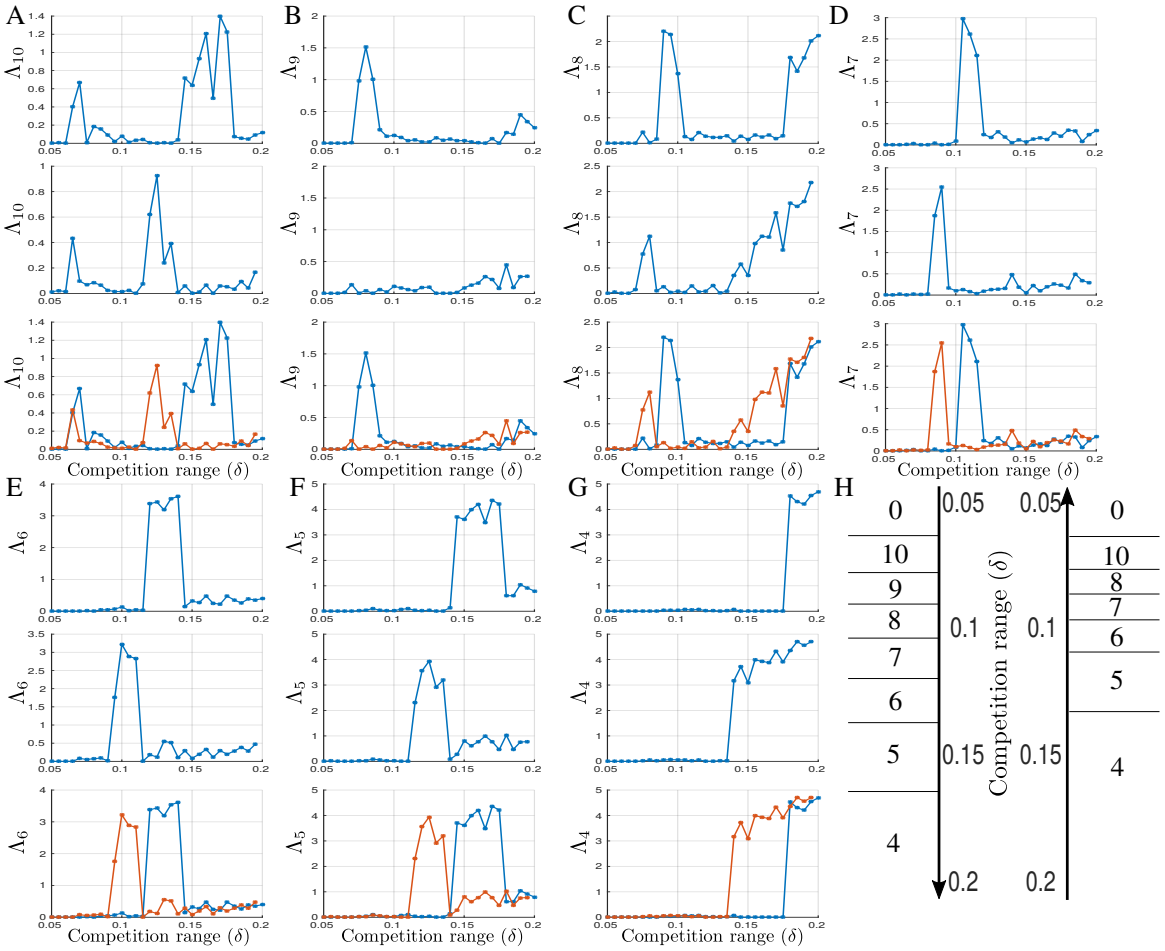

Figure V.3: Dependence of the macroscopic variables Λ_n on the competition range δ. (Top) Forward-sweep (Middle) Backward-sweep (Bottom) Forward and backward-sweep for $n = 10$ (panel A), $n = 9$ (panel B), $n = 8$ (panel C), $n = 7$ (panel D) $n = 6$ (panel E), $n = 5$ (panel F), and $n = 4$ (panel G). Panel H. Same as Fig. V.2. See Sections V.4.1 and V.4.2 and Tables V.1 and V.2 for details on the numerical methods and the parameters used.

These relations are shown in Fig. V.5 together with their fittings and the values of α_1, α_2 and α_3 found in each case.

We construct then our Lifting Operators $\mathcal{L}_n$ based on the map $(\Lambda_n, \delta) \longmapsto (n, \sigma_c, N_0)$, where

$$\sigma_c = \alpha_3 \left(-\log\left(\frac{\Lambda_n}{\alpha_1}\right)\right)^{\frac{1}{2}} + \alpha_2. \tag{V.1}$$

Using the triplet (n, σ_c, N_0), we build our initial distribution. For each individual, we first randomly select the cluster it belongs to and then generate both the position x and the trait u by randomly sampling from Gaussian distributions.

This gives us the Lifting Operators $\mathcal{L}_n(\Lambda_n, \delta) = f_0 = \sum_{i=j=1}^{N_0} \delta_{(x_j, u_j)}$ where f_0 is con-

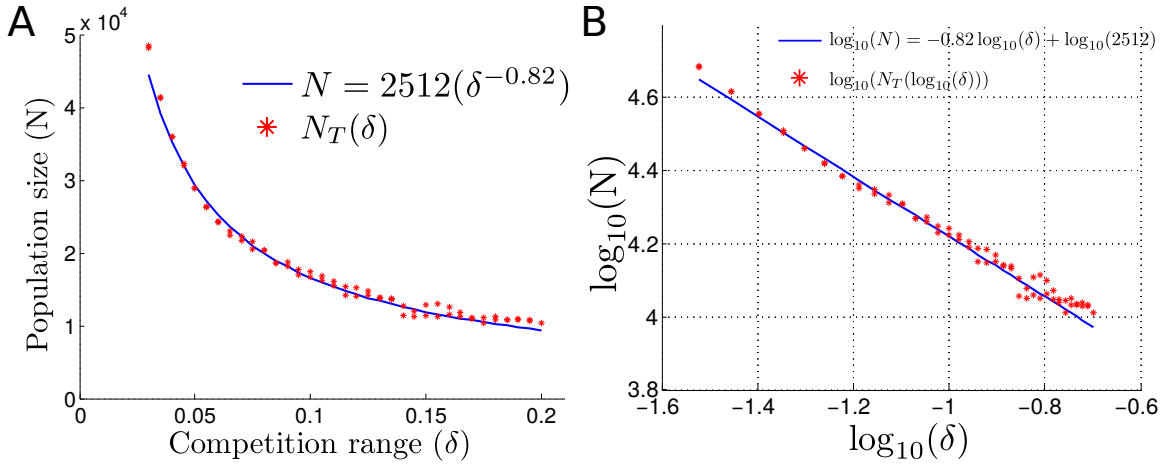

Figure V.4: Long-term population size in terms of the competition range δ. Population size (panel A) for different values of the parameter δ (red asterisks) together with the curve fitting (blue line) of their relation. (Panel B) Log-log plot of (panel A). See Section V.4.1 and Tables V.1 and V.2 for details on the numerical methods and the parameters used.

structed as described above.

V.3.4 Implementation of a semi-implicit scheme

It is reasonable to expect that the Lifting Operators $\mathcal{L}_n$ map pairs (Λ_n, δ) to micro-states far from the slow manifold where the dynamics can be reduced and studied in a low-dimensional space with equation-free methods. In particular, it is not true that the distribution of the individuals in a cluster or in continuous patterns is a Gaussian with equal standard deviation on both dimensions. With respect to 'cline-like' distributions, it was noted in [8, 9, 228] that the approximation with a Gaussian can be made under appropriate conditions on D_m and σ when the boundary conditions are periodic. To correct these intrinsic flaws in $\mathcal{L}_n$, we implement what we call a 'semi-implicit' scheme for the computation of the macroscopic time-stepper based on [293].

An implicit scheme in equation-free analysis involves running the microscopic time-stepper $\mathcal{M}$ for a healing time t_{heal} (after constructing the initial micro-state), hence bringing the dynamics close to the slow manifold, and then computing using a numerical continuation method the value of Λ_n to which the new microscopic state corresponds to. Since our algorithm is already substantially expensive we use a 'semi-implicit' scheme, where instead we make corrections to the Lifting Operators directly, by running for a small healing time, and hence avoid using iterative methods for finding solutions afterwards. We implement this correction (as mentioned before) by calculating the relation in Eq. (V.1) after the healing-time.

The determination of the healing time normally requires careful attention. However, as shown in Fig. V.6, the averaged time trajectories of Λ_n are quite stable (in contrast, single realizations have a behavior which rather resembles Brownian motion). For this reason we

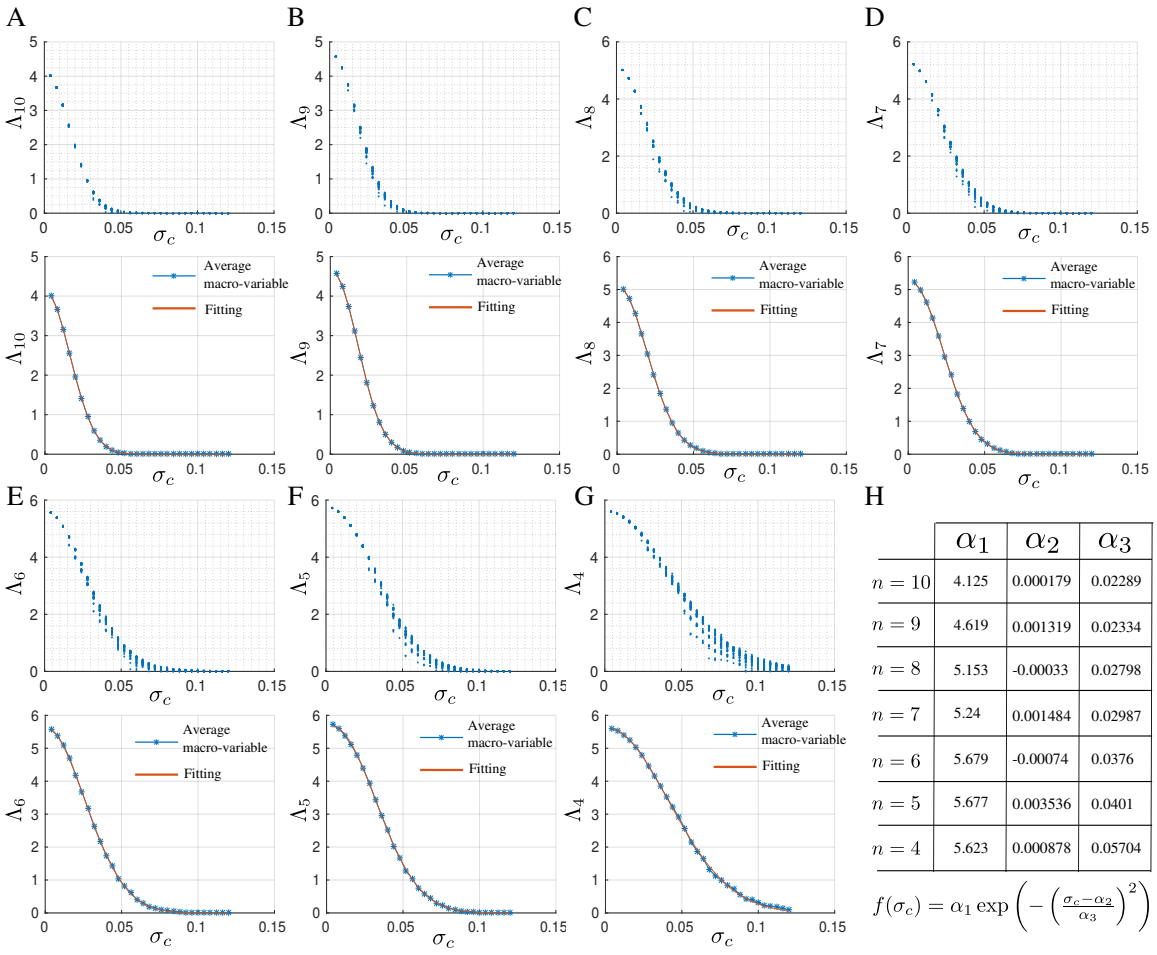

	α_1	α_2	α_3
$n = 10$	4.125	0.000179	0.02289
$n = 9$	4.619	0.001319	0.02334
$n = 8$	5.153	-0.00033	0.02798
$n = 7$	5.24	0.001484	0.02987
$n = 6$	5.679	-0.00074	0.0376
$n = 5$	5.677	0.003536	0.0401
$n = 4$	5.623	0.000878	0.05704

$$f(\sigma_c) = \alpha_1 \exp\left(-\left(\frac{\sigma_c - \alpha_2}{\alpha_3}\right)^2\right)$$

Figure V.5: Dependence of the macroscopic variables Λ_n on the clusters' initial standard deviation σ_c for every repetition (Top) and on average together with exponential fitting (Bottom) for $n = 10$ (panel A), $n = 9$ (panel B), $n = 8$ (panel C), $n = 7$ (panel D) $n = 6$ (panel E), $n = 5$ (panel F), and $n = 4$ (panel G). Panel H. Fitting coefficients and equation. See Sections V.3.3 and V.3.4 and Tables V.1 and V.2 for details on the numerical methods and the parameters used.

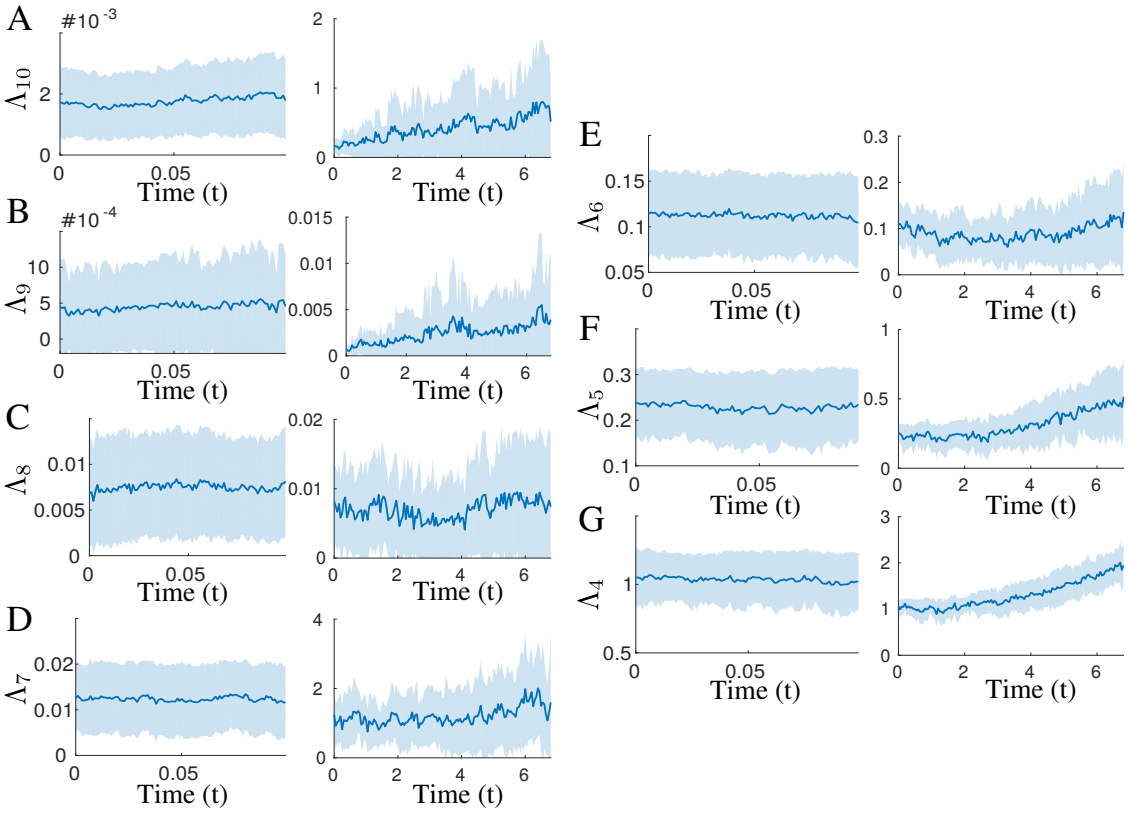

Figure V.6: Short-term (left) and long-term (right) time-evolution of macroscopic variables Λ_n for $n = 10$ (panel A), $n = 9$ (panel B), $n = 8$ (panel C), $n = 7$ (panel D) $n = 6$ (panel E), $n = 5$ (panel F), and $n = 4$ (panel G). In all simulations $\sigma_c = 0.075$. Results averaged over 100 repetitions (left) and 20 repetitions (right), $\delta = 0.07$ (panel A), $\delta = 0.08$ (panel B), $\delta = 0.095$ (panel C) $\delta = 0.11$ (panel D), $\delta = 0.13$ (panel E), $\delta = 0.16$ (panel F), and $\delta = 0.19$ (panel G). See Sections V.3.3 and V.3.4 and Tables V.1 and V.2 for details on the numerical methods and the parameters used.

chose the healing time to be the shortest time for which the micro-states reach a 'transient' stability where the averaged variances (separately on $\mathcal{X}$ and $\mathcal{U}$) of the first cluster become stable. This value is shown in Table V.2. In general, we average over multiple liftings for each value of Λ_n to avoid miscalculations due to inadequate initial microscopic states.

When incorporating this healing time, and when making the corrections to the estimations of the relation between Λ_n and σ_c, one should observe that the following condition holds (on average):

$$\Lambda_n \simeq \mathcal{R}_n(\mathcal{M}(\mathcal{L}_n(\Lambda_n, \delta), t_{heal}))).$$

As observed in Fig. V.7, this relation holds with great precision for all values considered of n

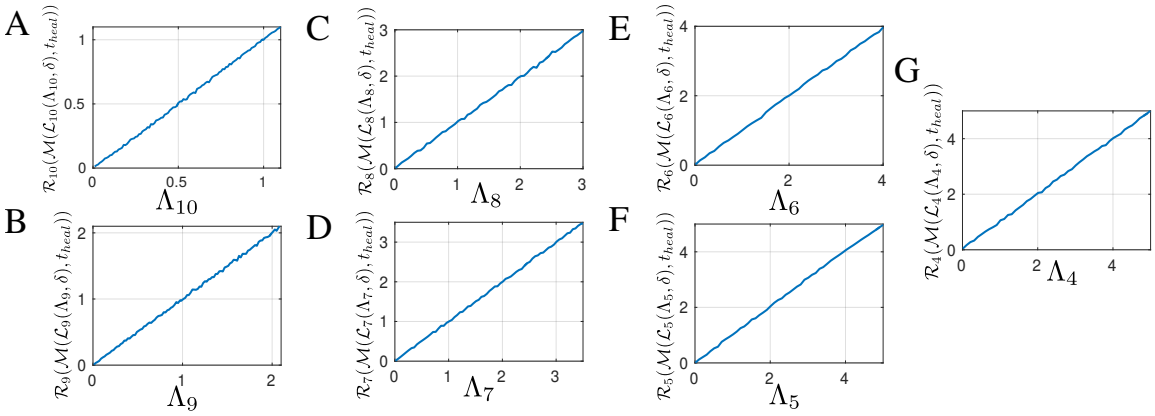

Figure V.7: Validation of "semi-implicit" scheme. Relation between $\mathcal{R}_n(\mathcal{M}(\mathcal{L}_n(\Lambda_n, \delta), t_{heal})))$ and Λ_n for $n = 10$ (panel A), $n = 9$ (panel B), $n = 8$ (panel C), $n = 7$ (panel D) $n = 6$ (panel E), $n = 5$ (panel F), and $n = 4$ (panel G). See Sections V.3.3 and V.3.4 and Tables V.1 and V.2 for details on the numerical methods and the parameters used.

V.3.5 Bifurcation analyses

Computation of the derivatives

This work aims to compute the bifurcation diagrams of each macro-variable Λ_n by combining short simulation bursts of the microscopic time stepper and the "lift-heal-restrict" scheme. Broadly, we search for the values of Λ_n for which the macroscopic time-stepper $\Phi(\Lambda_n, t; \delta) = \Lambda_n(t)$ is invariant on t (the macroscopic equilibria). The formal definition of Φ is:

$$\Phi(\Lambda_n, t; \delta) = \langle \mathcal{R}_n(\mathcal{M}(\mathcal{L}_n(\Lambda_n, \delta), t_{heal} + t)))\rangle,$$

for a fixed parameter value of δ. The average is done over a number M_L Liftings.

We implement Newton's method to search for the zeros of $F(\Lambda_n; \delta) = \frac{d\Lambda_n}{dt}$. For this, we require to numerically approximate the derivatives $F(\Lambda_n; \delta) = d\Lambda_n/dt$, $\partial F/\partial \Lambda_n$ and $\partial F/\partial \delta$ (see below).

For a value of Λ_n we approximate the derivative $d\Lambda_n/dt$ with Euler's method with a time-step of length Δt;

$$\frac{d\Lambda_n}{dt} \simeq \frac{1}{\Delta t} \langle \mathcal{R}(\mathcal{M}(\mathcal{L}(\Lambda_n, p), t_{heal} + \Delta t)) - \mathcal{R}(\mathcal{M}(\mathcal{L}(\Lambda_n, p), t_{heal}))\rangle .$$

The appropriate choice of Δt depends on M_L. We find, based on the long-term behavior of the macro-variables (shown in Fig. V.6), that this time should be generally long (around $\Delta t = 4$) to correctly detect the changes in macroscopic behavior.

With the estimations of $F(\Lambda_n; \delta) = \frac{d\Lambda_n}{dt}$, we approximate $\frac{\partial F}{\partial \Lambda_n}$ and $\frac{\partial F}{\partial \delta}$ again with Euler's method by:

$$\frac{\partial F}{\partial \Lambda_n} \simeq \frac{1}{\Delta \Lambda_n}(F(\Lambda_n + \Delta \Lambda_n; \delta) - F(\Lambda_n; \delta)),$$

$$\frac{\partial F}{\partial \delta} \simeq \frac{1}{\Delta\delta}(F(\Lambda_n; \delta + \Delta\delta) - F(\Lambda_n; \delta)),$$

where $\Delta\Lambda_n > 0$ needs to be carefully chosen so that ideally it is larger than the variance of the time-evolution after the time Δt. Also, one would expect to choose $\Delta\delta$ to be the smallest value for which Δt allows for a significant difference. In our case we rather hand-pick $\Delta\delta$ to be fine enough to (hopefully) be able to accurately compute the bifurcation diagram and to detect the presence of multi-stability.

We note that the correct choice of M_L, Δt, $\Delta\Lambda_n$ and $\Delta\delta$ involves properly analyzing the trade-off between extensive computational times and the accurate prediction and computation of the averaged macroscopic dynamics, which is not trivial.

Computation of equilibria

We implement a pseudo-arc-length condition –similarly as in [293]– to compute the equilibria and the folds near the bifurcations. The method uses a Newton's search in the two-dimensional space of the parameter δ and the macro-variable Λ_n. Suppose a sequence of equilibria (δ^i, Λ^i), $i = 1, ..., p$ have been computed. First, a prediction of the next equilibrium is made as $(\hat{\delta}^{p+1}, \hat{\Lambda}_n^{p+1}) := (\delta^p, \Lambda_n^p) + (\delta^p, \Lambda_n^p) - (\delta^{p-1}, \Lambda_n^{p-1})$. After, we compute the next point $(\delta^{p+1}, \Lambda_n^{p+1})$ by iterating a two-dimensional Newton's search on a function $G(\Lambda_n; \delta)$ defined as:

$$G(\Lambda_n; \delta) = \begin{pmatrix} F(\Lambda_n; \delta) \\ \Gamma(\Lambda_n; \delta) \end{pmatrix},$$

where $\Gamma(\Lambda_n; \delta) = [(\delta, \Lambda_n) - (\hat{\delta}^{p+1}, \hat{\Lambda}_n^{p+1})] \cdot [(\delta^p, \Lambda_n^m) - (\delta^{p-1}, \Lambda_n^{p-1})]$. This Newton's method iterates according to the rule:

$$(\delta^{l+1}, \Lambda_n^{l+1}) = (\delta^l, \Lambda_n^l) - J(\delta^l, \Lambda_n^l)^{-1} G(\Lambda_n; \delta), \qquad l \in \mathbb{N}^*,$$

with

$$J(\delta^l, \Lambda_n^l) = \begin{pmatrix} \partial F/\partial\delta & \partial F/\partial\Lambda_n \\ \partial\Gamma/\partial\delta & \partial\Gamma/\partial\Lambda_n \end{pmatrix}\Bigg|_{(\delta^l, \Lambda_n^l)}.$$

The condition for convergence is either $||(\delta^{l+1}, \Lambda_n^{l+1}) - (\delta^l, \Lambda_n^l)|| \leq \epsilon_1$ or $l = M_1$, where ϵ_1 and M_1 have been previously set. Once one of the convergence conditions has been satisfied, after s iterations, we approximate the position of the equilibrium as (δ^s, Λ_n^s). We determine whether equilibria are stable or unstable based on the final value of

$$\frac{\partial F}{\partial \Lambda_n}\Bigg|_{(\delta^s, \Lambda_n^s)}$$

.

V.3.6 Numerical parameters and values

The numerical parameters used in the methods described in the previous sections are presented in Table V.2.

Parameter	Description	Default value
T_{aff}	Time-step length to update all spatial locations	$T_{aff} = 0.025$
T_{end}	Long-term simulation time of the microscopic dynamics	$T_{end} = 150$
t_{heal}	Healing time	$t_{heal} = 0.05$
Δt	Time-step length for computation of derivatives	$\Delta t = 4$
$\Delta\Lambda_n$	Step size of Λ_n for computation of derivatives	$\Delta\Lambda_n = 0.4/n$
$\Delta\delta$	Step size of δ for computation of derivatives	$\Delta\delta = 0.0025$
M_L	Number of Liftings to average macroscopic time-stepper	$M_L = 40$
ϵ_1	Convergence threshold in Newton's method	$\epsilon_1 = 0.001$
M_1	Maximum of iterations in Newton's method	$M_1 = 50$

Table V.2: Numerical parameters, description and default values.

V.4 Results

V.4.1 Dependence of the long-term microscopic system on δ

We show in Figs. V.1 and V.2 (top), using long-term numerical simulations of the microscopic time-stepper, how the microscopic attractors vary when increasing the parameter δ by a fixed step of size 0.005.

In the computation of these long-term microscopic states, we run the microscopic time stepper for a population initially concentrated in the center of the domain for a long time $T_{max} = 600$. Then, for each subsequent value of δ, we take as initial condition the last state of the microscopic system from the previous simulation and run the microscopic dynamics for a time T_{end}.

As δ grows (from an initial value $\delta = 0.05$), the cline-like equilibrium first becomes unstable before decreasing progressively the number of clusters in which the population divides. The changes in cluster numbers seem abrupt. Once δ crosses thresholds values, the previous number of clusters is no longer viable due to an increase in competition. This produces and increase in deaths which in turn leads to a merger between two existing clusters. Once this merger occurs, the remaining clusters slowly change their position in the domain until –once again– they are equally spaced along the diagonal.

Multi-stability and strong hysteresis is detected. When decreasing the parameter δ (with

the same step size) and taking as initial condition the last microscopic state achieved in the previous simulation (for the largest δ), the dependence of the microscopic long-term attractors on the parameter is strongly altered (see bottom of Fig. V.2). Hence, the dynamics microscopic system are highly dependent on the initial conditions, with long-term patterns that can vary by one or even two clusters under the same parameter values.

V.4.2 Computation and parameter dependence of the macro-variables

The macro-variables Λ_n are efficient in capturing the transition from $n-1$ or $n+1$ to n clusters. This is shown in Fig. V.3, where the macro-variables are computed at the final states of the simulation described in Section V.4.1. At the values of δ for which the number of clusters change to n (or $n/2$), Λ_n increases and changes branches.

Hysteresis and multi-stability in the dynamics of the macro-variables are also present. As before, (and as anticipated) the equilibria change greatly when δ increases or decreases. During the forward and the backward sweep, Λ_n jumps between branches of equilibria at different values of the parameter. The only possible exception occurs at the transition between the cline-like equilibrium and the microscopic state of 10 clusters.

V.5 Expected results

We expect to construct the bifurcation diagrams of the macro-variables Λ_n using the equation-free methodology described in previous sections. Obtained results hint towards a succession of coupled saddle node bifurcations (folds) occurring for each $n = 10, 9, 8, 7, 6, 5, 4$. We expect to explicitly find the regions of multi-stability by superposing these diagrams and finding the regions where multiple branches co-occur. We conjecture that the results will be similar as the diagram shown in Fig. V.8.

V.6 Conclusion and perspectives

In this work we use equation-free analysis to study the emergence and stability of macroscopic patterns of populations along one-dimensional resource gradients. We use a microscopic individual-based model introduced in [7]. The 'back-bone' of the equation-free methodology relies in successive shifts between microscopic and macroscopic scales with the use of carefully constructed operators. We find macroscopic quantities (the macroscopic variables) which successfully capture characteristics of interest of microscopic behavior, namely cluster numbers and their dependence on the parameter δ (the spatial competition range). Then, we construct maps which link microscopic patterns to these macro-variables. With these maps, together with short simulation bursts of the microscopic system, we intend to compute the bifurcation diagram happening on low-dimensional space, through which we analyze as well microscopic behavior. We plan as well in extending our results to analyze the dependence on the parameter D_m (the individual diffusion coefficient).

Existing theoretical or numerical work on the emergence of multi-modal spatial or phenotypic patterns has generally relied on Turing's stability analysis applied to homogeneous distributions [8, 302–304, 306, 307]. This approach normally relies on different assumptions

concerning boundary conditions, population numbers and biological simplifications. To overcome some of this limitations, we also intend of taking advantage of the versatility of the equation-free methodology, allowing us to extend our analysis to different boundary conditions and extensions (or variants) of our original model.

Clustering in models of eco-evolutionary dynamics of populations along environmental gradients has strong implications concerning the emergence and stability of diversity in absence of geographic isolation. Furthermore, in relation with speciation occurring in parapatry (when reproduction is sexual). In our analysis, we aim to study the emergence of spatial and phenotypic patterns and their relation to quantifiable data (which can be measured empirically or experimentally). With this, we hope to contribute to the understanding of the processes behind the emergence of biodiversity.

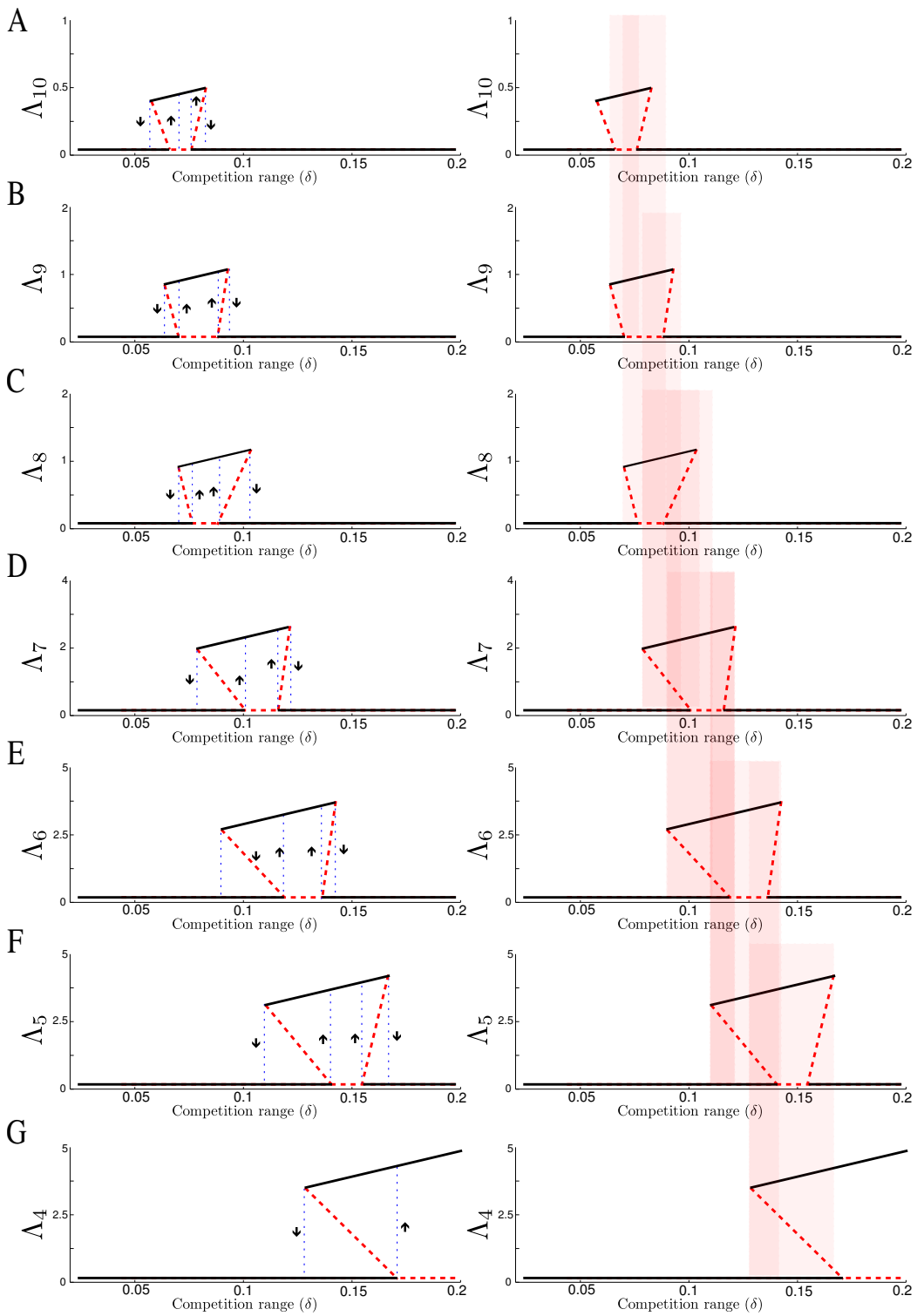

Figure V.8: Schematic picture of expected bifurcation diagram of Λ_n in terms of the parameter δ (left) and regions of multi-stability in grey (right) for $n = 10$ (panel A), $n = 9$ (panel B), $n = 8$ (panel C), $n = 7$ (panel D) $n = 6$ (panel E), $n = 5$ (panel F), and $n = 4$ (panel G).

Scientific communications

Publications

[**P0**] Andrade-Restrepo, Martín. "Is Aggregate-Dependent Yeast Aging Fortuitous? A Model of Damage Segregation and Aggregate Dynamics", Biophysical journal 113.11 (2017): 2464-2476.

[**P1**] Andrade-Restrepo, Martín, Nicolas Champagnat, and Régis Ferrière. "Local adaptation, dispersal evolution, and the spatial eco-evolutionary dynamics of invasion.", Ecology Letters, 22 (2019): 767-777

Unpublished articles

[**A3**] Andrade-Restrepo, Martín, Nicolas Champagnat, and Régis Ferrière. "Spatial eco-evolutionary dynamics along environmental gradients: multi-stability and cluster dynamics." (2018).

Working papers

[**A4**] Andrade-Restrepo, Martín, Jens Starke, "Equation-free analysis of equilibria and multi-stability in spatially-explicit eco-evolutionary dynamics of a population along a one-dimensional resource gradient".

Submitted proceedings

[**Pr5**] Martín Andrade-Restrepo, Paul Lemarre, Laurent Pujo-Menjouet,Leon Matar-Tine, Sorin Ionel Ciuperca. "Modeling the Spatial Propagation of Aβ Oligomers in Alzheimer's Disease".

Talks and posters

[**Po1**] **"On the emergence of clustering along space-trait gradients "(P)**, MMEE: Mathematical Models in Ecology and Evolution, Paris, July 2015.

[**Po2**] **"On the emergence of clustering along space-trait gradients "(P)**, Journées de l'Ecole Doctorale 393, Saint-Maló, October 2015.

[**T1**] **"Parallel Evolutionary Dynamics of Adaptive Diversification in Escherichia coli (Work from Herron and Doebeli, 2013)"(T)**, Evolution Journal Club Institut Jacques Monod, Paris, December 2015.

[**T2**] **"On the emergence of spatial and phenotypic clustering "(T)**, Rencontres math, bio et médecine de Sorbonne Paris Cité, Villetaneuse, January 2016.

[**Po3**] **"Population Patterns Along Space-Trait Gradients: The Emergence of Clustering"(P)**, Journées de l'Ecole Doctorale 393, Saint-Maló, October 2016.

[**T3**] **"Population Patterns Along Space-Trait Gradients: The Emergence of Clustering"(T)**, Internal Seminar Institut Jacques Monod, Paris, November 2016.

[**T4**] **"The spatial dynamics of evolutionary phenotypic clustering"(T)**, Coference on Multiscale analysis and modelling of collective migration in biological systems, Zif-Bielefeld, October 2017.

[**T5**] **"The spatial dynamics of evolutionary phenotypic clustering"(T)**, Internal Seminar at Rostock Universität, Rostock, October 2017.

[**Po4**] **"Is Aggregate-Dependent Yeast Aging Fortuitous? A Model of Damage Segregation and Aggregate Dynamics"(P)**, Journées de l'Ecole Doctorale 393, Saint-Maló, October 2017.

[**T6**] **"Mathematical Modeling of Spatial Propagation of Aβ oligomers"(T)**, CEMRACS 2018, CIRM Marseille, August 2018.

[**T7**] **"A computational look on whether aggregate-dependent yeast aging happens by chance"(T)**, IMYA 2018, KU Leuven, Belgium, August 2018.

Bibliography

[1] C. Zhou, B. D. Slaughter, J. R. Unruh, A. Eldakak, B. Rubinstein, and R. Li, Cell **147**, 1186 (2011).

[2] B. Liu, L. Larsson, V. Franssens, X. Hao, S. M. Hill, V. Andersson, D. Höglund, J. Song, X. Yang, D. Öling, J. Grantham, J. Winderickx, and T. Nyström, Cell **147**, 959 (2011).

[3] P. N. Lacor, M. C. Buniel, P. W. Furlow, A. S. Clemente, P. T. Velasco, M. Wood, K. L. Viola, and W. L. Klein, Journal of Neuroscience **27**, 796 (2007).

[4] U. Sengupta, A. N. Nilson, and R. Kayed, EBioMedicine **6**, 42 (2016).

[5] S. I. Cohen, S. Linse, L. M. Luheshi, E. Hellstrand, D. A. White, L. Rajah, D. E. Otzen, M. Vendruscolo, C. M. Dobson, and T. P. Knowles, Proceedings of the National Academy of Sciences **110**, 9758 (2013).

[6] H. Braak and K. Del Tredici, Acta neuropathologica **121**, 589 (2011).

[7] N. Champagnat and S. Méléard, Journal of Mathematical Biology **55**, 147 (2007).

[8] M. Andrade-Restrepo, N. Champagnat, and R. Ferrière, (2018).

[9] M. Andrade-Restrepo, N. Champagnat, and R. Ferrière, Ecology Letters (2019).

[10] B. Liu, L. Larsson, A. Caballero, X. Hao, D. Öling, J. Grantham, and T. Nyström, Cell **140**, 257 (2010).

[11] Z. Schuss, A. Singer, and D. Holcman, Proceedings of the National Academy of Sciences **104**, 16098 (2007).

[12] D. Holcman and Z. Schuss, J. of Statistical Physics **117**, 6 (2004).

[13] Z. Schuss, The Journal of Physical Chemistry C **114**, 20320 (2010).

[14] C. Paoletti, S. Quintin, A. Matifas, and G. Charvin, Biophysical journal **110**, 1605 (2016).

[15] A. Kinkhabwala, A. Khmelinskii, and M. Knop, BMC biophysics **7**, 10 (2014).

[16] J. Saarikangas, F. Caudron, R. Prasad, D. F. Moreno, A. Bolognesi, M. Aldea, and Y. Barral, Current Biology **27**, 773 (2017).

[17] J. Saarikangas and Y. Barral, Elife **4**, e06197 (2015).

[18] H. Aguilaniu, L. Gustafsson, M. Rigoulet, and T. Nyström, Science **299**, 1751 (2003).

[19] M. Andrade-Restrepo, Biophysical journal **113**, 2464 (2017).

[20] R. Durrett and S. Levin, Theoretical population biology **46**, 363 (1994).

[21] J. A. Endler, *Geographic variation, speciation, and clines*, 10 (Princeton University Press, 1977).

[22] M. Doebeli and U. Dieckmann, Nature **421**, 259 (2003).

[23] E. Mayr, E. Mayr, E. Mayr, and E. Mayr, *Animal species and evolution*, Vol. 797 (Belknap Press of Harvard University Press Cambridge, Massachusetts, 1963).

[24] J. K. James and R. J. Abbott, Evolution **59**, 2533 (2005).

[25] J. Hey, Molecular biology and evolution **27**, 921 (2010).

[26] J. A. Coyne, H. A. Orr, *et al.*, *Speciation*, Vol. 37 (Sinauer Associates Sunderland, MA, 2004).

[27] M. Barluenga, K. N. Stölting, W. Salzburger, M. Muschick, and A. Meyer, Nature **439**, 719 (2006).

[28] D. Gíslason, M. M. Ferguson, S. Skúlason, and S. S. Snorrason, Canadian Journal of Fisheries and Aquatic Sciences **56**, 2229 (1999).

[29] V. Savolainen, M.-C. Anstett, C. Lexer, I. Hutton, J. J. Clarkson, M. V. Norup, M. P. Powell, D. Springate, N. Salamin, and W. J. Baker, Nature **441**, 210 (2006).

[30] U. K. Schliewen, D. Tautz, and S. Pääbo, Nature **368**, 629 (1994).

[31] U. Schliewen, K. Rassmann, M. Markmann, J. Markert, T. Kocher, and D. Tautz, Molecular Ecology **10**, 1471 (2001).

[32] K. Johannesson, E. Rolan-Alvarez, and A. Ekendahl, Evolution , 1180 (1995).

[33] D. Schluter, Science **266**, 798 (1994).

[34] J. L. Feder, S. H. Berlocher, and S. B. Opp, in *Genetic structure and local adaptation in natural insect populations* (Springer, 1998) pp. 408–441.

[35] S. Via, Trends in Ecology & Evolution **16**, 381 (2001).

[36] M. L. Friesen, G. Saxer, M. Travisano, and M. Doebeli, Evolution **58**, 245 (2004).

[37] M. D. Herron and M. Doebeli, PLoS Biol **11**, e1001490 (2013).

[38] P. B. Rainey and M. Travisano, Nature **394**, 69 (1998).

[39] R. F. Rosenzweig, R. Sharp, D. S. Treves, and J. Adams, Genetics **137**, 903 (1994).

[40] D. E. Rozen and R. E. Lenski, The American Naturalist **155**, 24 (2000).

[41] O. Diekmann, P.-E. Jabin, S. Mischler, and B. Perthame, Theoretical population biology **67**, 257 (2005).

[42] G. Barles and B. Perthame, Contemporary Mathematics **439**, 57 (2007).

[43] J. A. Carrillo, S. Cuadrado, and B. Perthame, Mathematical Biosciences **205**, 137 (2007).

[44] B. Perthame and G. Barles, arXiv preprint arXiv:0708.3720 (2007).

[45] B. Perthame and S. Génieys, Mathematical Modelling of Natural Phenomena **2**, 135 (2007).

[46] W. F. Fagan, M. A. Lewis, M. G. Neubert, and P. Van Den Driessche, Ecology Letters **5**, 148 (2002).

[47] H. F. Weinberger, SIAM journal on Mathematical Analysis **13**, 353 (1982).

[48] J. G. Skellam, Biometrika **38**, 196 (1951).

[49] L. L. Sullivan, B. Li, T. E. Miller, M. G. Neubert, and A. K. Shaw, Proceedings of the National Academy of Sciences , 201618744 (2017).

[50] G. Dwyer and W. F. Morris, The American Naturalist **167**, 165 (2005).

[51] I. Kevrekidis, in *Plenary Lecture, CAST Division, AIChE Annual Meeting, Los Angeles* (2000).

[52] I. G. Kevrekidis, C. W. Gear, J. M. Hyman, P. G. Kevrekidid, O. Runborg, C. Theodoropoulos, *et al.*, Communications in Mathematical Sciences **1**, 715 (2003).

[53] I. G. Kevrekidis, C. W. Gear, and G. Hummer, AIChE Journal **50**, 1346 (2004).

[54] T. B. Kirkwood and S. N. Austad, Nature **408**, 233 (2000).

[55] D. Gems and L. Partridge, Annual review of physiology **75**, 621 (2013).

[56] C. López-Otín, M. A. Blasco, L. Partridge, M. Serrano, and G. Kroemer, Cell **153**, 1194 (2013).

[57] L. Fontana, L. Partridge, and V. D. Longo, science **328**, 321 (2010).

[58] M. Ackermann, S. C. Stearns, and U. Jenal, Science **300**, 1920 (2003).

[59] J. G. Evans, in *Research and the ageing population* (Wiley, Chichester, 1988) pp. 38–57.

[60] N. W. Shock, Annual Review of Physiology **23**, 97 (1961).

[61] E. R. Stadtman, Annals of the new York Academy of Sciences **928**, 22 (2001).

[62] T. B. Kirkwood, Cell **120**, 437 (2005).

[63] T. C. Squier, Experimental gerontology **36**, 1539 (2001).

[64] N. Erjavec, L. Larsson, J. Grantham, and T. Nyström, Genes & development **21**, 2410 (2007).

[65] P. Alam, K. Siddiqi, S. K. Chturvedi, and R. H. Khan, International journal of biological macromolecules **103**, 208 (2017).

[66] C. Soto, Nature Reviews Neuroscience **4**, 49 (2003).

[67] M. Ott, V. Gogvadze, S. Orrenius, and B. Zhivotovsky, Apoptosis **12**, 913 (2007).

[68] F. Madeo, E. Fröhlich, M. Ligr, M. Grey, S. J. Sigrist, D. H. Wolf, and K.-U. Fröhlich, The Journal of cell biology **145**, 757 (1999).

[69] F. Chiti and C. M. Dobson, Annu. Rev. Biochem. **75**, 333 (2006).

[70] C. Pimentel, L. Batista-Nascimento, C. Rodrigues-Pousada, and R. A. Menezes, Oxidative medicine and cellular longevity **2012** (2012).

[71] M. P. Mattson, Nature **430**, 631 (2004).

[72] A. Y. Abramov, A. V. Berezhnov, E. I. Fedotova, V. P. Zinchenko, and L. P. Dolgacheva, Biochemical Society Transactions **45**, 1025 (2017).

[73] P. Flagmeier, S. De, D. C. Wirthensohn, S. F. Lee, C. Vincke, S. Muyldermans, T. P. Knowles, S. Gandhi, C. M. Dobson, and D. Klenerman, Angewandte Chemie International Edition **56**, 7750 (2017).

[74] J. Díaz-Villanueva, R. Díaz-Molina, and V. García-González, International journal of molecular sciences **16**, 17193 (2015).

[75] A. P. Ben-Zvi and P. Goloubinoff, Journal of structural biology **135**, 84 (2001).

[76] F. U. Hartl, A. Bracher, and M. Hayer-Hartl, Nature **475**, 324 (2011).

[77] S. Orrenius, V. Gogvadze, and B. Zhivotovsky, Annu. Rev. Pharmacol. Toxicol. **47**, 143 (2007).

[78] M. Hashimoto, E. Rockenstein, L. Crews, and E. Masliah, Neuromolecular medicine **4**, 21 (2003).

[79] A. King, M. Selak, , and E. Gottlieb, Oncogene **25**, 4675 (2006).

[80] B. B. Lowell and G. I. Shulman, Science **307**, 384 (2005).

[81] A. L. Hughes and D. E. Gottschling, Nature **492**, 261 (2012).

[82] I. Amm, T. Sommer, and D. H. Wolf, Biochimica et Biophysica Acta (BBA)-Molecular Cell Research **1843**, 182 (2014).

[83] T. Nyström and B. Liu, FEMS yeast research **14**, 40 (2014).

[84] T. R. Flower, L. S. Chesnokova, C. A. Froelich, C. Dixon, and S. N. Witt, Journal of molecular biology **351**, 1081 (2005).

[85] D. Botstein, S. A. Chervitz, and M. Cherry, Science **277**, 1259 (1997).

[86] T. F. Outeiro and S. Lindquist, Science **302**, 1772 (2003).

[87] P. Fabrizio and V. D. Longo, Biochimica et Biophysica Acta (BBA)-Molecular Cell Research **1783**, 1280 (2008).

[88] C. W. Pratt and K. Cornely, *Essential biochemistry* (Wiley Hoboken, NJ, 2004).

[89] J. Tyedmers, A. Mogk, and B. Bukau, Nature reviews Molecular cell biology **11**, 777 (2010).

[90] F. Chiti, M. Stefani, N. Taddei, G. Ramponi, and C. M. Dobson, Nature **424**, 805 (2003).

[91] L. O. Narhi, J. Schmit, K. Bechtold-Peters, and D. Sharma, Journal of pharmaceutical sciences **101**, 493 (2012).

[92] M. G. Santoro, Biochemical pharmacology **59**, 55 (2000).

[93] V. Grimminger-Marquardt and H. A. Lashuel, Biopolymers: Original Research on Biomolecules **93**, 252 (2010).

[94] J. O'driscoll, D. Clare, and H. Saibil, J Cell Biol **211**, 145 (2015).

[95] S. Guyot, E. Ferret, and P. Gervais, Biotechnology and bioengineering **92**, 403 (2005).

[96] H.-C. Mahler, W. Friess, U. Grauschopf, and S. Kiese, Journal of pharmaceutical sciences **98**, 2909 (2009).

[97] T. Nyström, Molecular microbiology **48**, 17 (2003).

[98] S. M. Jazwinski, in *Genetics and Evolution of Aging* (Springer, 1994) pp. 54–70.

[99] C.-Y. Lai, E. Jaruga, C. Borghouts, and S. M. Jazwinski, Genetics **162**, 73 (2002).

[100] E. J. Stewart, R. Madden, G. Paul, and F. Taddei, PLoS Biol **3**, e45 (2005).

[101] A. B. Lindner, R. Madden, A. Demarez, E. J. Stewart, and F. Taddei, Proceedings of the National Academy of Sciences **105**, 3076 (2008).

[102] N. Erjavec and T. Nyström, Proc. Natl Acad. Sci. USA **104**, 877 (2007).

[103] D. A. Knorre, I. A. Kulemzina, M. I. Sorokin, S. A. Kochmak, N. A. Bocharova, S. S. Sokolov, and F. F. Severin, Cell Cycle **9**, 4501 (2010).

[104] R. Higuchi, J. D. Vevea, T. C. Swayne, R. Chojnowski, V. Hill, I. R. Boldogh, and L. A. Pon, Current Biology **23**, 2417 (2013).

[105] R. Spokoini, O. Moldavski, Y. Nahmias, J. L. England, M. Schuldiner, and D. Kaganovich, Cell reports **2**, 738 (2012).

[106] L. Ruan, C. Zhou, E. Jin, A. Kucharavy, Y. Zhang, Z. Wen, L. Florens, and R. Li, Nature **543**, 443 (2017).

[107] C. Zhou, B. D. Slaughter, J. R. Unruh, F. Guo, Z. Yu, K. Mickey, A. Narkar, R. T. Ross, M. McClain, and R. Li, Cell **159**, 530 (2014).

[108] S. M. Hill, S. Hanzén, and T. Nyström, EMBO reports **18**, 377 (2017).

[109] M. Coelho, S. J. Lade, S. Alberti, T. Gross, and I. M. Tolić, PLoS Biol **12**, e1001886 (2014).

[110] J. Labbadia and R. I. Morimoto, Annual review of biochemistry **84**, 435 (2015).

[111] J. Borgqvist, N. Welkenhuysen, and M. Cvijovic, bioRxiv , 446302 (2018).

[112] O. Marques and T. Outeiro, Cell death & disease **3**, e350 (2012).

[113] J. A. Hardy and G. A. Higgins, Science **256**, 184 (1992).

[114] M. Hiltunen, T. van Groen, and J. Jolkkonen, Journal of Alzheimer's Disease **18**, 401 (2009).

[115] L. M. Ittner and J. Götz, Nature Reviews Neuroscience **12**, 67 (2011).

[116] C. R. Jack Jr, D. S. Knopman, W. J. Jagust, R. C. Petersen, M. W. Weiner, P. S. Aisen, L. M. Shaw, P. Vemuri, H. J. Wiste, S. D. Weigand, *et al.*, The Lancet Neurology **12**, 207 (2013).

[117] P. Čižas, A. Jekabsonė, V. Borutaitė, and R. Morkūnienė, Medicina **47**, 15 (2011).

[118] L. N. Zhao, H. W. Long, Y. Mu, and L. Y. Chew, International journal of molecular sciences **13**, 7303 (2012).

[119] H. B. Nygaard and S. M. Strittmatter, Archives of neurology **66**, 1325 (2009).

[120] S. B. Prusiner, Science **252**, 1515 (1991).

[121] C. Elliott, A. I. Rojo, E. Ribe, M. Broadstock, W. Xia, P. Morin, M. Semenov, G. Baillie, A. Cuadrado, R. Al-Shawi, *et al.*, Translational psychiatry **8**, 179 (2018).

[122] R. J. Perrin, A. M. Fagan, and D. M. Holtzman, Nature **461**, 916 (2009).

[123] M. Storandt, E. A. Grant, J. P. Miller, and J. C. Morris, Neurology **59**, 1034 (2002).

[124] T. Ohm, H. Müller, H. Braak, and J. Bohl, Neuroscience **64**, 209 (1995).

[125] A. D. Smith, Proceedings of the National Academy of Sciences **99**, 4135 (2002).

[126] R. F. Sowade and T. R. Jahn, Nature communications **8**, 512 (2017).

[127] F. Carbonell, Y. Iturria-Medina, and A. C. Evans, Frontiers in Neurology **9**, 37 (2018).

[128] M. Eigen, Biophysical chemistry **63**, A1 (1996).

[129] J. D. Harper and P. T. Lansbury Jr, Annual review of biochemistry **66**, 385 (1997).

[130] M. A. Nowak, D. C. Krakauer, A. Klug, and R. M. May, Integrative Biology: Issues, News, and Reviews: Published in Association with The Society for Integrative and Comparative Biology **1**, 3 (1998).

[131] M. L. Greer, L. Pujo-Menjouet, and G. F. Webb, Journal of theoretical biology **242**, 598 (2006).

[132] F. Matthäus, Journal of theoretical biology **240**, 104 (2006).

[133] F. Matthaeus, Journal of Biological Systems **17**, 623 (2009).

[134] M. P. Stumpf and D. C. Krakauer, Proceedings of the National Academy of Sciences **97**, 10573 (2000).

[135] I. S. Ciuperca, M. Dumont, A. Lakmeche, P. Mazzocco, L. Pujo-Menjouet, H. Rezaei, and L. M. Tine, Discrete and Continuous Dynamical Systems-Series B (2018).

[136] M. Helal, E. Hingant, L. Pujo-Menjouet, and G. F. Webb, Journal of mathematical biology **69**, 1207 (2014).

[137] M. Helal, A. Igel-Egalon, A. Lakmeche, P. Mazzocco, A. Perrillat-Mercerot, L. Pujo-Menjouet, H. Rezaei, and L. M. Tine, Journal of mathematical biology , 1 (2018).

[138] J. Rasmussen, M. Jucker, and L. C. Walker, Prion **11**, 215 (2017).

[139] D. Burdick, B. Soreghan, M. Kwon, J. Kosmoski, M. Knauer, A. Henschen, J. Yates, C. Cotman, and C. Glabe, Journal of Biological Chemistry **267**, 546 (1992).

[140] A. Lomakin, D. B. Teplow, D. A. Kirschner, and G. B. Benedek, Proceedings of the National Academy of Sciences **94**, 7942 (1997).

[141] M. Doumic, T. Goudon, T. Lepoutre, *et al.*, Communications in Mathematical Sciences **7**, 839 (2009).

[142] A. Vasseur, F. Poupaud, J.-F. Collet, and T. Goudon, SIAM Journal on Applied Mathematics **62**, 1488 (2002).

[143] J. Velázquez, Journal of statistical physics **92**, 195 (1998).

[144] M. Bertsch, B. Franchi, N. Marcello, M. C. Tesi, and A. Tosin, Mathematical medicine and biology: a journal of the IMA **34**, 193 (2016).

[145] M. Bertsch, B. Franchi, M. C. Tesi, and A. Tosin, Journal of Physics A: Mathematical and Theoretical **50**, 414003 (2017).

[146] P. M. Altrock, L. L. Liu, and F. Michor, Nature Reviews Cancer **15**, 730 (2015).

[147] C. Haass and D. J. Selkoe, Nature reviews Molecular cell biology **8**, 101 (2007).

[148] W. Yong, A. Lomakin, M. D. Kirkitadze, D. B. Teplow, S.-H. Chen, and G. B. Benedek, Proceedings of the National Academy of Sciences **99**, 150 (2002).

[149] L. Rajendran, M. Honsho, T. R. Zahn, P. Keller, K. D. Geiger, P. Verkade, and K. Simons, Proceedings of the National Academy of Sciences **103**, 11172 (2006).

[150] M. S. Sinha, A. Ansell-Schultz, L. Civitelli, C. Hildesjö, M. Larsson, L. Lannfelt, M. Ingelsson, and M. Hallbeck, Acta neuropathologica **136**, 41 (2018).

[151] J. Hey, Molecular biology and evolution **27**, 921 (2009).

[152] D. S. Jordan, Science , 545 (1905).

[153] R. Lande, American Naturalist , 463 (1980).

[154] L. Caro, P. Caycedo-Rosales, R. Bowie, H. Slabbekoorn, and C. Cadena, Journal of evolutionary biology **26**, 357 (2013).

[155] C. Darwin, M. J. Adler, and R. M. Hutchins, *The origin of species by means of natural selection* (J. Murray, 1872).

[156] T. W. Schoener, Science **331**, 426 (2011).

[157] W. L. Brown and E. O. Wilson, Systematic zoology **5**, 49 (1956).

[158] J. A. Metz, R. M. Nisbet, and S. A. Geritz, Trends in Ecology & Evolution **7**, 198 (1992).

[159] J. A. Metz, S. A. Geritz, G. Meszéna, F. J. Jacobs, and J. S. Van Heerwaarden, (1995).

[160] R. Ferrière, U. Dieckmann, and D. Couvet, *Evolutionary conservation biology*, Vol. 4 (Cambridge University Press, 2004).

[161] H. Kokko and A. López-Sepulcre, Ecology Letters **10**, 773 (2007).

[162] G. Fussmann, M. Loreau, and P. Abrams, Functional Ecology **21**, 465 (2007).

[163] M. Doebeli and I. Ispolatov, Evolution **68**, 1365 (2014).

[164] U. Dieckmann and M. Doebeli, Nature **400**, 354 (1999).

[165] J. M. Smith, American Naturalist , 637 (1966).

[166] K. Mather, Evolution **9**, 52 (1955).

[167] J. Maynard Smith, Nature **195**, 60 (1962).

[168] C. Rueffler, T. J. Van Dooren, O. Leimar, and P. A. Abrams, Trends in Ecology & Evolution **21**, 238 (2006).

[169] S. Via, Trends in Ecology & Evolution **16**, 381 (2001).

[170] J. Lederberg, Genetics **153**, 1 (1999).

[171] A. Tellier and J. K. Brown, BMC evolutionary biology **11**, 319 (2011).

[172] A. Kashiwagi, W. Noumachi, M. Katsuno, M. T. Alam, I. Urabe, and T. Yomo, Journal of molecular evolution **52**, 502 (2001).

[173] D. I. Bolnick and B. M. Fitzpatrick, Annual Review of Ecology, Evolution, and Systematics , 459 (2007).

[174] J. Mavárez, C. A. Salazar, E. Bermingham, C. Salcedo, C. D. Jiggins, and M. Linares, Nature **441**, 868 (2006).

[175] E. B. Knox and J. D. Palmer, Proceedings of the National Academy of Sciences **92**, 10349 (1995).

[176] M. C. Fisher-Reid, T. N. Engstrom, C. A. Kuczynski, P. R. Stephens, and J. J. Wiens, Molecular ecology **22**, 4681 (2013).

[177] B. Kramer, H. Van der Bank, N. Flint, H. Sauer-Gürth, and M. Wink, Environmental Biology of Fishes **67**, 47 (2003).

[178] M. C. Melo, A. Grealy, B. Brittain, G. M. Walter, and D. Ortiz-Barrientos, New Phytologist **203**, 323 (2014).

[179] E. Kisdi and S. A. Geritz, Evolution , 993 (1999).

[180] S. A. Geritz and K. Éva, Proceedings of the Royal Society of London B: Biological Sciences **267**, 1671 (2000).

[181] M. Doebeli and U. Dieckmann, The american naturalist **156**, S77 (2000).

[182] J. A. Metz, S. A. Geritz, G. Meszéna, F. J. Jacobs, and J. S. Van Heerwaarden, (1995).

[183] S. A. Geritz, J. A. Metz, É. Kisdi, and G. Meszéna, Physical Review Letters **78**, 2024 (1997).

[184] S. A. Geritz, G. Mesze, J. A. Metz, *et al.*, Evolutionary ecology **12**, 35 (1998).

[185] N. Champagnat, R. Ferrière, and S. Méléard, Theoretical population biology **69**, 297 (2006).

[186] U. Dieckmann and R. Law, Journal of mathematical biology **34**, 579 (1996).

[187] M. Doebeli and I. Ispolatov, Science **328**, 494 (2010).

[188] I. Ispolatov, V. Madhok, and M. Doebeli, Journal of theoretical biology **390**, 97 (2016).

[189] M. Doebeli and I. Ispolatov, The American Naturalist **189**, 105 (2017).

[190] H. Svardal, C. Rueffler, and J. Hermisson, Evolution **65**, 2492 (2011).

[191] H. Svardal, C. Rueffler, and M. Doebeli, Evolution **68**, 3248 (2014).

[192] T. J. Van Dooren, M. Durinx, and I. Demon, Evolutionary Ecology Research **6**, 857 (2004).

[193] D. E. Rozen, D. Schneider, and R. E. Lenski, Journal of Molecular Evolution **61**, 171 (2005).

[194] M. Le Gac, J. Plucain, T. Hindré, R. E. Lenski, and D. Schneider, Proceedings of the National Academy of Sciences **109**, 9487 (2012).

[195] J. Plucain, T. Hindré, M. Le Gac, O. Tenaillon, S. Cruveiller, C. Médigue, N. Leiby, W. R. Harcombe, C. J. Marx, R. E. Lenski, *et al.*, Science **343**, 1366 (2014).

[196] F. Aboagye-Antwi, N. Alhafez, G. D. Weedall, J. Brothwood, S. Kandola, D. Paton, A. Fofana, L. Olohan, M. P. Betancourth, N. E. Ekechukwu, *et al.*, PLoS Genet **11**, e1005141 (2015).

[197] A. F. Kautt, G. Machado-Schiaffino, and A. Meyer, PLoS Genet **12**, e1006157 (2016).

[198] A. F. Kautt, G. Machado-Schiaffino, J. Torres-Dowdall, and A. Meyer, Ecology and Evolution **6**, 5342 (2016).

[199] U. K. Schliewen and B. Klee, Frontiers in zoology **1**, 1 (2004).

[200] A. Klemetsen, J. Elliott, R. Knudsen, and P. Sørensen, Journal of Fish Biology **60**, 933 (2002).

[201] A. S. Papadopulos, M. Kaye, C. Devaux, H. Hipperson, J. Lighten, L. T. Dunning, I. Hutton, W. J. Baker, R. K. Butlin, and V. Savolainen, Phil. Trans. R. Soc. B **369**, 20130342 (2014).

[202] C. Wilding, R. Butlin, and J. Grahame, Journal of Evolutionary Biology **14**, 611 (2001).

[203] Y. Hadid, T. Pavlíček, A. Beiles, R. Ianovici, S. Raz, and E. Nevo, Proceedings of the National Academy of Sciences **111**, 1043 (2014).

[204] K. Li, W. Hong, H. Jiao, G.-D. Wang, K. A. Rodriguez, R. Buffenstein, Y. Zhao, E. Nevo, and H. Zhao, Proceedings of the National Academy of Sciences **112**, 11905 (2015).

[205] P. G. Ryan, P. Bloomer, C. L. Moloney, T. J. Grant, and W. Delport, science **315**, 1420 (2007).

[206] P. B. Rainey and M. Travisano, Nature **394**, 69 (1998).

[207] P. B. Rainey, A. Buckling, R. Kassen, and M. Travisano, Trends in ecology & evolution **15**, 243 (2000).

[208] A. J. Spiers, S. G. Kahn, J. Bohannon, M. Travisano, and P. B. Rainey, Genetics **161**, 33 (2002).

[209] D. B. Wake and K. P. Yanev, Evolution , 702 (1986).

[210] R. J. Pereira, W. B. Monahan, and D. B. Wake, BMC evolutionary biology **11**, 1 (2011).

[211] D. E. Irwin, S. Bensch, and T. D. Price, Nature **409**, 333 (2001).

[212] R. Kassen, M. Llewellyn, and P. B. Rainey, Nature **431**, 984 (2004).

[213] R. C. Flohr, C. J. Blom, P. B. Rainey, and H. J. Beaumont, Proceedings of the National Academy of Sciences **110**, 20663 (2013).

[214] J. B. Losos, T. R. Jackman, A. Larson, K. de Queiroz, and L. Rodrıéguez-Schettino, Science **279**, 2115 (1998).

[215] O. Madsen, M. Scally, C. J. Douady, D. J. Kao, R. W. DeBry, R. Adkins, H. M. Amrine, M. J. Stanhope, W. W. de Jong, and M. S. Springer, Nature **409**, 610 (2001).

[216] R. Gillespie, Science **303**, 356 (2004).

[217] H. López-Fernández, J. H. Arbour, K. Winemiller, R. L. Honeycutt, *et al.*, Evolution **67**, 1321 (2013).

[218] J. Ohlberger, T. Mehner, G. Staaks, and F. Hölker, Functional Ecology **22**, 501 (2008).

[219] P. Shum, C. Pampoulie, C. Sacchi, and S. Mariani, PeerJ **2**, e525 (2014).

[220] T. Ingram, Proceedings of the Royal Society B: Biological Sciences **278**, 613 (2010).

[221] J. M. Smith, Nature **201**, 1145 (1964).

[222] R. Ferriere and M. Gatto, Theoretical Population Biology **48**, 126 (1995).

[223] N. Champagnat, R. Ferričre, and G. Ben Arous4, Selection **2**, 73 (2002).

[224] O. Diekmann, P.-E. Jabin, S. Mischler, and B. Perthame, Theoretical population biology **67**, 257 (2005).

[225] G. Barles and B. Perthame, in *Recent developments in nonlinear partial differential equations*, Contemp. Math., Vol. 439 (Amer. Math. Soc., Providence, RI, 2007) pp. 57–68.

[226] J. A. Carrillo, S. Cuadrado, and B. Perthame, Mathematical Biosciences **205**, 137 (2007).

[227] J. Polechová and N. H. Barton, Evolution **59**, 1194 (2005).

[228] O. Leimar, M. Doebeli, and U. Dieckmann, Evolution **62**, 807 (2008).

[229] R. Ferriere, Options Spring **2000**, 12 (2000).

[230] M. Gyllenberg and K. Parvinen, Bulletin of mathematical biology **63**, 981 (2001).

[231] J. Ohlberger, Å. Brännström, and U. Dieckmann, The American Naturalist **182**, 359 (2013).

[232] M. Doebeli and G. D. Ruxton, Evolution **51**, 1730 (1997).

[233] M. Boots and Y. Haraguchi, The american naturalist **153**, 359 (1999).

[234] T. Day, P. A. Abrams, and J. M. Chase, Evolution **56**, 877 (2002).

[235] O. Diekmann, Summer School on Mathematical Biology , 63 (2002).

[236] M. Doebeli, *Adaptive Diversification (MPB-48)* (Princeton University Press, 2011).

[237] M. Hassell and R. May, The Journal of Animal Ecology , 567 (1974).

[238] M. P. Hassell, S. W. Pacala, and G. Tingley, Philosophical Transactions of the Royal Society of London B: Biological Sciences **330**, 203 (1990).

[239] H.-S. Niwa, Journal of theoretical Biology **171**, 123 (1994).

[240] G. Flierl, D. Grünbaum, S. Levins, and D. Olson, Journal of Theoretical biology **196**, 397 (1999).

[241] W. Young, A. Roberts, and G. Stuhne, Nature **412**, 328 (2001).

[242] J. Haldane, Journal of genetics **48**, 277 (1948).

[243] R. A. Fisher, Biometrics **6**, 353 (1950).

[244] A. Bazykin, Evolution **23**, 685 (1969).

[245] T. Ingram, Proceedings of the Royal Society of London B: Biological Sciences **278**, 613 (2011).

[246] M. Slatkin, Journal of Theoretical Biology **70**, 213 (1978).

[247] M. Kirkpatrick and N. H. Barton, The American Naturalist **150**, 1 (1997).

[248] N. H. Barton, Genetical research **74**, 223 (1999).

[249] T. J. Case, M. L. Taper, *et al.*, The American Naturalist **155**, 583 (2000).

[250] J. Roughgarden, American Naturalist , 683 (1972).

[251] J. Roughgarden, (1979).

[252] R. H. MacArthur, *Geographical ecology: patterns in the distribution of species* (Princeton University Press, 1972).

[253] R. M. May, *Stability and complexity in model ecosystems*, Vol. 6 (Princeton University Press, 1973).

[254] E. Dolgin, M. Whitlock, and A. Agrawal, Journal of evolutionary biology **19**, 1894 (2006).

[255] N. Fournier and S. Méléard, Annals of applied probability , 1880 (2004).

[256] S. Vignieri, Science **345**, 392 (2014).

[257] A. D. Barnosky, N. Matzke, S. Tomiya, G. O. Wogan, B. Swartz, T. B. Quental, C. Marshall, J. L. McGuire, E. L. Lindsey, K. C. Maguire, *et al.*, Nature **471**, 51 (2011).

[258] M. B. Davis, R. G. Shaw, and J. R. Etterson, Ecology **86**, 1704 (2005).

[259] M. M. Osmond and C. A. Klausmeier, Evolution **71**, 2930 (2017).

[260] K. Atkins and J. Travis, Journal of Theoretical Biology **266**, 449 (2010).

[261] A. S. Kondrashov and M. Shpak, Proceedings of the Royal Society of London. Series B: Biological Sciences **265**, 2273 (1998).

[262] C. D. Thomas, A. Cameron, R. E. Green, M. Bakkenes, L. J. Beaumont, Y. C. Collingham, B. F. Erasmus, M. F. De Siqueira, A. Grainger, L. Hannah, *et al.*, Nature **427**, 145 (2004).

[263] C. D. Thomas, A. M. Franco, and J. K. Hill, Trends in Ecology & Evolution **21**, 415 (2006).

[264] Z. Liu, C. He, and J. Wu, PLoS One **11**, e0154613 (2016).

[265] M. L. McKinney, Bioscience **52**, 883 (2002).

[266] D. C. Morton, R. S. DeFries, Y. E. Shimabukuro, L. O. Anderson, E. Arai, F. del Bon Espirito-Santo, R. Freitas, and J. Morisette, Proceedings of the National Academy of Sciences **103**, 14637 (2006).

[267] C. Van Dover, J. Ardron, E. Escobar, M. Gianni, K. Gjerde, A. Jaeckel, D. Jones, L. Levin, H. Niner, L. Pendleton, *et al.*, Nature Geoscience **10**, 464 (2017).

[268] M. Williamson, *Biological invasions*, Vol. 15 (Springer Science & Business Media, 1996).

[269] M. G. Neubert, M. Kot, and M. A. Lewis, Proceedings of the Royal Society B: Biological Sciences **267**, 1603 (2000).

[270] M. Kot, J. Medlock, T. Reluga, and D. B. Walton, Theoretical Population Biology **66**, 175 (2004).

[271] M. Kirkpatrick and N. H. Barton, The American Naturalist **150**, 1 (1997).

[272] B. L. Phillips, G. P. Brown, J. K. Webb, and R. Shine, Nature **439**, 803 (2006).

[273] D. Andow, P. M. Kareiva, S. A. Levin, and A. Okubo, Landscape Ecology **4**, 177 (1990).

[274] A. Okubo, Biomathematics (1980).

[275] A. Hastings, K. Cuddington, K. F. Davies, C. J. Dugaw, S. Elmendorf, A. Freestone, S. Harrison, M. Holland, J. Lambrinos, U. Malvadkar, *et al.*, Ecology Letters **8**, 91 (2005).

[276] E. Bouin, V. Calvez, N. Meunier, S. Mirrahimi, B. Perthame, G. Raoul, and R. Voituriez, arXiv preprint arXiv:1207.2355 (2012).

[277] M. Szűcs, M. Vahsen, B. Melbourne, C. Hoover, C. Weiss-Lehman, and R. Hufbauer, Proceedings of the National Academy of Sciences **114**, 13501 (2017).

[278] C. Marschler, J. Sieber, P. G. Hjorth, and J. Starke, in *Traffic and Granular Flow'13* (Springer, 2015) pp. 423–439.

[279] O. Corradi, P. G. Hjorth, and J. Starke, SIAM Journal on Applied Dynamical Systems **11**, 1007 (2012).

[280] D. Helbing and P. Molnar, Physical review E **51**, 4282 (1995).

[281] M. Bando, K. Hasebe, A. Nakayama, A. Shibata, and Y. Sugiyama, Physical review E **51**, 1035 (1995).

[282] T. S. Deisboeck and G. S. Stamatakos, *Multiscale cancer modeling* (CRC press, 2010).

[283] S. Schnell, R. Grima, and P. K. Maini, American Scientist **95**, 134 (2007).

[284] J. S. Lowengrub, H. B. Frieboes, F. Jin, Y.-L. Chuang, X. Li, P. Macklin, S. M. Wise, and V. Cristini, Nonlinearity **23**, R1 (2009).

[285] A. Khuong, G. Theraulaz, C. Jost, A. Perna, and J. Gautrais, in *ECAL* (2011) pp. 404–411.

[286] Z. Wang, B. J. Ramsey, D. Wang, K. Wong, H. Li, E. Wang, and Z. Bao, PloS one **11**, e0166551 (2016).

[287] M. Scheffer, J. Bascompte, W. A. Brock, V. Brovkin, S. R. Carpenter, V. Dakos, H. Held, E. H. Van Nes, M. Rietkerk, and G. Sugihara, Nature **461**, 53 (2009).

[288] K. Parvinen, Evolutionary Ecology Research **9**, 619 (2007).

[289] J. Touboul, arXiv preprint arXiv:1410.8001 (2014).

[290] J. S. Juul and M. A. Porter, arXiv preprint arXiv:1707.07187 (2017).

[291] I. G. Kevrekidis and G. Samaey, Annual review of physical chemistry **60**, 321 (2009).

[292] N. Fenichel, Journal of differential equations **31**, 53 (1979).

[293] C. Marschler, J. Sieber, R. Berkemer, A. Kawamoto, and J. Starke, SIAM Journal on Applied Dynamical Systems **13**, 1202 (2014).

[294] E. Vanden-Eijnden *et al.*, arXiv preprint arXiv:0806.1621 (2008).

[295] D. I. Kopelevich, A. Z. Panagiotopoulos, and I. G. Kevrekidis, The Journal of chemical physics **122**, 044907 (2005).

[296] K. Budde, T. Warnke, A. M. Uhrmacher, E. Schätz, J. Starke, and F. Haack, in *2017 Winter Simulation Conference (WSC)* (IEEE, 2017) pp. 4564–4565.

[297] A. G. Makeev and I. G. Kevrekidis, Chemical engineering science **59**, 1733 (2004).

[298] F. Schilder, E. Bureau, I. F. Santos, J. J. Thomsen, and J. Starke, Journal of Sound and Vibration **358**, 251 (2015).

[299] R. A. Fisher, Annals of eugenics **7**, 355 (1937).

[300] J. D. Murray, "Mathematical biology, vol. 19 of biomathematics," (1989).

[301] A. Kolmogorov, I. Petrovskii, and N. Piskunov, Moskovskogo Gos. Univ **1**, 1 (1937).

[302] S. Genieys, V. Volpert, and P. Auger, Mathematical Modelling of Natural Phenomena **1**, 63 (2006).

[303] S. Genieys, N. Bessonov, and V. Volpert, Mathematical and computer modelling **49**, 2109 (2009).

[304] S. Pigolotti, C. López, and E. Hernández-García, Physical review letters **98**, 258101 (2007).

[305] F. V. Barbosa, A. A. Penna, R. M. Ferreira, K. L. Novais, J. A. da Cunha, and F. A. Oliveira, Physica A: Statistical Mechanics and its Applications **473**, 301 (2017).

[306] S. Génieys and B. Perthame, Mathematical Modeling in Natural Phenomenon **2**, 135 (2007).

[307] O. Leimar, M. Doebeli, and U. Dieckmann, Evolution **62**, 807 (2008).

[308] X.-X. Liao and J. Li, Nonlinear Analysis: Theory, Methods & Applications **28**, 1751 (1997).

[309] M. A. Cohen and S. Grossberg, IEEE transactions on systems, man, and cybernetics , 815 (1983).

[310] Y. Takeuchi, Journal of mathematical analysis and applications **116**, 209 (1986).

[311] N. Champagnat, P.-E. Jabin, and G. Raoul, Comptes Rendus Mathematique **348**, 1267 (2010).

[312] I. Stewart, T. Elmhirst, and J. Cohen, "Symmetry-breaking as an origin of species," in *Bifurcation, Symmetry and Patterns*, edited by J. Buescu, S. B. S. D. Castro, A. P. da Silva Dias, and I. S. Labouriau (Birkhäuser Basel, Basel, 2003) pp. 3–54.

[313] M. Golubitsky and I. Stewart, São Paulo Journal of Mathematical Sciences **9**, 1 (2015).

[314] I. Stewart, Univ Iagellonicae Acta Math **41**, 67 (2003).

[315] R. K. Mortimer and J. R. Johnston, Nature **183**, 1751 (1959).

[316] B. K. Kennedy, N. R. Austriaco, and L. Guarente, The Journal of cell biology **127**, 1985 (1994).

[317] N. Erjavec, M. Cvijovic, E. Klipp, and T. Nyström, Proceedings of the National Academy of Sciences **105**, 18764 (2008).

[318] H. Olzscha, S. M. Schermann, A. C. Woerner, S. Pinkert, M. H. Hecht, G. G. Tartaglia, M. Vendruscolo, M. Hayer-Hartl, F. U. Hartl, and R. M. Vabulas, Cell **144**, 67 (2011).

[319] A.-S. Coquel, J.-P. Jacob, M. Primet, A. Demarez, M. Dimiccoli, T. Julou, L. Moisan, A. B. Lindner, and H. Berry, PLoS Comput Biol **9**, e1003038 (2013).

[320] L. R. Gehlen, S. Nagai, K. Shimada, P. Meister, A. Taddei, and S. M. Gasser, Current Biology **21**, 25 (2011).

[321] A. Lovrics, A. Csikász-Nagy, I. G. Zsély, J. Zádor, T. Turányi, and B. Novák, BMC bioinformatics **7**, 494 (2006).

[322] A. Singer, Z. Schuss, D. Holcman, and R. Eisenberg, Journal of Statistical Physics **122**, 437 (2006).

[323] A. Singer, Z. Schuss, and D. Holcman, Journal of statistical physics **122**, 465 (2006).

[324] A. Singer, Z. Schuss, and D. Holcman, Journal of Statistical Physics **122**, 491 (2006).

[325] T. Bickel, Physica A: Statistical Mechanics and its Applications **377**, 24 (2007).

[326] P. S. Riseborough and P. Hanggi, Surface Science **122**, 459 (1982).

[327] M. J. Saxton, Biophysical journal **64**, 1766 (1993).

[328] A. Kusumi, Y. Sako, and M. Yamamoto, Biophysical journal **65**, 2021 (1993).

[329] R. Morales, C. Duran-Aniotz, J. Castilla, L. Estrada, and C. Soto, Molecular psychiatry **17**, 1347 (2012).

[330] T. Olsson, O. Klementieva, and G. Gouras, Neurobiology of disease **113**, 1 (2018).

[331] T. Xiao, W. Zhang, B. Jiao, C.-Z. Pan, X. Liu, and L. Shen, Translational neurodegeneration **6**, 3 (2017).

[332] S. Eleuteri, S. Di Giovanni, E. Rockenstein, M. Mante, A. Adame, M. Trejo, W. Wrasidlo, F. Wu, P. Fraering, E. Masliah, *et al.*, Neurobiology of disease **74**, 144 (2015).

[333] M. Doumic, T. Goudon, and T. Lepoutre, Commun. Math. Sci. **7**, 839 (2009).

[334] J. Masel, V. A. Jansen, and M. A. Nowak, Biophysical chemistry **77**, 139 (1999).

[335] I. Ciuperca, M. Dumont, A. Lakmeche, P. Mazzocco, L. Pujo-Menjouet, H. Rezaei, and L. Tine, (2016).

[336] R. Yvinec, J. Deschamps, and E. Hingant, in *ITM Web of Conferences*, Vol. 5 (EDP Sciences, 2015) p. 00017.

[337] F. Carbonell, Y. Iturria-Medina, and A. Evans, Frontiers in Neurology **9**, 37 (2018).

[338] G. B. Arfken and H. J. Weber, "Mathematical methods for physicists," (1999).

[339] W. Everitt and C. Markett, Journal of Computational and Applied Mathematics **54**, 325 (1994).

[340] W. N. Everitt, in *Sturm-Liouville Theory* (Springer, 2005) pp. 271–331.

[341] R. Murphy and M. Pallitto, Journal of structural biology **130**, 109 (2000).

[342] I. Bloomfield, I. Johnston, and L. Bilston, Pediatric neurosurgery **28**, 246 (1998).

[343] S. Nag, B. Sarkar, A. Bandyopadhyay, B. Sahoo, V. Sreenivasan, M. Kombrabail, C. Muralidharan, and S. Maiti, Journal of Biological Chemistry , jbc (2011).

[344] P. Mehta, T. Pirttilä, S. Mehta, E. Sersen, P. Aisen, and H. Wisniewski, Archives of neurology **57**, 100 (2000).

[345] F. Hecht, J. Numer. Math. **20**, 251 (2012).

[346] U. Ayachit, (2015).

[347] N. Shigesada and K. Kawasaki, *Biological invasions: theory and practice* (Oxford University Press, UK, 1997).

[348] J. Lockwood, M. Hoopes, and M. Marchetti, "Modeling the geographic spread of invasive species," (2007).

[349] R. D. Holt, T. H. Keitt, M. A. Lewis, B. A. Maurer, and M. L. Taper, Oikos **108**, 18 (2005).

[350] N. Shigesada, K. Kawasaki, and E. Teramoto, Theoretical Population Biology **30**, 143 (1986).

[351] S. V. Petrovskii, A. Y. Morozov, and E. Venturino, Ecology Letters **5**, 345 (2002).

[352] S. Petrovskii, A. Morozov, and B.-L. Li, Bulletin of mathematical biology **67**, 637 (2005).

[353] H. Caswell, M. G. Neubert, and C. M. Hunter, Theoretical Ecology **4**, 407 (2011).

[354] S. J. Schreiber and M. E. Ryan, Theoretical Ecology **4**, 423 (2011).

[355] J. Travis, D. Reznick, R. D. Bassar, A. López-Sepulcre, R. Ferriere, and T. Coulson, in *Advances in Ecological Research*, Vol. 50 (Elsevier, 2014) pp. 1–40.

[356] K. M. Dlugosch and I. M. Parker, Ecology Letters **11**, 701 (2008).

[357] R. I. Colautti and J. A. Lau, Molecular Ecology **24**, 1999 (2015).

[358] R. B. Huey, G. W. Gilchrist, M. L. Carlson, D. Berrigan, and L. Serra, Science **287**, 308 (2000).

[359] R. I. Colautti and S. C. Barrett, Science **342**, 364 (2013).

[360] B. L. Phillips, G. P. Brown, J. K. Webb, and R. Shine, Nature **439**, 803 (2006).

[361] E. Lombaert, A. Estoup, B. Facon, B. Joubard, J.-C. Grégoire, A. Jannin, A. Blin, and T. Guillemaud, Journal of evolutionary biology **27**, 508 (2014).

[362] N. Barton, in *Integrating Ecology and Evolution in a Spatial Context (eds Silvertown J, Antonovics J)*, Vol. 14 (Blackwell Science, Oxford, UK, 2001) pp. 365–392.

[363] G. García-Ramos and D. Rodríguez, Evolution **56**, 661 (2002).

[364] L. Excoffier and N. Ray, Trends in ecology & evolution **23**, 347 (2008).

[365] O. Hallatschek and D. R. Nelson, Theoretical population biology **73**, 158 (2008).

[366] S. Peischl, M. Kirkpatrick, and L. Excoffier, The American Naturalist **185**, E81 (2015).

[367] R. Gomulkiewicz, R. D. Holt, and M. Barfield, Theoretical population biology **55**, 283 (1999).

[368] R. D. Holt, Evolutionary ecology research **5**, 159 (2003).

[369] R. D. Holt and T. H. Keitt, Oikos **108**, 3 (2005).

[370] M. Alleaume-Benharira, I. Pen, and O. Ronce, Journal of evolutionary biology **19**, 203 (2006).

[371] J. R. Bridle, J. Polechová, M. Kawata, and R. K. Butlin, Ecology Letters **13**, 485 (2010).

[372] J. Polechova, PLoS biology **16**, e2005372 (2018).

[373] B. L. Phillips, G. P. Brown, and R. Shine, Ecology **91**, 1617 (2010).

[374] R. Shine, G. P. Brown, and B. L. Phillips, Proceedings of the National Academy of Sciences **108**, 5708 (2011).

[375] O. Ronce, Annu. Rev. Ecol. Evol. Syst. **38**, 231 (2007).

[376] O. J. Burton, B. L. Phillips, and J. M. Travis, Ecology letters **13**, 1210 (2010).

[377] D. Bonte, H. Van Dyck, J. M. Bullock, A. Coulon, M. Delgado, M. Gibbs, V. Lehouck, E. Matthysen, K. Mustin, M. Saastamoinen, *et al.*, Biological Reviews **87**, 290 (2012).

[378] J. Clobert, M. Baguette, T. G. Benton, and J. M. Bullock, *Dispersal ecology and evolution* (Oxford University Press, 2012).

[379] C. Dytham, Proceedings of the Royal Society of London B: Biological Sciences **276**, 1407 (2009).

[380] A. Kubisch, R. D. Holt, H.-J. Poethke, and E. A. Fronhofer, Oikos **123**, 5 (2014).

[381] W. D. Hamilton and R. M. May, Nature **269**, 578 (1977).

[382] M. A. McPeek and R. D. Holt, The American Naturalist **140**, 1010 (1992).

[383] C. Cadet, R. Ferrière, J. A. Metz, and M. Van Baalen, The American Naturalist **162**, 427 (2003).

[384] E. A. Fronhofer and F. Altermatt, Nature communications **6**, 6844 (2015).

[385] J. G. Lambrinos, Ecology **85**, 2061 (2004).

[386] C. A. Stockwell, A. P. Hendry, and M. T. Kinnison, Trends in Ecology & Evolution **18**, 94 (2003).

[387] M. Alfaro and J. Coville, Applied Mathematics Letters **25**, 2095 (2012).

[388] H. Han and C. Zheng, Journal of Mathematical Analysis and Applications **437**, 720 (2016).

[389] A. Duputié and F. Massol, Interface focus **3**, 20130028 (2013).

[390] A. Hastings, Theoretical Population Biology **24**, 244 (1983).

[391] V. Hutson, S. Martinez, K. Mischaikow, and G. T. Vickers, Journal of mathematical biology **47**, 483 (2003).

[392] R. S. Cantrell, C. Cosner, and Y. Lou, Spatial ecology , 213 (2009).

[393] B. Bolker, Spatial ecology , 231 (2010).

[394] A. North, S. Cornell, and O. Ovaskainen, Evolution: International Journal of Organic Evolution **65**, 1739 (2011).

[395] R. S. Cantrell, C. Cosner, and Y. Lou, Mathematical biosciences **204**, 199 (2006).

[396] S. Billiard and T. Lenormand, Evolution **59**, 13 (2005).

[397] F. Blanquart and S. Gandon, Evolution **68**, 1617 (2014).

[398] F. Massol and F. Débarre, Evolution **69**, 1925 (2015).

[399] J. M. Travis and C. Dytham, Evolutionary Ecology Research **4**, 1119 (2002).

[400] J. M. Travis, K. Mustin, T. G. Benton, and C. Dytham, Journal of theoretical biology **259**, 151 (2009).

[401] A. Kubisch, T. Hovestadt, and H.-J. Poethke, Ecology **91**, 3094 (2010).

[402] B. L. Phillips, G. P. Brown, J. M. Travis, and R. Shine, the american naturalist **172**, S34 (2008).

[403] K. Bartoń, T. Hovestadt, B. Phillips, and J. Travis, Proceedings of the Royal Society B: Biological Sciences **279**, 1194 (2011).

[404] J. Cote, J. Clobert, and P. Fitze, Proceedings of the National Academy of Sciences **104**, 9703 (2007).

[405] A. Kubisch, E. A. Fronhofer, H. J. Poethke, and T. Hovestadt, The American Naturalist **181**, 700 (2013).

[406] É. Kisdi, The American Naturalist **159**, 579 (2002).

[407] T. A. Perkins, B. L. Phillips, M. L. Baskett, and A. Hastings, Ecology Letters **16**, 1079 (2013).

[408] B. L. Phillips, G. P. Brown, and R. Shine, Journal of evolutionary biology **23**, 2595 (2010).

[409] O. Benichou, V. Calvez, N. Meunier, and R. Voituriez, Physical Review E **86**, 041908 (2012).

[410] I. Filin, R. D. Holt, and M. Barfield, The American Naturalist **172**, 233 (2008).

[411] J. L. Williams, B. E. Kendall, and J. M. Levine, Science **353**, 482 (2016).

[412] B. M. Ochocki and T. E. Miller, Nature communications **8**, 14315 (2017).

[413] L. Excoffier, M. Foll, and R. J. Petit, Annual Review of Ecology, Evolution, and Systematics **40**, 481 (2009).

[414] M. Cobben, J. Verboom, P. Opdam, R. Hoekstra, R. Jochem, and M. Smulders, Journal of theoretical biology **373**, 92 (2015).

[415] L. Roques, J. Garnier, F. Hamel, and E. K. Klein, Proceedings of the National Academy of Sciences **109**, 8828 (2012).

[416] J. Garnier and M. A. Lewis, Bulletin of mathematical biology **78**, 2165 (2016).

[417] D. M. Johnson, A. M. Liebhold, P. C. Tobin, and O. N. Bjørnstad, Nature **444**, 361 (2006).

[418] B. A. Melbourne and A. Hastings, Science **325**, 1536 (2009).

[419] H. Chen, Ecography **37**, 344 (2014).

[420] C. Weiss-Lehman, R. A. Hufbauer, and B. A. Melbourne, Nature communications **8**, 14303 (2017).

[421] M. Peltonen, A. M. Liebhold, O. N. Bjørnstad, and D. W. Williams, Ecology **83**, 3120 (2002).

[422] A. K. Sakai, F. W. Allendorf, J. S. Holt, D. M. Lodge, J. Molofsky, K. A. With, S. Baughman, R. J. Cabin, J. E. Cohen, N. C. Ellstrand, *et al.*, Annual review of ecology and systematics **32**, 305 (2001).

[423] W. E. Snyder and A. R. Ives, Ecology **84**, 91 (2003).

[424] A. M. Liebhold and P. C. Tobin, Population Ecology **48**, 253 (2006).

[425] N. Shigesada, K. Kawasaki, and Y. Takeda, The American Naturalist **146**, 229 (1995).

[426] M. Kot, M. A. Lewis, and P. van den Driessche, Ecology **77**, 2027 (1996).

[427] T. H. Keitt, M. A. Lewis, and R. D. Holt, The American Naturalist **157**, 203 (2001).

[428] R. D. Holt, M. Barfield, I. Filin, and S. Forde, The American Naturalist **178**, 488 (2011).

[429] Q.-X. Liu, M. Rietkerk, P. M. Herman, T. Piersma, J. M. Fryxell, and J. van de Koppel, Physics of life reviews **19**, 107 (2016).

[430] A. R. Kanarek and C. T. Webb, Evolutionary Applications **3**, 122 (2010).

[431] A. M. Turing, Philosophical Transactions of the Royal Society of London B: Biological Sciences **237**, 37 (1952).

[432] W. N. Everitt, in *Sturm-Liouville Theory* (Springer, 2005) pp. 271–331.

[433] B. Levitan and I. Sargsjan, "Sturm-liouville and dirac operators, volume 59 of mathematics and its applications (soviet series)," (1991).

[434] G. Teschl, *Ordinary differential equations and dynamical systems*, Vol. 140 (American Mathematical Society Providence, RI, 2012).

[435] B. Perthame and G. Barles, Indiana Univ. Math. J. **57**, 3275 (2008).

[436] G. Barles, S. Mirrahimi, B. Perthame, *et al.*, Methods and Applications of Analysis **16**, 321 (2009).

[437] A. Lorz, S. Mirrahimi, and B. Perthame, Communications in Partial Differential Equations **36**, 1071 (2011).

[438] N. Champagnat and P.-E. Jabin, Journal of Differential Equations **251**, 176 (2011).

[439] S. Mirrahimi, B. Perthame, and J. Y. Wakano, Journal of mathematical biology **64**, 1189 (2012).

[440] S. Mirrahimi and J.-M. Roquejoffre, C. R. Math. Acad. Sci. Paris **353**, 489 (2015).

[441] S. Mirrahimi and J.-M. Roquejoffre, J. Differential Equations **260**, 4717 (2016).

[442] B. Perthame and M. Gauduchon, Math Med Biol. **27**, 195 (2010).

[443] W. R. Rice and E. E. Hostert, Evolution **47**, 1637 (1993).

[444] E. Mayr, Evolution **1**, 263 (1947).

[445] E. Mayr, *Systematics and the origin of species, from the viewpoint of a zoologist* (Harvard University Press, 1999).

[446] T. Dobzhansky, *Genetics and the Origin of Species*, Vol. 11 (Columbia university press, 1982).

[447] R. Ferriere and M. Gatto, in *Proc. R. Soc. Lond. B*, Vol. 251 (The Royal Society, 1993) pp. 33–38.

[448] R. Ferriere, J. L. Bronstein, S. Rinaldi, R. Law, and M. Gauduchon, Proceedings of the Royal Society of London B: Biological Sciences **269**, 773 (2002).

[449] I. Hanski, Annals of the New York Academy of Sciences **1249**, 1 (2012).

[450] G. Bocedi, S. C. Palmer, G. Pe'er, R. K. Heikkinen, Y. G. Matsinos, K. Watts, and J. M. Travis, Methods in Ecology and Evolution **5**, 388 (2014).

[451] M. Scheffer and E. H. van Nes, Proceedings of the National Academy of Sciences **103**, 6230 (2006).

[452] I. Keller and O. Seehausen, Molecular ecology **21**, 782 (2012).

[453] D. Lépingle, Mathematics and Computers in Simulation **38**, 119 (1995).

[454] F. Tuerlinckx, E. Maris, R. Ratcliff, and P. De Boeck, Behavior Research Methods, Instruments, & Computers **33**, 443 (2001).

[455] A. Banerjee and R. N. Dave, in *Fuzzy systems, 2004. Proceedings. 2004 IEEE international conference on*, Vol. 1 (IEEE, 2004) pp. 149–153.

[456] B. W. Silverman, Journal of the Royal Statistical Society. Series B (Methodological) , 97 (1981).

[457] J. A. Hartigan, P. M. Hartigan, *et al.*, The annals of Statistics **13**, 70 (1985).

[458] G. P. M. Rozál and J. Hartigan, Journal of Classification **11**, 5 (1994).

[459] S. M. Bajgier and L. K. Aggarwal, Educational and Psychological Measurement **51**, 253 (1991).

[460] R. I. Andrushkiw, D. D. Klyushin, and Y. I. Petunin, (2008).

[461] D. W. Müller and G. Sawitzki, Journal of the American Statistical Association **86**, 738 (1991).

[462] C. Hösler, *Adaptive Species*, Ph.D. thesis, Universität Tübingen (2016).

[463] D. M. King, (2015).

[464] C. W. Clark, M. Mangel, *et al.*, *Dynamic state variable models in ecology* (Oxford University Press, 2000).

[465] U. Dieckmann and R. Law, *The geometry of ecological interactions: simplifying spatial complexity* (Cambridge University Press, 2000).

[466] R. H. MacArthur, *Geographical ecology: patterns in the distribution of species* (Princeton University Press, 1972).

[467] I. Sargsjan *et al.*, *Sturm—Liouville and Dirac Operators*, Vol. 59 (Springer Science & Business Media, 2012).

[468] G. Teschl, *Ordinary differential equations and dynamical systems*, Vol. 140 (American Mathematical Soc., 2012).

[469] M. Mangel, "The theoretical biologist's toolbox," (2006).

[470] M. Ackermann, M. Doebeli, and R. Gomulkiewicz, Evolution **58**, 2599 (2004).

[471] M. E. Arnegard and A. S. Kondrashov, Evolution **58**, 222 (2004).

[472] T. G. Barraclough and A. P. Vogler, The American Naturalist **155**, 419 (2000).

[473] N. H. Barton, A. M. Etheridge, and A. Véber, bioRxiv , 039768 (2016).

[474] S. F. Bailey, J. R. Dettman, P. B. Rainey, and R. Kassen, in *Proc. R. Soc. B*, Vol. 280 (The Royal Society, 2013) p. 20131253.

[475] R. E. Beardmore, I. Gudelj, D. A. Lipson, and L. D. Hurst, Nature **472**, 342 (2011).

[476] S. H. Berlocher, Heredity **83**, 652 (1999).

[477] S. H. Berlocher and J. L. Feder, Annual review of entomology **47**, 773 (2002).

[478] D. I. Bolnick, Nature **410**, 463 (2001).

[479] D. I. Bolnick and M. Doebeli, Evolution **57**, 2433 (2003).

[480] B. Bolker and S. W. Pacala, Theoretical population biology **52**, 179 (1997).

[481] B. M. Bolker and S. W. Pacala, The American Naturalist **153**, 575 (1999).

[482] E. Bouin and S. Mirrahimi, arXiv preprint arXiv:1307.8332 (2013).

[483] A. Buckling and P. B. Rainey, Nature **420**, 496 (2002).

[484] R. Bürger, Journal of mathematical biology **50**, 355 (2005).

[485] R. Byles, American Anthropologist **77**, 615 (1975).

[486] N. Champagnat, R. Ferrière, and S. Méléard, Theoretical population biology **69**, 297 (2006).

[487] N. Champagnat and S. Méléard, Journal of Mathematical Biology **55**, 147 (2007).

[488] N. Champagnat and S. Méléard, Probability Theory and Related Fields **151**, 45 (2011).

[489] N. Champagnat and P.-E. Jabin, Journal of Differential Equations **251**, 176 (2011).

[490] M. H. Chan, K. Hawkes, and P. S. Kim, Journal of Theoretical Biology (2016).

[491] R. T. Chesser and R. M. Zink, Evolution **48**, 490 (1994).

[492] L.-M. Chevin, G. Decorzent, and T. Lenormand, Evolution **68**, 1244 (2014).

[493] M. F. Claridge, H. A. Dawah, and M. R. Wilson, *Species: the units of biodiversity* (Chapman and Hall Ltd, 1997).

[494] J. A. Coyne and T. D. Price, Evolution **54**, 2166 (2000).

[495] K. D. Crow, H. Munehara, and G. Bernardi, Molecular Ecology **19**, 2089 (2010).

[496] D. A. Dawson, *Introductory lectures on stochastic population systems*, Tech. Rep. (Technical Report, 2010).

[497] M. de Manuel, M. Kuhlwilm, P. Frandsen, V. C. Sousa, T. Desai, J. Prado-Martinez, J. Hernandez-Rodriguez, I. Dupanloup, O. Lao, P. Hallast, *et al.*, Science **354**, 477 (2016).

[498] F. Débarre, S. Nuismer, and M. Doebeli, The American Naturalist **184**, 158 (2014).

[499] U. Dieckmann and M. Doebeli, Nature **400**, 354 (1999).

[500] R. Dirzo, H. S. Young, M. Galetti, G. Ceballos, N. J. Isaac, and B. Collen, Science **345**, 401 (2014).

[501] M. Doebeli, Journal of evolutionary biology **9**, 893 (1996).

[502] M. Doebeli and U. Dieckmann, Nature **421**, 259 (2003).

[503] M. Doebeli, U. Dieckmann, J. A. Metz, and D. Tautz, Evolution **59**, 691 (2005).

[504] M. Doebeli, H. J. Blok, O. Leimar, and U. Dieckmann, Proceedings of the Royal Society of London B: Biological Sciences **274**, 347 (2007).

[505] M. Drès and J. Mallet, Philosophical Transactions of the Royal Society B: Biological Sciences **357**, 471 (2002).

[506] M. Durinx, J. H. Metz, and G. Meszéna, Journal of mathematical biology **56**, 673 (2008).

[507] R. Durrett and S. Levin, Theoretical population biology **46**, 363 (1994).

[508] C. Eizaguirre, T. L. Lenz, A. Traulsen, and M. Milinski, Ecology letters **12**, 5 (2009).

[509] R. Erban, J. Chapman, and P. Maini, arXiv preprint arXiv:0704.1908 (2007).

[510] R. Erban and S. J. Chapman, Physical Biology **4**, 16 (2007).

[511] W. N. Everitt, in *Sturm-Liouville Theory* (Springer, 2005) pp. 271–331.

[512] M. Fasiolo and S. N. Wood, arXiv preprint arXiv:1511.02644 (2015).

[513] J. L. Feder, S. H. Berlocher, and S. B. Opp, in *Genetic structure and local adaptation in natural insect populations* (Springer, 1998) pp. 408–441.

[514] J. Felsenstein, Evolution , 124 (1981).

[515] K. E. Filchak, J. L. Feder, J. B. Roethel, and U. Stolz, Evolution , 187 (1999).

[516] S. M. Flaxman, J. L. Feder, and P. Nosil, Evolution **67**, 2577 (2013).

[517] G. Flierl, D. Grünbaum, S. Levins, and D. Olson, Journal of Theoretical biology **196**, 397 (1999).

[518] J. D. Fry, Evolution **57**, 1735 (2003).

[519] S. Gavrilets, Evolution **57**, 2197 (2003).

[520] S. Gavrilets, Journal of Heredity **105**, 743 (2014).

[521] A. J. Giraldez, R. M. Cinalli, M. E. Glasner, A. J. Enright, J. M. Thomson, S. Baskerville, S. M. Hammond, D. P. Bartel, and A. F. Schier, Science **308**, 833 (2005).

[522] E. E. Goldberg, J. R. Kohn, R. Lande, K. A. Robertson, S. A. Smith, and B. Igić, Science **330**, 493 (2010).

[523] Z. Gompert, J. A. Fordyce, M. L. Forister, A. M. Shapiro, and C. C. Nice, Science **314**, 1923 (2006).

[524] L. D. Gottlieb, in *Topics in plant population biology* (Springer, 1979) pp. 264–286.

[525] S. Gueron, S. A. Levin, and D. I. Rubenstein, Journal of Theoretical Biology **182**, 85 (1996).

[526] M. J. Hamilton, J. Lobo, E. Rupley, H. Youn, and G. B. West, arXiv preprint arXiv:1602.00631 (2016).

[527] M. Hassell and R. May, The Journal of Animal Ecology , 567 (1974).

[528] M. P. Hassell, S. W. Pacala, and G. Tingley, Philosophical Transactions of the Royal Society of London B: Biological Sciences **330**, 203 (1990).

[529] F. Herrerías-Azcué, V. Pérez-Muñuzuri, and T. Galla, Scientific Reports **8**, 4068 (2018).

[530] M. Higashi, G. Takimoto, and N. Yamamura, Nature **402**, 523 (1999).

[531] R. Highton, Herpetologica , 254 (1998).

[532] C. Hurt, K. Silliman, A. Anker, and N. Knowlton, Molecular ecology **22**, 4532 (2013).

[533] R. W. Ibrahim, M. Ahmad, and H. F. Al-Janaby, Saudi Journal of Biological Sciences **23**, S45 (2016).

[534] R. Ibsen-Jensen, K. Chatterjee, and M. A. Nowak, Proceedings of the National Academy of Sciences **112**, 15636 (2015).

[535] P.-E. Jabin and R. S. Schram, arXiv preprint arXiv:1601.04553 (2016).

[536] D. Jana and S. Ray, Modeling Earth Systems and Environment **2**, 1 (2016).

[537] D. Jana, R. Pathak, and M. Agarwal, Chaos, Solitons & Fractals **83**, 252 (2016).

[538] J. Johansson and J. Ripa, The American Naturalist **168**, 572 (2006).

[539] T. Joyce and J. Herrmann, in *Integral Biomathics* (Springer, 2012) pp. 191–193.

[540] E. Kisdi, Journal of Theoretical Biology **197**, 149 (1999).

[541] E. B. Knox and J. D. Palmer, Proceedings of the National Academy of Sciences **92**, 10349 (1995).

[542] A. S. Kondrashov and F. A. Kondrashov, Nature **400**, 351 (1999).

[543] A. S. Kondrashov, Theoretical population biology **24**, 121 (1983).

[544] A. S. Kondrashov, Theoretical population biology **29**, 1 (1986).

[545] A. S. Kondrashov and M. V. Mina, Biological Journal of the Linnean Society **27**, 201 (1986).

[546] S. Lamichhaney, J. Berglund, M. S. Almén, K. Maqbool, M. Grabherr, A. Martinez-Barrio, M. Promerová, C.-J. Rubin, C. Wang, N. Zamani, *et al.*, Nature **518**, 371 (2015).

[547] H. Le Nagard, L. Chao, and O. Tenaillon, BMC evolutionary biology **11**, 326 (2011).

[548] O. Leimar, Elements of Adaptive Dynamics , 117 (2005).

[549] D. Lépingle, Mathematics and Computers in Simulation **38**, 119 (1995).

[550] H. Levene, The American Naturalist **87**, 331 (1953).

[551] D. Liebers, P. De Knijff, A. J. Helbig, *et al.*, Proceedings of the Royal Society of London-B **271**, 893 (2004).

[552] C. Linn, J. L. Feder, S. Nojima, H. R. Dambroski, S. H. Berlocher, and W. Roelofs, Proceedings of the National Academy of Sciences **100**, 11490 (2003).

[553] S. Lion, Journal of theoretical biology (2015).

[554] A. Lorz, S. Mirrahimi, and B. Perthame, Communications in Partial Differential Equations **36**, 1071 (2011).

[555] P. Marrow, U. Dieckmann, and R. Law, Journal of mathematical biology **34**, 556 (1996).

[556] C. H. Martin, The American Naturalist **180**, E90 (2012).

[557] C. H. Martin, J. S. Cutler, J. P. Friel, C. Dening Touokong, G. Coop, and P. C. Wainwright, Evolution **69**, 1406 (2015).

[558] S. H. Martin, A. Eriksson, K. M. Kozak, A. Manica, and C. D. Jiggins, bioRxiv , 015800 (2015).

[559] K. D. McCoy, Trends in Parasitology **19**, 400 (2003).

[560] G. Meszéna, I. Czibula, and S. Geritz, Journal of Biological Systems **5**, 265 (1997).

[561] G. Meszena, É. Kisdi, U. Dieckmann, S. A. Geritz, and J. A. Metz, Selection **2**, 193 (2002).

[562] J. A. Metz, S. A. Geritz, G. Meszéna, F. J. Jacobs, and J. S. Van Heerwaarden, (1995).

[563] J. A. Metz, S. A. Geritz, G. Meszéna, F. J. Jacobs, J. S. Van Heerwaarden, *et al.*, Stochastic and spatial structures of dynamical systems **45**, 183 (1996).

[564] K. Meyer, arXiv preprint arXiv:1509.08175 (2015).

[565] S. Mirrahimi, B. Perthame, and J. Y. Wakano, Journal of mathematical biology **64**, 1189 (2012).

[566] G. G. Mittelbach, D. W. Schemske, H. V. Cornell, A. P. Allen, J. M. Brown, M. B. Bush, S. P. Harrison, A. H. Hurlbert, N. Knowlton, H. A. Lessios, *et al.*, Ecology letters **10**, 315 (2007).

[567] D. Morale, Future Generation Computer Systems **17**, 883 (2001).

[568] K. Mustin, T. G. Benton, C. Dytham, and J. M. Travis, Oikos **118**, 131 (2009).

[569] T. J. Near, D. I. Bolnick, and P. C. Wainwright, Evolution **59**, 1768 (2005).

[570] P. Nosil, Molecular Ecology **17**, 2103 (2008).

[571] M. A. Nowak, K. Sigmund, *et al.*, The Geometry of Ecological Interactions: Simplifying Spatial Complexity , 135 (2000).

[572] A. Okubo, Advances in biophysics **22**, 1 (1986).

[573] S. P. Otto and J. Whitton, Annual review of genetics **34**, 401 (2000).

[574] A. S. Papadopulos, W. J. Baker, and V. Savolainen, NATURAL PROCESSES, GENETICS AND BIODIVERSITY , 37 (2013).

[575] Y. Peng and T. Zhang, Applied Mathematics and Computation **275**, 1 (2016).

[576] A. B. Phillimore, C. D. L. Orme, G. H. Thomas, T. M. Blackburn, P. M. Bennett, K. J. Gaston, and I. P. Owens, The American Naturalist **171**, 646 (2008).

[577] J. Polechová and N. H. Barton, Evolution **59**, 1194 (2005).

[578] J. Polechová, N. Barton, and G. Marion, The American Naturalist **174**, E186 (2009).

[579] D. P. Prowell, M. McMichael, and J.-F. Silvain, Annals of the Entomological Society of America **97**, 1034 (2004).

[580] T. Rajala, S. Olhede, and D. Murrell, arXiv preprint arXiv:1803.01639 (2018).

[581] J. Ramsey and D. W. Schemske, Annual Review of Ecology and Systematics , 467 (1998).

[582] K. S. Reddy, M. Srinivas, A. Sabarmathi, K. Das, and N. Gazi, International Journal of Dynamical Systems and Differential Equations **6**, 36 (2016).

[583] M. L. Rosenzweig, Biological Journal of the Linnean Society **10**, 275 (1978).

[584] N. Rosser, K. M. Kozak, A. B. Phillimore, and J. Mallet, BMC evolutionary biology **15**, 125 (2015).

[585] P. Saratchandran, K. Ajithprasad, and K. Harikrishnan, Copyright (c) 2015 Annual Review of Chaos Theory, Bifurcations and Dynamical Systems (ARCTBDS). ISSN 2253-0371. All Rights Reserved. www. arctbds. com. , 10 (2015).

[586] D. Schluter *et al.*, SCIENCE-NEW YORK THEN WASHINGTON- , 798 (1994).

[587] D. Schluter, The American Naturalist **156**, S4 (2000).

[588] P. Shum, C. Pampoulie, K. Kristinsson, and S. Mariani, Molecular ecology **24**, 3652 (2015).

[589] M. Schulz, J. Freyhof, R. Saint-Laurent, K. Østbye, T. Mehner, and L. Bernatchez, Journal of Fish Biology **68**, 119 (2006).

[590] O. Seehausen, Trends in ecology & evolution **19**, 198 (2004).

[591] O. Seehausen and C. E. Wagner, Annual Review of Ecology, Evolution, and Systematics **45**, 621 (2014).

[592] M. Sezer and R. Butlin, Proceedings of the Royal Society of London B: Biological Sciences **265**, 2399 (1998).

[593] M. Slatkin, The American Naturalist **114**, 384 (1979).

[594] M. Slatkin, Genetics **93**, 755 (1979).

[595] S. S. Snorrason and S. Skúlason, Adaptive speciation. Cambridge University Press, Cambridge , 210 (2004).

[596] M. D. Sorenson, K. M. Sefc, and R. B. Payne, Nature **424**, 928 (2003).

[597] J. Stella, G. Jones, and M. Pratchett, Coral Reefs **29**, 957 (2010).

[598] T. F. Stuessy, Taxon **53**, 3 (2004).

[599] W. Sun, Y. Zhang, and X. Zhang, International Journal of Computer Mathematics , 1 (2015).

[600] G.-Q. Sun, Nonlinear Dynamics , 1 (2016).

[601] X. Tang and Y. Song, Chaos, Solitons & Fractals **81**, 303 (2015).

[602] H. Tang and Z. Liu, Applied Mathematical Modelling **40**, 726 (2016).

[603] C. E. Tarnita, C. H. Taubes, and M. A. Nowak, Journal of theoretical biology **320**, 10 (2013).

[604] E. B. Taylor and J. D. McPhail, Proceedings of the Royal Society of London B: Biological Sciences **267**, 2375 (2000).

[605] R. Taylor and V. Friesen, Molecular Ecology (2017).

[606] G. Teschl, *Ordinary differential equations and dynamical systems*, Vol. 140 (American Mathematical Society Providence, RI, 2012).

[607] C. Theodoropoulos, Y.-H. Qian, and I. G. Kevrekidis, Proceedings of the National Academy of Sciences **97**, 9840 (2000).

[608] G. F. Turner and M. T. Burrows, Proceedings of the Royal Society of London B: Biological Sciences **260**, 287 (1995).

[609] D. Udovic, American Naturalist , 621 (1980).

[610] J. T. Van Leuven, R. C. Meister, C. Simon, and J. P. McCutcheon, Cell **158**, 1270 (2014).

[611] G. S. van Doorn, U. Dieckmann, and F. J. Weissing, The American Naturalist **163**, 709 (2004).

[612] S. Wallace, J. Morris-Pocock, J. González-Solís, P. Quillfeldt, and V. Friesen, Molecular Phylogenetics and Evolution **107**, 39 (2017).

[613] X. Wang, M. Fan, and L. Hao, Mathematical Biosciences (2016).

[614] F. J. Weissing, P. Edelaar, and G. S. van Doorn, Behavioral ecology and sociobiology **65**, 461 (2011).

[615] J. H. Werren, Endless forms: species and speciation , 245 (1998).

[616] D. S. Wilson and M. Turelli, American Naturalist , 835 (1986).

[617] T. K. Wood and M. Keese, Evolution , 619 (1990).

[618] J. B. Yoder and S. L. Nuismer, The American Naturalist **176**, 802 (2010).

[619] W. Young, A. Roberts, and G. Stuhne, Nature **412**, 328 (2001).

[620] F. Yu, The Annals of Applied Probability , 840 (2007).

[621] V. I. Yukalov, E. Yukalova, and D. Sornette, Physica D: Nonlinear Phenomena **241**, 1270 (2012).

[622] R. Yukilevich, Evolution **68**, 1150 (2014).

[623] Y. Zhang, X. Yan, B. Liao, Y. Zhang, and Y. Ding, Mathematical biosciences **272**, 15 (2016).

[624] Y. Zhao and S. Yuan, Chaos, Solitons & Fractals **85**, 98 (2016).

[625] Y. Zhao, J.-W. Tang, Z. Yang, Y.-B. Cao, J.-L. Ren, Y. Ben-Abu, K. Li, X.-Q. Chen, J.-Z. Du, and E. Nevo, Proceedings of the National Academy of Sciences **113**, 2146 (2016).

[626] O. Zhdanova and E. Frisman, Ecological Complexity (2015).

[627] H. C. Berg, *Random walks in biology* (Princeton University Press, 1993).

[628] G. B. Folland, *Fourier analysis and its applications*, Vol. 4 (American Mathematical Soc., 1992).

[629] T. Nyström, Personal Communication (2012).

[630] M. Andrade-Restrepo, Biophysical journal .

[631] P. S. Burada, P. Hänggi, F. Marchesoni, G. Schmid, and P. Talkner, ChemPhysChem **10**, 45 (2009).

[632] H. S. Carslaw and J. C. Jaeger, Oxford: Clarendon Press, 1959, 2nd ed. (1959).

[633] A. Kusumi and Y. Sako, Current opinion in cell biology **8**, 566 (1996).

[634] M. J. Saxton, Biophysical journal **66**, 394 (1994).

[635] M. J. Saxton, Biophysical journal **70**, 1250 (1996).

[636] P. Tessarz, M. Schwarz, A. Mogk, and B. Bukau, Molecular and cellular biology **29**, 3738 (2009).

[637] P. B. Visscher, Physical Review B **13**, 3272 (1976).

[638] S. Wang, M. Zhao, and X. Li, Physica A: Statistical Mechanics and its Applications **390**, 3397 (2011).

[639] D. Carval and R. Ferriere, Evolution **64**, 2988 (2010).

[640] N. Champagnat and S. Méléard, Journal of Mathematical Biology **55**, 147 (2007).

[641] N. Champagnat and P.-E. Jabin, Journal of Differential Equations **251**, 176 (2011).

[642] L. De Meester and J. Pantel, Journal of Limnology **73** (2014).

[643] F. Dercole, R. Ferrière, and S. Rinaldi, Evolution **56**, 1081 (2002).

[644] F. Dercole, R. Ferriere, and S. Rinaldi, Proceedings of the Royal Society of London B: Biological Sciences , rspb20100209 (2010).

[645] R. Ferriere and S. Legendre, Phil. Trans. R. Soc. B **368**, 20120081 (2013).

[646] S. A. Geritz, E. van der Meijden, and J. A. Metz, Theoretical population biology **55**, 324 (1999).

[647] D. Gíslason, M. M. Ferguson, S. Skúlason, and S. S. Snorrason, Canadian Journal of Fisheries and Aquatic Sciences **56**, 2229 (1999).

[648] L. E. Hallacher and D. A. Roberts, Environmental Biology of Fishes **12**, 91 (1985).

[649] K. Johannesson, E. Rolan-Alvarez, and A. Ekendahl, Evolution , 1180 (1995).

[650] A. Kubisch, T. Degen, T. Hovestadt, and H. J. Poethke, Ecography **36**, 873 (2013).

[651] O. Leimar, M. Doebeli, and U. Dieckmann, Evolution **62**, 807 (2008).

[652] N. Loeuille, M. Loreau, and R. Ferrière, Journal of theoretical biology **217**, 369 (2002).

[653] S. Mirrahimi, B. Perthame, and J. Y. Wakano, Journal of mathematical biology **64**, 1189 (2012).

[654] M. A. Nowak, K. Sigmund, *et al.*, The Geometry of Ecological Interactions: Simplifying Spatial Complexity , 135 (2000).

[655] J. Polechová, N. Barton, and G. Marion, The American Naturalist **174**, E186 (2009).

[656] P. B. Rainey and M. Travisano, Nature **394**, 69 (1998).

[657] D. N. Reznick, The American Naturalist **181**, S1 (2013).

[658] I. M. Smallegange and T. Coulson, Trends in ecology & evolution **28**, 143 (2013).

[659] J. C. Stegen, B. J. Enquist, and R. Ferriere, Ecology letters **12**, 1001 (2009).

[660] J. C. Stegen, B. J. Enquist, and R. Ferriere, The American Naturalist **180**, E110 (2012).

[661] U. K. Schliewen, D. Tautz, and S. Pääbo, Nature **368**, 629 (1994).

[662] U. Schliewen, K. Rassmann, M. Markmann, J. Markert, T. Kocher, and D. Tautz, Molecular Ecology **10**, 1471 (2001).

[663] C. M. Taylor and A. Hastings, Ecology Letters **8**, 895 (2005).

[664] A. J. Tack and A.-L. Laine, European journal of plant pathology **138**, 667 (2014).

[665] C. Wilding, R. Butlin, and J. Grahame, Journal of Evolutionary Biology **14**, 611 (2001).

[666] L. You, J. S. Brown, F. Thuijsman, J. J. Cunningham, R. A. Gatenby, J. Zhang, and K. Staňková, Journal of theoretical biology **435**, 78 (2017).

[667] R. D. Holt and M. Barfield, Proceedings of the Royal Society of London B: Biological Sciences **276**, 1435 (2009).

[668] J. M. Travis, M. Delgado, G. Bocedi, M. Baguette, K. Bartoń, D. Bonte, I. Boulangeat, J. A. Hodgson, A. Kubisch, V. Penteriani, *et al.*, Oikos **122**, 1532 (2013).

[669] A. Hastings and D. Wollkind, Theoretical Population Biology **21**, 44 (1982).

[670] J. M. Greenwood-Lee and P. D. Taylor, Evolutionary Ecology Research **3**, 649 (2001).

[671] B. J. Balkau and M. W. Feldman, Genetics **74**, 171 (1973).

[672] D. M. Drown, M. F. Dybdahl, and R. Gomulkiewicz, Evolution **67**, 3290 (2013).

[673] C. L. Hughes, C. Dytham, and J. K. Hill, Ecological Entomology **32**, 437 (2007).

[674] J. Travis, T. Münkemüller, and O. Burton, Journal of evolutionary biology **23**, 2656 (2010).

[675] R. C. Henry, G. Bocedi, and J. M. Travis, Journal of Theoretical Biology **321**, 1 (2013).

[676] M. R. Klass, Mechanisms of ageing and development **22**, 279 (1983).

[677] M. V. Blagosklonny, Cell cycle **7**, 3344 (2008).

[678] J. Miquel, A. Economos, J. Fleming, and J. Johnson Jr, Experimental gerontology **15**, 575 (1980).

[679] H. Van Remmen and A. Richardson, Experimental gerontology **36**, 957 (2001).

[680] M. A. Mastrangelo and W. J. Bowers, BMC neuroscience **9**, 81 (2008).

[681] J. R. D. Simoes, P. Bourgine, D. Grebenkov, and N. Peyriéras, in *6th International Conference on Pattern Recognition Applications and Methods* (SCITEPRESS-Science and Technology Publications, 2017) pp. pp–746.

[682] N. Bellomo, A. Bellouquid, and M. Delitala, Mathematical Models and Methods in Applied Sciences **14**, 1683 (2004).

[683] A. Kumar, K. Pate, M. Moss, D. Dean, and V. Rangachari, PLoS One **9**, e111492 (2014).

[684] D. Dean, K. Pate, M. Moss, and V. Rangachari, Biochemistry **55**, 2238 (2016).

[685] S. Linse, Biophysical reviews **9**, 329 (2017).

[686] J. Prüss, L. Pujo-Menjouet, G. Webb, and R. Zacher, Discrete Contin. Dyn. Syst. Ser. B **6**, 225 (2006).